



ΠΟΛΥΤΕΧΝΕΙΟ ΚΡΗΤΗΣ
TECHNICAL UNIVERSITY OF CRETE

School of Mineral Resources Engineering

BSc Thesis

**Mineralogical and spectroscopical study of ordinary chondrites and
implications on potential asteroid mining**

Myrto Simopoulou

Examination committee

Dr. Platon N. Gamaletsos, Assistant Professor, School of Mineral Resources Engineering, Chania, Greece (supervisor)

Dr. Ioannis Baziotis, Associate Professor, Agricultural University of Athens, Laboratory of Mineralogy and Geology, Athens, Greece

Dr. Dimitrios Palles, Research Scientist, Theoretical & Physical Chemistry Institute, National Hellenic Research Foundation, Athens, Greece

Chania, 2024

Υπεύθυνη Δήλωση Συγγραφέα

Η προπτυχιακή φοιτήτρια που εκπόνησε την παρούσα διπλωματική εργασία φέρει ολόκληρη την ευθύνη προσδιορισμού της δίκαιης χρήσης του υλικού, η οποία ορίζεται στη βάση των εξής παραγόντων: του σκοπού και χαρακτήρα της χρήσης (μη-εμπορικός, μη-κερδοσκοπικός, αλλά εκπαιδευτικός και ερευνητικός), της φύσης του υλικού που χρησιμοποιεί (τμήμα κειμένου, πίνακες, σχήματα, εικόνες κλπ.), του ποσοστού και της σημαντικότητας του τμήματος που χρησιμοποιεί σε σχέση με το όλο κείμενο υπό copyright, και των πιθανών συνεπειών της χρήσης αυτής στην αγορά ή τη γενικότερη αξία του υπό copyright κειμένου. Κατά συνέπεια, δηλώνει ρητά ότι, η παρούσα εργασία αποτελεί αποκλειστικά προϊόν προσωπικής εργασίας και δεν προσβάλλει κάθε μορφής πνευματικά δικαιώματα τρίτων και δεν είναι προϊόν μερικής ή ολικής αντιγραφής, οι πηγές δε που χρησιμοποιήθηκαν περιορίζονται στις βιβλιογραφικές αναφορές και μόνον. Η έγκριση της παρούσας διπλωματικής εργασίας από το Πολυτεχνείο Κρήτης, δε σημαίνει αποδοχή των απόψεων της/του συγγραφέα (Νόμος 5343/1932, άρθρο 202).

Author's Disclaimer

The undergraduate student who prepared this thesis bears the entire responsibility of determining the fair use of the material, which is defined based on the following factors: the purpose and nature of the use (non-commercial, non-profit, but educational and research), the nature of the material it uses (part of text, tables, figures, images, etc.), the percentage and importance of the part it uses in relation to the whole text under copyright, and the possible consequences of this use on the market or the general value of the copyrighted text.

Prologue

The experimental part of the present study was conducted partially at the Department of Mineralogy and Petrography of the National History Museum Vienna (Vienna, Austria) under the guidance of Dr. Ludovic Ferrière and assistance by Dr. Wencke Wegner, at the University of Münster (Münster, Germany) under the guidance of Prof. Dr. Stephan Klemme and assistance by Dr. Jasper Berndt, at the Agricultural University of Athens (Athens, Greece) under the guidance of Assoc. Prof. Dr. Ioannis Baziotis and at the National Hellenic Research Foundation (Athens, Greece) co-coordinated by Dr. Dimitrios Palles. The present BSc thesis was supervised by Asst. Prof. Dr. Platon N. Gamaletsos (School of Mineral Resources Engineering /SMRE – Technical University of Crete / TUC - Chania, Greece). In this work, a meteorite sample was evaluated - through laboratory methods. The thin section of the meteorite Slobodka NHMW-L4372 was collected from the collection of the Natural History Museum of Vienna (Vienna, Austria). It is important to mention that the undergraduate student Ms. Myrto Simopoulou from SMRE/TUC received support for this research from the Erasmus+ traineeship program of the European Union.

Acknowledgments

I am extremely thankful to those who contributed in their way to complete this thesis. Without the help of my examination committee, this journey would not have been possible. Firstly, I would like to express my deepest gratitude to my supervisor, Asst. Prof. Dr. Platon N. Gamaletsos, for his unwavering support, valuable guidance, and prompt responses to my queries. I want to express my sincere gratitude towards Assoc. Prof. Dr. Ioannis Baziotis for sharing his knowledge and expertise with me and for his invaluable patience and feedback. Moreover, I would like to express my heartfelt appreciation and gratitude to Dr. Dimitrios Palles for the knowledge and advice he imparted to me on his expertise and for giving me the opportunity to work and collaborate with him in the laboratory.

Additionally, this endeavor would not have been possible without the generous support from the Erasmus+ traineeship program of the European Union approved by the Technical University of Crete (TUC), which financed my research at the Natural History Museum of Vienna (Vienna, Austria). Many thanks for allowing EPMA work to be completed at the Natural History Museum of Vienna (Vienna, Austria) and at the University of Münster (Münster, Germany), and Raman Spectroscopy work at the National Hellenic Research Foundation (Athens, Greece) and at the University of Münster. Special thanks to Mr. Ludovic Ferrière, Curator of the meteorite collection of NHMW, for supervising the Erasmus+ traineeship program. I would like to express my gratitude for his guidance, support, and contribution throughout the program. Also, I would like to express my sincere appreciation to Dr. Wencke Wegner for her assistance and for providing knowledge and expertise in acquiring EPMA data, shaping my understanding of the subject matter. Last but not least, I deeply acknowledge Prof. Dr. Stephan Klemme and especially Dr. Jasper Berndt for additional EPMA study of the meteorite sample at the University of Münster.

We are also thankful for the use of open access software packages such as ImageJ, CrystalSleuth, and Fityk. To reference minerals, we utilized the websites of Mindat.org, Webmineral.com, and highpmineral.com (High-Pressure Mineral Database). For meteorite references, we referred to the Meteoritical Bulletin Database. To conduct Raman spectroscopy, we used the RRUFF Database. Additionally, we used PTGui software and

CorelDraw, specifically XtalDraw software for image editing, and AmScope camera software for microscope imaging including the scale.

Finally, I would be remiss in not mentioning my family, especially my parents, and my sisters. I want to thank them for their unlimited support throughout my undergraduate studies. I would like to thank my close friends for being always there for me. Their support and belief in me have kept my spirits and motivation high during this process.

Abstract

A refined view of mineralogy and the spectroscopic study of the fallen Slobodka is presented, and this research has been conducted to complete the study of this thesis. The meteorite is an L4 ordinary chondrite. The thin section of the meteorite highlights the features that indicate a shock impact, including a shock melt vein. To the best of our knowledge, it is reported for the first time in this meteorite, a shock vein containing four high-pressure polymorphs, albitic jadeite, majorite, wadsleyite, and tuite. After studying the characteristics of the sample, it is concluded that Slobodka is a shocked sample with shock stage S4.

Περίληψη

Στα πλαίσια της παρούσης διπλωματικής εργασίας, παρουσιάζονται τα δεδομένα που εξήχθησαν από την ορυκτολογική και φασματοσκοπική μελέτη του μετεωρίτη Slobodka. Ο μετεωρίτης είναι ένας τυπικός χονδρίτης, τύπου L4. Η λεπτή τομή του μετεωρίτη τονίζει τα χαρακτηριστικά που υποδηλώνουν την πρόσκρουσή του, συμπεριλαμβανομένης της ύπαρξης μιας φλέβας τήξης κρούσης (shock melt vein). Εξ' όσον γνωρίζουμε, για πρώτη φορά στη βιβλιογραφία και στα πλαίσια της παρούσης, αποδεικνύεται ότι ο μετεωρίτης εμφανίζει στη φλέβα κρούσης ορυκτά υψηλών πιέσεων, που συμπεριλαμβάνει τέσσερις φάσεις πολύμορφων υψηλών πιέσεων (albitic jadeite, majorite, wadsleyite και tuite). Έπειτα από τη μελέτη των χαρακτηριστικών του δείγματος συμπεραίνεται ότι ο μετεωρίτης Slobodka έχει υποστεί σοκ με στάδιο κρούσης S4.

Keywords

Slobodka meteorite; Ordinary chondrite; L-chondrite; asteroids; High-pressure polymorphs; shock stage

Λέξεις κλειδιά

Slobodka μετεωρίτης, τυπικός χονδρίτης, χονδρίτης τύπου-L, αστεροειδής, υψηλών πιέσεων πολύμορφα, στάδιο μεταμόρφωσης λόγω σοκ

CONTENTS

1	INTRODUCTION	1
1.1	Goal of the Study	1
1.2	Celestial-objects Definition.....	2
1.2.1	Meteoroid	2
1.2.2	Meteor	2
1.2.3	Meteorite	2
1.2.4	Asteroid	3
1.2.5	Comet	3
1.3	Meteorite Classification.....	3
1.3.1	Chondritic Meteorites	4
1.3.2	Chondrules	4
1.3.3	Chondrite Classification.....	8
1.3.4	Petrologic Type.....	9
1.3.5	Ordinary Chondrites	9
1.4	Minerals in Meteorites – Definitions	10
1.4.1	Olivine Group of Minerals	10
1.4.2	Pyroxene Group of Minerals	12
1.4.3	Feldspar Group of Minerals.....	14
1.4.4	Iron-Nickel Minerals	15
1.4.5	Iron Sulfide Mineral.....	15
1.4.6	Phosphates	16
1.4.7	Chromite.....	16
1.5	Polymorphs – Definitions	16
1.5.1	Wadsleyite.....	17
1.5.2	Majorite.....	18
1.5.3	Albitic Jadeite	18
1.5.4	Tuite	19
1.6	Melt Veins.....	19
1.7	The Shock Classification of Meteorites.....	20
1.7.1	Shock Conditions	20
1.7.2	Shock Features	21
1.7.3	Shock Classification	23
2	MATERIALS AND METHODS	28
2.1	Sample	28
2.2	Optical Microscope.....	28
2.3	ImageJ / FIJI	30
2.4	Electron Probe Micro-Analysis (EPMA)	31
2.5	Raman Spectroscopy	34
3	RESULTS.....	39
3.1	Petrography	39
3.1.1	Groundmass	39
3.1.2	Melt Vein	57
3.2	Mineral Chemistry	61
3.2.1	Regions of Interest	61
3.2.2	Groundmass	62
3.2.3	Melt Vein	68
3.3	Raman Data Acquisition	69
3.3.1	Annotated Marked Areas in the Studied Melt Vein	72
4	Discussion.....	91
4.1	Classification of the Slobodka meteorite.....	91
4.1.1	Petrologic Characterization for Major Chondrite Groups	91
4.1.2	Petrologic Type.....	93
4.2	Shock Stage Distribution.....	96
4.2.1	Shock Features – Shock Classification	98
4.3	Shock Conditions and Barometry	99

4.4	Implications of Potential Asteroid Mining	101
5	CONCLUSIONS	104
6	REFERENCES	105
7	APPENDIX	112

Tables

Table 1: Shock classification scheme by Stöffler & Grieve (2007): Classification of shocked chondritic meteorites and olivine-rich crystalline rocks (progressive stages of shock metamorphism) modified after Stöffler <i>et al.</i> (1991); shock pressure data are based on experimental data given in Stöffler <i>et al.</i> (1991); pressures given in columns 4 – 6 indicate the upper limit of the shock stage in question; temperature data refer to the ambient temperature before shock compression; *from Stöffler <i>et al.</i> (1991); **from Schmitt (2000).	25
Table 2: Shock classification scheme by Fritz <i>et al.</i> (2017): Revision of the shock classification scheme for olivine-rich crystalline rocks including chondrites initially proposed by Stöffler <i>et al.</i> (1991) and Stöffler & Grieve (2007).	26
Table 3: Shock classification scheme by Stöffler <i>et al.</i> (2018). Definition of progressive stages of shock metamorphism for classification system C.	27
Table 4: Standards for silicates and chromites.	34
Table 5: Results of the calculations.	54
Table 6: Measurements of the lengths[min-max] [mm].....	56
Table 7: Calculated length of feldspar grains in the groundmass using the FIJI software package.	57
Table 8: Average petrologic characteristics of the major chondrite groups (Weisberg <i>et al.</i> , 2006).	92
Table 9: Results of criteria for classifying the Slobodka meteorite according to petrologic type, based on Van Schmus & Wood (1967). The painted squares indicate the regions that the results revealed to this BSc Thesis.	95
Table 10: The results for the shock classifications in the Slobodka meteorite based on the scheme by Stöffler & Grieve (2007). The colored rectangles correspond to the observations of the present work. *from Stöffler <i>et al.</i> (1991); **from Schmitt (2000).	98
Table 11: Observation of Slobodka meteorite from the thin section (NHMW-L4372) and assignment of the shock stage based on Stöffler <i>et al.</i> , 1991, Stöffler <i>et al.</i> , 2018, and Fritz <i>et al.</i> , 2017.	99

Figures

Figure 1: Textures of chondrules present in chondrites (viewed under BSE images; Russel et al., 2018). (A) Cryptocrystalline nonporphyritic chondrule (CC); (B) Radiating nonporphyritic chondrule (R); and (C) Barred textures such as barred olivine (BO); (D) Porphyritic (P) textures include olivine-rich (PO, type IA); (E) Porphyritic olivine-and pyroxene-rich (POP, type IAB); (F) Porphyritic pyroxene-rich (PP, type IB); (G) Porphyritic olivine (PO, type IIA); (H) Porphyritic olivine, and pyroxene-rich (POP, type IAB); (I) Porphyritic pyroxene (PP, type IIB). Abbreviations: O = olivine, P = pyroxene, MgO-rich = type I, FeO-rich = type II.	5
Figure 2: Graphical depiction by Russell et al. (2018) shows the thermal history relative to the chondrule liquidus of porphyritic (peak temperature below the liquidus), bared-dendritic (peak temperature slightly above the liquidus), and radial (peak temperature exceeds the liquidus) chondrules. The liquidus temperature varies from around 1400-1700 °C and the time spent at peak temperatures is relatively short (less than two hours)...	8
Figure 3: The chondritic meteorites are subdivided into three major classes, one group and one grouplet (Norton & Chitwood, 2008).	8
Figure 4: Ternary system of Ca_2SiO_4 - Mg_2SiO_4 - Fe_2SiO_4 for minerals of olivines (Davidson & Mukhopadhyay, 1984).	11
Figure 5: Ternary system (Morimoto, 1988) of CaSiO_3 - Mg_2SiO_6 - $\text{Fe}_2\text{Si}_2\text{O}_6$ for minerals of pyroxene group (Enstatite and Ferrosilite respectively) along with pyroxenoids (Wollastonite).	13
Figure 6: Diagram of feldspar classification: albite (Ab): $\text{NaAlSi}_3\text{O}_8$; orthoclase (Or): KAlSi_3O_8 ; anorthite (An): $\text{CaAl}_2\text{Si}_2\text{O}_8$ (Ghiorso, 1984)	14
Figure 7: Shock wave barometry with shock pressures based on the shock features of olivine and pyroxene in the meteorites (Stöffler et al. 2018 and reference therein).	22
Figure 8: The components of a conventional optical microscope (OM) used for rocks and minerals observation (aka petrographic microscope). Image Source: https://opengeology.org/Mineralogy/5-optical-mineralogy	29
Figure 9: Optical petrographic microscope equipped with a camera (Laboratory at Department of Natural Resources Development & Agricultural Engineering, Agriculture University of Athens).	30
Figure 10: EPMA and WDS operation. Image Source: https://www.cameca.com/products/epma/epma-introduce	32
Figure 11: Electron Probe Micro-Analysis / EPMA (Natural History Museum of Vienna); Ms Myrto Simopoulou visited the Department of Mineralogy and Petrography of the National History Museum Vienna (Vienna, Austria) in the frame of ERASMUS+ Student Mobility for Traineeships. The responsible person from the National History Museum Vienna was Dr. Ludovic Ferrière.	33
Figure 12: Schematic of Raman Spectrometer with microscopic attachment. Image Source: http://cnx.org	37
Figure 13: Raman Spectrometer at the Theoretical & Physical Chemistry Institute, National Hellenic Research Foundation (Athens, Greece).	38
Figure 14: (A) Slobodka image map in transmitted light (PPL); (B) Slobodka image map in reflected light.	40
Figure 15: (A) Slobodka image map in transmitted light (XPL, position 1); (B) Slobodka image map in transmitted light (XPL, position 2).	41
Figure 16: A representative olivine grain in the groundmass taken with the optical microscope in (A)PPL, and (B) XPL light.	42
Figure 17: A representative pyroxene grain in the groundmass taken with the optical microscope in (A)PPL, and (B) XPL light.	43
Figure 18: A representative plagioclase grain in the groundmass taken with the optical microscope in (A)PPL, and (B) XPL light.	43
Figure 19: Regions of interest (ROIs) with marked numbered chondrules.	44
Figure 20: Optical features of Slobodka thin section (ROIs: 01-03): (A) Radial Pyroxene (RP) chondrule (PPL), ROI 01; (B) Radial Pyroxene (RP)chondrule (XPL), ROI 01; (C) Radial Pyroxene (RP) chondrule (PPL), ROI 02; (D) Radial Pyroxene (RP) chondrule (XPL), ROI 02; (E) Radial Pyroxene (RP) chondrule (PPL), ROI 03; (F) Radial Pyroxene (RP) chondrule (XPL), ROI 03.	45
Figure 21: Optical features of Slobodka thin section (ROIs: 05,14): (A) Coarse grains Porphyritic Olivine (PO) chondrule (PPL), ROI 14; (B) Coarse grains Porphyritic Olivine (PO) chondrule (XPL), ROI 14; (C) Barred Olivine (BO) chondrule (PPL), ROI 05; (D) Barred Olivine (BO) chondrule (XPL), ROI 05; (E) Radial pyroxene(RP) chondrule (PPL), ROI 04; (F) Radial Pyroxene (RP) chondrule (XPL), ROI 04.	46
Figure 22: BSE images taken for the ROIs B, C, D, and E respectively in the groundmass (see: Fig. 39). (A) region B with Pl, Ol, Px, and Chr minerals detected; (B) region C with Ol, Pl, Px, and Chr minerals detected; (C) region D with Ol, Px, and Pl minerals detected; (D): region E with Ol, Pl, and Px minerals detected. For reference the abbreviations of Ol: olivine, Px: pyroxene, Pl: plagioclase, Chr: chromite, Met: metals.	47

Figure 23: BSE images taken for the ROIs G, H, I, and J respectively in the groundmass (see: Fig. 39). (A) region G with Met and Chr minerals detected; (B) region H with Chr, and FeS minerals detected; (C) region I with Chr minerals detected; (D) region J with Px, and Pl minerals detected. For reference the abbreviations of Ol: olivine, Px: pyroxene, Pl: plagioclase, Chr: chromite, Met: metals.	48
Figure 24: (A) two sets of planar fractures in olivine (PPL); (B) irregular fractures in olivine (XPL); (C) irregular fractures in olivine and pyroxene (XPL); (D) undulatory extinction in olivine (XPL); (E) one set of planar fractures in olivine (PPL); (F) moderate to strong mosaicism in orthopyroxene (XPL).	49
Figure 25: (A) plagioclase crystal with irregular fractures (XPL); (B) planar fractures in olivine (XPL); (C) two sets of planar fractures in an olivine crystal that exhibit undulatory extinction (PPL); (D) irregular fractures in olivine and pyroxene (XPL); (E) irregular fractures in olivine and pyroxene (PPL); (F) pyroxene and olivine at extinction to show mosaicism (XPL).	50
Figure 26: Statistic percentage of magnesium silicates and feldspar (N=100 olivines N=7 plagioclase).	51
Figure 27: Statistic percentage of shock features of magnesium silicates.	51
Figure 28: Regions of Interest (ROIs) for measuring the areas of each chondrule.	52
Figure 29: (A) Area of melt vein using FIJI software; (B) Area of the chondrule 1 in the groundmass.	53
Figure 30: Area of the measured percentage of the metal abundance in Slobodka.	55
Figure 31: Measured minimum and maximum length of the chondrule with the FIJI software package.	56
Figure 32: Overview of the Melt vein (back-scattered mosaic) of Slobodka meteorite.	58
Figure 33: BSE image of MV2 region.	58
Figure 34: An overview of the MV2 region (BEI image).	58
Figure 35: An overview of the MV2g region (BEI image).	58
Figure 36: BSE images were taken for the 2a,2b,2c, and 2d positions respectively in the melt vein (MV). (A-D) regions MV2a, MV2b, MV2c & MV2d with HP mineral (albitic jadeite). Abbreviations: Ol for olivine, Abjd for albitic jadeite.	59
Figure 37: Overview (back-scattered mosaic) of the investigated shock melt vein (MV) in the Slobodka meteorite. The locations of the HP phases are denoted with white rectangles and further expanded in the following figure (see: Fig. 38).	60
Figure 38: HP phase from the investigated MV of the Slobodka meteorite as it is denoted in the figure above (see: Fig. 37): (A) Majorite (Maj) in the form of euhedral to subhedral crystals; (B) tuite (Tu) grain (up to ~20 μm); (C) albitic jadeite (Abjd) crystals within a large irregular felsic domain; (D) wadsleyite (Wds) at the contact of a large clast with the SMV groundmass.	60
Figure 39: Annotated regions of interest (ROIs) in the groundmass.	62
Figure 40: En-Di-Hd-Fs quadrilateral with results based on the quadrilateral chart system (Morimoto, 1988). .	63
Figure 41: Statistic overview of the pyroxene grains in the studied sample.	63
Figure 42: An-Or-Ab ternary chart with results based on the ternary system of Ghiorso (1984).	64
Figure 43: Spinel group of Chr-Al-Usp spinel ternary chart with Slobodka NHMW-L4372 data based on ulvöspinel prism with endmembers of FeAl_2O_4 Hercynite- FeCr_2O_4 Chromite- Fe_2TiO_4 Ulvöspinel (Ganuza et al., 2014; Stevens, 1944).	65
Figure 44: Variation in Fe/Mn, and Fe/Mg ratios in L-chondrites with chemical analysis results of olivine and pyroxene.	66
Figure 45: Projection of the Fs/Fa results (see: Appendix Tables A1-2) adjusted to the referenced diagram based on the state of oxidation to conclude the H-L-LL Group of the meteorite (Lucas et al., 2019; Kei and Fredriksson, 1964).	67
Figure 46: Molar Fe-Mn-Mg ratio adjusted to the areas of Diopside, Low-Ca, and Olivine (Gastineau-Lyons et al. 2002).	68
Figure 47: Raman shifts of minerals from RRUFF Database: (A) olivine (R040018.3) and wadsleyite (R090004-532nm); (B) tuite (R120115-532nm), merrillite (R150063-532nm), and fluorapatite (R040098.3); (C) diopside (R040009.3), omphacite (R061129-532nm), jadeite (R050220.3); (D) majorite (R210005), and enstatite (R070418.3).	71
Figure 48: Regions displayed on the BSE images. (A) Region A with the positioned Raman regions of interest; (B) Region B with the positioned Raman regions of interest; (C) Region C with the positioned Raman regions of interest.	72
Figure 49: (A) BSE image with selected position of grain #01 in the melt vein, (B) Annotated Raman position at the rim of the grain, (C) Selected Raman spectrum mv_A_a_11, compared to reference spectra for olivine (black line; RRUFF R040018.3) and for wadsleyite (grey line; RRUFF R090004, 532 nm).	73

Figure 50: (A) BSE image with selected position of grain #02 in the melt vein, (B) Annotated Raman position at the rim of the grain, (C) Selected Raman spectrum mv_A_b_11, compared to reference spectrum for diopside (black line; RRUFF R040009.3)	74
Figure 51: (A) BSE image with selected position of grain #03 in the melt vein; (B) Annotated Raman position at the rim of the grain; (C) Selected Raman spectrum mv_A1_21, compared to reference spectra for jadeite (black line; RRUFF R050220.3) and omphacite (grey line; RRUFF R061129, 532 nm)	75
Figure 52: (A) BSE image with selected mv_B_b_226 position in the melt vein; (B) Annotated Raman position of wadsleyite grain with scale for reference (~ up to 2 μ m long); (C) Selected Raman spectrum mv_B_b_226 compared to referenced spectra from RRUFF database for wadsleyite (black line; RRUFF R090004, 532 nm) and for olivine (grey line; RRUFF R040018.3)	76
Figure 53: (A) BSE image with selected mv_B_g_11 position in the melt vein; (B) Annotated Raman position of jadeite grain; (C) Selected Raman spectrum mv_B_g_11 compared to referenced spectra from RRUFF database for jadeite (black line; RRUFF R050220.3) and for the omphacite (grey line; RRUFF R061129, 532 nm).	77
Figure 54: (A) BSE image with selected mv_B_a_21 position in the melt vein; (B) Annotated Raman position of the pyroxene grain; (C) Selected Raman spectrum mv_B_a_21 compared to referenced spectrum from RRUFF database for enstatite (black line; RRUFF R070418.3).	78
Figure 55: (A) BSE image with selected mv_B_c_21 position in the melt vein; (B) Annotated Raman position of the jadeite-tuite grain; (C) Selected Raman spectrum mv_B_c_21 compared to referenced spectra from RRUFF database for jadeite (grey line; RRUFF R050220.3) and for tuite (black line; R120115, 532 nm).	79
Figure 56: (A) BSE image with selected MV2c position in the melt vein; (B) Annotated Raman position of the jadeite-olivine grain; (C) Selected Raman spectra MV2c_11 and MV2c_21 compared to referenced spectra from RRUFF database for jadeite (grey line; RRUFF R050220.3) and for forsterite (black line; RRUFF R040018.3).	80
Figure 57: (A) BSE image with selected mv_C1_b_21 position in the melt vein; (B) Annotated Raman position of the jadeite grain; (C) Selected Raman spectrum mv_C1_b_21 compared to referenced spectra from RRUFF database for jadeite (grey line; RRUFF R050220.3) and for omphacite (black line; R061129, 532 nm).	81
Figure 58: (A) BSE image with selected mv_C_E_21 position in the melt vein; (B) Annotated Raman position of the tuite grain; (C) Selected Raman spectrum mv_C_E_21 compared to referenced spectra from RRUFF database for tuite (grey line; RRUFF R120115, 532 nm) and for fluorapatite (black line; RRUFF R040098.3).	82
Figure 59: (A) BSE image with selected mv_C_E_31 position in the melt vein; (B) Annotated Raman position of the pyroxene grain; (C) Selected Raman spectrum mv_C_E_31 compared to referenced spectra from RRUFF database for enstatite (black line; RRUFF R070418.3) and for majorite (blue line; RRUFF R210005).	83
Figure 60: (A) BSE image with selected MVF_11 position in the melt vein; (B) Annotated Raman position of the tuite grain; (C) Selected Raman spectrum MVF_11 compared to referenced spectra from RRUFF database for tuite (grey line; RRUFF R120115, 532 nm) and for fluorapatite (black line; RRUFF R040098.3).	84
Figure 61: (A) BSE image with selected mv_D_d_11 position in the melt vein; (B) Annotated Raman position of olivine grain; (C) Selected Raman spectrum mv_D_d_11 compared to referenced spectra from RRUFF database for wadsleyite (grey line; RRUFF R090004, 532 nm) and for olivine (black line; RRUFF R040018.3).	85
Figure 62: (A) BSE image with selected mv_A3_11 position in the melt vein; (B) Annotated Raman position of jadeite grain; (C) Selected Raman spectrum mv_A3_11 compared to referenced spectra from RRUFF database for jadeite (black line; RRUFF R050220.3), for enstatite (blue line; R070418.3), and for the diopside (grey line; RRUFF R040009.3).	86
Figure 63: (A) BSE image with selected positions in the melt vein; (B) Annotated Raman position of the tuite grain; (C) Selected Raman spectrum MVA1_11 and MVA1_21 compared to referenced spectra from RRUFF database for tuite (black line; RRUFF R120115, 532 nm) and for wustite (purple lines; Hazan et al., 2013).	87
Figure 64: (A) BSE image with selected position of grain mv_G_c_311 in the melt vein, (B) Annotated Raman position at the rim of the grain, (C) Selected Raman spectrum mv_G_c_311, compared to reference spectrum for majorite (black line; RRUFF R210005).	88
Figure 65: (A) BSE image with selected position of grain in the melt vein, (B) Annotated Raman position at the rim of the grain, (C) Selected Raman spectrum mv_E1_21, compared to reference spectra for olivine (black line; RRUFF R040018.3) and for wadsleyite (grey line; RRUFF R090004, 532 nm).	89
Figure 66: (A) BSE image with selected mv_C_A_11 position in the melt vein; (B) Annotated Raman position of jadeite grain; (C) Selected Raman spectrum mv_C_A_11 compared to referenced spectra from RRUFF database for Jadeite (black line; RRUFF R050220.3) and for the omphacite (grey line; RRUFF R061129, 532 nm).	90
Figure 67: Diagram showing the petrologic types for each chondrite group (Weissberg <i>et al.</i> 2006).	93
Figure 68: Illustration of the shock features: (A) Layer irregular fractures only; (B) Layer Planar Fractures only.	96
Figure 69: Image (A) image of the thin section of meteorite Slobodka; (B) illustrates the shock stage classification map of stages between S2 and S4.	97

Figure 70: (A) Phase diagram of MgSiO_3 (Tomioka <i>et al.</i> , 2017); (B) Phase diagram of $\text{CaMgSi}_2\text{O}_6$ (Tomioka <i>et al.</i> , 2017); Abbreviations: Ca-Pv: CaSiO_3 -perovskite	100
Figure 71: Phase diagram of $\text{CaMgSi}_2\text{O}_6$ (Tomioka <i>et al.</i> , 2017); Abbreviations: Ca-Pv: CaSiO_3 - perovskite	101

Appendix

Figures A

Figure A 1: BSE annotated images were taken for the Regions of interest B, C, D, and E respectively in the groundmass. Chemical composition of the annotated regions: (A) 1-5: olivine, 6 & 10-12: plagioclase, 7-9: pyroxene; (B) 1-5: chromite, 6-7, 12-13 & 17: pyroxene, 8-11: olivine, 14-16: plagioclase; (C) 1-5, 13-14 & 16: chromite, 6-9 & 11: plagioclase, 10-12: olivine, 15, 17: pyroxene; (D) 1-5: chromite, 6 & 7: olivine, 8 & 9: pyroxene, 10-12: plagioclase. 112

Figure A 2: BSE annotated images taken for the Regions of interest G, H, I, and J respectively in the groundmass. Chemical composition of the annotated regions: (A) 1-6 & 9: chromite, 7-8, 10-12 & 14-16: metal, 13: plagioclase; (B) 1-3: chromite, 4-7: FeS; (C) 1-4: chromite; (D) 1-2 & 5-9: olivine, 3 & 12-15: plagioclase... 113

Figure A 3: BSE annotated images taken for the 2a, 2b, 2c and 2d positions respectively in the melt vein. Chemical composition of the annotated regions: (A) 1 & 2: plagioclase; (B) 1: plagioclase; (C) 1 & 2: plagioclase; (D) 1-3: olivine. 114

Tables A

Table A 1: EPMA analysis of Olivine Group.....	115
Table A 2: EPMA analysis of Pyroxene Group.....	119
Table A 3: EPMA analysis of Plagioclase Group.	123
Table A 4: EPMA analysis of Spinel Group.	126
Table A 5: EPMA analysis of Metal Group	130
Table A 6: EPMA analysis of Sulfide Group.	131
Table A 7: Homogeneity of olivine composition.....	131

1 INTRODUCTION

1.1 Goal of the Study

The purpose of this study was to reclassify the Slobodka NHMW-L4372 meteorite, to identify the minerals that are present in the groundmass and the high-pressure phases in the melt vein of it, as well as to analyze the shock conditions and barometry of the sample. Besides, upon the results yielded in the frame of the present work, implications on potential asteroid mining have been discussed.

Meteorite classification, especially for historic falls, can be challenging due to limited and sometimes contradictory information in existing databases (Meteoritic Bulletin, MetBase). In addition to questions of provenance, although changes in compositional and textural classification standards for the identification of meteorite classes, petrologic types and shock stages have evolved over decades, however, they have not been consistently applied retroactively to historic falls. One consequence is that attempts to make statistical comparisons among the populations of meteorite falls and finds may be biased. Moreover, recent discoveries concerning shock-induced phases and the high-temperature (HT) and high-pressure (HP) conditions at which they form, motivate re-evaluation of the pressure-temperature-time history corresponding to each shock stage. For example, the presence, texture, and chemistry of the newly described phase albitic jadeite may become an important calibrant (alongside other HP phases with known stability fields) once it is synthesized (Gillet *et al.*, 2000; Ma *et al.*, 2022; Baziotis *et al.*, 2022a; Baziotis *et al.*, 2022b; Baziotis *et al.*, 2023). The primary reason for reclassifying the Slobodka meteorite is the information found during the present study about its classification while searching through the MetBull database. Specifically, the MetBull database (MB13) describes it as “L4 (fall, 1818)”, but it has recently been reclassified as H4(Rochette *et al.*, 2003). There may be some confusion about this meteorite because of another meteorite named “Slobodka (of P. Partsch)”, described as “L6 (find, 1838)”. The discovery of these data has brought to light the need for a reclassification of the specific sample of Slobodka NHMW-L4372 meteorite. The present work provides new petrographic and compositional data to update the class, petrologic type, and shock stage of

the ordinary chondrite Slobodka. The final classification of a meteorite sample is determined through the evaluation of mineralogical and spectroscopic data gathered during the research. Among the main objectives of this thesis, is to identify high-pressure polymorphs in the melt vein of the Slobodka meteorite, and it is intriguing to observe how these polymorphs are distributed throughout the main mass of the melt vein and study its conditions. In this thesis, the crucial terminology -necessary for understanding this study- has been defined.

1.2 Celestial-objects Definition

1.2.1 Meteoroid

A meteoroid is a rocky, sometimes metallic, body orbiting in interplanetary space around the sun (McCoy & Hutchison, 2004). It can be of any composition and may consist mainly of silicate, metallic Fe-Ni, sulfide, or ice (Rubin & Ma, 2021). It is roughly between the size of tiny grains of dust to the size of large boulders. Its length is considerably smaller than an asteroid and can become meteors or meteorites (Norton & Chitwood, 2008).

1.2.2 Meteor

A meteor is a meteoroid (McCoy & Hutchison, 2004) that has entered the Earth's atmosphere and was absorbed by the gravity of the planet. Many meteors are fragments from comets, asteroids, or planets that broke off when an asteroid crashed into them. It is a small body of rock but because of the friction from the atmosphere, causes it to heat up and glow (McCoy & Hutchison, 2004).

1.2.3 Meteorite

A meteorite is a meteoroid that enters Earth's atmosphere, goes through the atmosphere, and survives the crash to the surface. (Rubin & Ma, 2021). It is important to mention the impact a meteorite can have on the Earth's surface, not only a meteorite, but also an asteroid or comet, can be violent leading to the creation of numerous huge cavities called impact craters (Hodge, 1994). Also, meteorites can be categorized as falls or finds, with

falls being the ones that were witnessed upon their arrival, whilst finds are the ones that can be identified based on their composition and characteristics (Li *et al.*, 2019).

1.2.4 Asteroid

An asteroid is a rock object orbiting the sun, containing minerals such as silicates, and metals, and does not have a present atmosphere, often irregular in shape larger than meteoroids, and much smaller than a planet (Rubin & Ma, 2021). Most of the concentrations of known asteroids are in the asteroid belt between the orbit of Mars and Jupiter, and the Kuiper belt in the outer solar system (Weissman,1995).

1.2.5 Comet

A comet mostly consists of an ice core, often with a gas halo and tail (McCoy & Hutchison, 2004). This sets them apart from asteroids, which mostly contain rock or metal minerals. It is a small body orbiting the sun and when comets get closer to the sun, they release gasses, forming a halo of dust and gas, and this is caused mainly by solar radiation (de Val-Borro *et al.*, 2012). Most comets come from outside of or from the edge of the solar system, mainly from the Kuiper Belt (Weissman,1995).

1.3 Meteorite Classification

The classification system for meteorites was developed to help scientists efficiently categorize and refer to the different types of meteorites they study. This system was created with specific terminology for each characteristic feature, including mineralogical, petrological, chemical, and isotopic properties. There are three overall categories based on the abundant material of the composition of the meteorite: stony, metallic, and stony-iron meteorites (Weisberg *et al.*, 2006). The category of stony meteorites is divided into two major categories: chondrites and achondrites. The stony-iron category is divided into the pallasites and mesosiderite groups, while the metallic category is divided into primitive iron and magmatic iron meteorite groups (Weisberg *et al.*, 2006). The proportions of these components show very clear differences between classes of categorization of meteorites (Weisberg *et al.*, 2006).

1.3.1 Chondritic Meteorites

The chondritic meteorites belong to the stony meteorite category and are the most common type of meteorite found on Earth based on the Meteoritical Bulletin database (Weisberg *et al.*, 2006). They undergo shock, deformation, and mineral phase transformation, and the shock melting causes the creation of black melted veins, they are composed of chondrules and refractory inclusions along with isolated metal and sulfide grains, all surrounded by a fine-grained matrix (Weisberg *et al.*, 2006; Russell *et al.*, 2018). Most chondrites contain anhydrous silicate minerals (such as olivine, pyroxene, and plagioclase) alloys of iron and nickel (such as kamacite and taenite), iron-sulfides (such as troilite), and oxides (such as chromite) (Weisberg *et al.*, 2006; Russell *et al.*, 2018).

1.3.2 Chondrules

Chondrules are spherical-shaped inclusions, often described as molten droplets, and the majority consists of metal, silicates, and sulfides, which are abundant in the groundmass of chondritic meteorites (McCoy & Hutchison, 2004; Russell *et al.*, 2018). The conditions in which the chondrules have formed raise questions about their mechanism of formation. The formation of chondrules can be explained into two primary models, that have been described by many researchers (e.g., Huang *et al.*, 1996; Connolly & Desch, 2004; Connelly *et al.*, 2012; Johnson *et al.*, 2014; Villeneuve *et al.*, 2015). The open system model suggests that chondrules formed by the melting of dust in the solar protoplanetary disk, the solar nebula, interacted with the nearby gas, causing changes in their overall composition, including isotopes, and then cooled quickly to preserve disequilibrium features (Huang *et al.*, 1996; Connolly & Desch, 2004; Villeneuve *et al.*, 2015). The closed system model proposes that chondrules formed during protoplanetary impacts, and the duration of the collision is estimated at milliseconds (Huang *et al.*, 1996; Connolly & Desch, 2004; Connelly *et al.*, 2012). During an impact event, a small amount of crustal material is ejected at high velocity, some of which melts and forms droplets, while the remaining material may be transformed into proto-matrix material (Johnson *et al.*, 2014). As the material moves outward, it gradually cools. Despite this, most of the impact ejecta remain attached to the target body. The parent body of a chondrite may contain minerals from chondrites that were freely floating in space before being aggregated.

Understanding the distinctions between these models is of great significance, not only for understanding the origin of chondrules but also for assessing the potential impact of chondrule formation on planet formation. Therefore, many of these features are pivotal for petrological and chemical analysis to gain insights into the conditions of meteorite formation.

Chondrules are classified based on their texture and process of crystallization, with the texture range being proportional to the grain size (Russell *et al.*, 2018). There are two major types of texture, porphyritic and non-porphyritic chondrules (**Fig. 1**). The term porphyritic describes an igneous rock with larger crystals or phenocrysts embedded in a finer-grained matrix (Norton & Chitwood, 2008).

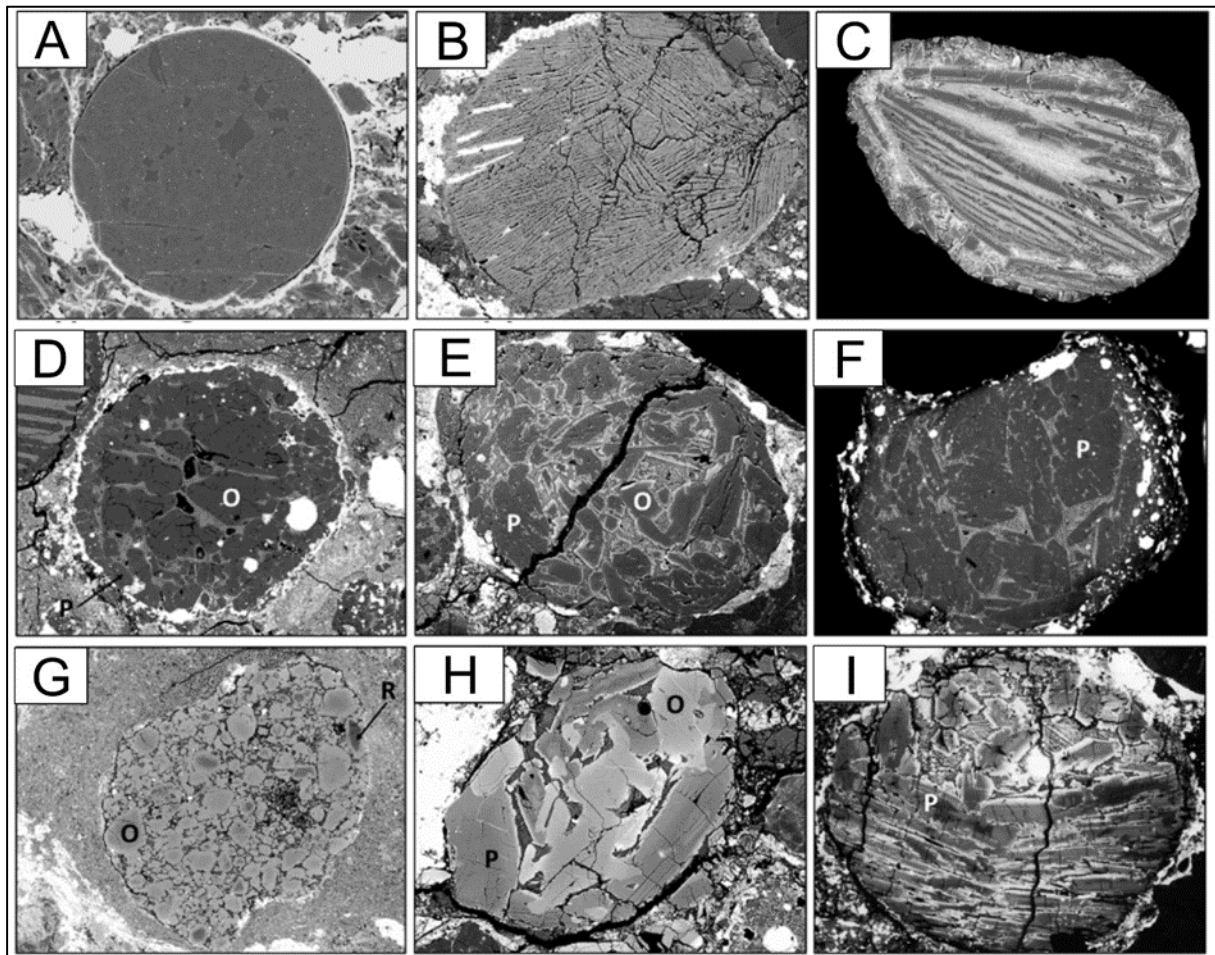


Figure 1: Textures of chondrules present in chondrites (viewed under BSE images; Russel *et al.*, 2018). (A) Cryptocrystalline nonporphyritic chondrule (CC); (B) Radiating nonporphyritic chondrule (R); and (C) Barred textures such as barred olivine (BO); (D) Porphyritic (P) textures include olivine-rich (PO, type IA); (E) Porphyritic olivine-and pyroxene-rich (POP, type IAB); (F) Porphyritic pyroxene-rich (PP, type IB); (G) Porphyritic olivine (PO, type IIA); (H) Porphyritic olivine, and pyroxene-rich (POP, type IAB); (I) Porphyritic pyroxene (PP, type IIB). Abbreviations: O = olivine, P = pyroxene, MgO-rich = type I, FeO-rich = type II.

The most commonly found minerals in these chondrules are olivine and pyroxene, which are both formed from complete silicate melts (Oulton *et al.*, 2016). The most abundant textural type of chondrules is the porphyritic type, and it is most frequent in the chondrite groups. Porphyritic textures can include silicates named as “PO” for porphyritic olivine (**Figs. 1D, 1G**), “PP” for porphyritic pyroxene (**Figs. 1F, 1I**), “POP” for the combination of porphyritic olivine and pyroxene (**Figs. 1E, 1H**), “GOP” for granular olivine and pyroxene combination, and “PPP” for porphyritic poikilitic pyroxene (Russell *et al.*, 2018). The term “poikilitic” refers to a texture in which small grains of one mineral are scattered irregularly within a larger crystal of another mineral (Norton & Chitwood, 2008).

Nonporphyritic textural chondrules can be classified into three types, cryptocrystalline / CC (**Fig. 1A**), Radiant / R (**Fig. 1B**), and Barred-dendritic / B (**Fig. 1C**), based on their appearance (Russell *et al.*, 2018). Barred textures are composed of bars of olivine (also known as “BO” chondrules) while radiating textures are composed of needles of pyroxene (also known as “RP” chondrules), and cryptocrystalline textures are composed of small grains that cannot be distinguished as individual crystals under the microscope (known as “CC” chondrules) (Russell *et al.*, 2018).

Apart from the latter categorization of the chondrule types, their classification can also be done based on the chemical composition of the crystal. At first, the type I chondrules can be named, which consist of olivine, low-Ca pyroxene, and iron (Russell *et al.*, 2018). The latter is typically present in the form of metal blebs rather than being combined with silicates (Russell *et al.*, 2018). Chondrules that have Fa and Fs values less than 10 mole % are classified as type I based on the FeO content of olivine and pyroxene (Brearley & Jones, 1998). Within this classification, olivine-rich chondrules are classified as type A, and pyroxene-rich chondrules are classified as type B (Russell *et al.*, 2018). On the other hand, type II chondrules are more oxidized and contain ferromagnesian olivine and pyroxene, with Fa and Fs values higher than 10 mole % (Fa = atomic Fe / (Fe+Mg) in olivine; Fs = atomic Fe / (Fe+Mg+Ca) in pyroxene) (Russell *et al.*, 2018).

Type I and type II chondrules coexist in most chondrite groups, differ in several important petrological aspects (Russell *et al.*, 2018). For instance, type I chondrules are highly reduced and can contain abundant Fe and Ni metals, most are typically found in unaltered chondrites of type 3 based on the petrologic type (Russell *et al.*, 2018). Olivine and pyroxene

grains in type II chondrules are often larger than those in type I chondrules, and commonly show significant compositional zoning arising from disequilibrium growth (Russell *et al.*, 2018). However, the proportion of type I and type II chondrules varies between ordinary chondrites, carbonaceous chondrites, and enstatite chondrites (Russell *et al.*, 2018). As mentioned above, these types are subdivided (Russell *et al.*, 2018) into type IA for MgO-rich and olivine-rich (**Fig. 1D**), type IB for MgO-rich and pyroxene-rich (**Fig. 1F**), and type IAB for MgO-rich and olivine and pyroxene-rich (**Fig. 1E**), whilst type IIA for FeO-rich and olivine-rich (**Fig. 1G**), type IIB for FeO-rich and pyroxene-rich (**Fig. 1I**) and type IIAB for FeO-rich and olivine and pyroxene-rich (**Fig. 1G**).

Porphyritic chondrites can be formed in two ways: through a thermal pulse that does not destroy many nuclei, or through the introduction of nuclei during cooling when dust impacts the surface of a chondrule (Russell *et al.*, 2018). Chondrules may have formed over a wide range of temperatures and heating durations, with cooling rates varying within chondrites and chondrule groups (Connolly & Hewins, 1990). When a chondrule is heated to a temperature close to its liquidus in the range from 1400 to 1700 °C (Radomsky & Hewins, 1990), porphyritic textures are formed when the grain is heated below the liquidus, and finally cools at initial rates between 10 and 1000 °C/h (Russell *et al.*, 2018; **Fig. 2**). Nonporphyritic chondrules are formed when the temperature peaks slightly above the liquidus and after that, they are cooled and, so, the range for barred and dendritic textures is at 500-3000 °C/h, and significantly for radiating textures is at 1000-3000 °C/h (Russell *et al.*, 2018; **Fig. 2**).

Chondrule mesostasis is the material that separates olivine and pyroxene in meteorites and sometimes this material is glassy and has a feldspathic composition (Russell *et al.*, 2018). During the cooling process, the final liquid present in the glass contains fine-grained elongated micro-crystallites, which are called quench crystals (Russell *et al.*, 2018). In unequilibrated chondrites, mesostasis can also be predominantly crystalline, typically consists of an intergrowth of plagioclase and high-Ca pyroxene with minor amounts of glass (Russell *et al.*, 2018). Also, metal and sulfide grains are often found as blebs in chondrules, typically concentrated in the outermost regions (Russell *et al.*, 2018).

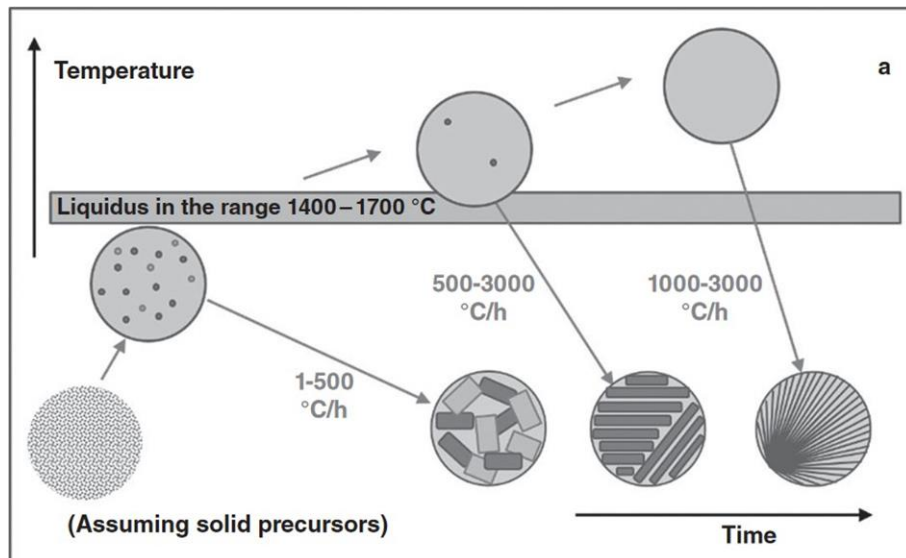


Figure 2: Graphical depiction by Russell et al. (2018) shows the thermal history relative to the chondrule liquidus of porphyritic (peak temperature below the liquidus), barred-dendritic (peak temperature slightly above the liquidus), and radial (peak temperature exceeds the liquidus) chondrites. The liquidus temperature varies from around 1400-1700 °C and the time spent at peak temperatures is relatively short (less than two hours).

1.3.3 Chondrite Classification

Chondrites are undifferentiated meteorites and are divided into classes, groups, grouplets, and clans (Norton & Chitwood, 2008). The three major classes are Enstatite (EH and EL), Carbonaceous (CI, CM, CR, CO, CV, CK, CH, and CB), and Ordinary (H, L, and LL) chondrites (**Fig. 3**). Rumuruti chondrites (aka “R” chondrites) make up a group, and K chondrites form a grouplet since there are fewer than 5 distinct ones (Norton & Chitwood, 2008).

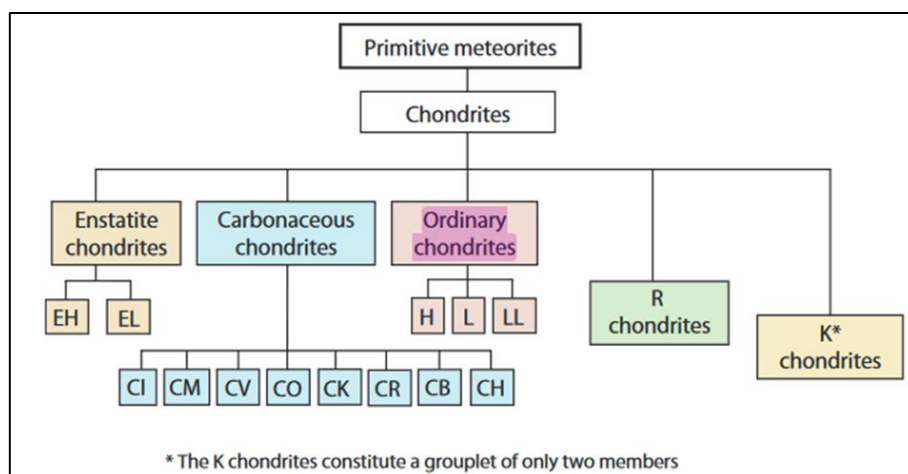


Figure 3: The chondritic meteorites are subdivided into three major classes, one group and one grouplet (Norton & Chitwood, 2008).

1.3.4 Petrologic Type

Chondrites also can be categorized based on their petrologic type, which indicates the degree to which chondrites were thermally metamorphosed or aqueously altered (Weissberg *et al.* 2006). On the one hand, thermal metamorphism is described as a sequence of mineralogical and textural changes that occur with increasing metamorphic temperatures (Norton & Chitwood, 2008). On the other hand, the extensive aqueous alteration has the characteristic that most of the containing olivines and pyroxenes have been altered to hydrous phases (Norton & Chitwood, 2008). The presence of recognizable chondrules, unaltered olivines, and pyroxenes originated by the aqueous alteration, while the relevant matrix is generally fully hydrated and minerals inside chondrules may show variable degrees of hydration; yet these meteorites are not thermally metamorphosed (Norton & Chitwood, 2008).

The petrologic type of a chondrite is assigned a number between 1 and 7 (Weissberg *et al.*, 2006). If a chondrite is assigned as type “3”, it means that its chondrules have not been altered, if the number is higher, it indicates an increase in thermal metamorphosis up to a maximum of type “7”, where the chondrules have been destroyed, and on the other hand, numbers lower than type “3” are assigned to chondrites that have undergone changes due to the presence of water (Weissberg *et al.*, 2006). The lowest value (i.e., “1”) is given to chondrites whose chondrules have been obliterated by this alteration (e.g., Norton & Chitwood, 2008).

1.3.5 Ordinary Chondrites

Ordinary chondrites (O) are undifferentiated meteorites that can be categorized based on the chemical composition of the iron abundance and consist of H-L-LL chondritic group types (**Fig. 3**) (Weissberg *et al.*, 2006; Norton & Chitwood, 2008). They are a class of stony chondritic meteorites (Weissberg *et al.*, 2006) and the most numerous chondrite groups of all found meteorites (Meteoritical Bulletin database). The origin parent bodies of the ordinary chondrites are thought to be delivered samples from the main belt region of the asteroid belt (Norton & Chitwood, 2008). Their composition is primarily minerals such as olivine, pyroxene,

and iron-nickel metal. The metal composition is used to classify ordinary chondrites into three distinct chemical groups: H, L, and LL chondrites (e.g., Norton & Chitwood, 2008).

The H chondrites are possibly from the parent body of asteroid of 6 Hebe and have the highest total iron composition with high metal Fe (25-31 % w/w), in freeform Fe-Ni (15-19 % w/w) and low iron oxide (Fa), they belong to the petrologic type of 3 to 7 and have mainly minerals belonging to the olivine and orthopyroxene groups (Norton & Chitwood, 2008). L chondrites are possibly from the asteroid 433 Eros and have a lower total iron composition of Fe (20-25 % w/w), in freeform Fe-Ni (4-10 % w/w), lower metal but higher iron oxide (Fa) in the silicates, they belong to the petrologic type of 3 to 7 and have mainly minerals such as olivines and orthopyroxenes, magnetite, and Fe-Ni. (Norton & Chitwood, 2008). LL chondrites are possibly from the asteroid 3628 Boznemcova and have a low total iron composition of Fe (19-22 % w/w) and in freeform Fe-Ni (1-3 % w/w), low metal but highest iron oxide content (Fa) in the silicates, and they belong to the petrologic type of 3 to 7 and have mainly minerals such as olivines and orthopyroxenes (Norton & Chitwood, 2008).

1.4 Minerals in Meteorites – Definitions

The nomenclature of the minerals used in this BSc thesis is based on the paper “Abbreviations for names of rock-forming minerals” by Whitney & Evans (2010).

1.4.1 Olivine Group of Minerals

The chemical formula of the olivine group of minerals is $(\text{Mg}, \text{Fe})_2\text{SiO}_4$ and its symbol is Ol. Olivines have orthorhombic symmetry and their structure consists of independent SiO_4 tetrahedra linked by divalent cations in six-fold coordination (e.g., Howie *et al.*, 1997; Deer *et al.*, 2013; Gamaletsos, 2024a and references therein). The members of the olivine group, the Mg/Fe olivines (Davidson & Mukhopadhyay, 1984; **Fig. 4**), form a complete ternary system of solid solution series and consist mainly of Mg_2SiO_4 (forsterite), Ca_2SiO_4 (larnite) and Fe_2SiO_4 (fayalite). It must be noted that at higher pressures, olivines adopt the denser structure of a spinel (e.g., Howie *et al.*, 1997; Deer *et al.*, 2013). Compositions of olivines are typically expressed as molar percentages of forsterite (Fo) and fayalite (Fa). For example, Fo70Fa30 or

Fo70 implies that olivine has a composition that is 70 percent forsterite or, similarly, that its composition is 30 percent fayalite.

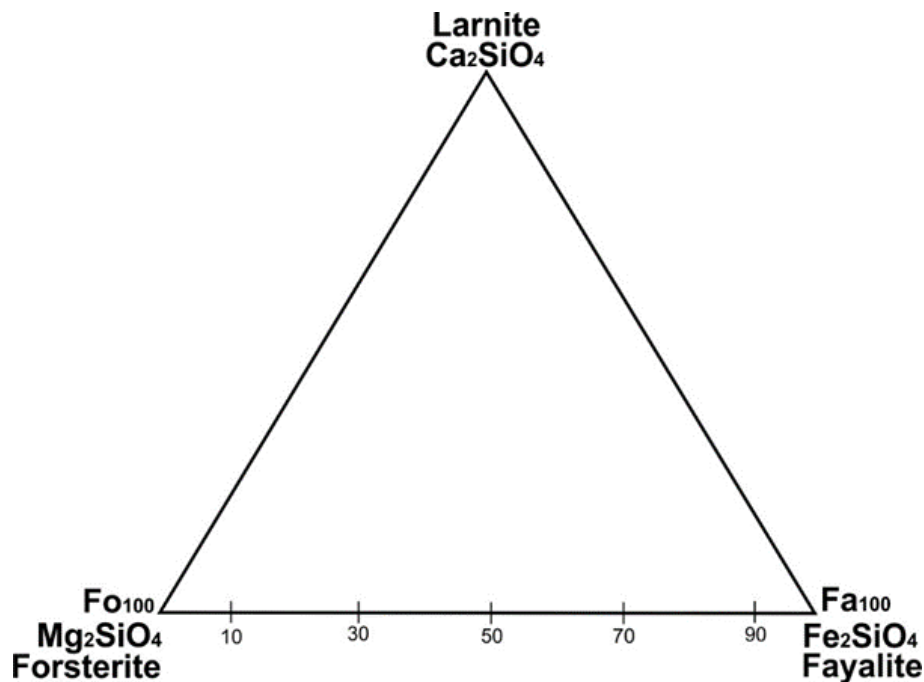


Figure 4: Ternary system of Ca_2SiO_4 - Mg_2SiO_4 - Fe_2SiO_4 for minerals of olivines (Davidson & Mukhopadhyay, 1984).

1.4.1.1 FORSTERITE

Forsterite is the magnesium-rich end-member of the olivine solid solution series. Its symbol is Fo and its formula is Mg_2SiO_4 . Two high-pressure polymorphs of olivine's forsterite are known, the orthorhombic wadsleyite and the isometric ringwoodite. The latter has a spinel structure. The melting point of forsterite under anhydrous conditions increases with pressure, and under water-saturated conditions decreases with pressure. The melting point of forsterite is 1890 (+/-) 20 °C and, because of the high melting point, olivine crystals are the first minerals to precipitate from a magmatic melt in a cumulate process, often with orthopyroxenes (Howie *et al.*, 1997; Deer *et al.*, 2013).

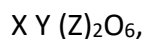
1.4.1.2 FAYALITE

Fayalite is a ferrous iron end-member of the olivine solid solution series. Its formula is $\text{Fe}^{+2}_2\text{SiO}_4$ and the symbol is Fa. It melts irreconcilably at 1205 °C, at atmospheric pressure to a liquid plus iron. Raising the temperature causes a rise in the pressure during phase transitions. At high pressure, fayalite undergoes a phase transition to Ahrensite. In high-pressure

experiments, the transformation may be delayed, so that it may remain stable to specific pressures, at which point it may become amorphous rather than take on a crystalline structure such as Ahrensite (e.g., Howie *et al.*, 1997; Deer *et al.*, 2013).

1.4.2 Pyroxene Group of Minerals

The pyroxene group of minerals are symbolized as Px, and their chemical formula is:



where: X = Na⁺, Ca²⁺, Mn²⁺, Fe²⁺, Mg²⁺ and Li⁺

Y = Mn²⁺, Fe²⁺, Mg²⁺, Fe³⁺, Al³⁺, Cr³⁺ and Ti⁴⁺

Z = Si⁴⁺ and Al³⁺ and its symbol is Px.

Pyroxenes are the most important group of rock-forming ferromagnesian silicates (e.g., Howie *et al.*, 1997; Morimoto, 1988; Deer *et al.*, 2013; Gamaletsos, 2024a and references therein). The pyroxene group includes orthorhombic minerals such as orthopyroxene and monoclinic minerals such as clinoenstatite (Mg₂Si₂O₆) – clinoferrosilite (Fe₂Si₂O₆). The abbreviations “OPX” and “CPX” are often used for orthopyroxene and clinopyroxene, respectively. Pyroxenes are a group of minerals that can be represented by the chemical ternary system of CaSiO₃-MgSiO₃-FeSiO₃ (Morimoto, 1988) (**Fig. 5**) including enstatite (MgSiO₃), ferrosilite (FeSiO₃), and a third chain silicate named as wollastonite (CaSiO₃). Actually, the latter is a calcium end-member of the pyroxenoids group (e.g., Morimoto, 1988). In particular, pyroxene does not exist with calcium contents, so any region above the clinopyroxenes series of diopside (CaMgSi₂O₆) – hedenbergite (CaFeSi₂O₆) does not represent pyroxene, and the section of this system below this join is known as the pyroxene quadrilateral (Morimoto, 1988). Also, more specifically, augite belongs in the range of 20%<Ca<45% and it is a high calcium pyroxene, while pigeonite is a low calcium pyroxene with 5%<Ca<20% and they both lie within the interior of the pyroxene quadrilateral.

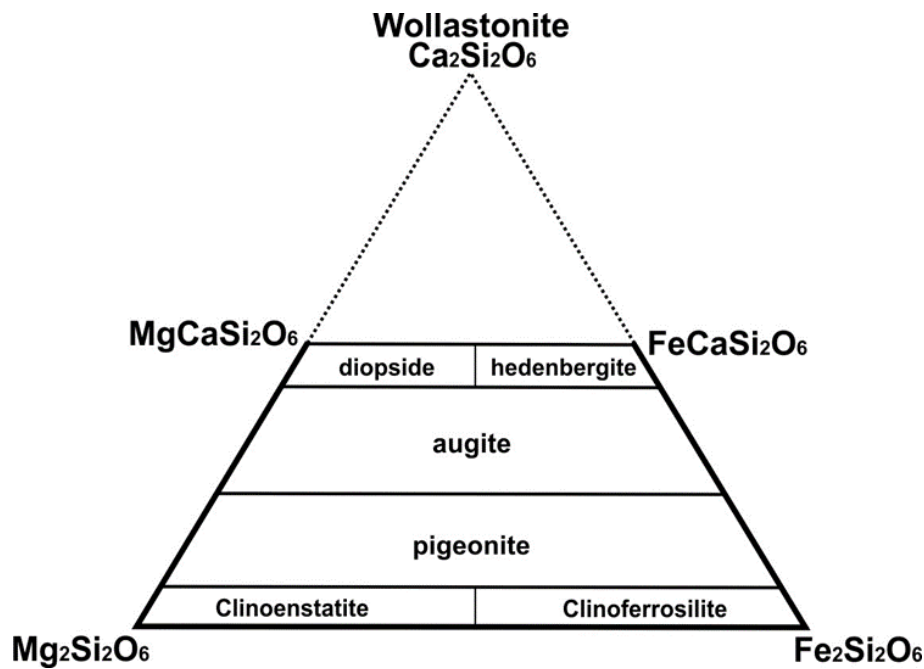


Figure 5: Ternary system (Morimoto, 1988) of CaSiO₃- Mg₂SiO₆- Fe₂SiO₆ for minerals of pyroxene group (Enstatite and Ferrosilite respectively) along with pyroxenoids (Wollastonite).

1.4.2.1 CLINOPYROXENES

The clinopyroxenes series crystallizes in the monoclinic system and has a general formula (Ca, Mg, Fe, Na) (Mg, Fe, Al) (Si, Al)₂O₆. The most significant clinopyroxene are diopside, hedenbergite, augite, and pigeonite (e.g., Howie *et al.*, 1997; Deer *et al.*, 2013; Gamaletsos, 2024a and references therein).

1.4.2.2 ORTHOPYROXENES

The orthopyroxene series crystallizes in the orthorhombic system and the term “hypersthene” is often used as a synonym for orthopyroxene (Howie *et al.*, 1997; Deer *et al.*, 2013). The formula (Mg, Fe) SiO₃ is for orthopyroxenes. These minerals differ in the ratio of magnesium to iron in the crystal structure. Their composition ranges from pure magnesium silicate, the end-member component of enstatite (MgSiO₃) to pure ferrous iron silicate, the end-member of ferrosilite / FeSiO₃ (e.g., Howie *et al.*, 1997; Deer *et al.*, 2013; Gamaletsos, 2024a and references therein). Aside from olivine, magnesium-rich orthopyroxene is the most common silicate in meteorites, especially in most chondrites.

1.4.3 Feldspar Group of Minerals

Feldspar is the name of a group of aluminum tectosilicate minerals with the symbol Fsp. The crystal structure of feldspar is based on aluminosilicate tetrahedra, and it crystallizes at a triclinic or monoclinic structure (e.g., Howie *et al.*, 1997; Deer *et al.*, 2013; Gamaletsos, 2024a and references therein). Common feldspars are ternary solid solutions of three components (e.g., Ghiorso, 1984; **Fig. 6**): albite (Ab): ($\text{NaAlSi}_3\text{O}_8$), orthoclase (Or): (KAlSi_3O_8), and anorthite (An): ($\text{CaAl}_2\text{Si}_2\text{O}_8$). The two major categories of Feldspars are Alkali feldspars, which lie compositionally between orthoclase and albite end-members, and plagioclase Feldspars, which lie between albite and anorthite end-members. Also, there is a miscibility gap between Orthoclase and Anorthite end-members because they have different ionic radii and charges, preventing the existence of intermediate feldspars.

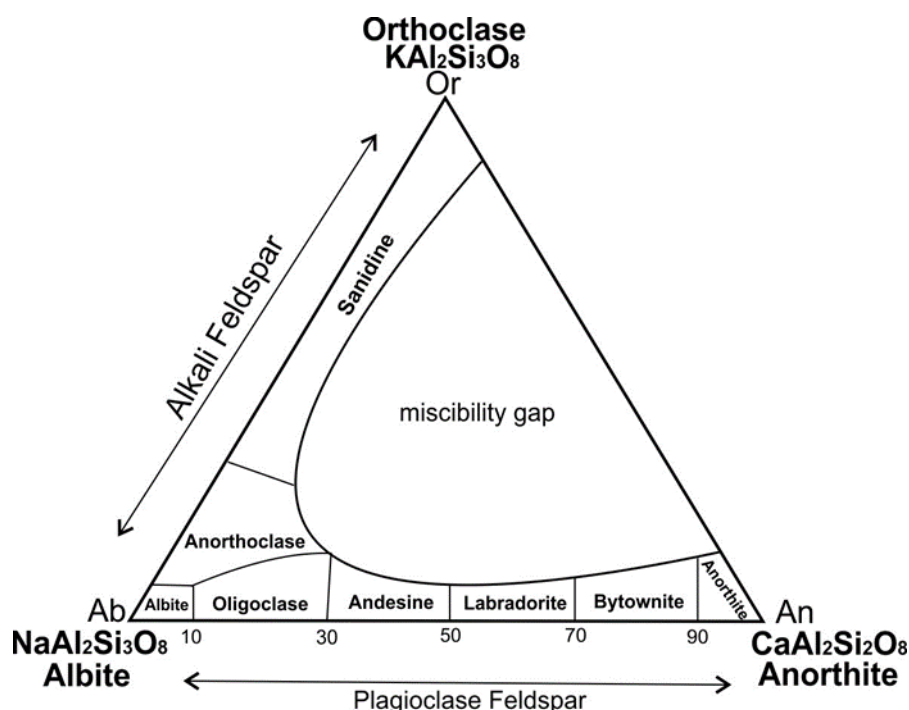


Figure 6: Diagram of feldspar classification: albite (Ab): $\text{NaAlSi}_3\text{O}_8$; orthoclase (Or): KAlSi_3O_8 ; anorthite (An): $\text{CaAl}_2\text{Si}_2\text{O}_8$ (Ghiorso, 1984)

The plagioclase series is commonly found in many stony meteorites. There are two main types of plagioclases based on their composition: An90-5 and An15-10. In meteorites, a high-density glass of plagioclase composition with a high refractive index is often found and is referred to as Maskelynite. The intense pressure generated during impact transforms the highly structured crystalline form of the plagioclase series into a disordered glass, without

obliterating the original crystal shape (Norton & Chitwood, 2008). Anorthosite, which makes up more than 80% of the Moon's exposed surface, is made up of plagioclases of composition An90-97 and is the most common type of lunar feldspars.

1.4.4 Iron-Nickel Minerals

Important minerals present in ordinary meteorites are also Fe-Ni alloys referred to as metals (e.g., Norton & Chitwood, 2008). The amount of their abundance present in an ordinary meteorite plays a crucial role in the categorization of the groups as mentioned above. There are four types of Fe-Ni alloys, taenite, kamacite, antitaenite, and tetrataenite (e.g., Gamaletsos, 2024a and references therein). Kamacite and taenite are the most common types, and depending on their chemical composition, they can be categorized as either. Taenite has a formula of γ -(Fe-Ni) and the crystal structure is isometric (Anthony *et al.*, 2001). To be classified as taenite, an alloy must have nickel proportions ranging from 20% to 65% (Goldstein & Short, 1967). Kamacite, on the other hand, has the formula of α -(Fe, Ni); Fe_{00.9}Ni_{00.1} (Ramsden & Cameron, 1966), and it is also isometric in the crystal structure. The proportion of iron: and nickel is between 90%:10% and 95%:5% (Goldstein & Short, 1967). Commonly, both can coexist in a meteorite and have the texture of bands called Widmanstätten pattern, a lamellae formation (Goldstein & Ogilvie, 1965).

1.4.5 Iron Sulfide Mineral

Troilite is an iron sulfide with the formula FeS (e.g., Anthony *et al.*, 2001; Gamaletsos, 2024a and references therein). It can be found in a meteorite and has a characteristic pale yellowish color that can be easily identified under the reflected light in the microscope. Sulfur is almost completely insoluble in solid metal, so it is only found in unevenly distributed nodules of troilite, which probably trapped the melt during the crystallization process (Goldstein *et al.*, 2009). To determine sulfur concentrations in the melt, the distributions of other elements that are more sensitive to the amount of sulfur present in the liquid during crystallization must be studied.

1.4.6 Phosphates

Phosphate minerals include the apatite and merrillite groups and have the formula of $\text{Ca}_5(\text{PO}_4)_3(\text{OH}, \text{F}, \text{Cl})$ (e.g., Howie *et al.*, 1997; Deer *et al.*, 2013; Gamaletsos, 2024a and references therein). They are also present in meteorites and other materials from the Solar System. The mineral merrillite is a calcium phosphate and the anhydrous end-member of the merrillite-whitlockite solid solution series (Hughes *et al.*, 2008). In Martian meteorites, the anhydrous nature of merrillite has been seen as evidence of water-limited late-stage Martian melts (Adcock *et al.*, 2017). However, recent research on apatite in the same meteorites suggests higher water content in melts. Apatite is important in the search for extraterrestrial life and water as it is the only mineral that contains volatiles found in a wide range of extraterrestrial materials and effectively retains them during thermal or shock events (McCubbin & Jones, 2015). This is why it's crucial to identify phosphates in meteorites.

1.4.7 Chromite

Chromite is an iron magnesium and chromium oxide, and has the formula of FeCr_2O_4 , with the oxide mineral and it is a member of the spinel group (e.g., Bosi *et al.*, 2019; Gamaletsos, 2024a and references therein). It has a cubic structure formed by atoms of oxygen with the aluminum atoms in octahedral coordination and the iron atoms in tetrahedral coordination. Its polymorphs are found in meteorites and are named xieite and chenmongite. Also, under the reflected light in an optical microscope, the chromite appears with a grey color.

1.5 Polymorphs – Definitions

Polymorphs are minerals with the same composition but different crystalline structures (e.g., Pabst & Thrush, 1968; Gamaletsos, 2023 and references therein). Crystalline structure is the property of atoms in minerals (as well as in many other compounds) to possess an orderly atomic arrangement giving them a definite structure that controls their properties.

Polymorphism is a property of many chemical substances crystallizing in more than one crystal structure, depending on the respective thermodynamic conditions of the situation (e.g., Pabst & Thrush, 1968).

High-pressure Polymorphs exist in heavily shocked meteorites and contain several types of polymorphic high-pressure minerals of olivine, pyroxene, and feldspar. These high-pressure minerals can be found inside the shock-induced melt veins and melt pockets in a chondrite meteorite and are usually micro-grain size crystals (Tomioka & Miyahara, 2017). The typical composition of ordinary chondrites includes several low-pressure phase minerals such as olivine, low-Ca pyroxene, plagioclase, high-Ca pyroxene, Ca-phosphate, chromite, metallic Fe-Ni, and FeS. Under high temperatures and pressures, the minerals transform their structure (Presnall, 1995) and for example, olivines (α -[Mg, Fe] $_2$ SiO $_4$) transform into a spinelloid structure known as wadsleyite β -(Mg, Fe) $_2$ SiO $_4$ (Price *et al.*, 1983) or spinel structure known as ringwoodite γ -(Mg, Fe) $_2$ SiO $_4$ (Binns *et al.*, 1969). Also, depending on their chemical composition being detected with EPMA analysis a sample can contain wadsleyite (Price *et al.*, 1983) or its Fe analog of wadsleyite, asimowite, Fe $_2$ SiO $_4$ (Bindi *et al.*, 2019), and ringwoodite (Binns *et al.*, 1969) or its Fe analog of ringwoodite, ahrensite (γ -Fe $_2$ SiO $_4$) (Ma *et al.*, 2016).

1.5.1 Wadsleyite

Wadsleyite is an orthorhombic mineral that has a formula of beta phase, β -(Mg, Fe) $_2$ SiO $_4$ (Price *et al.*, 1983). Wadsleyite can coexist in ordinary meteorites with ringwoodite and have values of Fa $_{6-20}$ (e.g., Miyahara *et al.*, 2008; Ono *et al.*, 2013). However, when it comes to shocked chondrites, sometimes a phase transformation can happen from olivine to wadsleyite/or asimowite as mentioned before, and this is mainly because olivine in these cases has a high concentration of iron (Bindi *et al.*, 2019). It has been proposed that the original olivine might have been entrained in the shock vein while it was melted once, and ringwoodite and wadsleyite assemblages subsequently formed from the olivine melt by fractional crystallization (Miyahara *et al.*, 2008; Miyahara *et al.*, 2009).

1.5.2 Majorite

As pressure and temperature increase, the low-calcium pyroxene $[\text{Mg}, \text{Fe}] \text{SiO}_3$ transforms into a high-pressure polymorph of majorite (Kato & Kumazawa, 1985). This process results in the formation of two different minerals with ilmenite structure: akimotoite with MgSiO_3 formula (Tomioka *et al.*, 1999), and hemleyite with FeSiO_3 formula (Bindi *et al.*, 2017). Meanwhile, MgSiO_3 with a garnet structure is known as majorite and can have cubic and tetragonal symmetries (Xie & Sharp, 2007; Tomioka *et al.*, 2016). The garnet structure has cubic symmetry, while the synthetic majorite has a tetragonal symmetry. The high-pressure polymorph, majorite, was successfully synthesized by Kato and Kumazawa in 1985 (Kato & Kumazawa, 1985).

1.5.3 Albitic Jadeite

The albitic jadeite has the chemical composition between the jadeite ($\text{NaAlSi}_2\text{O}_6$) and albite ($\text{NaAlSi}_3\text{O}_8$), and because it has the composition of pyroxene, its formula uses the distribution of 6 cations of oxygen, $(\text{M}2) (\text{M}1) \text{T}_2\text{O}_6$ or more specific $(\text{Na}, \text{Ca}, \square_{1/4})(\text{Al}, \text{Si})\text{Si}_2\text{O}_6$, where there is a high concentration of excess Si on the octahedral cation M1 site and an M2 site with $\frac{1}{4}$ vacancy (Ma *et al.*, 2022).

Albitic jadeite is found to be highly sensitive to electron beams and can become amorphous within a few seconds when exposed to a focused beam in the scanning electron microscope (SEM) (Ma *et al.*, 2022). The presence of the vacancies is important because a chemical analysis that has higher than $\frac{1}{4}$ vacancy in the M2 site, indicates that the analysis has damaged the grain, because of the sensitivity, and there is a loss of volatile components (alkali Na, Ca) and thus the silicates remain in the grain, and we have an underestimation of the chemical analysis (Ma *et al.*, 2022; Baziotis *et al.*, 2022b). On the other hand, ideal jadeite remains stable and maintains its structure during microanalysis with focused electron beams (Ma *et al.*, 2022). Most importantly, it is necessary to conduct a compositional analysis to confirm the Raman identification of jadeite before using the formation conditions of jadeite to establish a minimum pressure for a meteorite shock event (Baziotis *et al.*, 2022b). Also, it is worth mentioning that the synthesis of albitic jadeite has not yet been achieved in laboratories (Ma *et al.*, 2022).

It is of great interest to mention how the albitic jadeite appears in different meteorites. It has been observed at the Ozerki meteorite that the albitic jadeite is mixed with a particle-like texture of amorphous material and appears as fragmented grains, formed due to high-pressure and temperature conditions (Baziotis *et al.*, 2022b). Additionally, at the Chelyabinsk meteorite, feldspathic glass occurs with the characteristic form of needle-like crystals in jadeite, and it is suggested that has been rapidly crystallized (Baziotis *et al.*, 2022b). The needle-like jadeite appears to have been nucleated along interfaces between the original albitic feldspar and other minerals or shock melt vein matrix (Ozawa *et al.*, 2014). In addition, based on the Ostwald step rule grains of plagioclase that transformed into maskelynite (albitic maskelynite) due to shock events subsequently can decompose into albitic jadeite and then to lingunite (Tschauner *et al.*, 2021).

1.5.4 Tuite

Merrillite, which is also known as whitlockite, has a crystal structure and chemistry similar to the dense form of calcium phosphate minerals such as chlorapatite, specifically the trigonal $\gamma\text{-Ca}_3(\text{PO}_4)_2$ (Xie *et al.*, 2002, 2013, 2016). There are three types of apatites, namely hydroxylapatite ($\text{Ca}_3(\text{PO}_4)_2(\text{OH})$), fluorapatite ($\text{Ca}_3(\text{PO}_4)_2\text{F}$), and chlorapatite ($\text{Ca}_5(\text{PO}_4)_3\text{Cl}$) (Xie *et al.*, 2016). Tuite formation is supported by two formation pathways: decomposition of apatite and transformation of merrillite under high-pressure and temperature conditions (Gu *et al.*, 2022; Xie *et al.*, 2002, 2013, 2016). According to Gu *et al.*, 2022 tuite is the shock-induced high-pressure polymorph of chlorapatite and is the shock-induced recrystallization of whitlockite.

1.6 Melt Veins

The high-pressure minerals in meteorites form in shock-induced melt veins and pockets, and these minerals are evidence of being products of shock that can describe the formation of HP minerals but are not fully sufficient (Hu & Sharp, 2022). The HP minerals form through two mechanisms, the crystallization of shock melt under high pressure, and the solid-state transformation of minerals in contact with the melt vein (Tomioka *et al.*, 2016). As a result, these minerals have a nearly identical chemical composition to their parent minerals

and are typically submicron-sized (Tomioka *et al.*, 2016). The most important feature for the preservation of high-pressure minerals is the cooling temperature conditions that are present before or during the pressure release (Sharp & Hu, 2019). The matrix of shock veins is composed of aggregates of crystals and glasses that formed from the melt and rapidly cooled, featuring a distinctive texture characterized by the presence of abundant Fe-FeS blebs (Tomioka *et al.*, 2017).

The formation of a melt vein depends on local temperature peaks caused by various factors, such as pore collapse, which is the collapse of open fractures or pores during shock compression, shearing heating, which is the frictional heating along shear bands, and complex peak-pressure variations during compression from shock-wave collisions (Sharp & Hu, 2019). Porosity is present in meteorites whose origin is unclear, but it may be due to collisions that ejected the meteorites or porosity present within the parent bodies (Flynn *et al.*, 1999). This could explain the discrepancy between asteroid bulk densities and mineral densities. More specifically, pore collapse can absorb shock waves, generating higher temperatures, but the shock wave attenuates faster in porous materials due to low impedance pore contents, reducing the shock wave velocity and pressure, and resulting in a smaller volume of material experiencing high enough shock pressures for melting (Petrova & Grokhovsky, 2019). Most importantly, the collapse of the pores can amplify shock pressure by up to 4 times, creating hotspots and this amplification can explain why high-pressure phases are found next to unshocked grains (Güldemeister *et al.*, 2013).

1.7 The Shock Classification of Meteorites

1.7.1 Shock Conditions

The conditions required for a melt vein to form are directly related to the physics of shock metamorphism (Fritz *et al.*, 2017). There is a combination of shock pressure, temperature, and time simultaneously (Fritz *et al.*, 2017). As the body of the meteorite undergoes extreme heating, the cooling of the melt vein reveals the minerals that have been formed under the shock impact (Fritz *et al.*, 2017). Most meteorites experience hypervelocity collisions that drive shock waves through their bodies. To characterize the degree of shock

metamorphic overprint in meteorites, a variety of different shock classification schemes have been proposed (Stöffler & Grieve, 2007; Fritz *et al.*, 2017; Stöffler *et al.*, 2018).

1.7.2 Shock Features

Shock waves produce shock features on minerals that can be observed in a petrographic microscope and these features can be interrelated to the pressure and temperature conditions that affected the sample, and based on the high-temperature conditions, they can affect mechanical deformations, phase transformations, decomposition, and melting (Stöffler *et al.*, 2018). Their existence in a thin section of a groundmass has a crucial role in the identification of the shock metamorphism. The irregular fractures are called the features that appear as cracks on the surface of the grain. Planar fractures appear as multiple sets of parallel lines because they were developed at low pressures and are associated with the shock wave of the impact (Norton & Chitwood, 2008). However, planar deformation features are thin closely spaced parallel fracture lines that are only produced by extreme shock compressions (Müller & Hornemann, 1969). Mosaicism is a mechanism that can be easily observed under crossed polars with an optical microscope, and it is an indicator of moderate to heavy shock metamorphism (Norton & Chitwood, 2008). On the other hand, if the specimen exhibits extensive fracturing, it is associated with undulatory extinction and can be characterized as being lightly to moderately shocked and this feature can be observed under crossed polars with an optical microscope (Norton & Chitwood, 2008).

Studies have estimated that each shock feature is linked to a variation of high-pressures / GPa (Stöffler *et al.*, 2018 and references therein; **Fig. 7**). For olivines being present in a thin section of a meteorite, the undulatory extinction can be from 4-5 to 15-20 GPa, the planar fractures from 5-10 to 60-65 GPa, mosaicism can be from 15-20 to 60-65 GPa, planar deformation features from 30-35 to 55-60 GPa, and melting and recrystallization with pressures above 60-65 GPa (Stöffler *et al.*, 2018 and references therein; **Fig. 7**). For pyroxenes present in the thin section of a meteorite, the undulatory extinction can be from 5-10 to 20-30 GPa, the mechanical twinning from ~5 to ~70 GPa, mosaicism can be from 20-30 to ~70 GPa, planar deformation features from 30-35 to ~70 GPa, and incipient melting with pressures above ~70 GPa (Stöffler *et al.*, 2018 and references therein; **Fig. 7**).

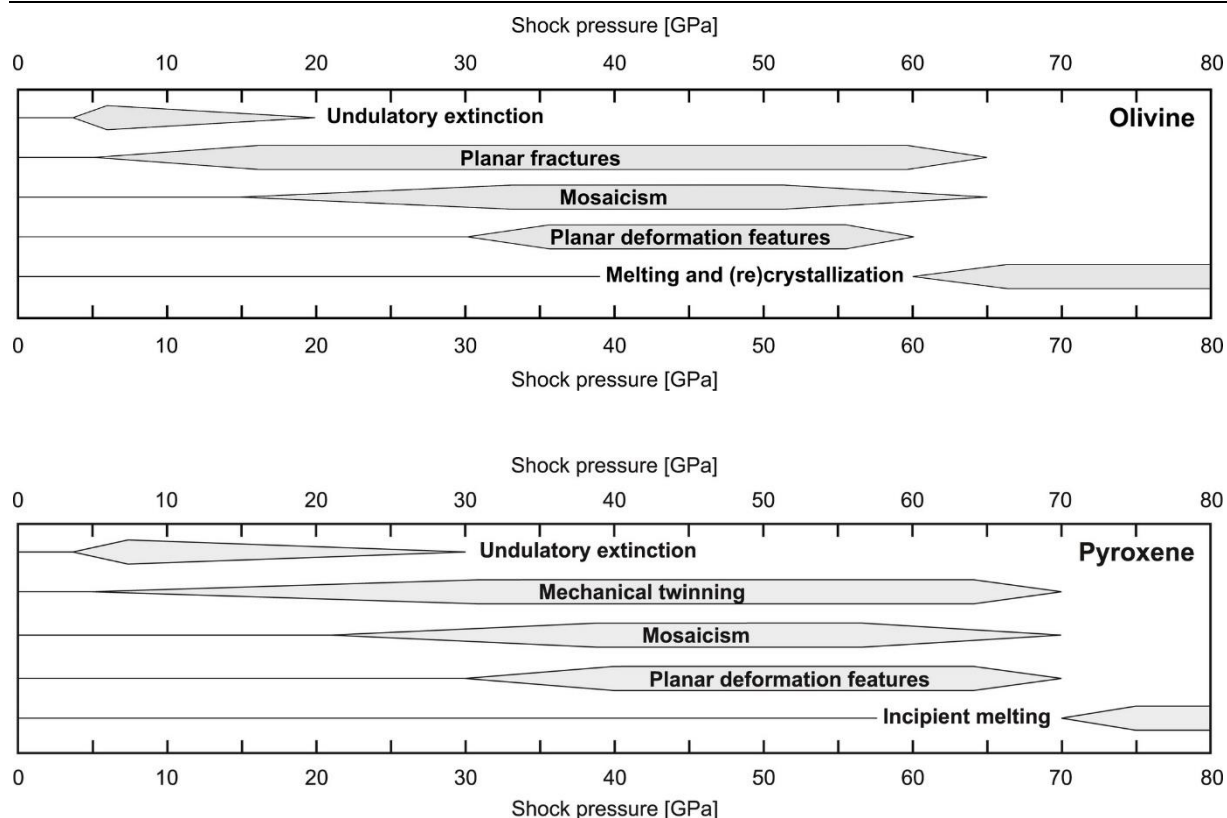


Figure 7: Shock wave barometry with shock pressures based on the shock features of olivine and pyroxene in the meteorites (Stöffler et al. 2018 and reference therein).

As mentioned above, the minerals have undergone extreme pressure conditions, resulting in characteristic shock features indicating their transformations. More specifically, in plagioclases, several features can be observed, such as the undulatory extinction, the mosaicism, the planar deformation lamellae (pdf), the partial (or complete) isotropization in the case of diaplectic glass, the hollandite-structured high-pressure phase, the jadeite in the case of albitic plagioclase and the normal flow-textured glass (Tomioka & Miyahara, 2017). Likewise, in olivines, the undulatory extinction, the mosaicism, the planar fractures, the planar deformation features, the transformation to wadsleyite, ringwoodite, or ahrensite, the partial-to-complete recrystallization as well as the melting and subsequent formation of polycrystalline olivine can be distinguished (Tomioka & Miyahara, 2017). Lastly, in pyroxenes, evidence of the undulatory extinction, the mosaicism, the mechanical twinning, the planar deformation features, the loss of pleochroism, the transformation to majorite, akimotoite, and bridgmanite, the decomposition to oxides, and the mixing with flow-textured feldspar glass can be found (Tomioka & Miyahara, 2017).

1.7.3 Shock Classification

There are proposed classification schemes that aim to categorize the outcomes of impacts after the collision a meteorite experienced, resulting in the surface of a meteorite. The basic classification criteria are based on texture, degree of shock metamorphism, and lithological components. Shock metamorphism is the irreversible changes in geologic materials resulting from the passage of a shock wave. A shock wave is a compressional wave with material transport that propagates through gaseous, liquid, or solid matter at supersonic velocity. Shock compression generates post-shock heat, which increases with pressure and can lead to the material melting or vaporizing (Duvall & Fowles, 1963; Asay & Shahinpoor, 1993; Graham, 1993).

The meteorite shock stage measures the degree to which the matrix of a common meteorite has been fractured, however, the degree of shock can vary within a meteorite on the scale of centimeters (Fritz *et al.*, 2017). The mineralogy of shock melt zones provides information on the shape and time duration of the shock wave, but not information on the general maximum shock pressure in the whole rock (Fritz *et al.*, 2017).

The common shock classification schemes of ordinary meteorites assign shock levels of S1 (unshocked) to S6 (very strongly shocked) using shock effects in rock-forming minerals such as olivine and plagioclase (Stöffler *et al.*, 1991; Schmitt, 2000; Stöffler & Grieve, 2007). Although, there are some differences between the shock classification schemes that have been suggested by different scientists (Stöffler & Grieve, 2007; Fritz *et al.*, 2017; Stöffler *et al.*, 2018). The definition of shock classification by Stöffler & Grieve (2007) is given with the range of the shock stage from S1 (unshocked) to S6 (very strongly shocked) and a seventh shock stage named Shock melted for specimens that are melted (**Table 1**). The shock classification scheme developed by Stöffler & Grieve in 2007 focuses on shocked chondritic meteorites (Stöffler & Grieve, 2007). The shock pressure data is based on experimental data provided by Stöffler *et al.*, (1991) and the shock features in the rock-forming minerals observed through optical microscopy (Schmitt, 2000). Also, the shock classification scheme that Fritz *et al.* revised (Fritz *et al.*, 2017), mentions that increasing the shock pressure eventually leads to whole rock melting and that the melted rocks are not a unique shock feature and, thus, not part of the shock classification scheme. So, the shock stages for classification are from S1

(unshocked) to S6 (very strongly shocked) with a seventh category of Shock melted that categorizes the whole rock melting (**Table 2**). The scheme relies on the revision summarizing relevant principles of shock physics, impact cratering, and the formation of shock effects in rock-forming minerals. It also aims to address controversies in shock thermo-barometry and the shock classification of meteorites. Lastly, there is another definition for the progressive stages of shock metamorphism that Stöffler *et al.* (2018) mention that the final shock stage is named S7, and it represents the category for the whole rock melting (Stöffler *et al.*, 2018). Therefore, in this scheme, the classification goes from S1 to S7 (**Table 3**). Also, this scheme focuses on the shock effects and its textures rather than the physics of the formation processes of each certain shock feature.

Following is a summary of the shock grades

Table 1: Shock classification scheme by Stöffler & Grieve (2007): Classification of shocked chondritic meteorites and olivine-rich crystalline rocks (progressive stages of shock metamorphism) modified after Stöffler *et al.* (1991); shock pressure data are based on experimental data given in Stöffler *et al.* (1991); pressures given in columns 4 – 6 indicate the upper limit of the shock stage in question; temperature data refer to the ambient temperature before shock compression; *from Stöffler *et al.* (1991); **from Schmitt (2000).

Shock stage	Effects resulting from equilibration peak shock pressure			Effects resulting from local P-T-excursions	Pressure GPa* (293 K)	Pressure GPa** (293 K)	Pressure GPa** (920 K)
	Olivine		Plagioclase				
Unshocked S1	Sharp optical extinction Irregular fractures	Angular variation of extinction position: Low grade: < 1° High grade: 1° – 2°	Sharp optical extinction Irregular fractures	none	< 4 - 5		
Very weakly shocked S2	Undulatory extinction Fractures	Angular variation of extinction position: < 2°	Undulatory extinction Irregular fractures	none	5 - 10		
Weakly shocked S3	Planar fractures (PF) Undulatory extinction Irregular fractures	Low grade: maximum of 2 sets of PF High grade: 3 or more sets of PF	Undulatory extinction	Opaque shock veins, incipient formation of melt pockets (sometimes interconnected)	15 - 20	10 - 15	10 - 15
Moderately shocked S4	Mosaicism (weak)	Low grade: incipient mosaicism, PF and PDF High grade: mosaicism, PF, and PDF	Low grade: undulatory extinction High grade: partially isotropic, PDF	Melt pockets, interconnected melt veins, opaque shock veins	30 - 35	25 - 30	20 - 25
Strongly shocked S5	Mosaicism (strong) Planar fractures Planar deformation features (PDF)		Maskelynite (diaplectic glass)	Pervasive formation of melt pockets, veins and dykes, opaque shock veins	45 - 55	45 - 60	35 - 45
	Restricted to local regions in or near melt zones						
Very strongly shocked S6	Recrystallisation; yellow-brown staining; ringwoodite and wadsleyite; high pressure phases of pyroxene (e.g. majorite, akimotoite)		Shock melted (normal glass)	as in stage S5	75 - 90		45 - 60
Shock melted	Whole rock melting and formation of melt rocks						

Table 2: Shock classification scheme by Fritz *et al.* (2017): Revision of the shock classification scheme for olivine-rich crystalline rocks including chondrites initially proposed by Stöffler *et al.* (1991) and Stöffler & Grieve (2007).

Shock stage	<i>P</i> (GPa)	<i>T</i> (°C) (postshock)	Destructive shock effects in rock-forming minerals		Mineralogy of localized polymineralic melt zones including constructive shock effects
			Olivine	Plagioclase	
S1 Unshocked	<4–5	10–20	Sharp optical extinction with <2° angular variation	Sharp optical extinction (for chemically unzoned plagioclase)	
S2 Very weakly shocked	5–10	20–50	Undulatory extinction with >2° angular variation	Undulatory extinction	
S3 Weakly shocked	15–20	100–150	Undulatory extinction, Planar fractures (PF)	Undulatory extinction	Glass, low pressure (LP), and possibly high-pressure (HP) minerals such as Wadsleyite (Wds), ringwoodite (Rwd), majorite (Maj)
S4 Moderately shocked	25–35	200–300	Weak mosaicism and PF	Low grade: undulatory extinction; High grade: partially isotropic, PDF	Glass, LP, and possibly HP minerals such as Wds, Rwd, Maj, bridgmanite (Bdm), ferropericlase (Fpc)
S5 Strongly shocked	45–60	600–900	Strong mosaicism, planar deformation features (PDF) and PF	Maskelynite; Note: minimum pressure for maskelynitization (20–35 GPa) falls with rising Ca-content	Glass, LP, and possibly HP minerals such as Wds, Rwd, Maj, Fpc; back reaction of bdm
S6 Very strongly shocked		1500–1700	Strong mosaicism, PDF, recrystallization, brown staining	Shock melted glass with flow structures, vesicles and fusing of adjacent minerals; recrystallization	Glass, devitrified glass, LP minerals; bleaching of brown stained olivine, recrystallization
Shock melted	Whole rock melting and formation of melt rock				

Table 3: Shock classification scheme by Stöffler et al. (2018). Definition of progressive stages of shock metamorphism for classification system C.

Shock stage IUGS 2007 and present proposal	Pressure GPa ^a (293 K)	Pressure GPa ^b (293 K)	Pressure GPa ^b (920 K)	Effects resulting from equilibration peak shock pressure		Effects resulting from local <i>P-T</i> -excursions
				Olivine	Plagioclase	
C—S1	<4–5			Sharp optical extinction Irregular fractures	Angular variation of extinction position: <2° Sharp optical extinction Irregular fractures	None
C—S2				Undulatory extinction Irregular fractures	Angular variation of extinction position: >2° Undulatory extinction Irregular fractures	None
C—S3	5–10			Planar fractures (pf) Undulatory extinction Irregular fractures	Low grade: maximum of 2 sets of pf High grade: 3 or more sets of pf Undulatory extinction	Opaque shock veins; incipient formation of melt pockets (sometimes interconnected)
C—S4	15–20	10–15	10–15	Mosaicism (weak)	Low grade: incipient mosaicism, pf, and pdf Low grade: undulatory extinction High grade: partially isotropic, pdf	Melt pockets; interconnected melt veins; opaque shock veins
C—S5	30–35	25–30	20–25	Mosaicism (strong)	High grade: strong mosaicism, pf, and pdf Diaplectic glass (maskelynite)	Pervasive formation of melt pockets, veins, and dikes; opaque shock veins
C—S6	45–55	45–60	35–45	Restricted to local regions in or near melt zones: Melting and (re)crystallization and yellow-brown staining of olivine	Shock melted (normal glass)	As in stage S5
C—S7	>70–75		45–60	Whole rock melting		

^aFrom Stöffler et al. (1991).^bFrom Schmitt (2000).

2 MATERIALS AND METHODS

2.1 Sample

A representative thin section of Slobodka (NHMW-L4372) meteorite was obtained from the collection of the Natural History Museum Vienna (Vienna, Austria). The principal objective was to study the mineralogical and spectroscopic characteristics of this ordinary chondrite and to focus on the shock features in the melt vein.

2.2 Optical Microscope

The optical microscope (OM) is a compound microscope. It uses visible light and a system of lenses to magnify images of small samples (**Fig. 8**). A sample is mounted on a rotating stage and directly be viewed through one or two binocular eyepieces on the OM with the naked eye (both eyepieces show the same image). The optical microscope uses multiple objective lenses with different magnifications, allowing them to be rotated into place and providing an ability to zoom in/out on the thin section of the sample. Often a digital camera can be fitted onto the microscope (**Fig. 9**) and be used to capture the image of the sample (Gamaletsos, 2024b and references therein).

The petrographic microscope is used for mineral observations and includes a Nicol prism polarizer filter for the light path beneath the sample slide. The illumination of the sample can be with plain-polarized light (PPL) and cross-polarized light (XPL) where the sample contrast comes from the rotation of polarized light through the sample (Shelley & Nesse, 1986).



Figure 8: The components of a conventional optical microscope (OM) used for rocks and minerals observation (aka petrographic microscope). Image Source: <https://opengeology.org/Mineralogy/5-optical-mineralogy>

It is primarily important to mention the conditions employed while capturing the images of the sample with the optical petrographic microscope of the laboratory (**Fig. 9**). The natural and artificial lighting of the room must be as low as possible so that the camera is ready to capture the correct colors. Also, no fingerprints, dust, tinny objects, or materials used in other experimental procedures must be on the thin section of the sample, so it must always be cleaned from both sides. Moreover, the power supply voltage used for the microscope light bulb should not exceed 10 Volts. In addition, all lenses should be aligned using set screws on the microscope's compensator to adjust the lens to be stable in the center of the circular rotating stage while rotating it with the sample on it.

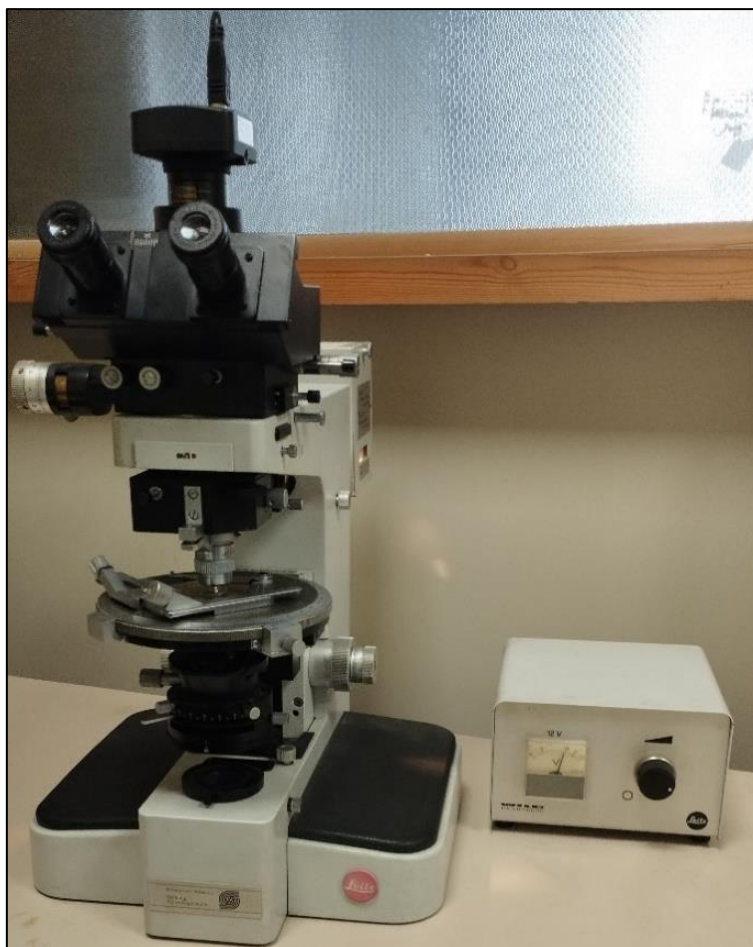


Figure 9: Optical petrographic microscope equipped with a camera (Laboratory at Department of Natural Resources Development & Agricultural Engineering, Agriculture University of Athens).

2.3 ImageJ / FIJI

The ImageJ / FIJI (Fiji Is Just ImageJ) is an open-source image processing software package (Schindelin *et al.*, 2012). Fiji's main purpose is to provide a distribution of ImageJ2 with many bundled plugins. Fiji features an integrated updating system and aims to provide users with a coherent menu structure to display, annotate, edit, calibrate, measure, analyze, process, print, and save raster image data. This software tool is usually focused on biological image analysis. However, it can be used for measuring the area of a chondrule in a meteorite, calculating the percentage of the allocation of the chondrules, and the percentage of the allocation of the metals distributed in the thin section.

The process for calculating the percentage of the allocation of the chondrules that are distributed in the studied thin section commences by setting the scale of the image

appropriately so that it applies to international units of measurement for the software. Then, the boundaries of the thin section were defined, and calculated the total area. However, to make sure that the calculated total area with the software matches the real area of the studied thin section, using a ruler, a selected region of the thin section was measured. By this approach, it was ensured that the measurements were accurate. Then, by utilizing software tools the same measurement was created for comparison. The area of the melt vein should be excluded to avoid to count it with the whole area of calculation. After that, each area of chondrule of the regions of interest (ROIs) in the thin section was calculated to determine their area and then the final percentage of the chondrule abundance over the groundmass was generated. For the calculation of the percentage of the metal abundance, the image analysis technique of the threshold was used. Adjustments of this feature to the mosaic of the reflected light map of the thin section were done to isolate the metals that had a specific off-white color. Thresholding is also known as binary thresholding, so this technique sets a threshold value and compares each pixel to that particular threshold value. If the pixel value is less than or equal to the assigned threshold, then the pixel value is set to zero or to the maximum value.

2.4 Electron Probe Micro-Analysis (EPMA)

The electron probe micro-analysis (EPMA) is an analytical technique that is used to establish the chemical composition of specimens at a micrometer spatial resolution. EPMA is a powerful microbeam electron microscope (aka e-microscope) equipped with multiple WDS spectrometers -usually four of five- facilitating non-destructive quantitative chemical analysis. Fundamentally, the theory behind EPMA's is similar to that of SEM's, whereas the capability of the former to be built with a multiple WDS system vertically mounted around the chamber provides higher sensitivity than that of the latter (e.g., Reed, 2005; Gamaletsos, 2024b and references therein). EPMA can also be used for mapping the geological thin sections, but the samples must be polished to yield a flat surface of the sample. The sample must be suitable for the e-microscope, especially must withstand the vacuum, be able to be stable under the electron beam, and have a conductive coating. The choice of coating depends on the type of material going to be analyzed. For geological thin sections, carbon coating to a 25 nm thickness was applied, protecting the sample from e-beam damage (e.g., heating phenomena). The

carbon coating is the best choice because it is mechanically stable and transparent for the electron beam and emitting x-rays. It is important to mention that most silicate minerals are electrical insulators.

The instrument consists of an optical microscope that has the same axis as the electron beam and can pinpoint the area of interest on the specimen surface (Llovet *et al.*, 2021). It also has three detectors for capturing the cathodoluminescence (CL), secondary electrons (SE) and back-scattered electrons (BSE), which are additionally emitted from the specimen under electron bombardment. A series of electromagnetic lenses located in the column of the instrument is used to condense/diverge and focus/defocus the electron beam emanating from the source (Fig. 10). Directing an electron beam at the sample from the electron source can lead to electrical charging of the sample, which must be dissipated. A charge-coupled device (CCD) camera allows samples to be viewed in reflected light and thin sections to be imaged in transmitted polarized light.

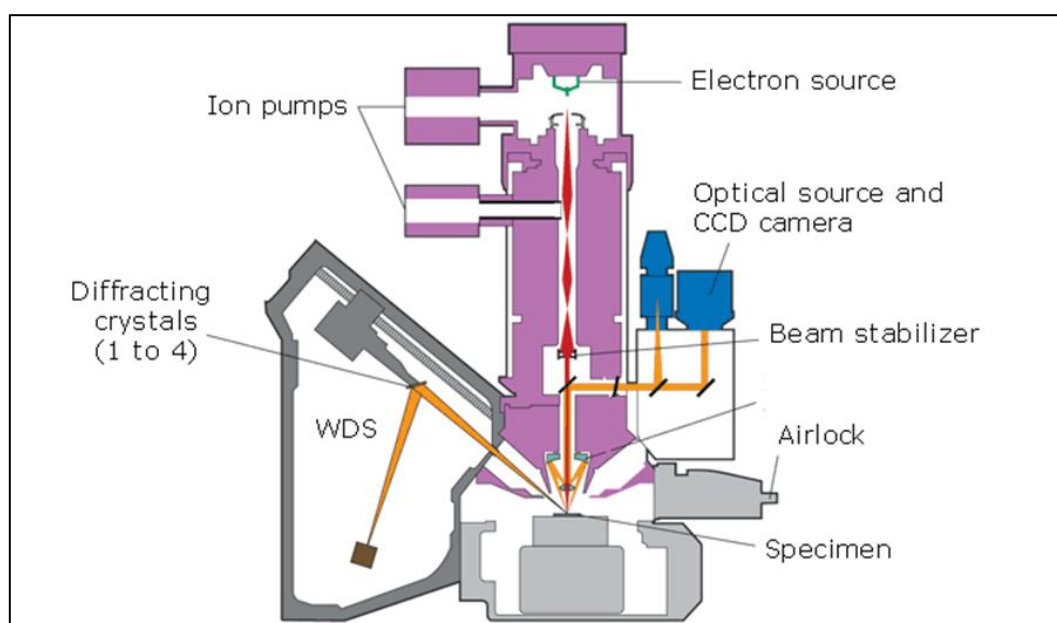


Figure 10: EPMA and WDS operation. Image Source: <https://www.cameca.com/products/epma/epma-introduce>

The instrument also has the analytical technique of wavelength dispersive spectroscopy (WDS) attached to the microprobe, as mentioned above. This technique functions by bombarding a specimen with electrons and collecting the x-rays emitted from its surface. The x-rays produce a spectrum in which each peak corresponds to a specific element, allowing for the identification of the sample's composition. It is important to mention that

wavelength-dispersive spectroscopy can perform a more detailed analysis to identify trace elements and measure the concentrations accurately.

Usually, EPMA instruments typically possess up to five WDS spectrometers, each of which is fitted with different diffracting crystals that reflect specific wavelengths. The most commonly used crystals can be lithium fluoride (LIF), pentaerythritol (PET), thallium acid phthalate (TAP), and artificial layered dispersive element (LDE) crystals. The multiple WDS's provide a more precise and accurate analysis, as they can produce spectra with higher spectral resolution.

EPMA instruments allow simultaneous x-ray (WDS and EDS), SEM and BSE imaging, and they provide very flexible sample inspection with image magnification ranging from 40 to 400,000 (<https://www.cameca.com/products/epma/epma-introduce>). The determination of thickness and elemental composition from nm to mm thick layers in stratified materials is possible. EPMA provides much better results than standard SEM-EDS systems, because of the internal properties of WDS, the general sensitivity, and the analysis of light elements. The excitation beam regulation system and the sample stage capabilities guarantee that this technique provides outstanding stability and measurement repeatability.



Figure 11: Electron Probe Micro-Analysis / EPMA (Natural History Museum of Vienna); Ms Myrto Simopoulou visited the Department of Mineralogy and Petrography of the National History Museum Vienna (Vienna, Austria) in the frame of ERASMUS+ Student Mobility for Traineeships. The responsible person from the National History Museum Vienna was Dr. Ludovic Ferrière.

It is of primary importance to mention the experimental conditions employed during measurements with the instrument in the laboratory in the frame of the present BSc thesis

(Fig. 11). The EPMA instrument was a JEOL JXA8530F Field Emission, equipped with five wavelength-dispersive spectrometers (WDS) and one energy-dispersive spectrometer (EDS). The analyzing crystals were TAP, LIF, LIFH, and PETJ (Table 4). Where there is a chemical formula mentioned, the standard is synthetic, while where there is a mineral name, the standard is of natural origin. For imaging, an accelerating voltage of 25 kV for better resolution was used, while when taking measurements, 15 kV with 20 nA probe current, 20 s counting time on peak position, and 10 s for each background was set.

Table 4: Standards for silicates and chromites.

Silicates 15 kV,20nA				
TAP CH-1	PETZ CH-2	CH-3	LIFH CH-4	TAP CH-5
Si (Wollastonite)	K (KCL)		Ni (Ni-Oxide)	Na (NaCl)
Al (Al ₂ O ₃)	Ca (Wollastonite)		Fe (Troilite)	Mg (MgO)
	Ti (TiO ₂)		Mn (Tephroite)	P (Apatite)
	Cr (Cr ₂ O ₃)			
Chromite 15kV,20nA				
TAP CH-1	LIF CH-2	CH-3	LIFH CH-4	PETZ CH-5
Mg (MgO)	Ni (Ni-Oxide)		V (Vanadite)	Ti (TiO ₂)
Al (Al ₂ O ₃)	Zn (ZnO)		Fe (Troilite)	Cr (Cr ₂ O ₃)
Si (Wollastonite)			Mn (Tephroite)	
Metals and Sulfides 15 kV,20nA				
TAP CH-1	PETZ CH-2	CH-3	LIFH CH-4	TAP CH-5
Si (Wollastonite)	Ti (TiO ₂)		Ni (Ni-Oxide)	P (Apatite)
P (schreibersite)	Cr (Cr ₂ O ₃)		Fe (Troilite)	Co (Co-metal)
			Mn (Tephroite)	
			S (Troilite)	

2.5 Raman Spectroscopy

Raman spectroscopy (aka Laser Raman spectroscopy) is a non-destructive technique being used to understand the mineral chemistry, and providing details on chemical structure, polymorphism, crystallinity, and molecular interactions. This spectroscopic technique is the process of inelastic scattering (i.e., in contrast to elastic scattering, it means that the energy of the incident photon does not remain constant) that describes a change in the wavelength of light that occurs when a beam of light interacts with molecular vibrations. After the invention of the laser, the light used is monochromatic. Although most of the scattered light

is emitted at the same wavelength as the laser source, a small amount of light (an intensity fraction of 10^{-6} to 10^{-8}) is scattered at different (longer, for the most part) wavelengths (the so-called Stokes part of the spectrum), which depend on the chemical structure of the material under investigation, and this is called Raman scattering or Raman scattered light. On the other hand, if a small amount of the incident light is slightly reduced, then the phenomenon is called “anti-Stokes Raman scattering” (e.g., McMillan & Hofmeister, 1988 and references therein; Nasdala *et al.*, 2004 and references therein).

Using the Raman technique various of geological samples can be analyzed (among a much wider sample variety) from a standard petrographic thin section. It is suitable for studying crystallographic structures and subtle changes in chemistry. At the same time, there are extensive libraries of reference spectra, online databases (such as the RRUFF Database), and published spectra, that can easily be used for comparison and/or identification of the minerals present in a measured sample. Each crystalline mineral has sharp Raman peaks (amorphous minerals usually have wider peaks) which form a unique pattern that can be identified as its particular “fingerprint”; on many occasions, several fingerprints of different minerals may coexist in a Raman spectrum acquired from a measured sample spot. Two advantages of the Raman technique are that (a) it requires practically no sample preparation and (b) its analysis usually takes a few minutes.

The Raman spectrum is a plot of light intensity versus the “frequency shift” ($\tilde{\nu}$) measured in wavenumbers, with $\tilde{\nu} = \nu/c = 1/\lambda$, where: ν is the usual frequency (measured in units of Hz), c is the speed of light (in cm/s) and the unit of wavenumber is $1/\text{cm}$ (McMillan & Hofmeister, 1988 and references therein; Nasdala *et al.*, 2004 and references therein). The physical quantity of wavenumber is used because it is directly proportional to the energies of the scattered photons (Planck’s law), as is the frequency. Additionally, the laser wavenumber is defined as zero in a Raman spectrum, and thus the so-called relative wavenumber of Raman scattering is proportional to the vibrational state energy levels, the values of which usually lie in the convenient range $100 - 4000 \text{ cm}^{-1}$; this way, the absolute laser wavenumber does not play a role in the result anymore and usually focus on the Stokes (the low-wavenumber side) part of the spectrum.

The Raman (or the infrared) peaks correspond to specific atomic vibrations of the structural units that make up each crystalline or amorphous phase. These vibrations depend

both on the type of structural unit (tetrahedron, octahedron, etc.) and the crystallographic group to which each phase belongs. Also, the relative intensities of the peaks usually depend on the crystal orientation relative to the incoming and scattered light polarization. Therefore, in Raman Spectroscopy, the characteristic Raman spectrum peaks of a measured sample can be identified and compared with a known mineral that is registered in a referenced library (RRUFF Database) using the Fityk software for the data processing.

Nowadays, the Raman microscope is a very frequently encountered version of a Raman spectrometer exploiting the spatial resolution of a microscope (of the order of 1 micrometer) for the study of sample inhomogeneities. It consists of a standard optical microscope, an excitation laser, laser rejection filters, a spectrometer or monochromator, and an optically sensitive detector such as a charge-coupled device / CCD (**Fig. 12**). The laser source has the property of a well-collimated beam that exits the laser that makes it easy to focus the coherent beam on a small sample area or extremely small sample volumes. The resolution of the spectrum relies on the bandwidth of the laser source used, as well as other parameters. Generally speaking, shorter wavelength lasers give stronger Raman scattering (a result of the Raman scattering intensity law $I_{\text{Raman}} \propto 1/\lambda^4$), but issues with sample degradation or fluorescence may result.

It is important to mention that on many occasions the fluorescence effect may mask the Raman signal. For mild fluorescence interference, the broad fluorescence background can be removed in data processing. Instead, if fluorescence is much more intense than the Raman scattered light, it may even cause saturation of the CCD detector. One way to avoid sample fluorescence is to change the wavelength of the laser. The green or blue-colored lasers have higher energy than red and near-IR-colored ones. Lower light energies usually do not excite molecules electronically (e.g., McMillan & Hofmeister, 1988 and references therein; Nasdala *et al.*, 2004 and references therein).

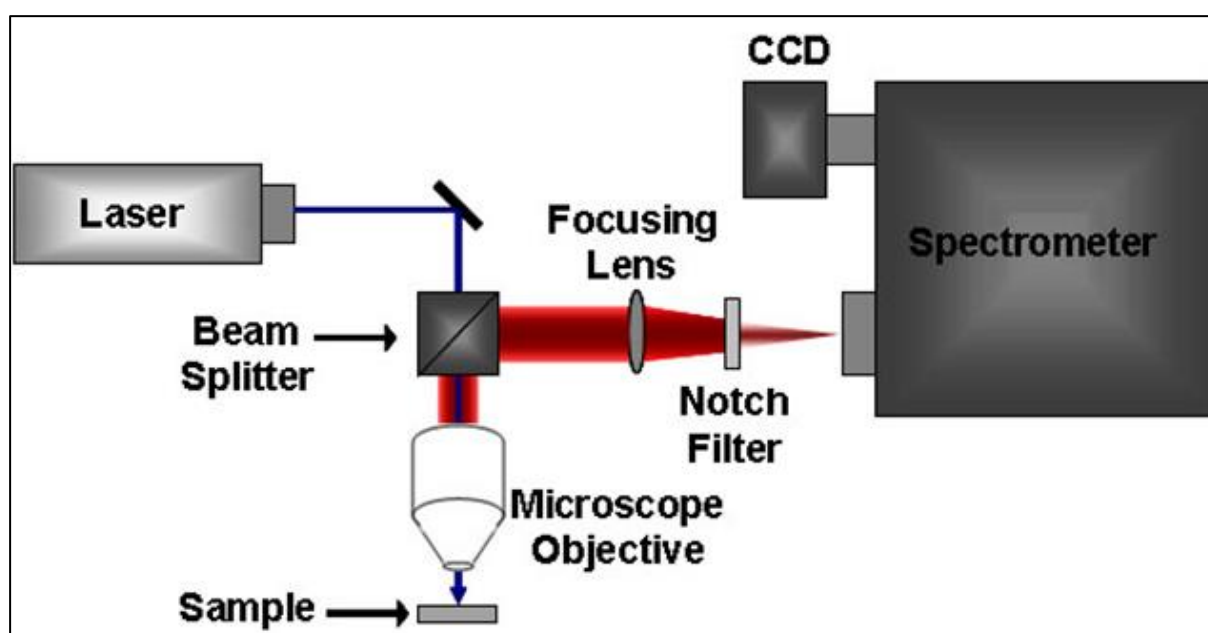


Figure 12: Schematic of Raman Spectrometer with microscopic attachment. Image Source: <http://cnx.org>

Caution should be exercised to the fact that the environmental conditions may cause a shift in the frequency axis values while taking measurements with a dispersive Raman spectrometer: the room temperature must be stabilized within less than 0.5 °C. In our case, a room temperature change of 1 °C can cause a frequency shift of ca. 0.5 cm^{-1} (x-axis) to the Raman spectrum. Therefore, modern Raman spectrometers have built-in reference samples (like e.g., Si) to aid in the automatic calibration of the frequency axis, whenever high accuracy is needed. In our case, each measurement session was started with a calibration using the Si main peak at 520.5 cm^{-1} . Since the Raman spectrum does not, for the most part, depend on the exciting laser frequency, the choice of the laser line that will be used for the measurement of a sample may be described as follows: it is the shortest wavelength (or highest frequency) possible, which does not cause additional laser-induced excitations (i.e., apart from Raman, like photoluminescence, sample heating, etc.) in the sample. The 532 nm (green) and 785 nm (near-IR) lasers are most used in Raman instruments.

The Raman spectra were acquired with the Raman spectrometer (manufacturer: Renishaw, model: InVia Reflex) of the Theoretical & Physical Chemistry Institute, National Hellenic Research Foundation (**Fig. 13**). The 514.5 nm laser was used which was set to <0.30 mW power to avoid sample laser damage through a x50 short working distance objective lens. Each spectrum was collected for 35 sec with a 2400 line/mm diffraction grating, spanning Raman shifts of 200 – 1200 cm^{-1} .

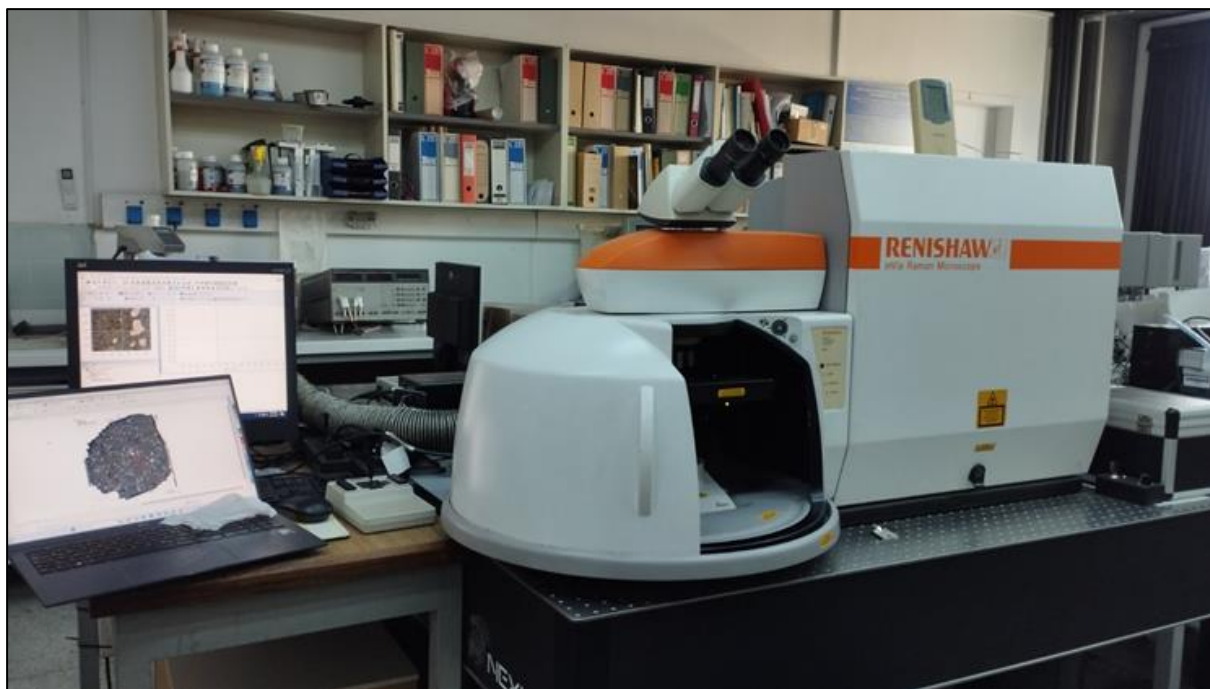


Figure 13: Raman Spectrometer at the Theoretical & Physical Chemistry Institute, National Hellenic Research Foundation (Athens, Greece).

3 RESULTS

The thin section of Slobodka (NHMW-L4372) meteorite was studied for its petrography, chemical analysis, and mineral identification. Maps of the thin section were created under transmitted and reflected light with the optical microscope. The characterization of shock features from the groundmass was used in shock stage classification (schemes from Stöffler *et al.*, 1991; Stöffler & Grieve, 2007; Fritz *et al.*, 2017; Stöffler *et al.*, 2018), and was initially investigated by optical microscopy. Several techniques were utilized including optical microscopy (both transmitted and reflected light), scanning electron microscopy with energy-dispersive x-ray analysis (EDS), electron probe micro-analysis (EPMA), and Raman spectroscopy (514 nm laser). There were eight distinct areas located in the groundmass and numerous distinct areas located in the MV that were analyzed for their texture and mineral chemistry.

3.1 Petrography

3.1.1 Groundmass

3.1.1.1 MOSAICS OF THE THIN SECTION

The mosaic A (**Fig. 14A**) shows the thin section of the meteorite taken with the optical microscope in transmitted light with plane-polarized light (PPL). The melted vein and the chondrules are recognizable; there is a color gradation in some areas that is visible in the groundmass due to possible oxidation of the olivines. The mosaic B (**Fig. 14B**) shows the thin section of the meteorite taken with the optical microscope in reflected light. The thin section of the meteorite is mainly depicted with darker colors throughout the groundmass. This helps us to identify the mineral grains in the groundmass mainly the metals, the troilites, and the plagioclases with white, off-white, and grey colors respectively.

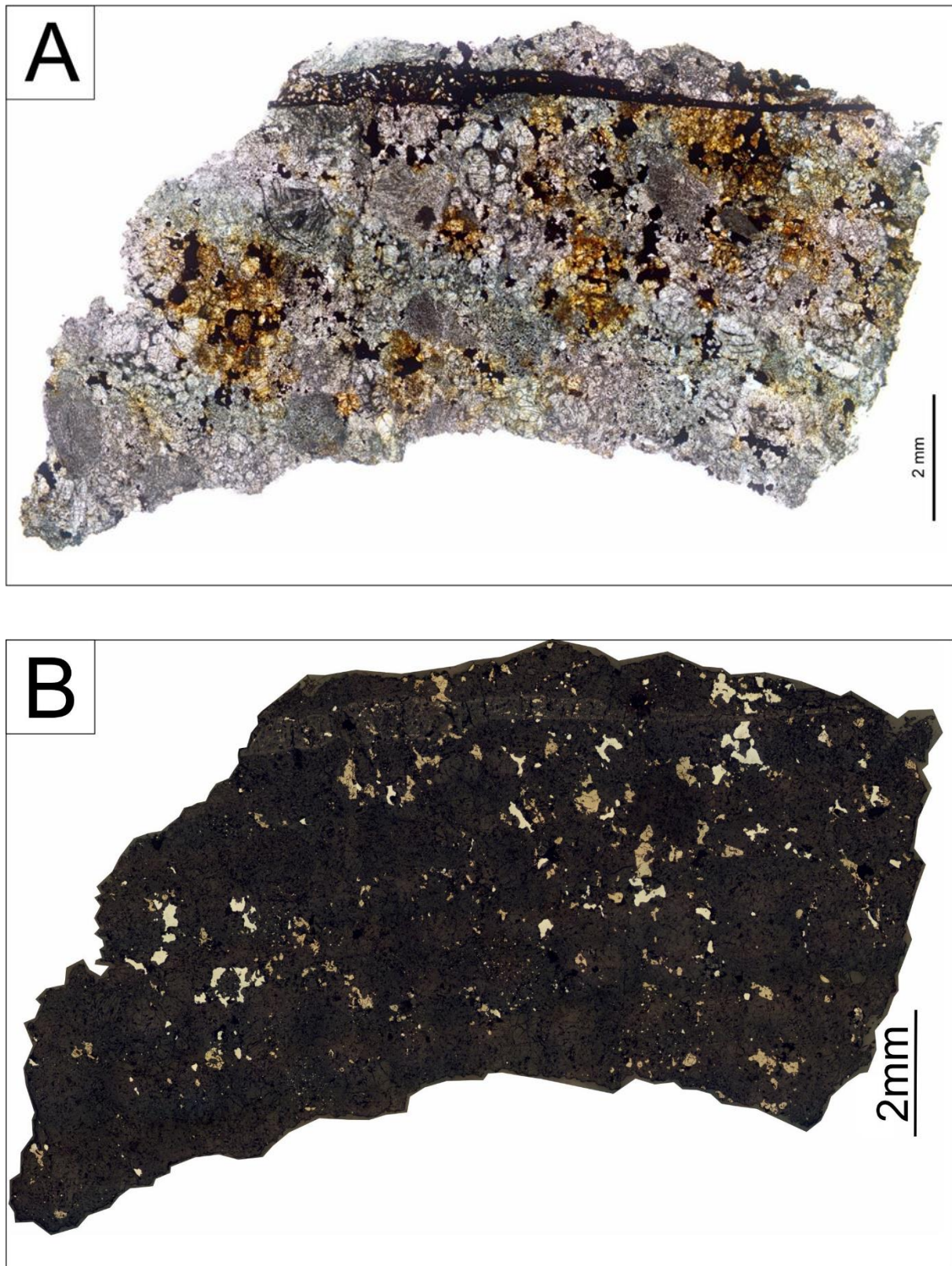


Figure 14: (A) Slobodka image map in transmitted light (PPL); (B) Slobodka image map in reflected light.

The following mosaics were created by using an optical microscope in cross-polarized light (XPL). The difference between images (A) and (B) of the **figure 15** is that the second one is 90° tilted, so the undulatory extinction of grains in the thin section would be visible.

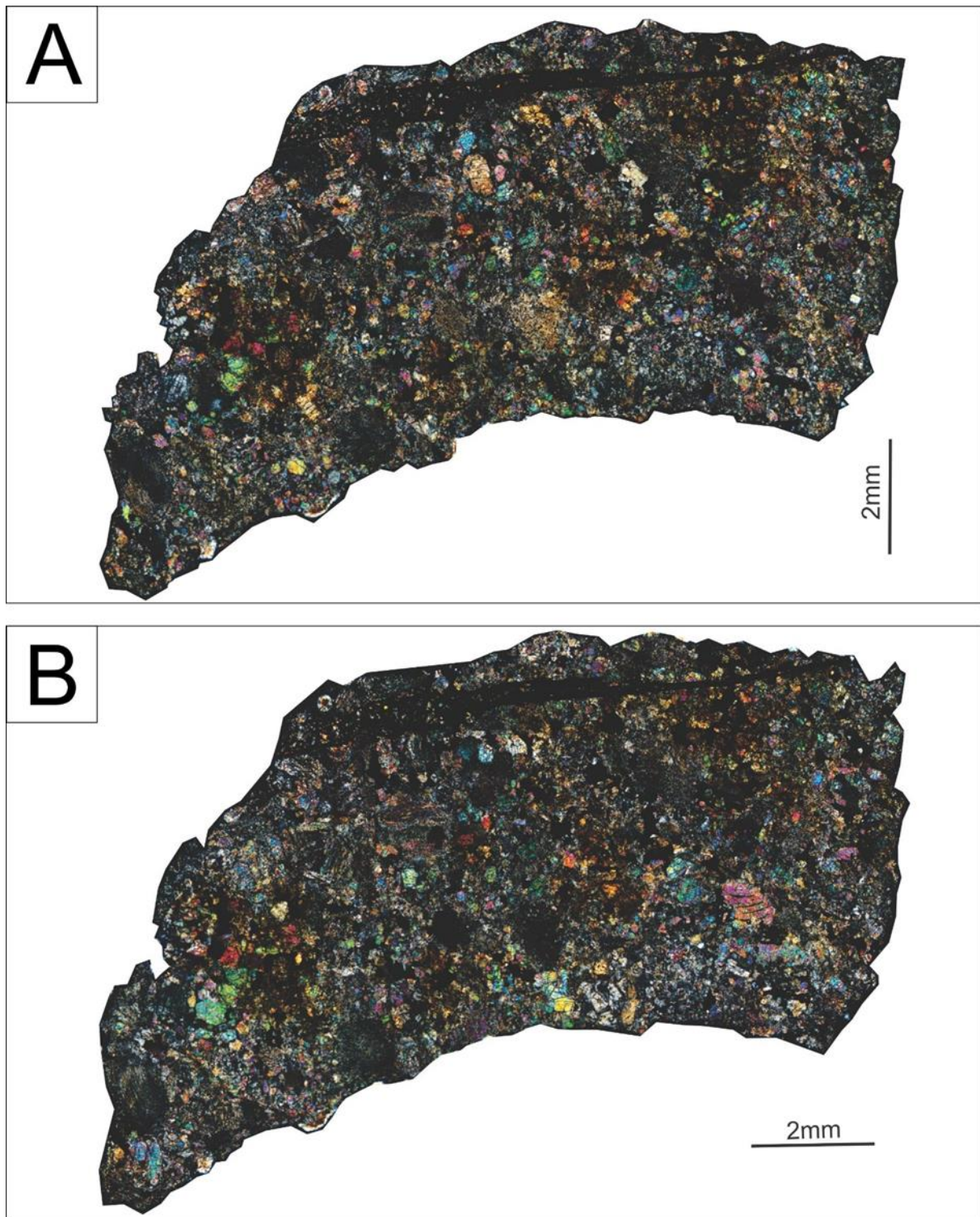


Figure 15: (A) Slobodka image map in transmitted light (XPL, position 1); (B) Slobodka image map in transmitted light (XPL, position 2).

3.1.1.2 TEXTURE

Olivines, pyroxenes, and plagioclases were detected in the groundmass of the meteorite, alongside chromites, sulfides, and metals. Most chondrules are poorly delineated and mainly show textures like non-porphyritic banded and radial types of chondrules. The average chondrule size is in the range of approx. 0.7-1.1 mm.

3.1.1.2.1 Olivine Grains

The olivine group of minerals are the most predominantly found in the groundmass of Slobodka. They exhibit various deformation-related features such as irregular fractures, planar fractures, mosaicism, and undulatory extinction. Variable olivine grains range from 100 to 1000 μm length can be observed. The main olivine grain in the figure (**Fig. 16**) is enclosed by metals, while smaller grains of olivine are also scattered around it. As for the shock features, the grain shows irregular fractures and undulatory extinction observed under the optical microscope, and the large black fragments contain metals.

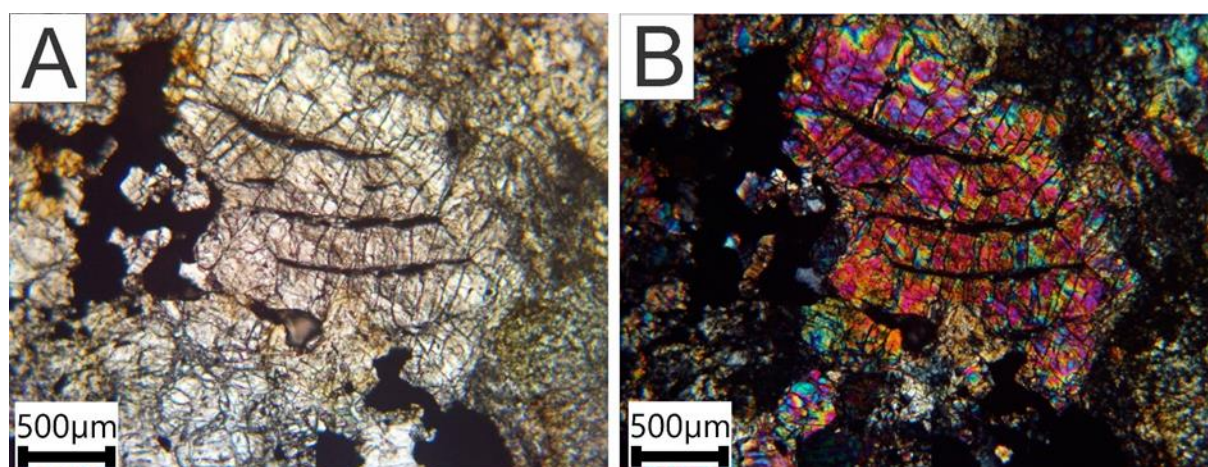


Figure 16: A representative olivine grain in the groundmass taken with the optical microscope in (A)PPL, and (B) XPL light.

3.1.1.2.2 Pyroxene Grains

Pyroxenes show both planar and irregular fractures and moderate degrees of mosaicism. The length of the pyroxene grains is comparable to olivines as it ranges from 100 to 1500 microns, throughout the groundmass. In the following figure (**Fig. 17**) a representative grain shows irregular fractures, exhibiting waves of extinction. It is surrounded by small olivine grains and metals.

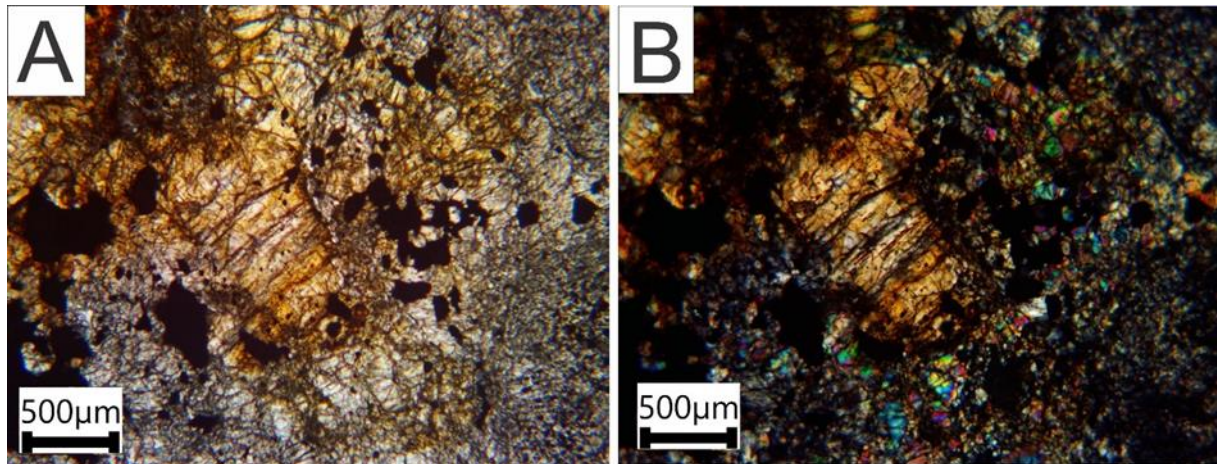


Figure 17: A representative pyroxene grain in the groundmass taken with the optical microscope in (A)PPL, and (B) XPL light.

3.1.1.2.3 Plagioclase Series Grains

The majority of the plagioclase grains that were studied had also the features of undulatory extinction and irregular fractures. In transmitted light, the plagioclase is always anisotropic, while no diaplectic glass was identified in the thin section. The grain in the following figure (**Fig. 18**) corresponds to a plagioclase, and it is surrounded by olivine and metal grains. It shows irregular fractures and undulatory extinction, too.

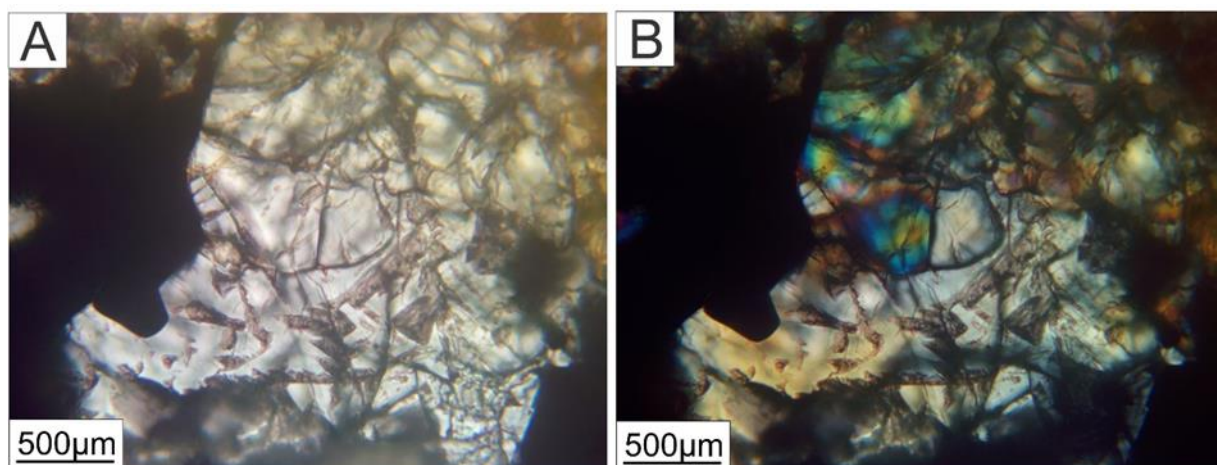


Figure 18: A representative plagioclase grain in the groundmass taken with the optical microscope in (A)PPL, and (B) XPL light.

3.1.1.2.4 Chondrules

The chondrules of the Slobodka meteorite were numbered throughout the groundmass and have been identified by means of optical microscopy (**Fig. 19**). They were mainly characterized as non-porphyritic chondrules that include radial and barred-dendritic textures, but also as porphyritic chondrules, with common olivine-rich and pyroxene-rich grains, with the characteristic optical features in both plane-polarized and cross-polarized transmitted light photographs (**Figs. 20-21**).

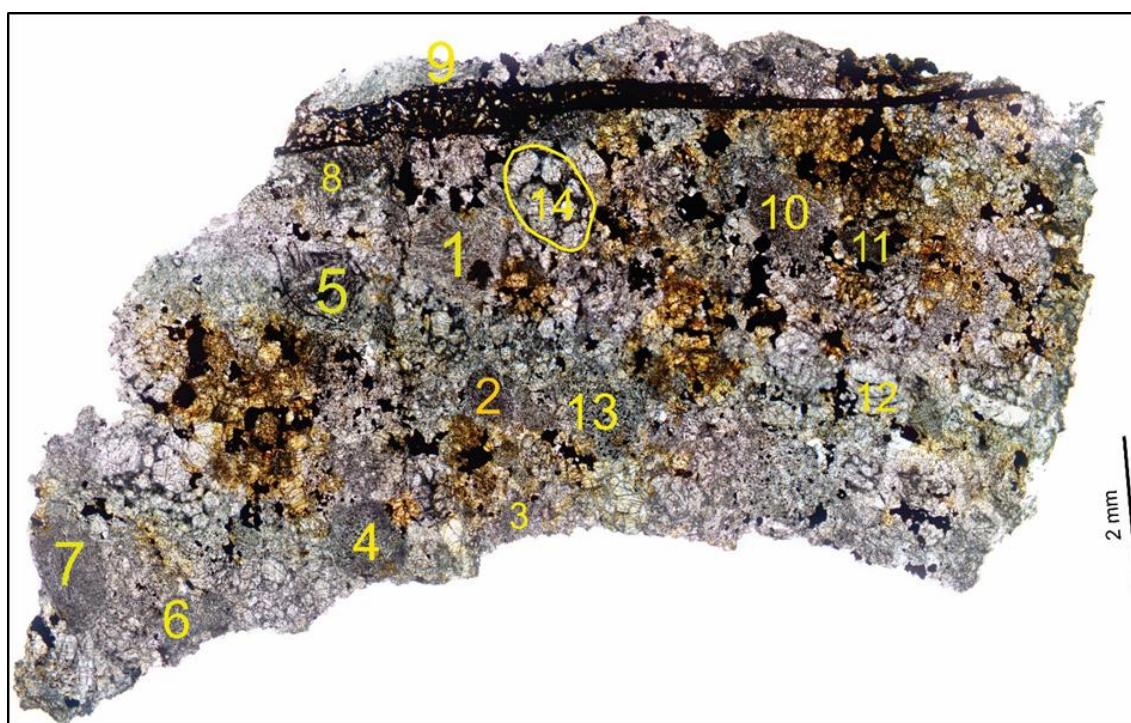


Figure 19: Regions of interest (ROIs) with marked numbered chondrules.

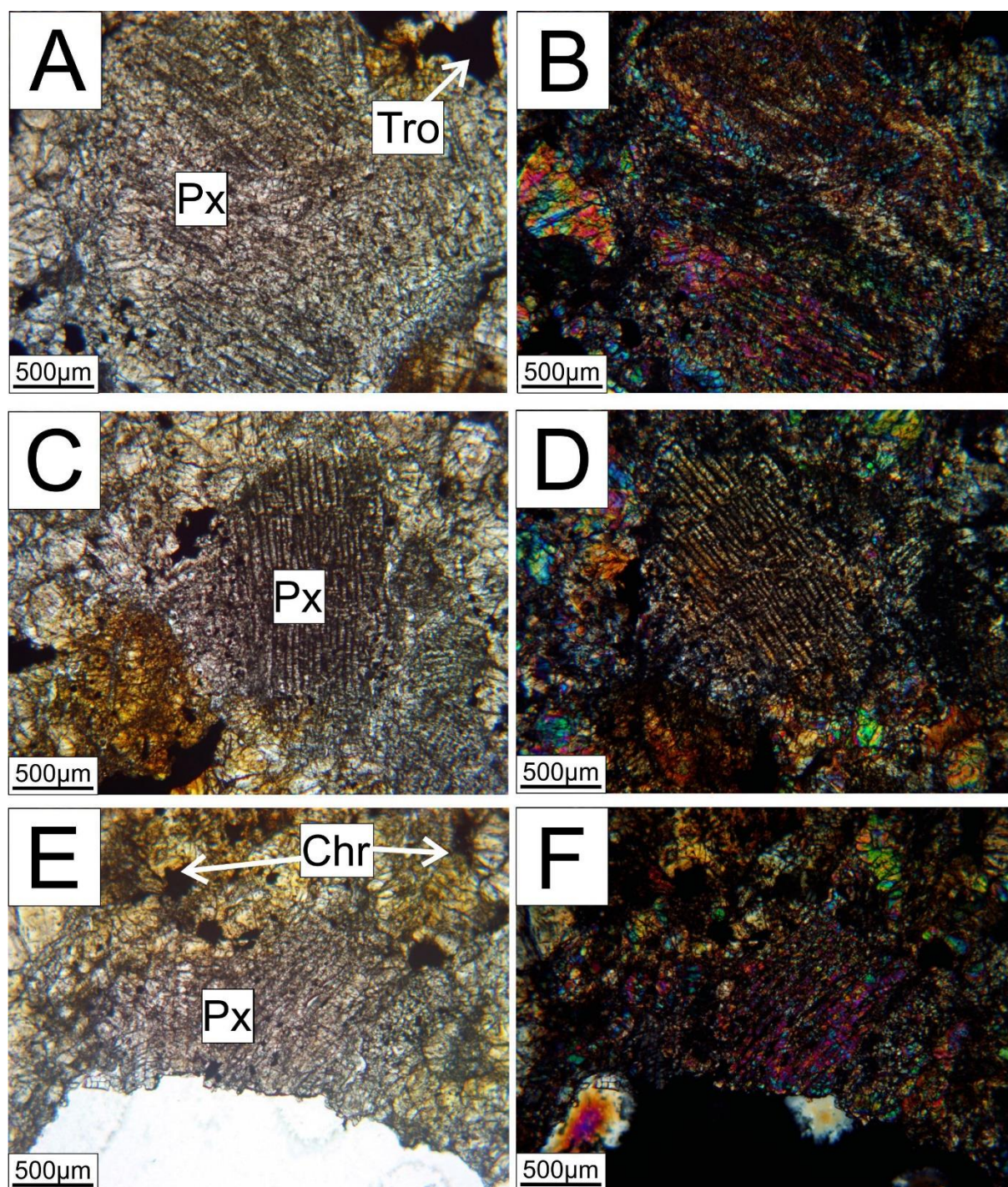


Figure 20: Optical features of Slobodka thin section (ROIs: 01-03): (A) Radial Pyroxene (RP) chondrule (PPL), ROI 01; (B) Radial Pyroxene (RP) chondrule (XPL), ROI 01; (C) Radial Pyroxene (RP) chondrule (PPL), ROI 02; (D) Radial Pyroxene (RP) chondrule (XPL), ROI 02; (E) Radial Pyroxene (RP) chondrule (PPL), ROI 03; (F) Radial Pyroxene (RP) chondrule (XPL), ROI 03.

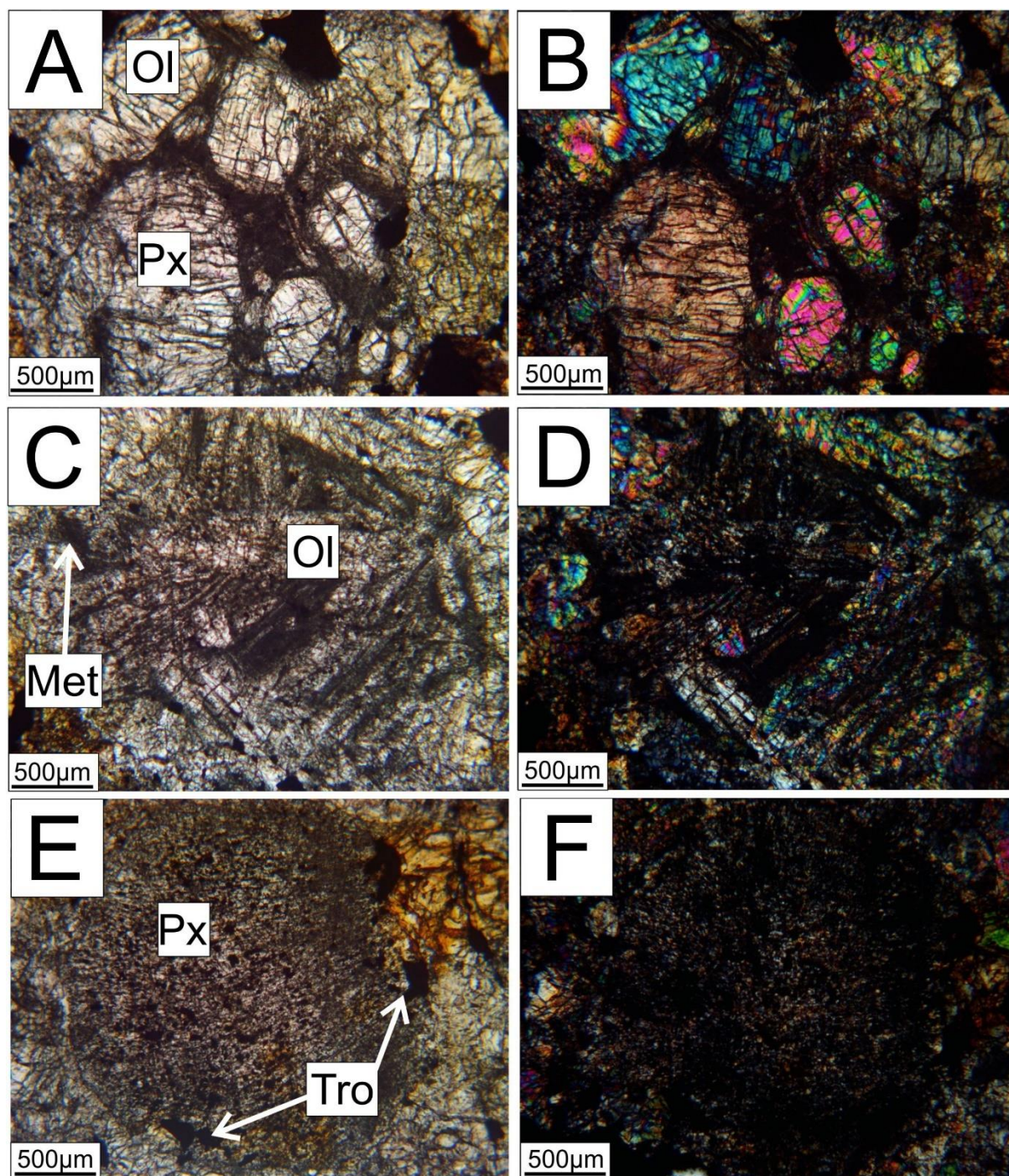


Figure 21: Optical features of Slobodka thin section (ROIs: 05,14): (A) Coarse grains Porphyritic Olivine (PO) chondrule (PPL), ROI 14; (B) Coarse grains Porphyritic Olivine (PO) chondrule (XPL), ROI 14; (C) Barred Olivine (BO) chondrule (PPL), ROI 05; (D) Barred Olivine (BO) chondrule (XPL), ROI 05; (E) Radial pyroxene (RP) chondrule (PPL), ROI 04; (F) Radial Pyroxene (RP) chondrule (XPL), ROI 04.

3.1.1.2.5 BSE images of the groundmass

Backscattered (BSE) images combine topographical, and compositional data as a function of atomic number z of the elements existing in the sample. They show characteristics of atomic number contrast, i.e., the high average z appears brighter than those of low average z (e.g., Gamaletsos, 2024b and references therein). Besides that, high-resolution BSE images from specific regions of the groundmass were taken (Fig. 22-23, Fig.39), and were interested in focusing on the Raman spectroscopy measurements and also were taken for chemical analysis.

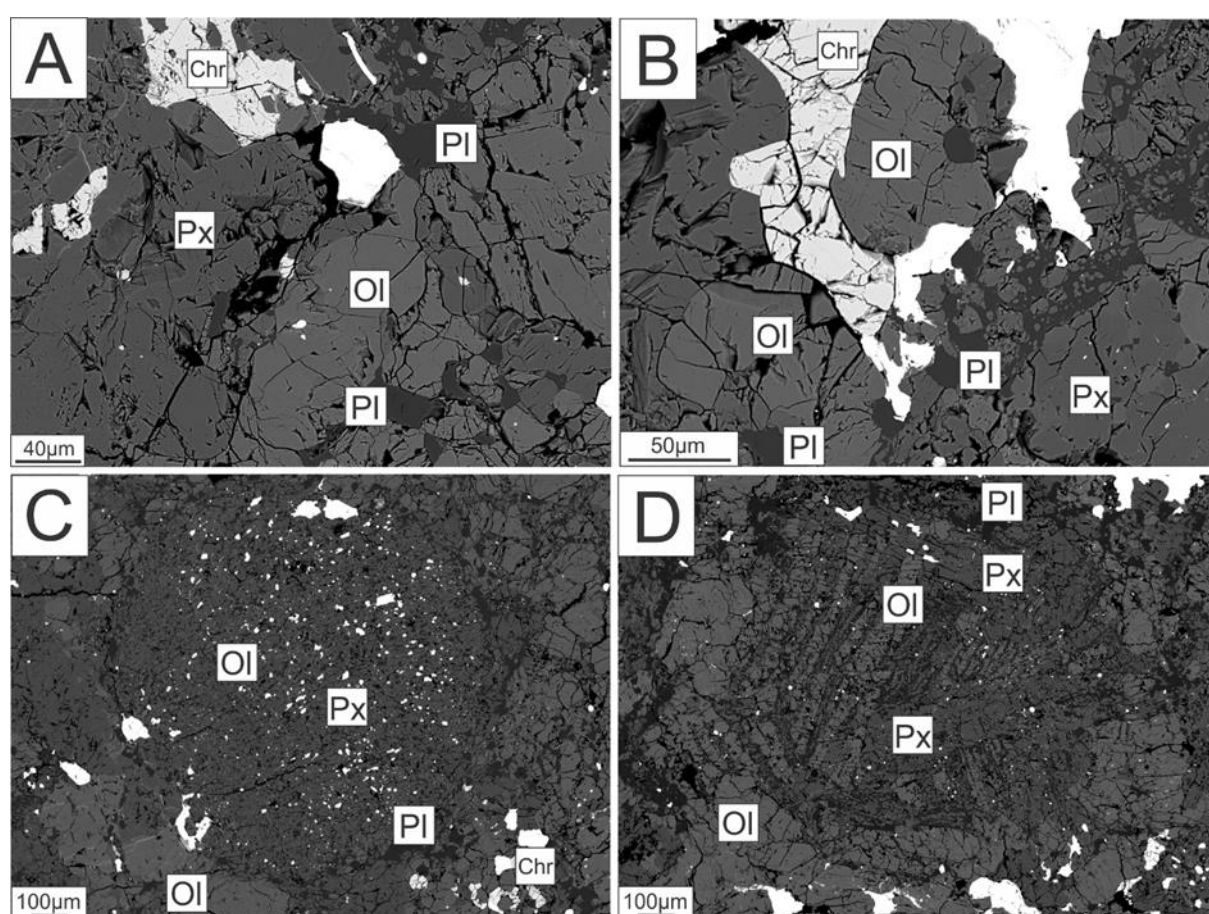


Figure 22: BSE images taken for the ROIs B, C, D, and E respectively in the groundmass (see: **Fig. 39**). (A) region B with Pl, Ol, Px, and Chr minerals detected; (B) region C with Ol, Pl, Px, and Chr minerals detected; (C) region D with Ol, Px, and Pl minerals detected; (D): region E with Ol, Pl, and Px minerals detected. For reference the abbreviations of Ol: olivine, Px: pyroxene, Pl: plagioclase, Chr: chromite, Met: metals.

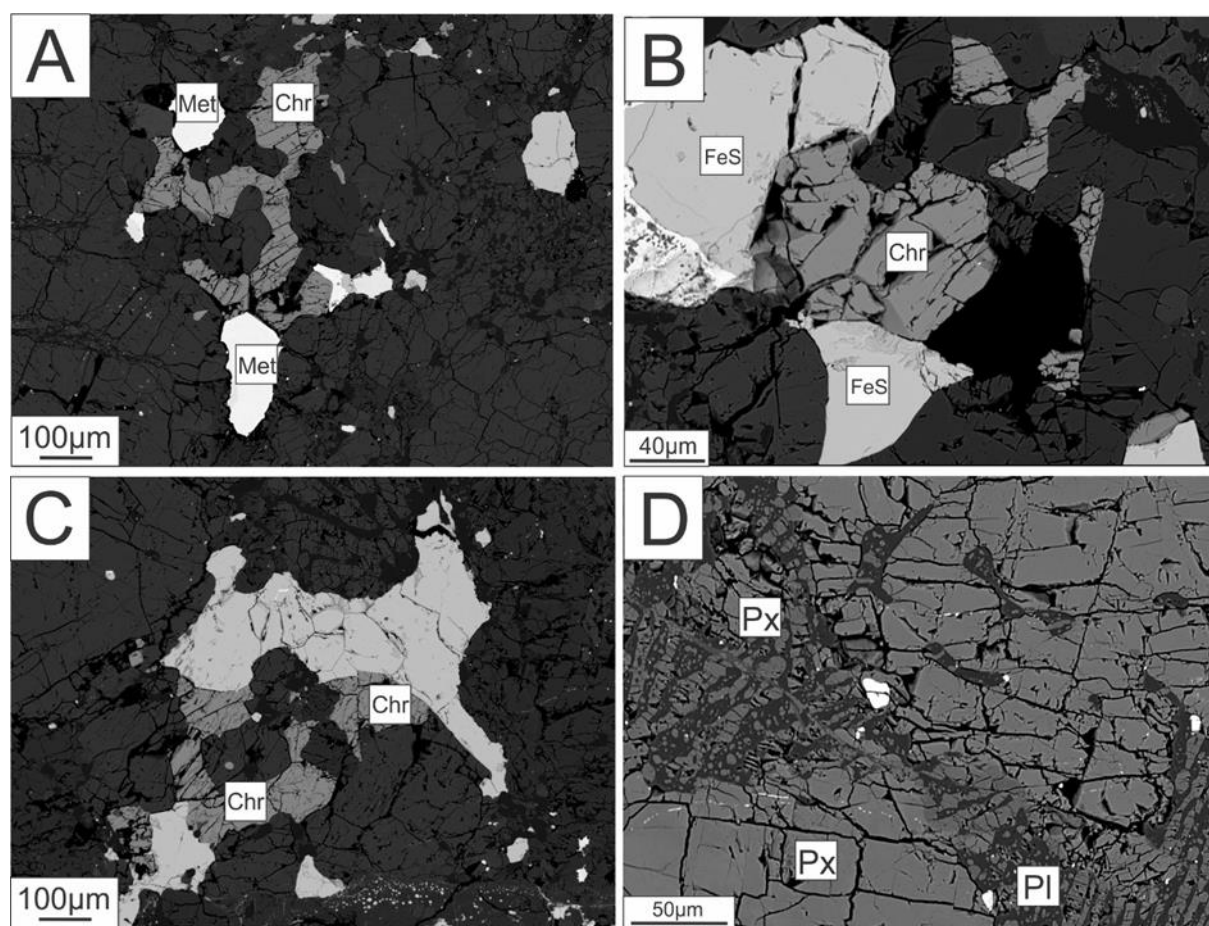


Figure 23: BSE images taken for the ROIs G, H, I, and J respectively in the groundmass (see: **Fig. 39**). (A) region G with Met and Chr minerals detected; (B) region H with Chr, and FeS minerals detected; (C) region I with Chr minerals detected; (D) region J with Px, and Pl minerals detected. For reference the abbreviations of Ol: olivine, Px: pyroxene, Pl: plagioclase, Chr: chromite, Met: metals.

3.1.1.3 SHOCK FEATURES

In the thin section, every grain in the groundmass was observed using an optical microscope. It's important to note that the texture of the minerals has been influenced by the shock wave the sample experienced, affecting their appearance in the microscope. We used magnifying lenses, focusing on their details, to identify the specific shock features. The most abundant feature in the thin section was irregular fractures present in pyroxenes and olivines and a few plagioclases (**Figs. 24B, 24C, 25A, 25D, 25E**). Also, undulatory extinction was present in both Fe-Mg-rich silicates and plagioclases (**Fig. 24D**). There was one set of planar fractures present in olivine grains (**Figs. 24E, 25B**), and two sets of planar fractures present in two olivine grains (**Figs. 24A, 25C**). Also, weak mosaicism prevails in quite a few pyroxenes and olivines (**Figs. 24F, 25F**). However, we report that planar deformation features and maskelynite were not found in this thin section.

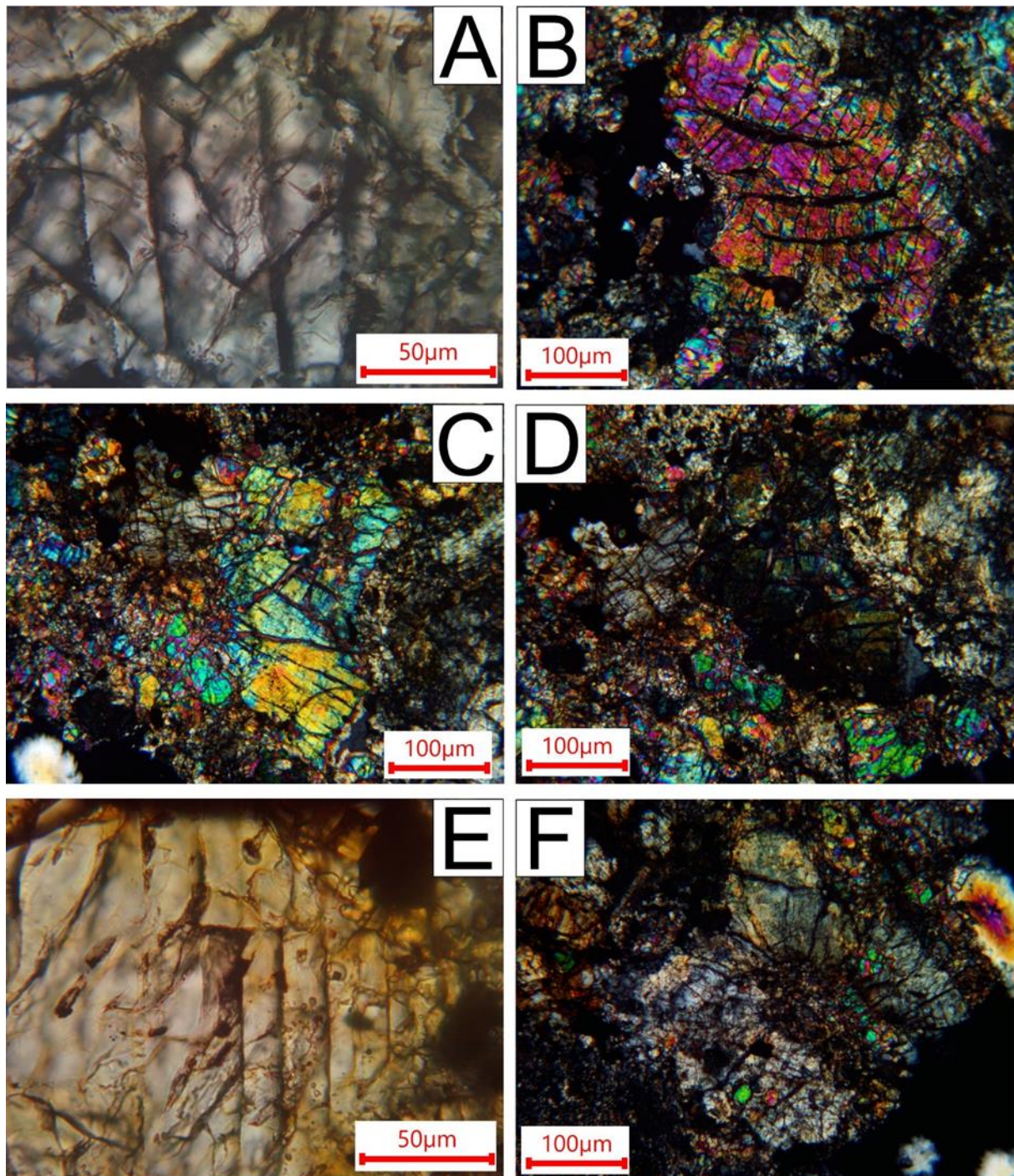


Figure 24: (A) two sets of planar fractures in olivine (PPL); (B) irregular fractures in olivine (XPL); (C) irregular fractures in olivine and pyroxene (XPL); (D) undulatory extinction in olivine (XPL); (E) one set of planar fractures in olivine (PPL); (F) moderate to strong mosaicism in orthopyroxene (XPL).

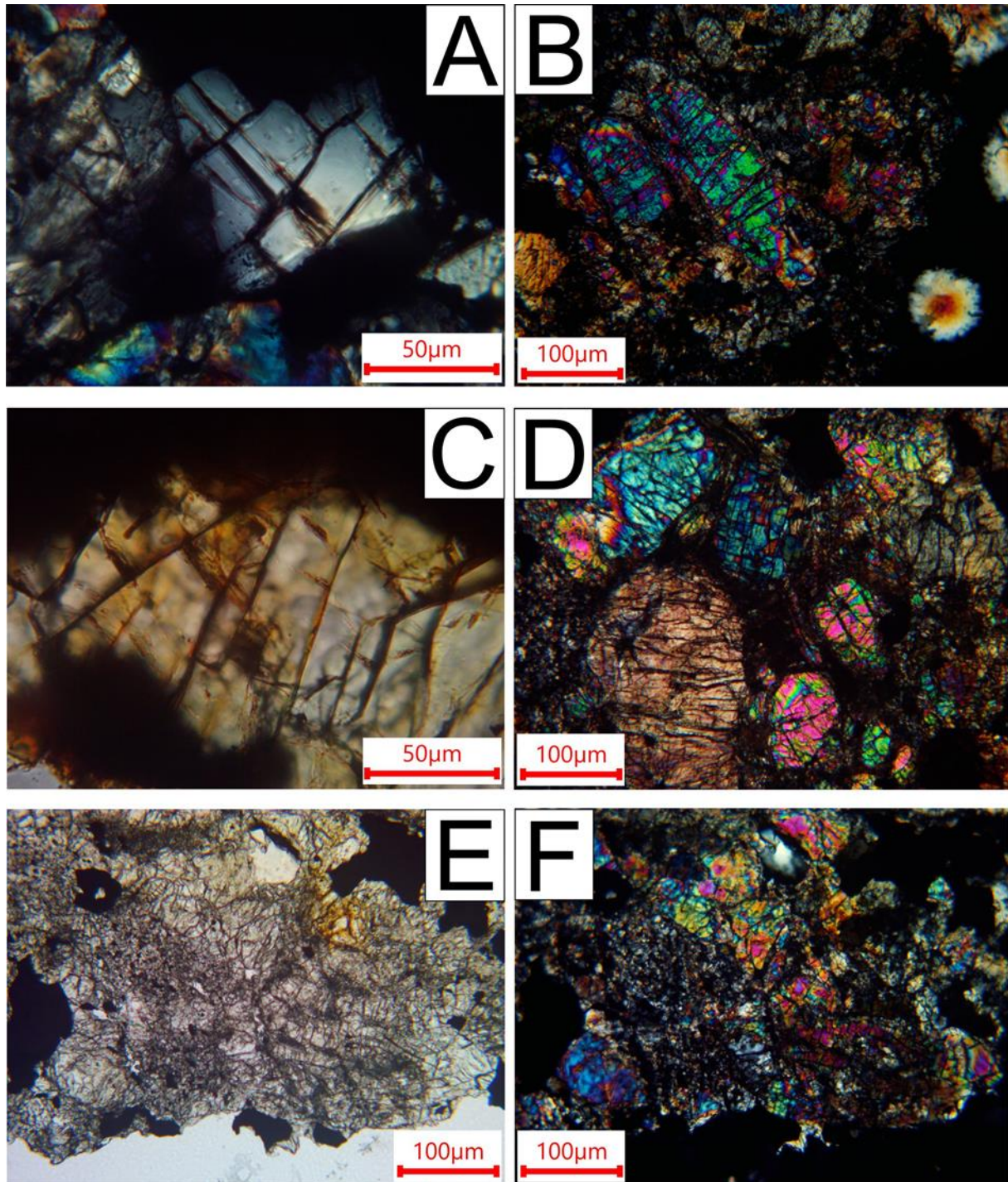


Figure 25: (A) plagioclase crystal with irregular fractures (XPL); (B) planar fractures in olivine (XPL); (C) two sets of planar fractures in an olivine crystal that exhibit undulatory extinction (PPL); (D) irregular fractures in olivine and pyroxene (XPL); (E) irregular fractures in olivine and pyroxene (PPL); (F) pyroxene and olivine at extinction to show mosaicism (XPL).

3.1.1.3.1 Statistics of Shock Features

A statistical depiction of the abundant minerals corresponding to the olivine (incl. pyroxenes) group and the plagioclases (feldspars) in the thin section of the studied meteorite is shown in the following chart (**Fig. 26**). A total of 107 grains of olivines (incl. pyroxenes) and plagioclases in the groundmass have been observed. For every single one of them, a thorough examination for the identification of shocked features was conducted, focusing on the statistics of shock features of the olivine (incl. pyroxene) minerals because they are the most abundant (**Fig. 27**).

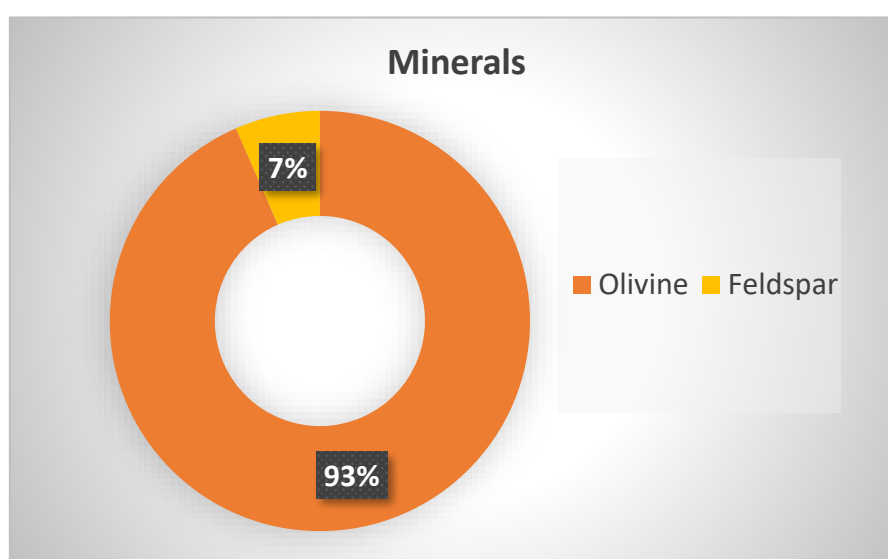


Figure 26: Statistic percentage of magnesium silicates and feldspar (N=100 olivines N=7 plagioclase).

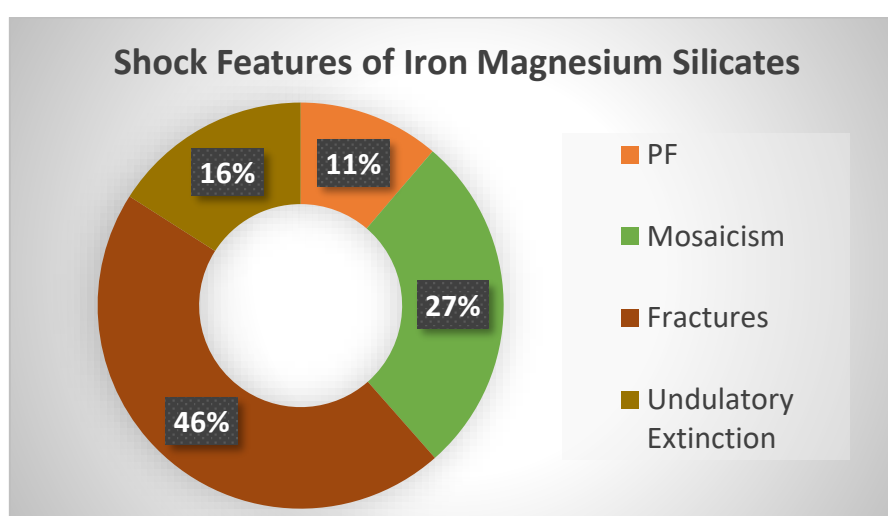


Figure 27: Statistic percentage of shock features of magnesium silicates.

3.1.1.4 CHONDRULE – MATRIX INTEGRATION

Both ImageJ/FIJI software packages were utilized to measure the area of each chondrule and calculate the percent allocation of the chondrules that are distributed in the studied thin section of the meteorite Slobodka. The total area of the thin section was calculated to be 80.1 mm^2 . Using a ruler, a selected region of the thin section was measured, so the measurement of the software matched the real area of the thin section, and the result was an area square of 44.3 mm^2 . The result of the ruler was a ruler area of $8 \text{ mm} \times 5.5 \text{ mm}$, i.e., 44 mm^2 . Assuming that the above results were accurate, calculations were continued. Subsequently, ROIs were marked in the thin section, numbering the chondrules (**Fig. 28**).

Furthermore, the area of the melt vein (MV) was also calculated (approx. 0.9 mm^2), avoiding counting the MV with the whole area of calculations (**Fig. 29A**). After that, measurements of the chondrules were proceeded, so that it was easy to calculate its area. For instance, the first chondrule's area that was calculated was: $\text{area_chond_1} = 1.4 \text{ mm}^2$ (**Fig. 29B**).

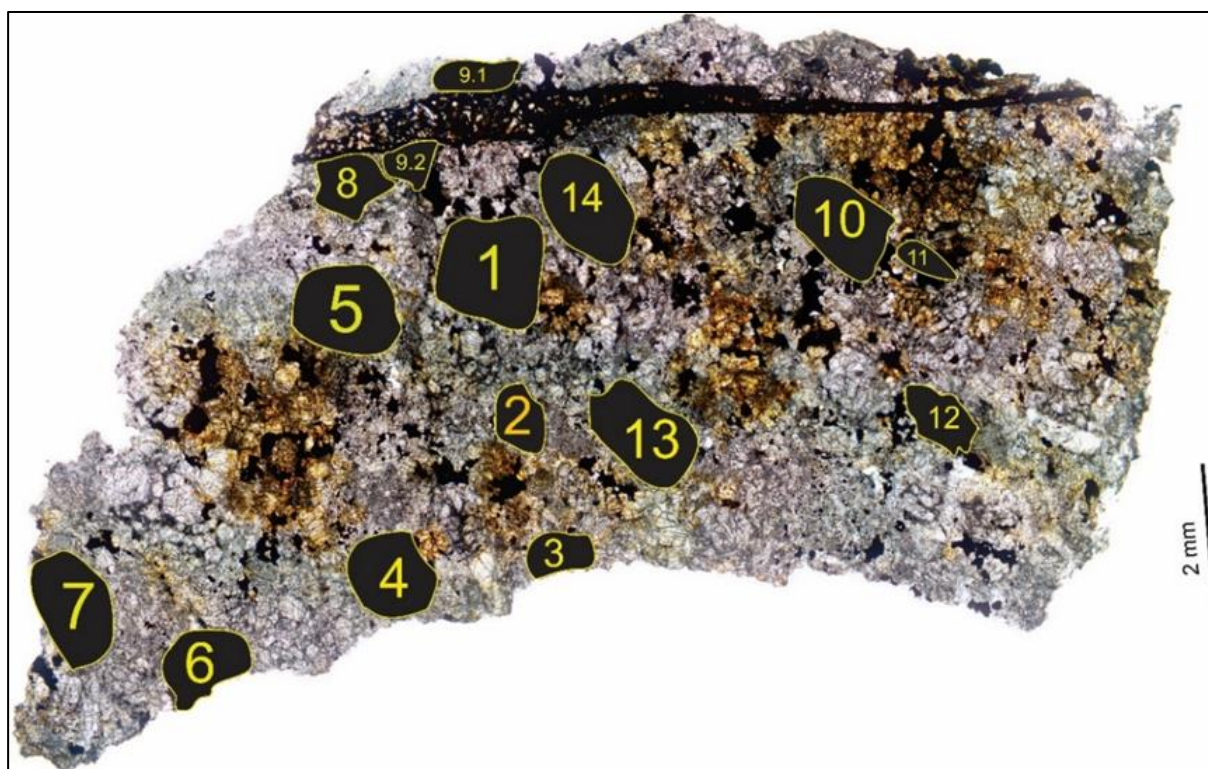


Figure 28: Regions of Interest (ROIs) for measuring the areas of each chondrule.

Finally, the areas of fourteen (14) total chondrules were measured, and calculating their percentage over the whole groundmass (**Table 5**). It is concluded that with this method the chondrule abundance that the chondrules occupy over the groundmass is in total 11.6 (vol %).

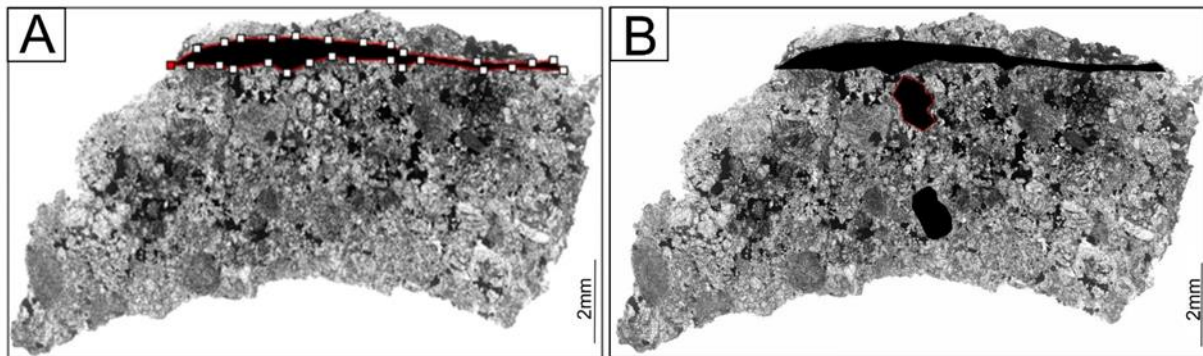


Figure 29: (A) Area of melt vein using FIJI software; (B) Area of the chondrule 1 in the groundmass.

Table 5: Results of the calculations.

Region of Interest (ROI)	Area(mm ²)	Percent (%)
1	1.4 mm ²	1.7 %
2	0.4 mm ²	0.5 %
3	0.2 mm ²	0.3 %
4	0.8 mm ²	1.0 %
5	1.4 mm ²	1.8 %
6	0.6 mm ²	0.8 %
7	1.0 mm ²	1.1 %
8	0.5 mm ²	0.6 %
9.1	0.3 mm ²	0.3 %
9.2	0.4 mm ²	0.5 %
10	1.3 mm ²	1.6 %
11	0.2 mm ²	0.2 %
12	0.5 mm ²	0.6 %
13	0.2 mm ²	0.3 %
14	0.2 mm ²	0.3 %
Melt Vein	0.9 mm ²	1.1 %
Total	10.1 mm ²	13.8%
Total' (minus melt vein)	9.2 mm ²	12.7%
Total' = Total-melt vein = 10.1 mm² - 0.9 mm² = 9.2 mm²		
Whole area = Total-Melt Vein = 80.1 mm² - 0.9 mm² = 79.2 mm²		
(Total'/Whole area') * 100 % = (9.2 mm² / 79.2 mm²) * 100 % = 11.6 %		

3.1.1.5 MODAL-ABUNDANCE

The ImageJ software package was used to measure the percentage of the metal abundance in the groundmass of Slobodka (**Fig. 30**). To this trajectory, an image of the whole groundmass of the meteorite was taken as a reference using reflected light, to identify the grains that consist of metals and iron sulfides (troilite). Metal grains appear with a white color, while troilite grains appear with an off-white color. By matching the red appearance on the image's threshold of the ImageJ software with the white one grain of the Slobodka's groundmass, the total metal abundance percentage was calculated at ~1.17 %.

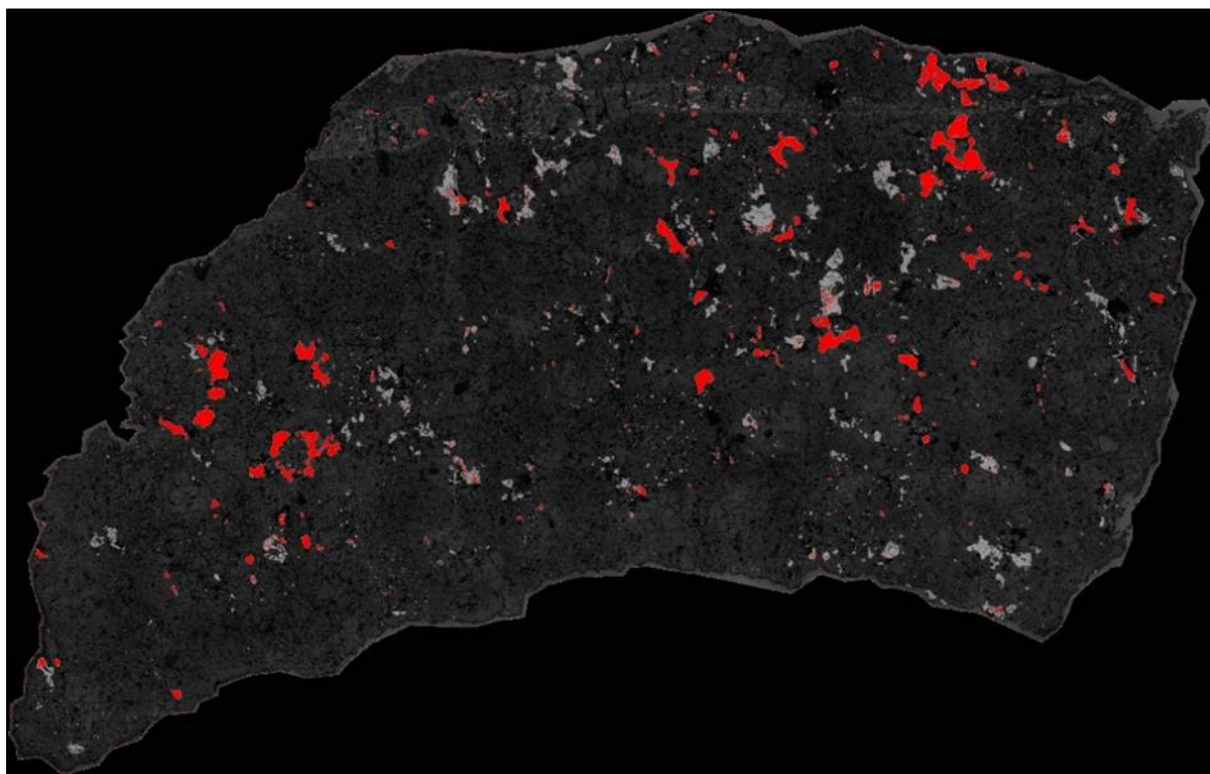


Figure 30: Area of the measured percentage of the metal abundance in Slobodka.

3.1.1.6 AVERAGE CHONDRULE DIMENSION

In order to measure the length and diameter of the chondrules in the studied thin section of Slobodka meteorite, the FIJI software package was utilized (**Fig. 31**). The average minimum and maximum length of thirteen (13) measured chondrules (actually the 9th chondrule was divided in two parts: 9.1 and 9.2) has been calculated to be 0.83 mm (**Table 6**).

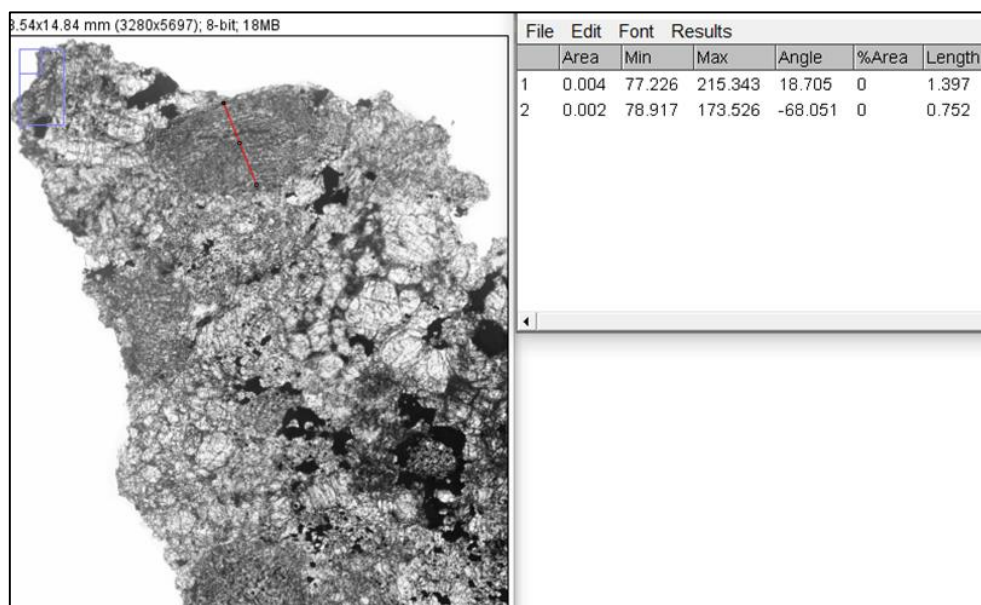


Figure 31: Measured minimum and maximum length of the chondrule with the FIJI software package.

Table 6: Measurements of the lengths[min-max] [mm].

Number	length(max)[mm]	length(min)[mm]	average min-max[mm]
1	1.40	0.75	1.07
2	0.94	0.62	0.78
3	1.03	0.87	0.95
4	0.82	0.49	0.65
5	1.28	1.09	1.19
6	1.27	0.68	0.98
7	1.26	0.84	1.06
8	0.59	0.43	0.51
9	0.97	0.47	0.72
10	0.80	0.53	0.72
11	0.65	0.40	0.72
12	1.09	0.40	0.72
13	1.20	1.14	0.72
average			0.83 [mm]

3.1.1.7 AVERAGE PLAGIOCLASE DIMENSIONS

The length of the plagioclase grains was calculated using the FIJI software package. The maximum length of a plagioclase grain was 40.0 μm (**Table 7**).

Table 7: Calculated length of feldspar grains in the groundmass using the FIJI software package.

Number	Length (μm)
1	40.0
2	46.5
3	19.1
4	17.5

3.1.2 Melt Vein

3.1.2.1 TEXTURE

A melt vein (MV) was easily observed within the upper edge of the round thin section of the studied meteorite sample (**Fig. 14**). The width of this MV is close to the true thickness of the veins in a meteorite. The minerals of the melt vein could not be observed using the optical microscope due to the low image resolution. Therefore, we used EPMA and backscattered imaging to study the characteristics of the melt vein, as it was a more suitable analytical method. The studied thin section was BSE scanned with the EPMA to create the melt vein overview (**Fig. 32**). Besides that, high-resolution BSE images from specific regions of the MV were taken (**Fig. 39**), and were interested in focusing on the Raman spectroscopy measurements (**Figs. 33-35**), and also were taken for chemical analysis.

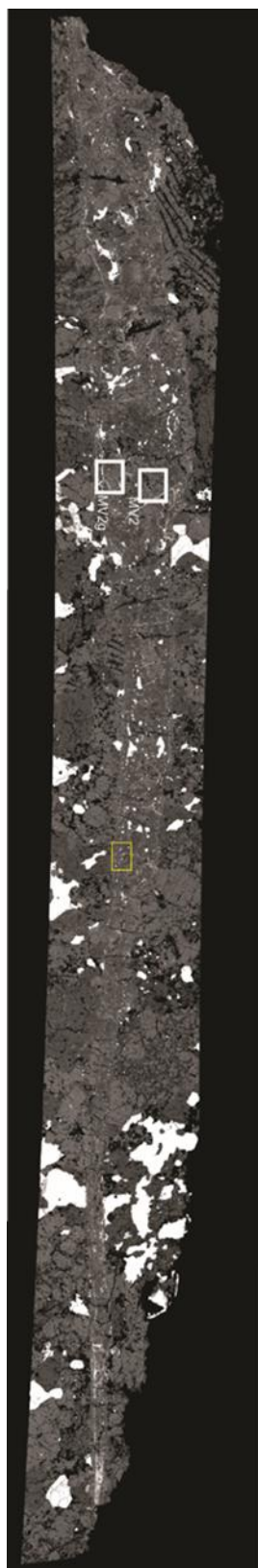


Figure 32: Overview of the Melt vein (back-scattered mosaic) of Slobodka meteorite.

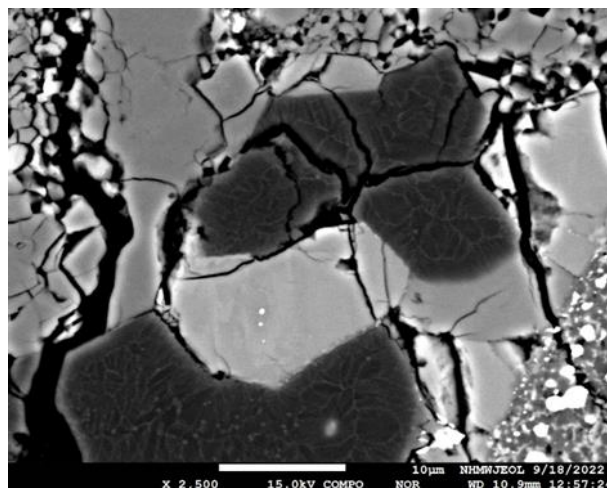


Figure 33: BSE image of MV2 region.

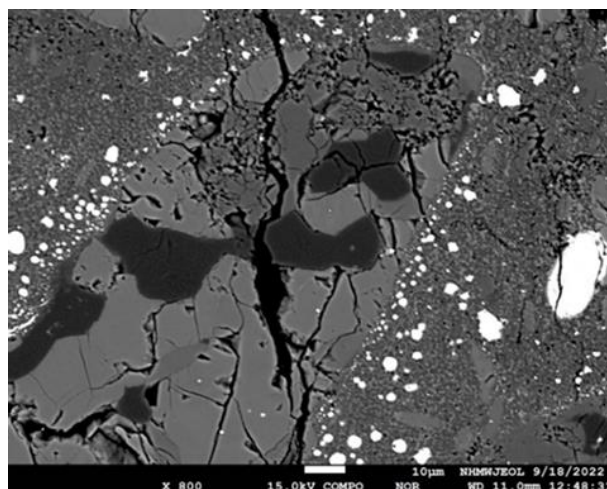


Figure 34: An overview of the MV2 region (BEI image).

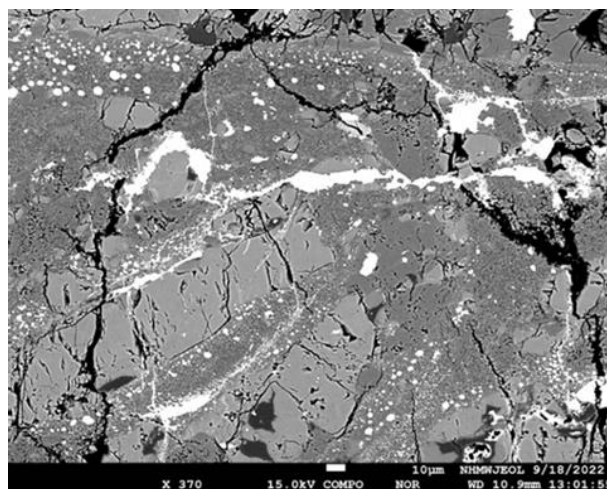


Figure 35: An overview of the MV2g region (BEI image).

The MV2 region (**Fig. 39**) was studied to investigate the distinct dendritic texture of the grains. The BSE images (**Fig. 36**) show the high-pressure (HP) form of albitic jadeite in the MV. It's important to note that albitic jadeite isn't stable under the beam, as the grains were damaged during chemical analysis.

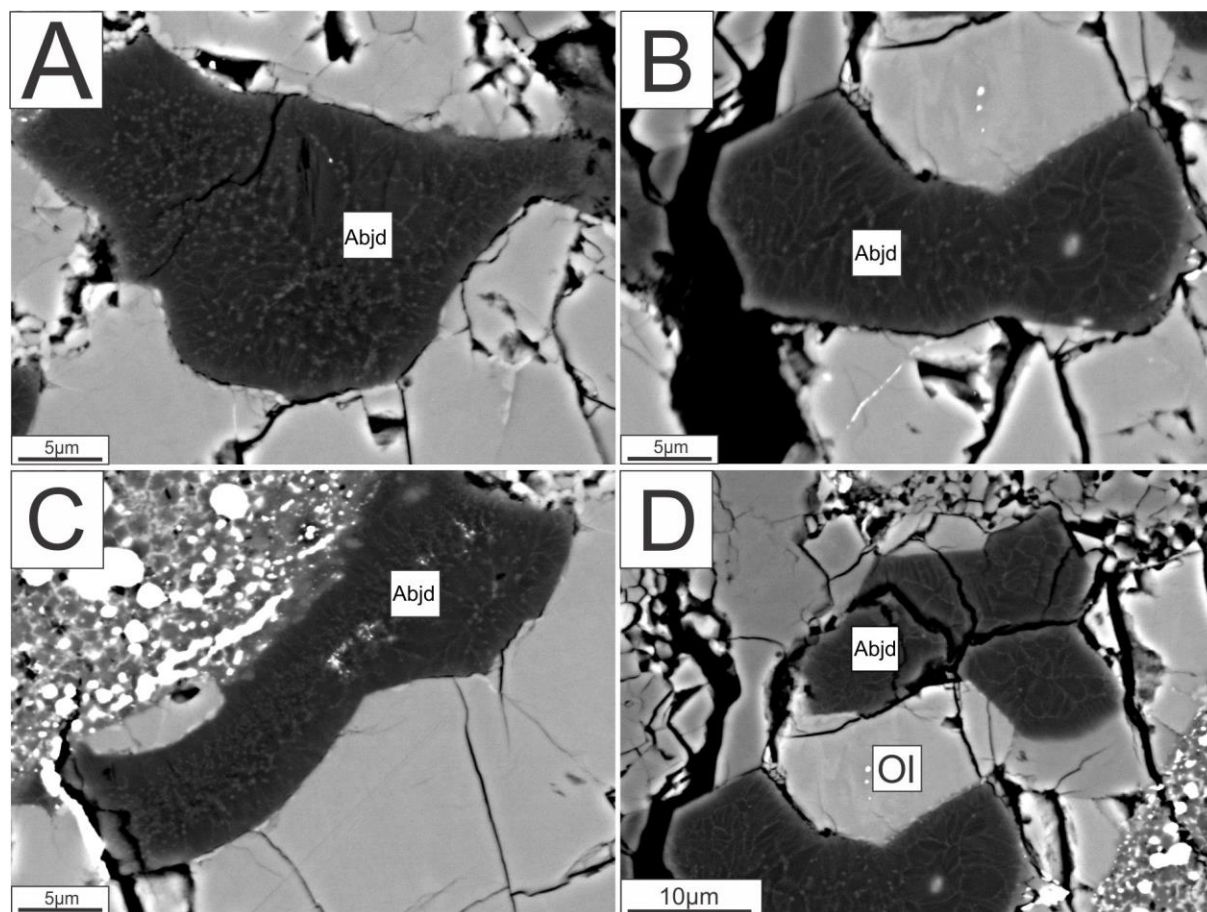


Figure 36: BSE images were taken for the 2a,2b,2c, and 2d positions respectively in the melt vein (MV). (A-D) regions MV2a, MV2b, MV2c & MV2d with HP mineral (albitic jadeite). Abbreviations: Ol for olivine, Abjd for albitic jadeite.

The width of this MV has been observed to have many fluctuations from 719μm to 85μm width (**Fig. 37**). Four high-pressure (HP) minerals have been observed and identified in the Slobodka meteorite, such as tuite, majorite, wadsleyite, and albitic jadeite (**Fig. 37**). Every high-pressure polymorph has its specific texture, the albitic jadeite is present as submicron dendritic crystals within irregularly shaped felsic domains (up to ~32 μm long) (**Fig. 38C**), and tuite as elongated crystals having a comparable length (up to ~20 μm long) or irregularly-shaped crystals within the melt vein matrix (**Fig. 38B**). Wadsleyite exists in the groundmass of the melt vein as smaller grains (up to ~2 μm) (**Fig.38D**), and majorite is the abundant mineral

of the groundmass of the melt vein and exists as small grains with forms of euhedral to subhedral crystals up to $\sim 5\text{--}7\text{ }\mu\text{m}$ long (**Fig. 38A**).

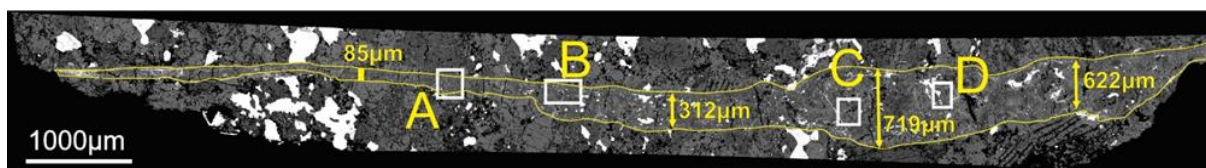


Figure 37: Overview (back-scattered mosaic) of the investigated shock melt vein (MV) in the Slobodka meteorite. The locations of the HP phases are denoted with white rectangles and further expanded in the following figure (see: **Fig. 38**).

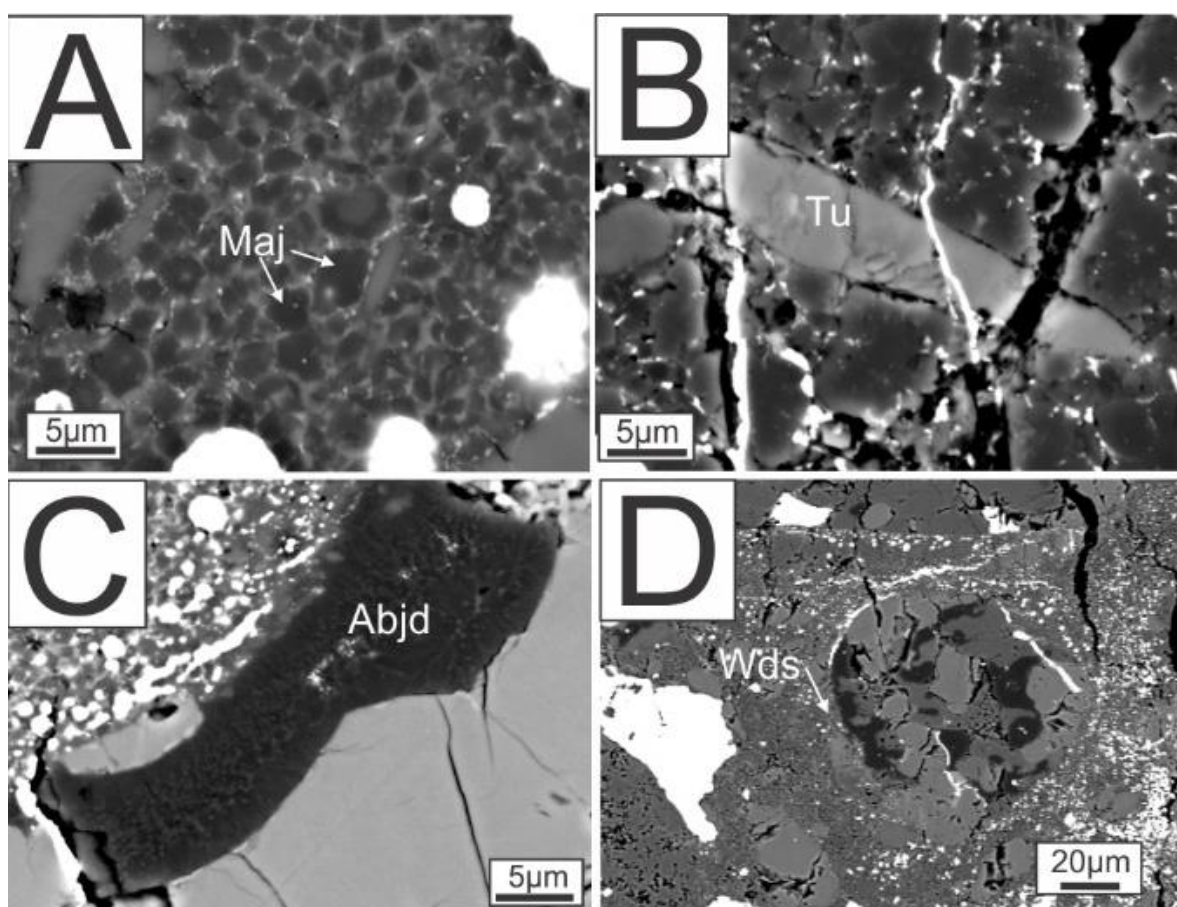


Figure 38: HP phase from the investigated MV of the Slobodka meteorite as it is denoted in the figure above (see: **Fig. 37**): (A) Majorite (Maj) in the form of euhedral to subhedral crystals; (B) tuite (Tu) grain (up to $\sim 20\text{ }\mu\text{m}$); (C) albitic jadeite (Abjd) crystals within a large irregular felsic domain; (D) wadsleyite (Wds) at the contact of a large clast with the SMV groundmass.

3.2 Mineral Chemistry

3.2.1 Regions of Interest

Electron microprobe (EPMA) analysis was performed in all the selected regions of interest (ROIs) in the studied thin section of the Slobodka meteorite. In particular, the annotated ROIs are displayed in the main groundmass (**Fig. 39**), in the area in which the following measurements were made. ROIs from **B** to **J** include grains from the groundmass. The MV2 region corresponds to the melt vein of the meteorite (**Fig. 39**). EPMA analysis of the MV2 region aims to identify new high-phase minerals that have not been identified, yet. Besides, additional EPMA measurements have been yielded for the purpose of the classification of the Slobodka meteorite, focusing on the chondrules that are within the regions of **D**, **E**, and **J** (Appendix **Tables A1-7** for each EPMA analysis, and Appendix **Figures A1-3** for each annotated image of each EPMA analysis). The electron microprobe analysis of the olivine group of minerals including the homogeneity of their composition, the pyroxene group of minerals, the plagioclase series, and the spinel group of minerals, as well as those from the metals and sulfides are shown in Tables A1 & A7, A2, A3, A4, A5 and A6, respectively.

As it is mentioned above, each ROI on the groundmass was subjected to detailed EPMA probing. Chemical analysis of the regions in the ROIs **B**, and **C** respectively in the groundmass (**Fig. 39**) reveal the mineral grains present in the groundmass of the meteorite, which are among olivines, pyroxenes, plagioclases, and chromites (**Figs. 24A, 24B**). Chemical analysis of the chondrules found in the ROIs **D**, **E**, and **J** respectively in the groundmass (**Fig. 39**) reveals the presence of pyroxene and olivine (**Figs. 24C, 24D**). As a result, there is a need of changing the categorization of the chondrules in this meteorite. Upon further examination through the EPMA, the chondrule shown in the **figure 25C** was identified as micro-granular pyroxene and olivine (GOP) instead of radial pyroxene due to the presence of both pyroxene and olivine and after observing its texture with the higher resolution imaging (**Figs. 21E, 21F**). Similarly, in **figure 25D**, the presence of olivine and pyroxene stated that the corresponding chondrule can be identified as porphyritic olivine and pyroxene (POP), instead of porphyritic olivine (**Figs. 21C, 21D**).

Chemical analysis of the regions in the ROIs **G**, **H**, and **I** respectively in the groundmass (**Fig. 34**) reveals that the features correspond to metals, chromites, and iron sulfides (**Figs. 25A, 25B, 25C**). The ROI of **J** in the groundmass corresponds to a close-up region of a porphyritic olivine and pyroxene chondrule (**Figs. 21A, 21B**) and the features correspond to pyroxenes and plagioclases (**Fig. 25D**).

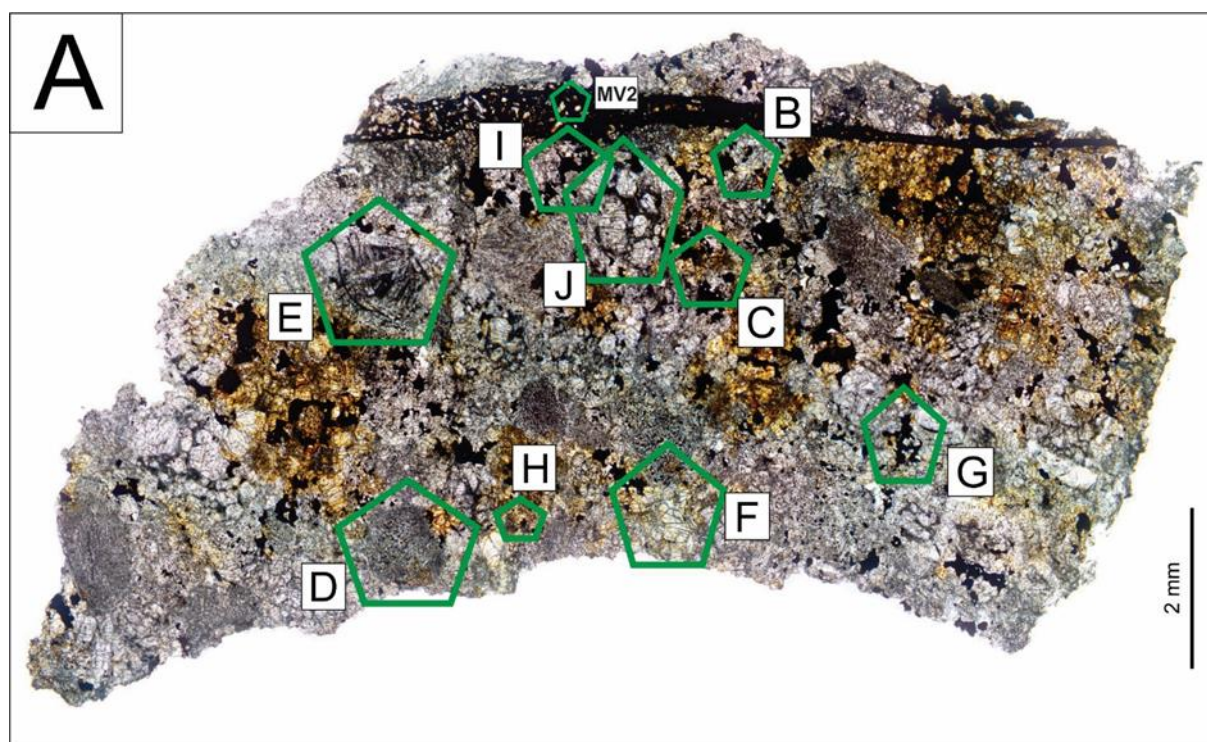


Figure 39: Annotated regions of interest (ROIs) in the groundmass.

3.2.2 Groundmass

3.2.2.1 CHEMICAL FORMULA- CHEMICAL ANALYSIS

3.2.2.1.1 Silicate minerals

The low-pressure phases of silicate minerals that are present in the thin section are olivines, pyroxenes, and plagioclases. The compositions of olivines, pyroxenes, and plagioclases range as follows: $\text{Fo}_{75.2-76.6}$ (for Ol), $\text{En}_{76.03-78.30}$, $\text{Fs}_{19.39-21.28}$, $\text{Wo}_{1.17-4.56}$ (for Px), and $\text{Ab}_{65.30-86.03}$, $\text{An}_{9.26-25.18}$, $\text{Or}_{4.54-10.00}$ (for Pl).

The composition of olivines (Appendix **Table A1**) is based on the endmember of forsterite, hence the chemical analysis was not plotted on a ternary chart. As for the

pyroxenes, collected data (Appendix **Table A2**) with respect to Orthopyroxene series / Opx, Clinopyroxene series / Cpx (20% Ca) and low-Ca pyroxenes ($5\% < \text{Ca} < 20\%$) were plotted in the En-Di-Hd-Fs quadrilateral chart system (Morimoto, 1988) (**Fig. 40**). It was found that only one Cpx is ascribed to augite and the majority were diopsides, whilst the majority of the Opx correspond to enstatite, and only one of them was a low-Ca pyroxene.

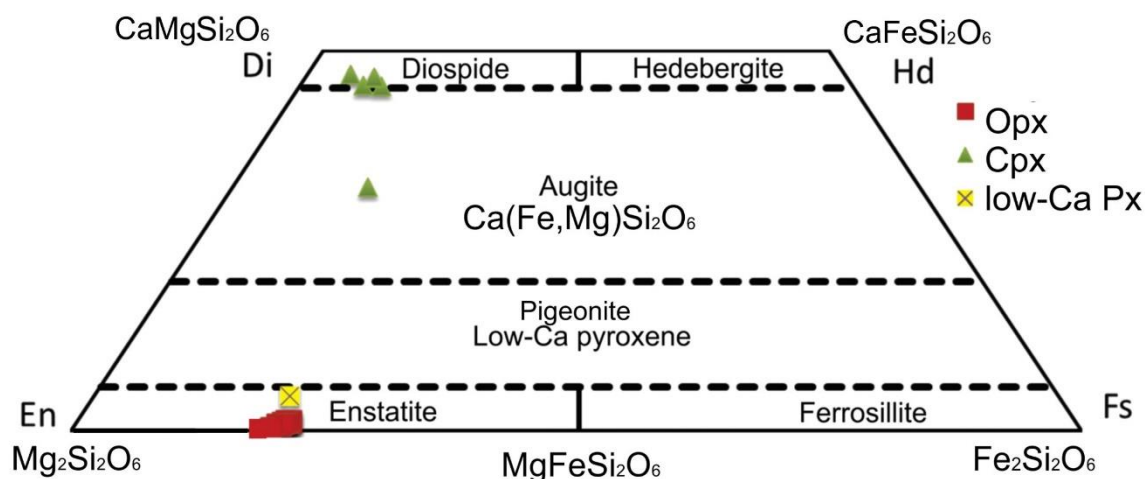


Figure 40: En-Di-Hd-Fs quadrilateral with results based on the quadrilateral chart system (Morimoto, 1988).

Based on the EPMA analysis, the structural state of the identified low-Ca pyroxenes in the studied sample was calculated and shown in the En-Di-Hd-Fs quadrilateral chart system (Morimoto, 1988) (**Fig. 40**). The majority of them correspond to the orthopyroxene series (~74 %) rather than the clinopyroxene series (~26 %) (**Fig. 41**).

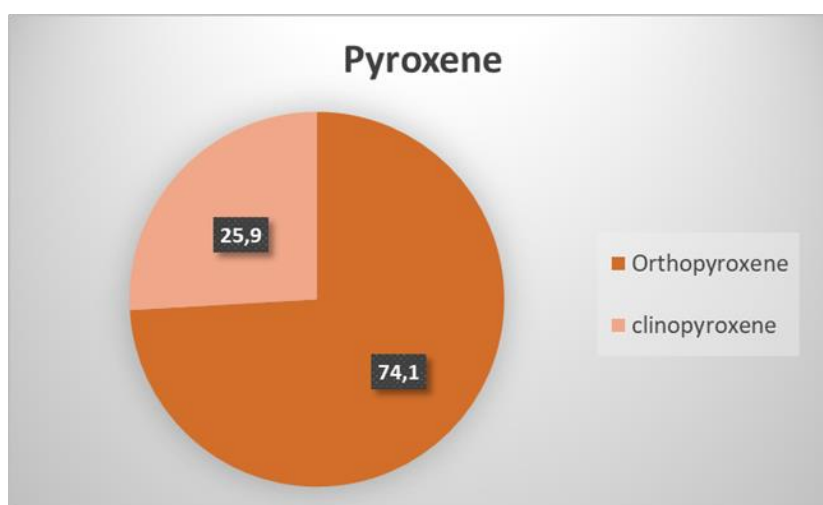


Figure 41: Statistic overview of the pyroxene grains in the studied sample.

Lastly, as for the plagioclases, results (Appendix **Table A3**) were plotted to the Albite (Ab) - Orthoclase (Or) - Anorthite (An) ternary chart based on (Ghiorso, 1984), revealing the results being plagioclases (**Fig. 42**).

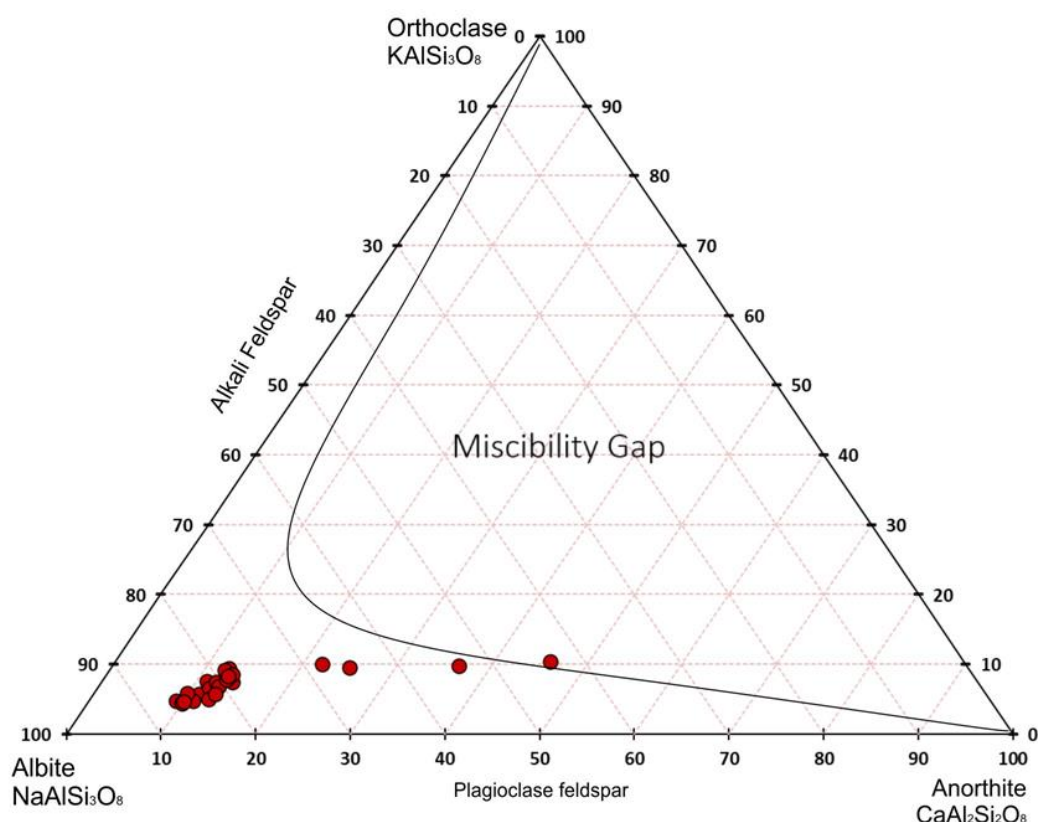


Figure 42: An-Or-Ab ternary chart with results based on the ternary system of Ghiorso (1984).

3.2.2.1.2 Spinel group

The results for the spinel group (Appendix **Table A4**) were plotted to the ternary chart showcasing spinel compositions ranging from Cr-rich to Al-rich to Fe-Ti-rich, based on the end members of Aluminum, Chromium, and ulvöspinel (Ganuza *et al.*, 2014; Stevens, 1944). This revealed homogenized compositions rich in chromium spinel (**Fig. 43**). We chose this ternary chart because the composition was based on TiO₂ wt.%, and the data needed to be plotted in the Ulvöspinel prism (Ganuza *et al.*, 2014).

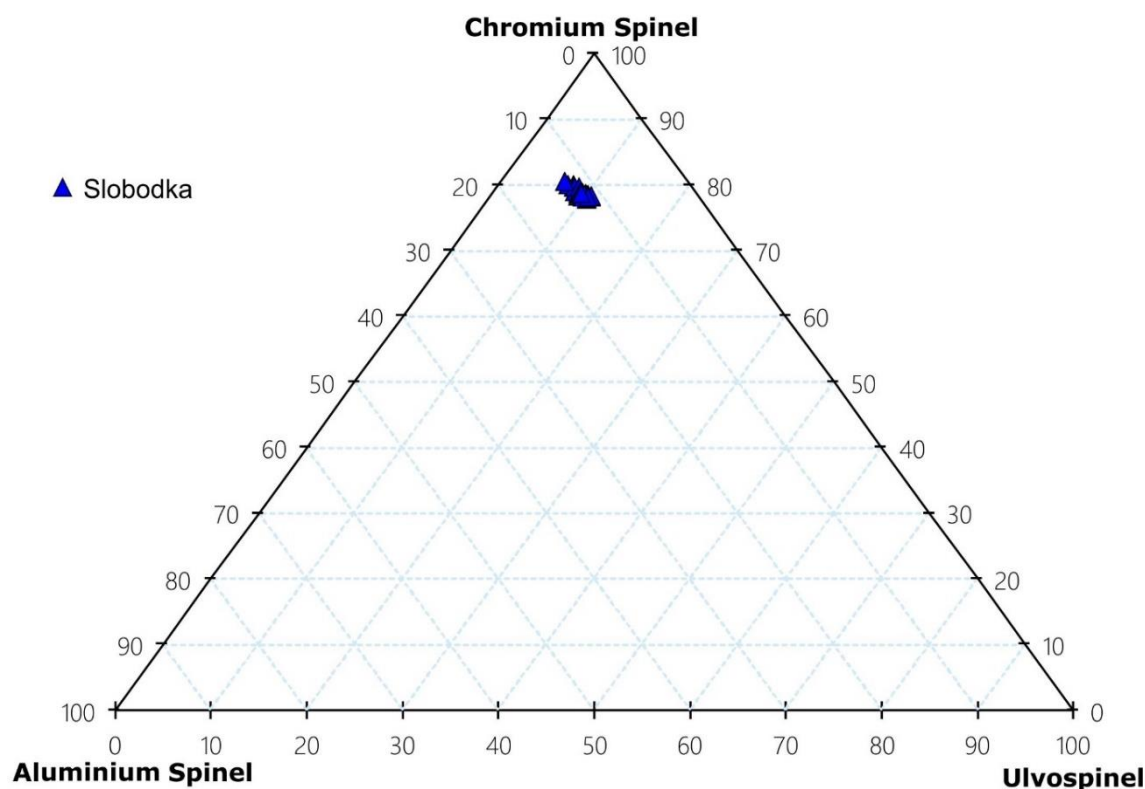


Figure 43: Spinel group of Chr-Al-Usp spinel ternary chart with Slobodka NHMW-L4372 data based on ulvöspinel prism with endmembers of FeAl_2O_4 Hercynite- FeCr_2O_4 Chromite- Fe_2TiO_4 Ulvöspinel (Ganuza et al., 2014; Stevens, 1944).

3.2.2.1.3 Metals and Sulfides

The maximum Ni percentage of metals (Appendix **Table A5**) and the mean Ni percentage of the sulfides (Appendix **Table A6**) have been calculated based on the EPMA analysis from the groundmass. The maximum Ni value for the metal is 29.7 wt.%, while the mean Ni value for the sulfides is ~0.2 wt.%. It can be concluded that the majority of the alloys of Fe-Ni are taenite based on the nickel proportions that are in the range of 20-30 wt.%, and only two measurements are kamacite with the Ni in the range of ~6 wt.% (Goldstein & Short, 1967).

3.2.2.2 GROUP CLASSIFICATION BASED ON CHEMICAL ANALYSIS

The Fe/Mn and Fe/Mg ratios for olivines and pyroxenes were calculated from their chemical composition data (Appendix **Tables A1-2**), and both minerals were plotted to the following chart to conclude the H-L-LL classification of the studied meteorite sample (**Fig. 44**).

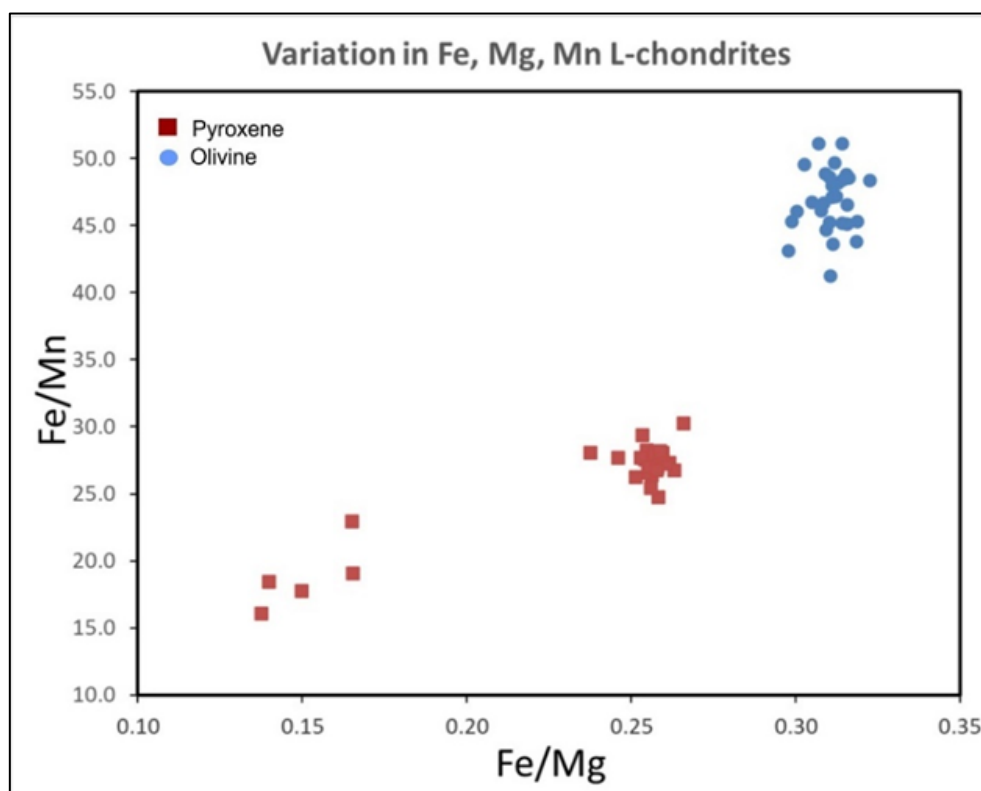


Figure 44: Variation in Fe/Mn, and Fe/Mg ratios in L-chondrites with chemical analysis results of olivine and pyroxene.

The EPMA chemical data (Appendix **Tables A1-2**) were adjusted to the referenced Fs(pyroxene)-Fa(olivine) chart of the equilibrated ordinary chondrites from the literature (Lucas *et al.*, 2019; Kei and Fredriksson, 1964) to define the distribution of the results according to the categorization that identifies the H-L-LL group (**Fig. 45**). The olivine composition is between 23-26 (mol% Fa) of the chart values (Appendix **Tables A1, A7**), so the identification shows an L-group according to the criteria of the categorization of chondrite groups.

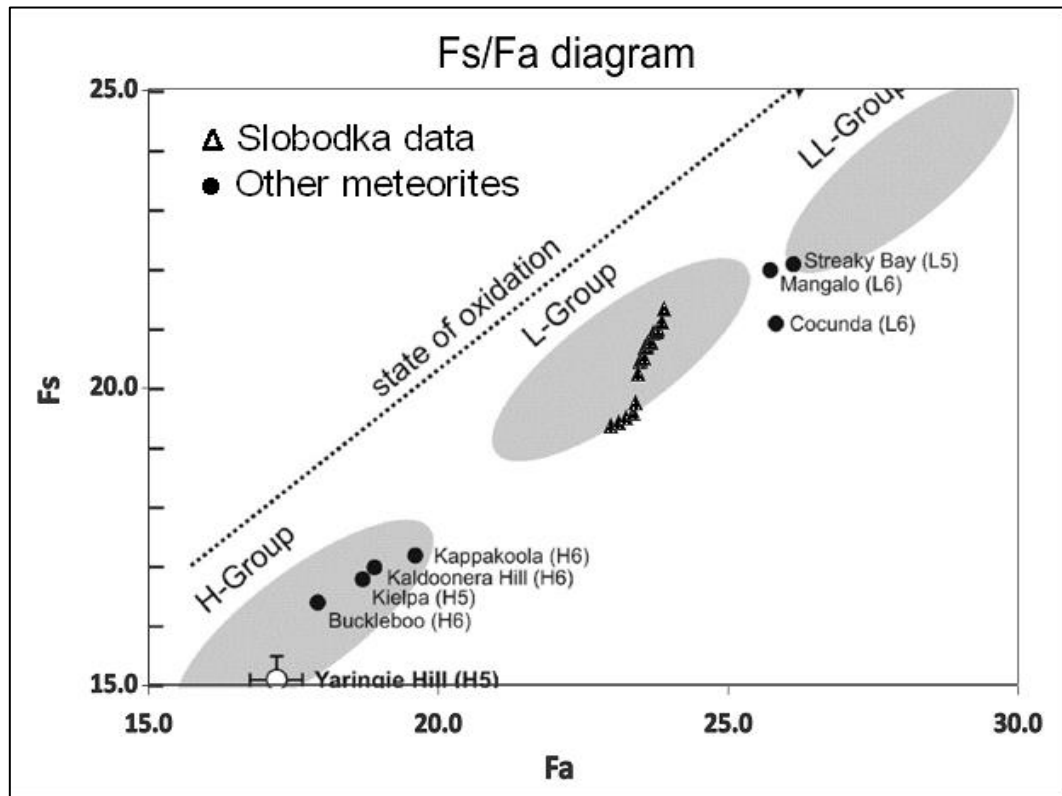


Figure 45: Projection of the Fs/Fa results (see: Appendix **Tables A1-2**) adjusted to the referenced diagram based on the state of oxidation to conclude the H-L-LL Group of the meteorite (Lucas et al., 2019; Kei and Fredriksson, 1964).

Lastly, based on the literature (Gastineau-Lyons *et al.*, 2002) and the measured Fe/Mn and Fe/Mg ratios, the observed minerals were categorized as diopside, low-Ca pyroxenes, and olivines, delimited by the categorization areas of the petrologic type L4-6 of the L chondrites (Fig. 46).

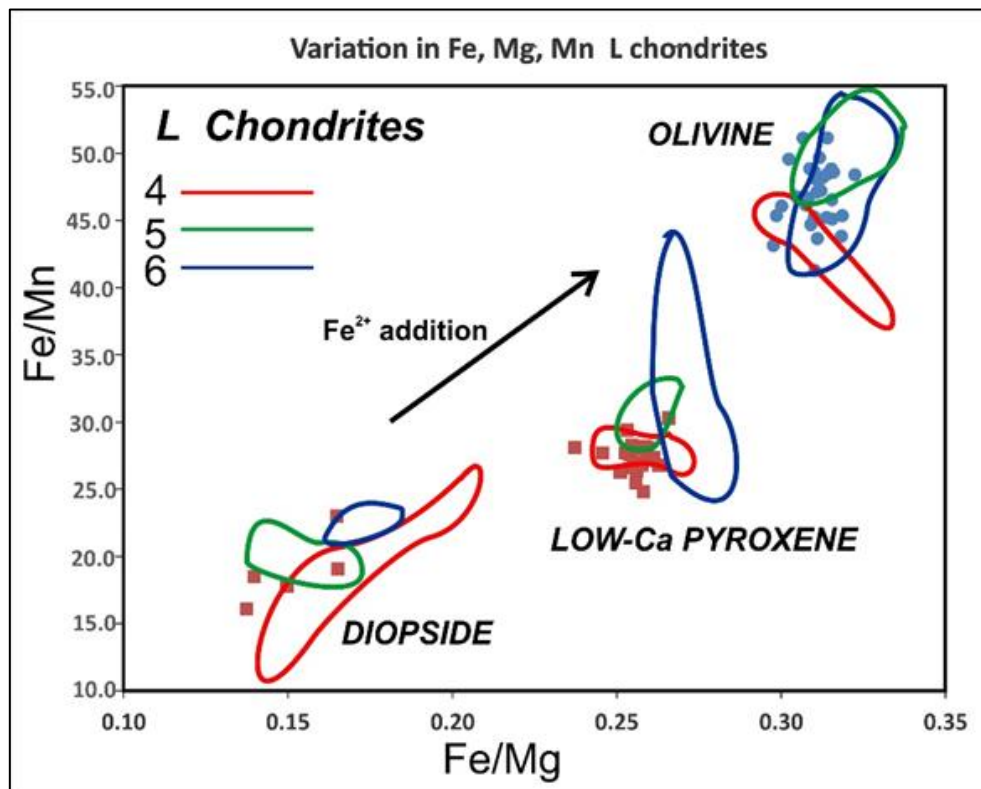


Figure 46: Molar Fe-Mn-Mg ratio adjusted to the areas of Diopside, Low-Ca, and Olivine (Gastineau-Lyons et al. 2002).

3.2.3 Melt Vein

3.2.3.1 CHEMICAL ANALYSIS – CHEMICAL FORMULA

The melt vein contains silicate mineral grains, small, rounded blebs of Fe-Ni metal, oxides (chromite), and troilite as the main components. The high-pressure phases identified are the albitic jadeite, tuite, wadsleyite, and majorite (**Figs. 37- 38**). The albitic jadeite has an empirical formula $(\text{Na}_{0.63-0.67}\text{Ca}_{0.07-0.08}\text{K}_{0.03-0.4}\square_{0.22-0.25})(\text{Al}_{0.85}\text{Si}_{0.13-0.15}\text{Fe}_{0.01-0.02})\text{Si}_2\text{O}_6$ and $\text{Ca}\# [100 \times \text{Ca}/(\text{Ca}+\text{Na})]$ in the range 9.7-10.6. It corresponds to a super silicic clinopyroxene with 0.13-0.15 atoms per formula unit of silica at octahedral coordination. Additionally, it has the nominal maximum allowed vacancies up to ~ 0.25 (Ma *et al.* 2022). The high-pressure polymorph of phosphate, with MgO content being up to ~ 3.62 - 3.67 wt.% and Na_2O content being up to ~ 2.16 - 2.79 wt.%, indicating it has the composition of a merrillite, meaning it has transformed from merrillite, so it can be identified as tuite. Wadsleyite could not be detected with the EPMA analysis because of its micro-grain appearance. It was present near the limit of the groundmass-melt vein and detected with the analytical method of Raman Spectroscopy

because it is a Raman active mineral, and it could easily be detected with this method. Majorite is present in the groundmass of the melt vein as micro-grains and has a composition in the range of $\text{Ca}_{0.18-0.20}\text{Mg}_{2.88-3.00}\text{Fe}_{0.54-0.57}\text{Al}_{0.01-0.36}\text{Si}_{3.81-3.90}\text{O}_{12}$.

3.3 Raman Data Acquisition

The measured Raman spectra for each mineral were compared with the unique Raman spectral collection of the RRUFF database (<https://rruff.info>). The Raman spectra were processed first by removing the background noise with CrystalSleuth software and then the peak positions were determined by placing the cursor approximately in the center of the peak range with the Fityk software. The selection of the suitable referenced Raman spectra from the RRUFF Database was based on the 532 nm laser selection or based on the 0 degrees depolarized. The major Raman peaks for forsterite are observed at 825 and 857 cm^{-1} , and for the high-pressure polymorph of the olivine, wadsleyite at 723 and 919 cm^{-1} (**Fig. 47A**). The major Raman peaks for phosphate references (**Fig. 47B**) are observed at 964 cm^{-1} (in the case of fluorapatite), at 977 cm^{-1} (in the case of the HP polymorph: tuite), at 960 cm^{-1} , and at 975 cm^{-1} (the latter two in the case of merrillite). The major Raman peaks for pyroxene references (**Fig. 47C**) are observed at 666 cm^{-1} and 1011 cm^{-1} (the latter two in the case of diopside), at 700 cm^{-1} , at 990 cm^{-1} and 1040 cm^{-1} (the latter three in the case of the HP polymorph: jadeite), and at 678 cm^{-1} (in the case of omphacite). The comparison with the omphacite reference has been chosen because it is the solid solution of Fe-bearing diopside and jadeite (Hao *et al.*, 2019). The Raman spectra of the albitic jadeite are very similar to ordinary jadeite, with a major peak at $\sim 700 \text{ cm}^{-1}$ which is distinctive to the composition of sodic pyroxene, whose composition and structure are those of omphacite (Baziotis *et al.*, 2018). In general, Raman spectra alone are not adequate for discriminating jadeite from albitic jadeite (Ma C. *et al.*, 2022; Baziotis I. *et al.*, 2022b; Baziotis I. *et al.*, 2023). The major Raman peaks for orthopyroxene (i.e., enstatite) are observed at 662 cm^{-1} , at 681 cm^{-1} , and at 1007 cm^{-1} , while for the HP polymorph of the low-Ca pyroxene (i.e., majorite) are observed at 670 cm^{-1} and at 930 cm^{-1} (**Fig. 47D**).

It is important to note that the Raman spectrum of pyroxene varies depending on its composition and crystal structure. Despite their similarities, the different structural units in the various types of pyroxene produce significant Raman spectral differences that are useful for identifying their structure. The number of peaks, their positions, and relative intensities in each region are unique for pyroxenes of different structural types and are utilized to characterize them. On the one hand, diopside, hedenbergite, high-T pigeonite, and augite belong in the space group of C2/c and have a monoclinic crystal system. On the other hand, low-T pigeonite belongs in the P21/c space group (e.g., Brown, 1972) and has a monoclinic crystal system as well. Additionally, the series of enstatite-orthoferrosilite belong to the Pbcu space group and have an orthorhombic crystal system. The main difference between monoclinic and orthorhombic pyroxenes is that the first ones have one type of chain because of the single-chain structure, whilst the second ones have two distinguishable types of chains (A and B; e.g., Papike *et al.*, 1973).

The pyroxenes exhibit a significant difference in their spectra, which is the presence of a distinct peak at $\sim 670\text{ cm}^{-1}$. This peak results from the stretching vibration of the Si-O-Si bridges, the number of which depends on the mineral's type of silicon-oxygen chains. This stretching mode is a characteristic type of the single chain silicates. The peak then can be single or double, depending on whether the mineral has one or two kinds of silicon-oxygen chains. In more detail, monoclinic pyroxenes have the strongest single peak near $\sim 670\text{ cm}^{-1}$ that can be recognized immediately, whilst the orthorhombic pyroxenes have a strong doublet peak near $\sim 670\text{ cm}^{-1}$. This doublet peak confirms that the Si-O-Si stretching vibrations originate from the chain units of chain A and chain B and suggests that these vibrations occur in parallel (Wang *et al.*, 2001).

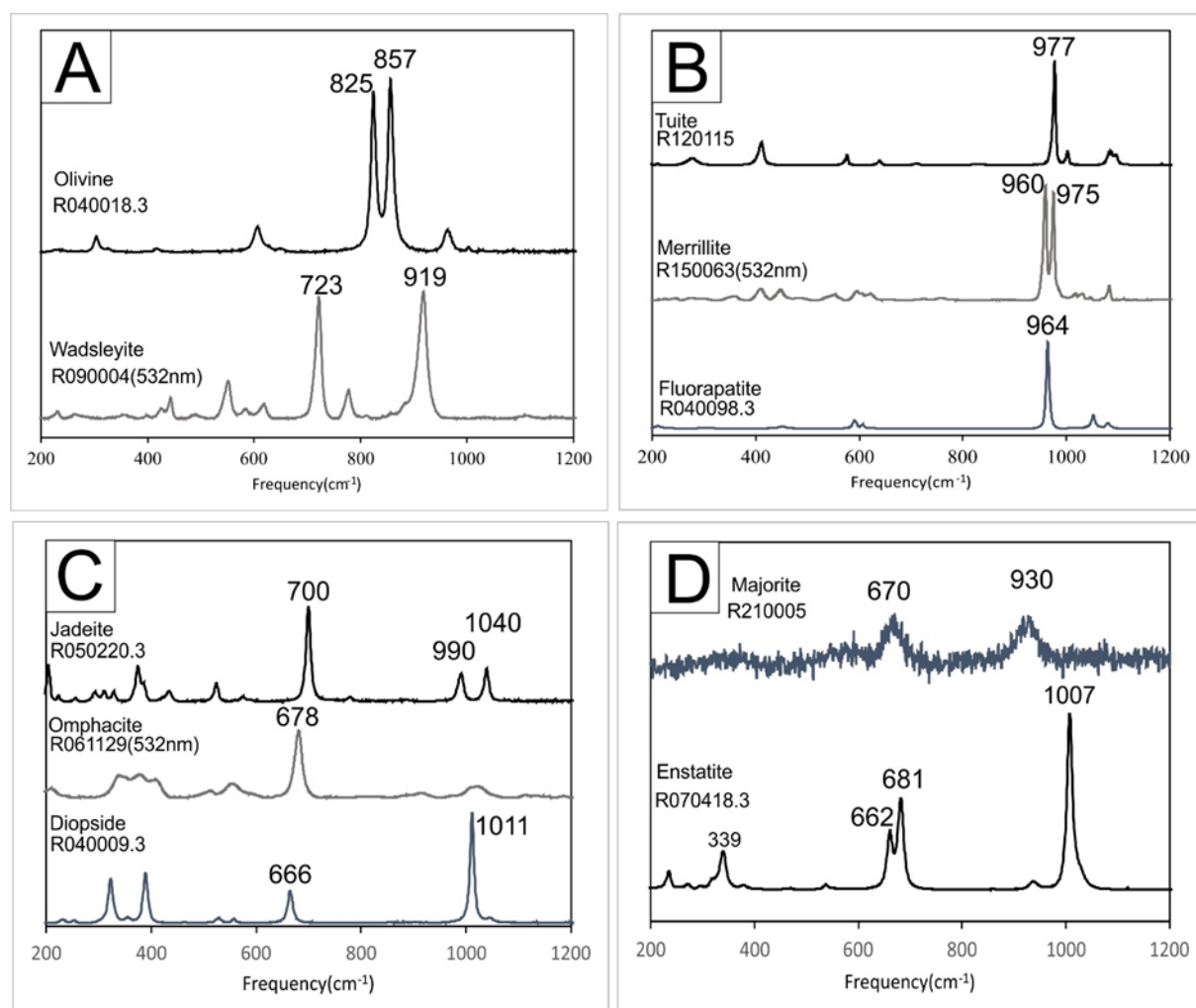


Figure 47: Raman shifts of minerals from RRUFF Database: (A) olivine (R040018.3) and wadsleyite (R090004-532nm); (B) tuite (R120115-532nm), merrillite (R150063-532nm), and fluorapatite (R040098.3); (C) diopside (R040009.3), omphacite (R061129-532nm), jadeite (R050220.3); (D) majorite (R210005), and enstatite (R070418.3).

It has been observed that both Pbca and P21/c pyroxenes have doublets in the spectral region. However, due to compositional differences, the peak positions of P21/c pyroxenes are around 10 cm^{-1} lower than those of Pbca pyroxenes. Additionally, the doublet is less distinct in the spectra of P21/c pyroxenes. The orthorhombic structure of Pbca produces a doublet that is very similar to the doublet found in high Mg, and low Ca Pbca pyroxene. Specifically, it has been found that only the major cations of Mg^{2+} , Fe^{2+} , and Ca^{2+} can affect the spectral peak positions (Wang *et al.*, 2001).

3.3.1 Annotated Marked Areas in the Studied Melt Vein

The following annotated regions display the areas in the melt vein where the measurements were taken. The width of the melt vein for region A is about 662-719 μm (**Fig. 48A**), for region B is about 312 μm (**Fig. 48B**), and for region C is about 85 μm (**Fig. 48C**). The Raman data with the referenced spectra (RRUFF database) are displayed for a better peak comparison, and thus to identify the mineral by peak matching. Moreover, the Raman spectrum from each high-/low-pressure phase -identified by the EPMA analysis- has also been plotted together with the referenced Raman spectra.

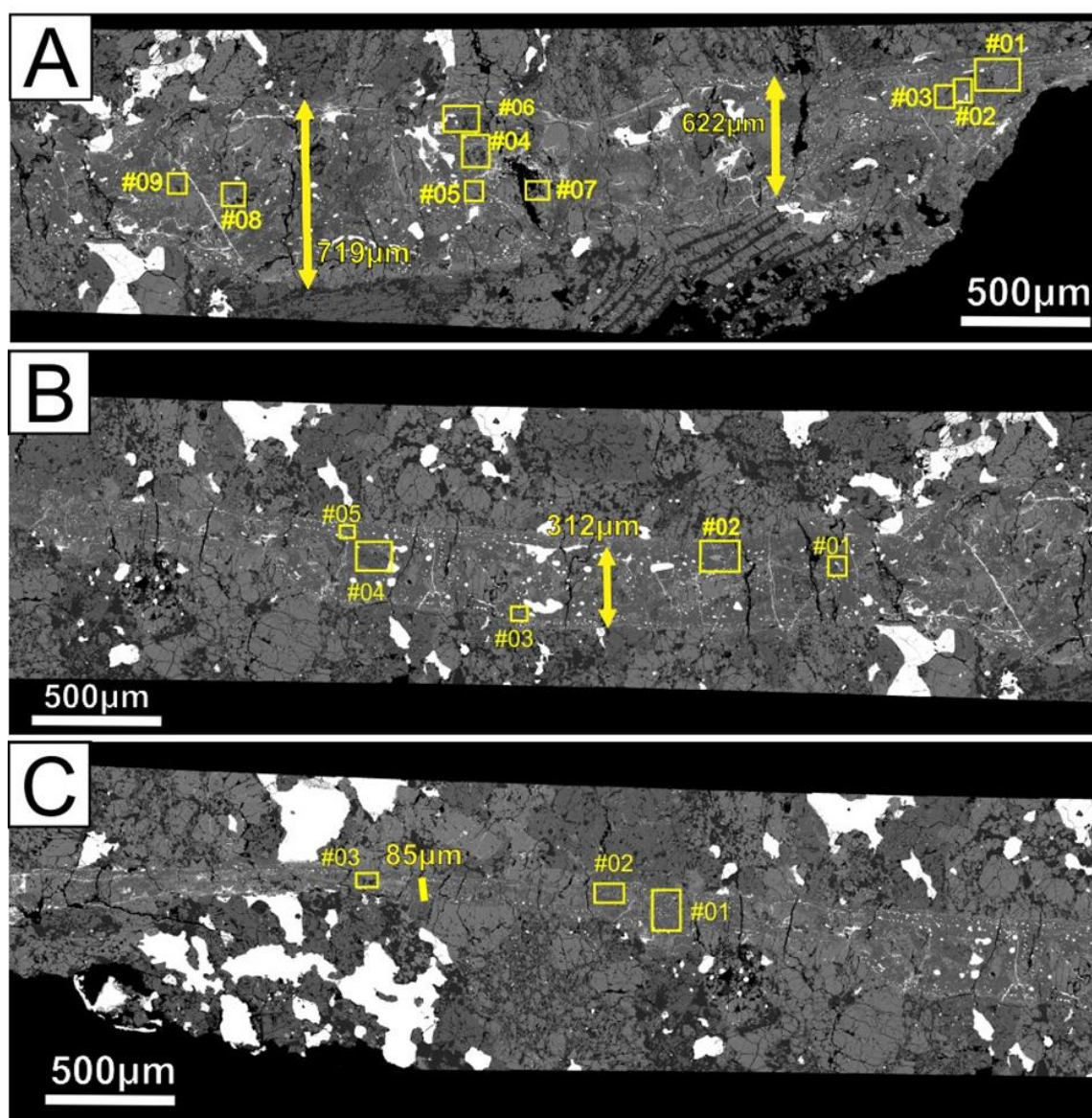


Figure 48: Regions displayed on the BSE images. (A) Region A with the positioned Raman regions of interest; (B) Region B with the positioned Raman regions of interest; (C) Region C with the positioned Raman regions of interest

➤ Raman spectrum mv_A_a_11

The Raman spectrum mv_A_a_11 was obtained from a grain inside the melt vein of region A (see #01 position in figure 48A). The annotated position is from the rim of the grain (Figs. 49A, 49B) with peaks at 667, 820, and 851 cm^{-1} the last two of which are typical of olivine (Fig. 49C). The spectrum of the forsterite from the RRUFF database (R040018.3) with peaks at ~ 825 and 857 cm^{-1} and the spectrum of the wadsleyite from the RRUFF database (R090004, 532 nm) with peaks at 723 and 919 cm^{-1} are used for comparison (Fig. 49C).

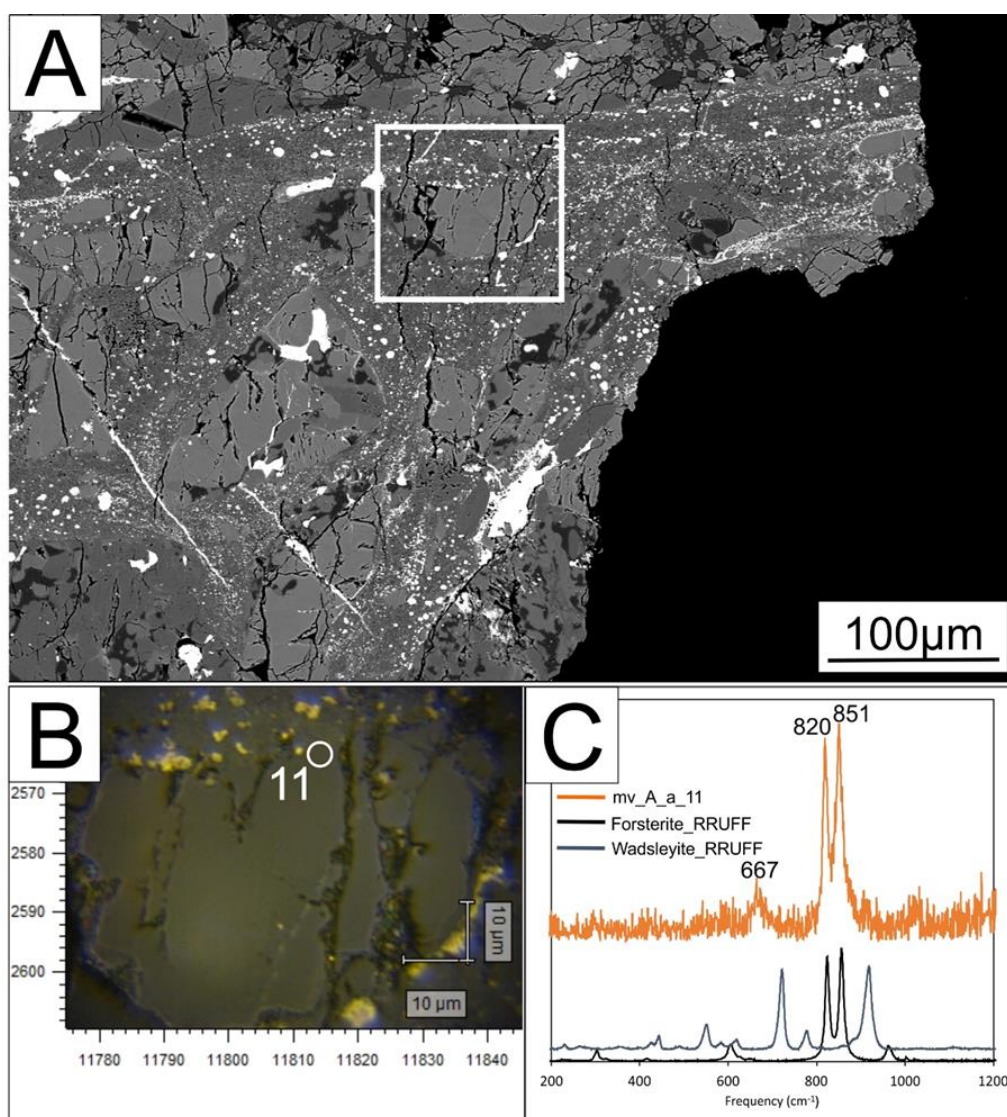


Figure 49: (A) BSE image with selected position of grain #01 in the melt vein, (B) Annotated Raman position at the rim of the grain, (C) Selected Raman spectrum mv_A_a_11, compared to reference spectra for olivine (black line; RRUFF R040018.3) and for wadsleyite (grey line; RRUFF R090004, 532 nm).

➤ Raman spectrum mv_A_b_11

The Raman spectrum mv_A_b_11 was obtained from a grain inside the melt vein of the region (see #02 position in figure 50A). The annotated position is from the rim of the grain (Figs. 48A, 50B) with peaks at 326, 391, 665, and 1011 cm^{-1} are typical of pyroxene (Fig. 50B). The spectrum of the diopside from the RRUFF database (R040009.3) with peaks at ~ 325 , 390, 666, and 1011 cm^{-1} is used for comparison (Fig. 50C) to match the peaks of the monoclinic pyroxene due to a single peak at ~ 670 cm^{-1} .

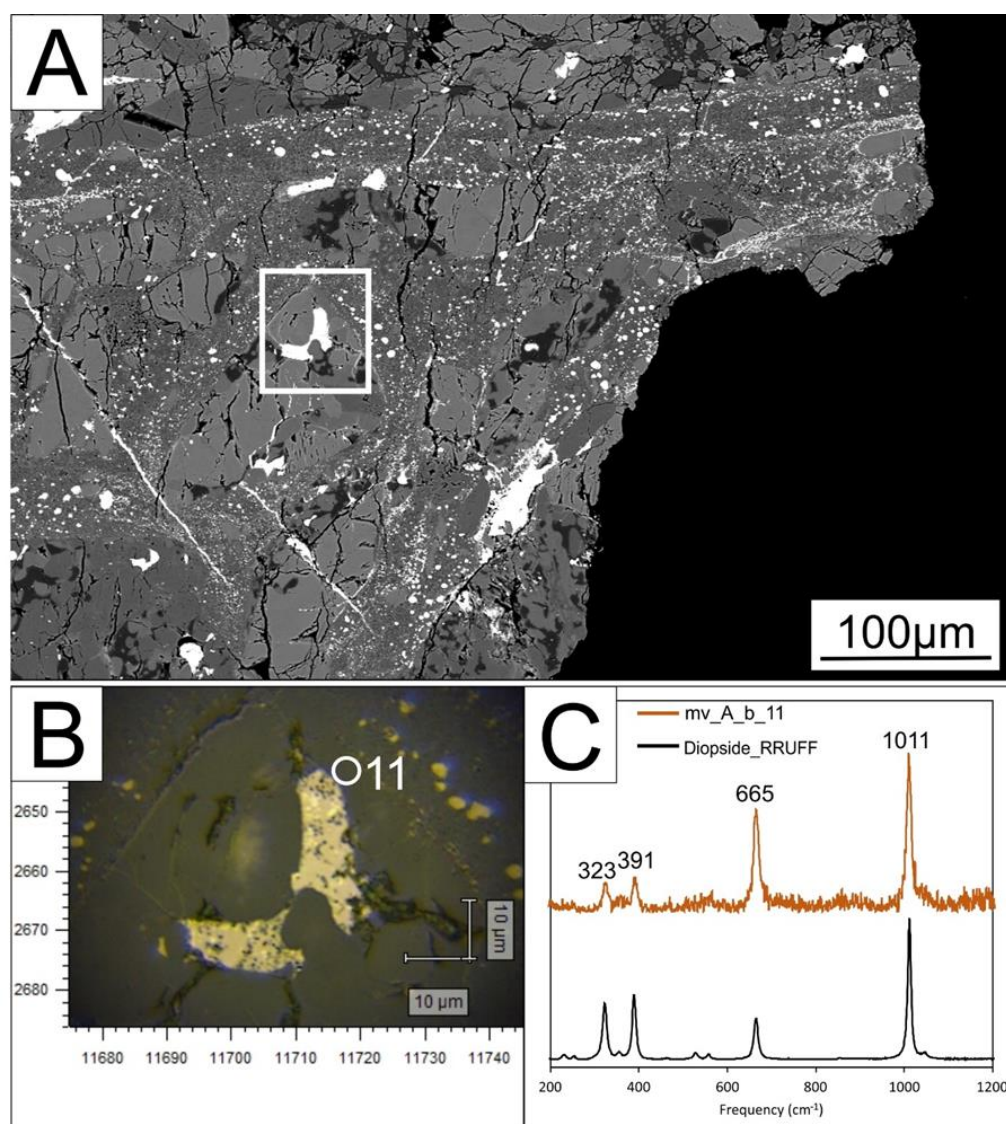


Figure 50: (A) BSE image with selected position of grain #02 in the melt vein, (B) Annotated Raman position at the rim of the grain, (C) Selected Raman spectrum mv_A_b_11, compared to reference spectrum for diopside (black line; RRUFF R040009.3)

➤ Raman spectrum mv_A1_21

The Raman spectrum mv_A1_21 was obtained from a grain inside the melt vein of the region (see #03 position in figure 51A). The annotated position is from the core of the grain (Figs. 51B, 48A) with peaks at 387, 528, 701, 990, and 1040 cm^{-1} are typical of jadeite (Fig. 51C). The spectrum of the jadeite from the RRUFF database (R050220.3) with peaks at ~ 387 , 528, 700, 990 and 1040 cm^{-1} , and the spectrum of the omphacite from the RRUFF database (R061129, 532 nm) with peaks at 678, 1008, and 1021 cm^{-1} are used for comparison to identify the phase with the more suitable spectrum of the monoclinic pyroxenes (Fig. 51C).

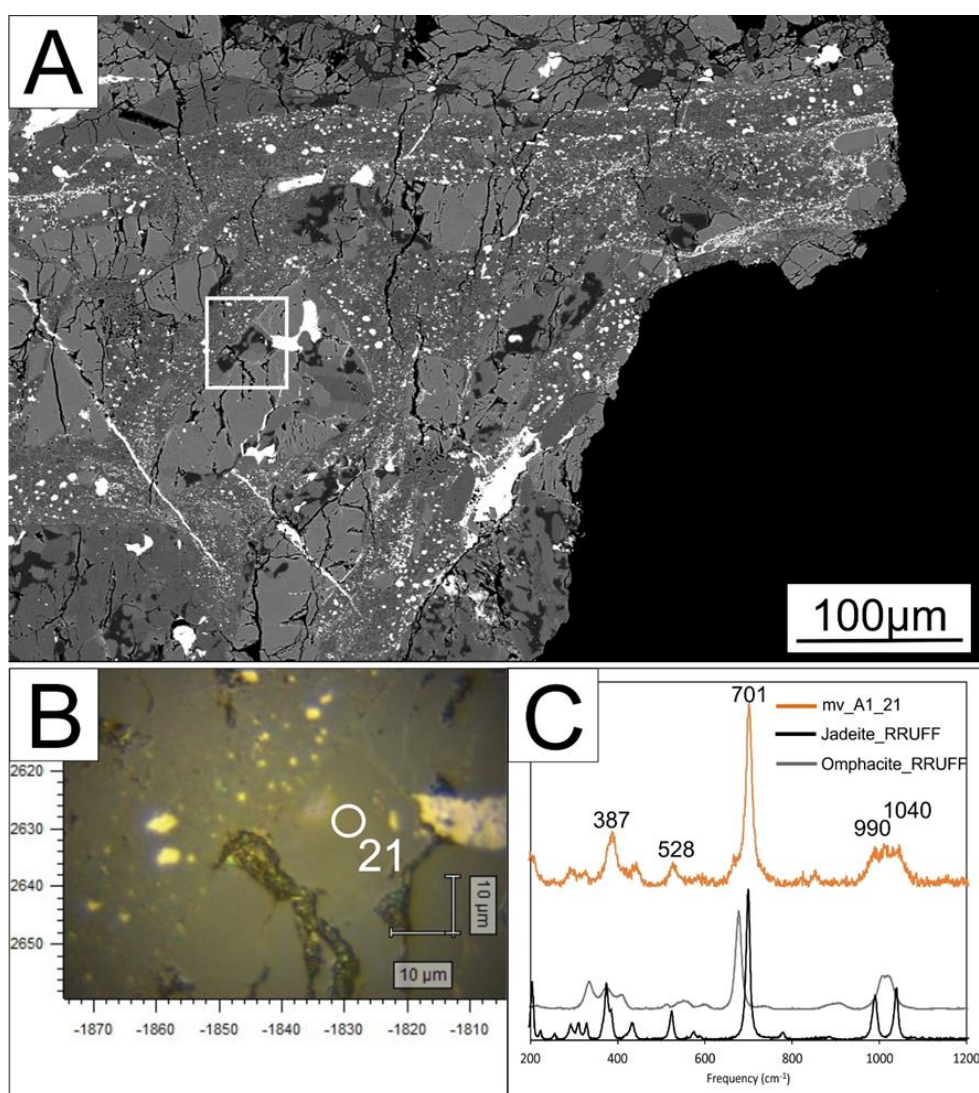


Figure 51: (A) BSE image with selected position of grain #03 in the melt vein; (B) Annotated Raman position at the rim of the grain; (C) Selected Raman spectrum mv_A1_21, compared to reference spectra for jadeite (black line; RRUFF R050220.3) and omphacite (grey line; RRUFF R061129, 532 nm)

➤ Raman spectrum mv_B_b2_226

The Raman spectrum mv_B_b2_226 was obtained from a grain inside the melt vein of the region (see #04 position in figure 52A). The annotated position is from the core of the grain (Figs. 52B, 48A) with peaks at 718, and 918 cm^{-1} are typical of wadsleyite (Fig. 52C). The spectrum of the wadsleyite from the RRUFF database (R090004, 532 nm) with peaks at ~ 723 and 919 cm^{-1} , and the spectrum of the olivine from the RRUFF database (R040018.3) with peaks at 825 and 857 cm^{-1} are used for comparison (Fig. 52C). So, in this case, both minerals coexist and can be assumed that the olivine is located below a surface layer of wadsleyite.

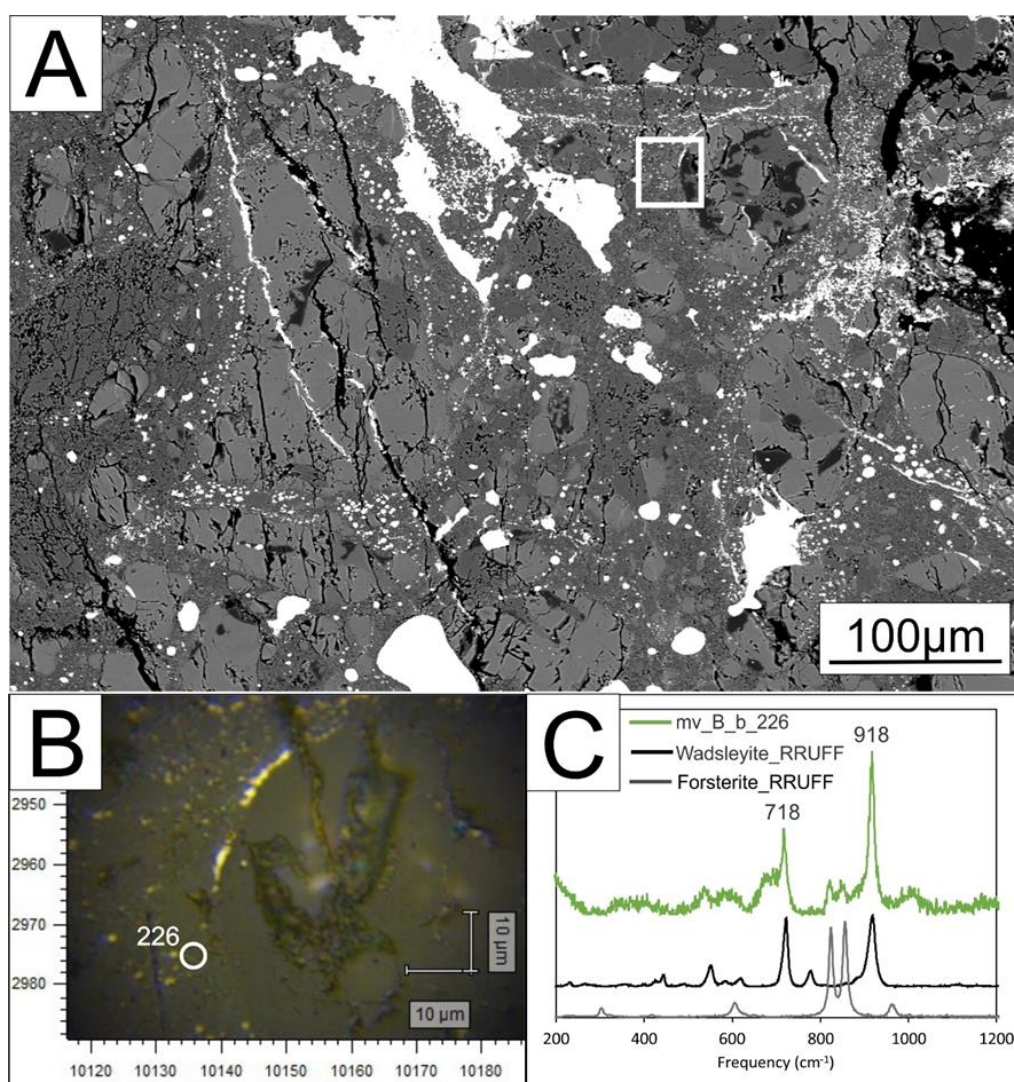


Figure 52: (A) BSE image with selected mv_B_b2_226 position in the melt vein; (B) Annotated Raman position of wadsleyite grain with scale for reference (\sim up to 2 μm long); (C) Selected Raman spectrum mv_B_b2_226 compared to referenced spectra from RRUFF database for wadsleyite (black line; RRUFF R090004, 532 nm) and for olivine (grey line; RRUFF R040018.3)

➤ Raman spectrum mv_B_g_11

The Raman spectrum mv_B_g_11 was obtained from a grain inside the melt vein of the region (see #05 position in figure 53A). The annotated position is from the rim of the grain (Figs. 53B, 48A) with peaks at 385, 702, and 1035 cm^{-1} , which are typical of Jadeite (Fig. 53C). The spectrum of the jadeite from the RRUFF database (R050220.3) with peaks at ~ 387 , 528, 700, 990 and 1040 cm^{-1} , and the spectrum of the omphacite from the RRUFF database (R061129, 532 nm) with peaks at 678, 1008 and 1021 cm^{-1} are used for comparison (Fig. 53C). A clear-cut case is observed for the existence of jadeite only.

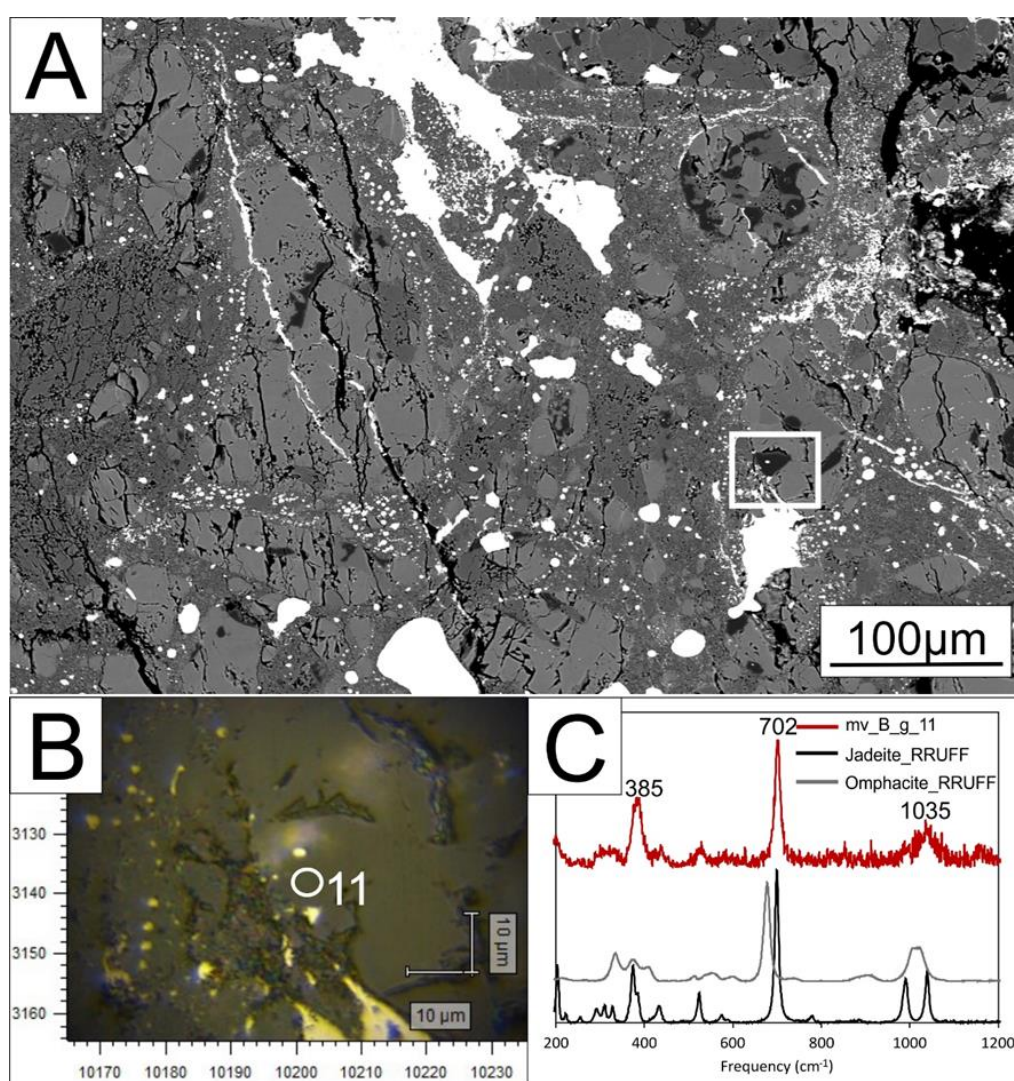


Figure 53: (A) BSE image with selected mv_B_g_11 position in the melt vein; (B) Annotated Raman position of jadeite grain; (C) Selected Raman spectrum mv_B_g_11 compared to referenced spectra from RRUFF database for jadeite (black line; RRUFF R050220.3) and for the omphacite (grey line; RRUFF R061129, 532 nm).

➤ Raman spectrum mv_B_a_21

The Raman spectrum mv_B_a_21 was obtained from a grain inside the melt vein of the region (see #06 position in figure 54A). The annotated position is from the core of the grain (Figs. 54B, 48A) with peaks at 335, 665, 681, and 1012 cm^{-1} are typical of orthopyroxene (Fig. 54C). The spectrum of the enstatite from the RRUFF database (R070418.3) with peaks at ~ 339 , 662, 681 and 1007 cm^{-1} , is used for comparison (Fig. 54C) to identify the orthopyroxene because the spectrum shows a doublet peak at ~ 670 cm^{-1} , which is characteristic of the orthorhombic crystal system.

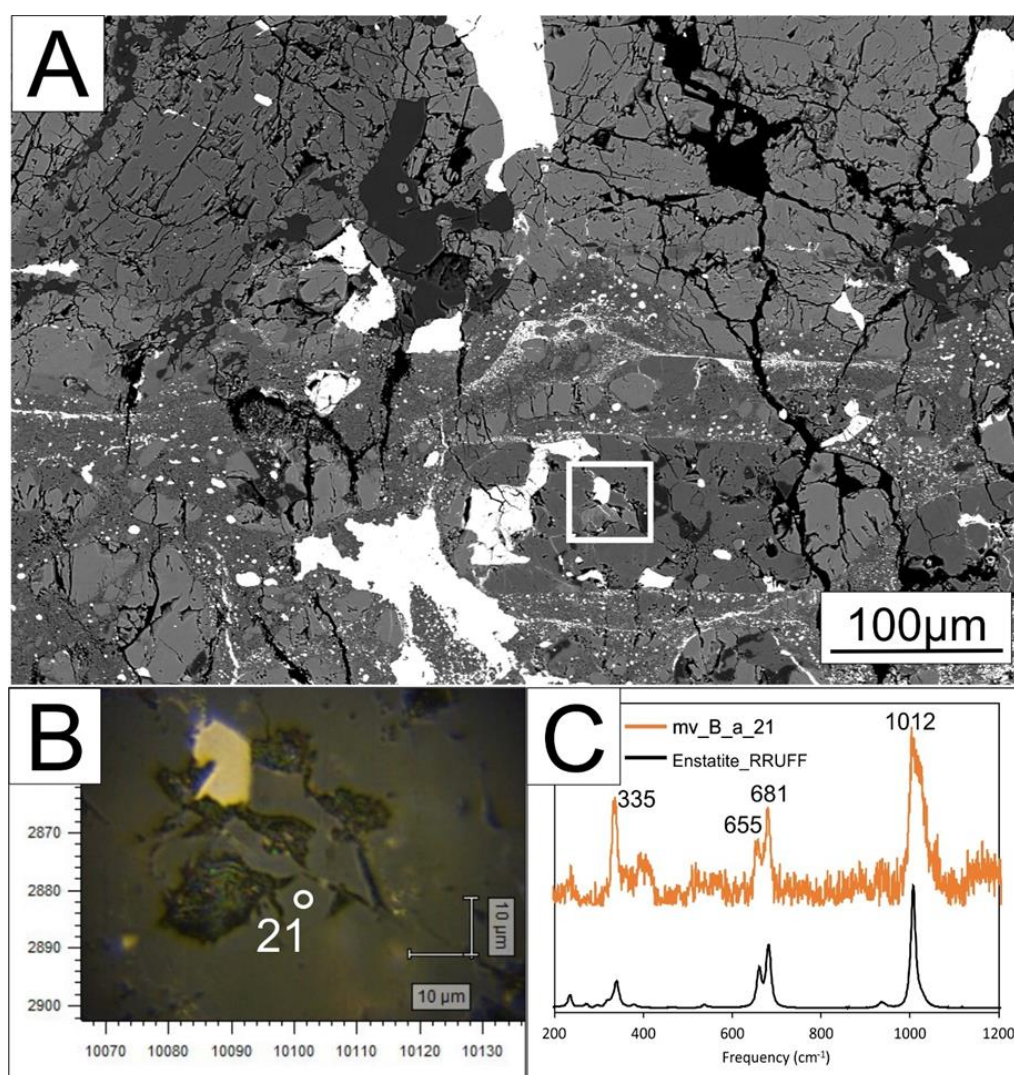


Figure 54: (A) BSE image with selected mv_B_a_21 position in the melt vein; (B) Annotated Raman position of the pyroxene grain; (C) Selected Raman spectrum mv_B_a_21 compared to referenced spectrum from RRUFF database for enstatite (black line; RRUFF R070418.3).

➤ Raman spectrum mv_B_c_21

The Raman spectrum mv_B_c_21 was obtained from a grain inside the melt vein of the region (see #07 position in figure 55A). The annotated position is from the rim of the grain (Figs. 55B, 48A) with peaks at 385, 575, 702.8 and 978 cm^{-1} are typical of jadeite and tuite (Fig. 55C). The spectrum of the jadeite from the RRUFF database (R050220.3) with peaks at ~ 379 , 700, 990 and 1040 cm^{-1} , and the spectrum of the tuite from the RRUFF database (R120115, 532 nm) with peak at 977 cm^{-1} , are used for comparison (Fig. 55C). Here, the coexistence of both high-pressure minerals is observed.

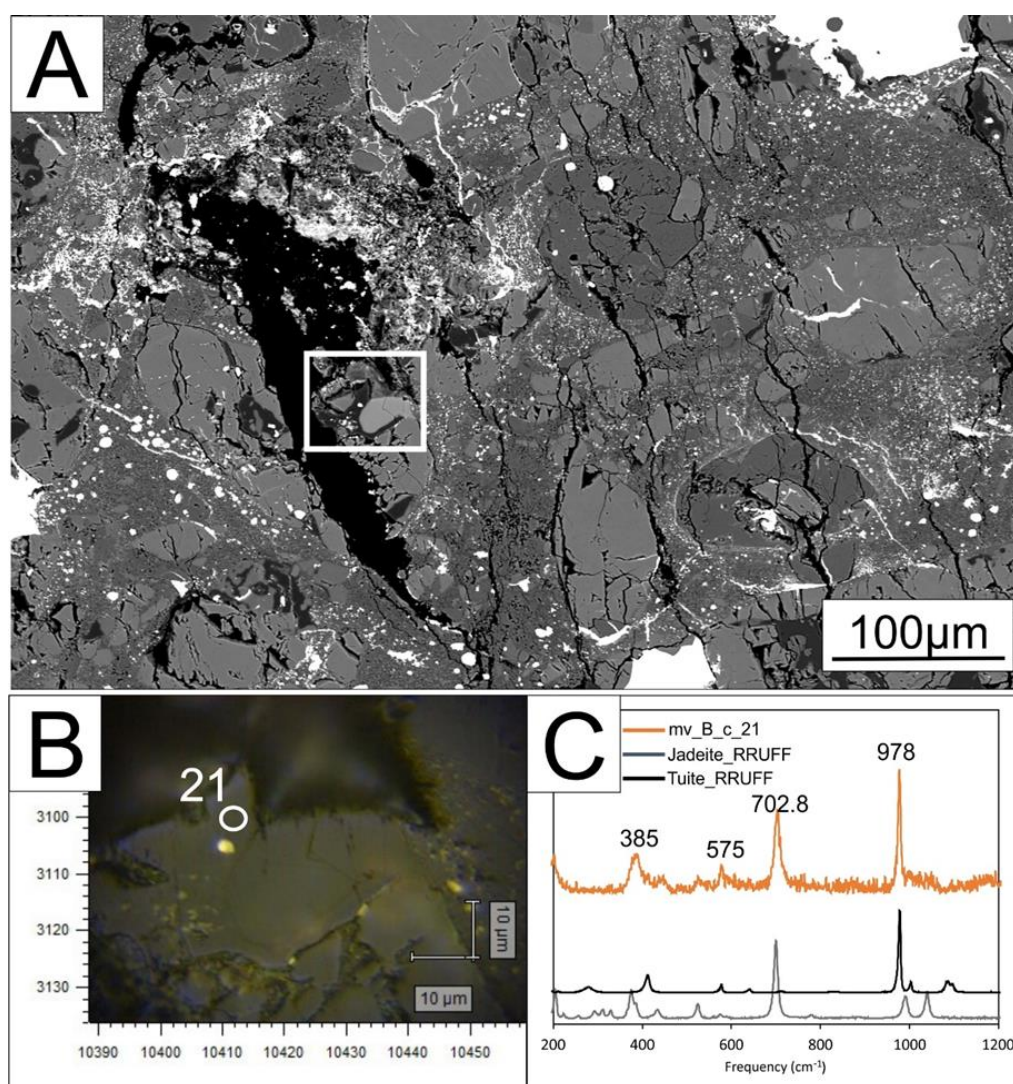


Figure 55: (A) BSE image with selected mv_B_c_21 position in the melt vein; (B) Annotated Raman position of the jadeite-tuite grain; (C) Selected Raman spectrum mv_B_c_21 compared to referenced spectra from RRUFF database for jadeite (grey line; RRUFF R050220.3) and for tuite (black line; R120115, 532 nm).

➤ Raman Spectra MV2c_11 & MV2c_21

The Raman spectra of MV2c were obtained from a grain inside the melt vein of the region (see #08 position in figure 56A). The annotated positions are from the core of the grain (Figs. 56B, 48A) with peaks at 379, 822, 853, 703, and 1045 cm^{-1} are typical of jadeite and olivine (Fig.56C). The spectrum of the jadeite from the RRUFF database (R050220.3) with peaks at ~ 379 , 700, 990 and 1040 cm^{-1} , and the spectrum of the olivine from the RRUFF database (R040018.3) with peaks at 825 and 857 cm^{-1} , are used for comparison (Fig. 56C). Both spectra reveal that the mineral is jadeite, but also peaks with low intensity of forsterite are present; the latter indicates that the forsterite is in a layer below the mineral.

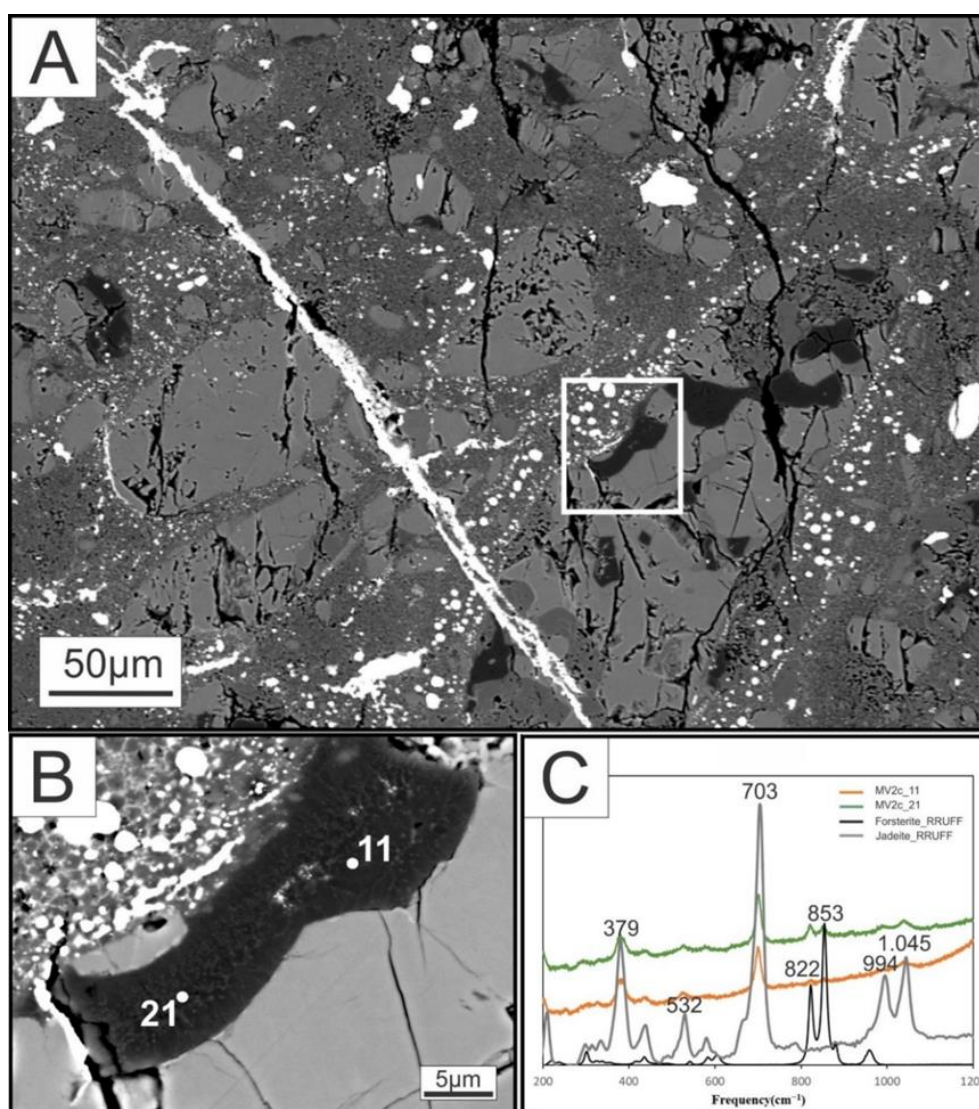


Figure 56: (A) BSE image with selected MV2c position in the melt vein; (B) Annotated Raman position of the jadeite-olivine grain; (C) Selected Raman spectra MV2c_11 and MV2c_21 compared to referenced spectra from RRUFF database for jadeite (grey line; RRUFF R050220.3) and for forsterite (black line; RRUFF R040018.3).

➤ Raman spectrum mv_C1_b_21

The Raman spectrum mv_C1_b_21 was obtained from a grain inside the melt vein of the region (see #09 position figure 57A). The annotated position is from the core of the grain (Figs. 57B, 48A) with peaks at 384, 702.2, and 1022 cm^{-1} is typical of Jadeite (Fig. 57C). The spectrum of the jadeite from the RRUFF database (R050220.3) with peaks at ~ 379 , 700, 990 and 1040 cm^{-1} , and the spectrum of the omphacite from the RRUFF database (R061129, 532 nm) with peaks at 678, 1008 and 1021 cm^{-1} , are used for comparison (Fig. 57C). A clear-cut case is observed for the existence of jadeite only.

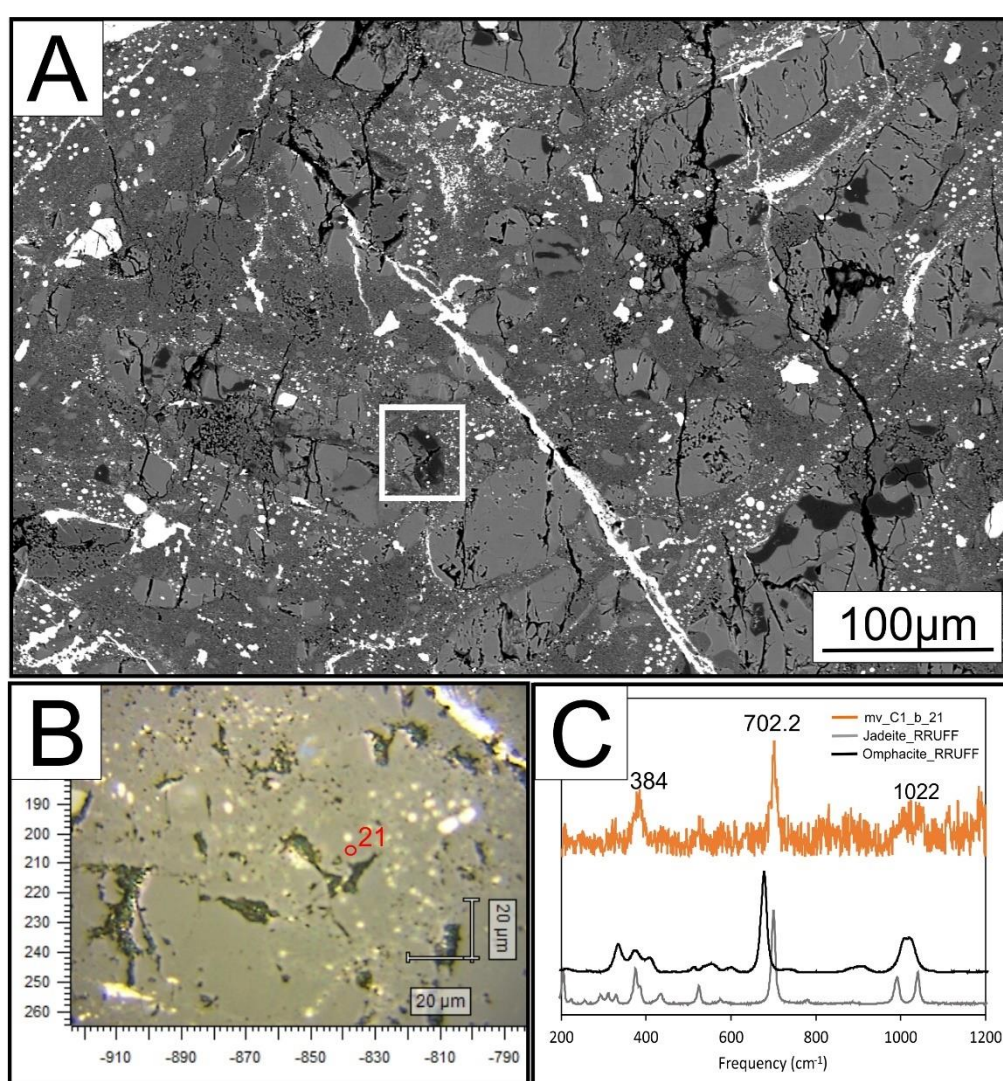


Figure 57: (A) BSE image with selected mv_C1_b_21 position in the melt vein; (B) Annotated Raman position of the jadeite grain; (C) Selected Raman spectrum mv_C1_b_21 compared to referenced spectra from RRUFF database for jadeite (grey line; RRUFF R050220.3) and for omphacite (black line; R061129, 532 nm).

➤ Raman spectrum mv_C_E_21

The Raman spectrum mv_C_E_21 was obtained from a grain inside the melt vein of the region (see #01 position in figure 58A). The annotated position is from the core of the grain (Figs. 58B, 48B) with peaks at 410, 576, 675, 978, and 1005 cm^{-1} is typical of tuite (Fig. 58C). The spectrum of the tuite from the RRUFF database (R120115, 532 nm) with a peak at $\sim 977 \text{ cm}^{-1}$, and the spectrum of the fluorapatite from the RRUFF database (R040098.3) with peaks at 964 and 1045 cm^{-1} , are used for comparison (Fig. 58C) to identify the mineral that is more suitable to the peaks.

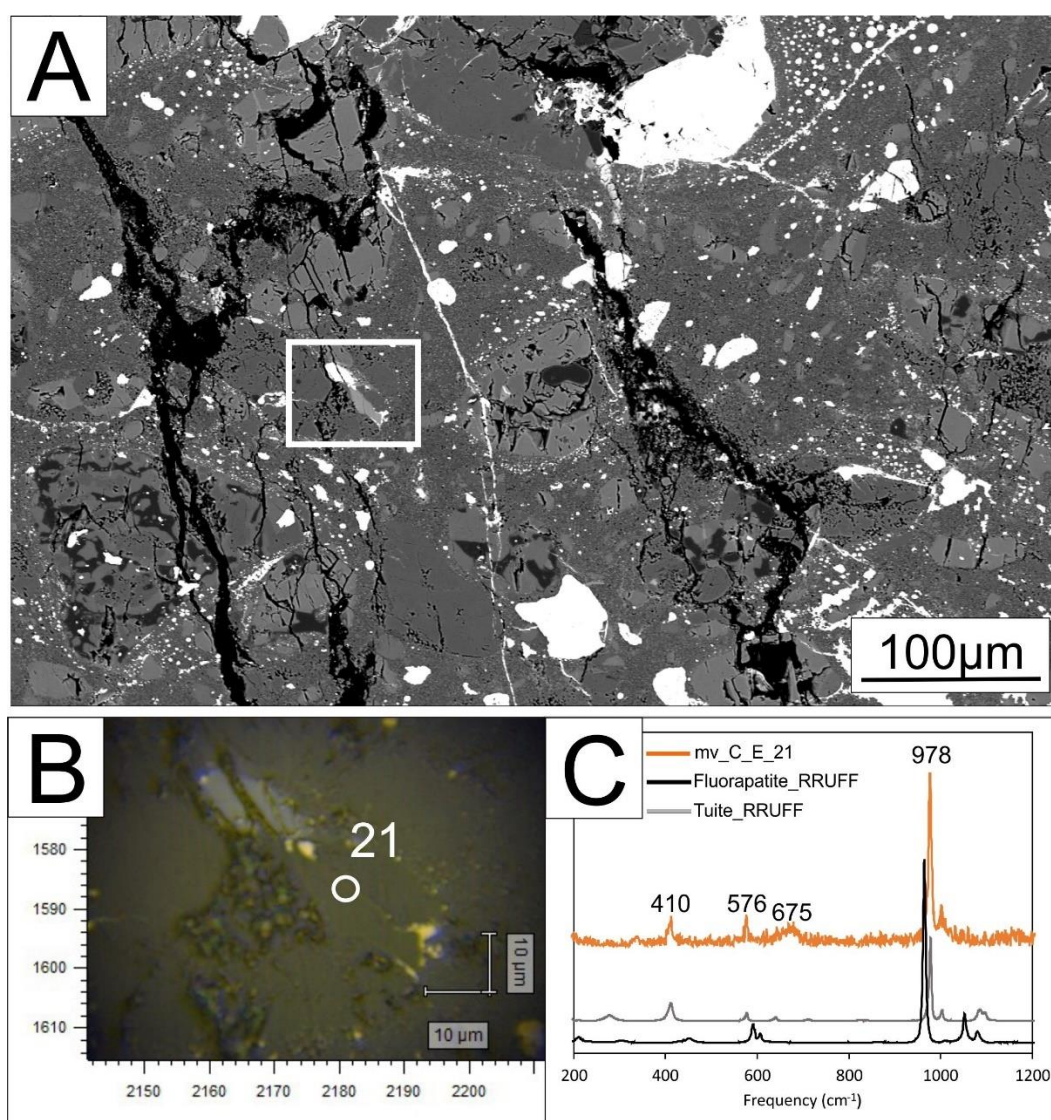


Figure 58: (A) BSE image with selected mv_C_E_21 position in the melt vein; (B) Annotated Raman position of the tuite grain; (C) Selected Raman spectrum mv_C_E_21 compared to referenced spectra from RRUFF database for tuite (grey line; RRUFF R120115, 532 nm) and for fluorapatite (black line; RRUFF R040098.3).

➤ Raman spectrum mv_C_E_31

The Raman spectrum mv_C_E_31 was obtained from a grain inside the melt vein of the region (see #01 position in figure 59A). The annotated position is from the core of the grain (Figs. 59B, 48B) with peaks at 337, 412, 660, 681, and 1010 cm^{-1} is typical of pyroxene (Fig. 59C). The spectrum of the enstatite from the RRUFF database (R070418.3) with peaks at ~ 339 , 662, 681, and 1007 cm^{-1} , and the spectrum of the majorite from the RRUFF database (R210005) with peaks at 670 and 930 cm^{-1} , are used for comparison (Fig. 59C) to identify the phase of the mineral that is present.

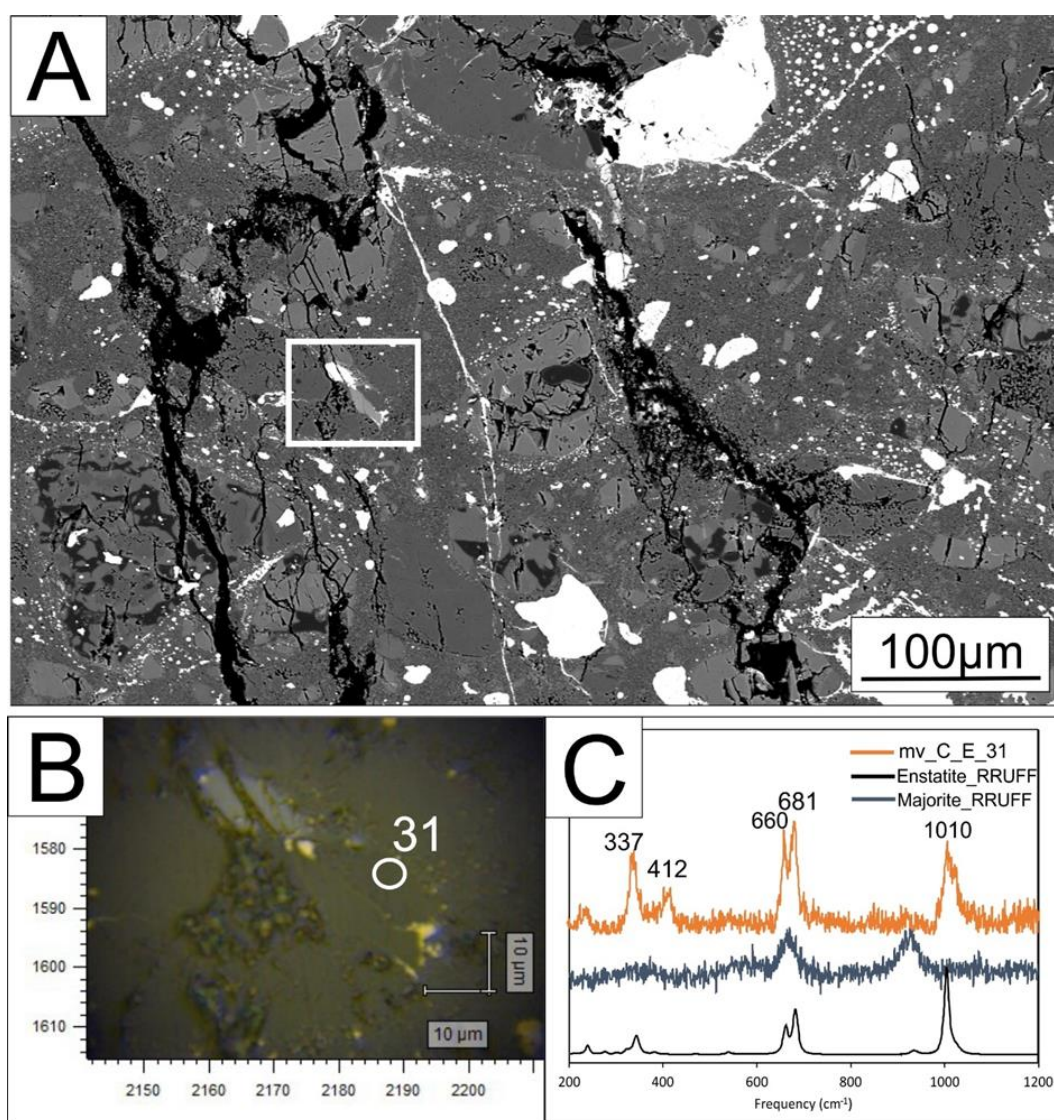


Figure 59: (A) BSE image with selected mv_C_E_31 position in the melt vein; (B) Annotated Raman position of the pyroxene grain; (C) Selected Raman spectrum mv_C_E_31 compared to referenced spectra from RRUFF database for enstatite (black line; RRUFF R070418.3) and for majorite (blue line; RRUFF R210005).

➤ Raman spectrum MVF_11

The Raman spectrum MVF_11 was obtained from a grain inside the melt vein of the region (see #02 position in figure 60A). The annotated position is from the core of the grain (Figs. 60B, 48B) with peaks at 411, 577, 640, 670, and 976 cm^{-1} is typical of tuite (Fig. 60C). The spectrum of the tuite from the RRUFF database (R120115, 532 nm) with peak at 977 cm^{-1} , and the spectrum of the fluorapatite from the RRUFF database (R040098.3) with peak at 964 cm^{-1} , are used for comparison (Fig. 60C) to identify the phase of the mineral with the suitable peaks.

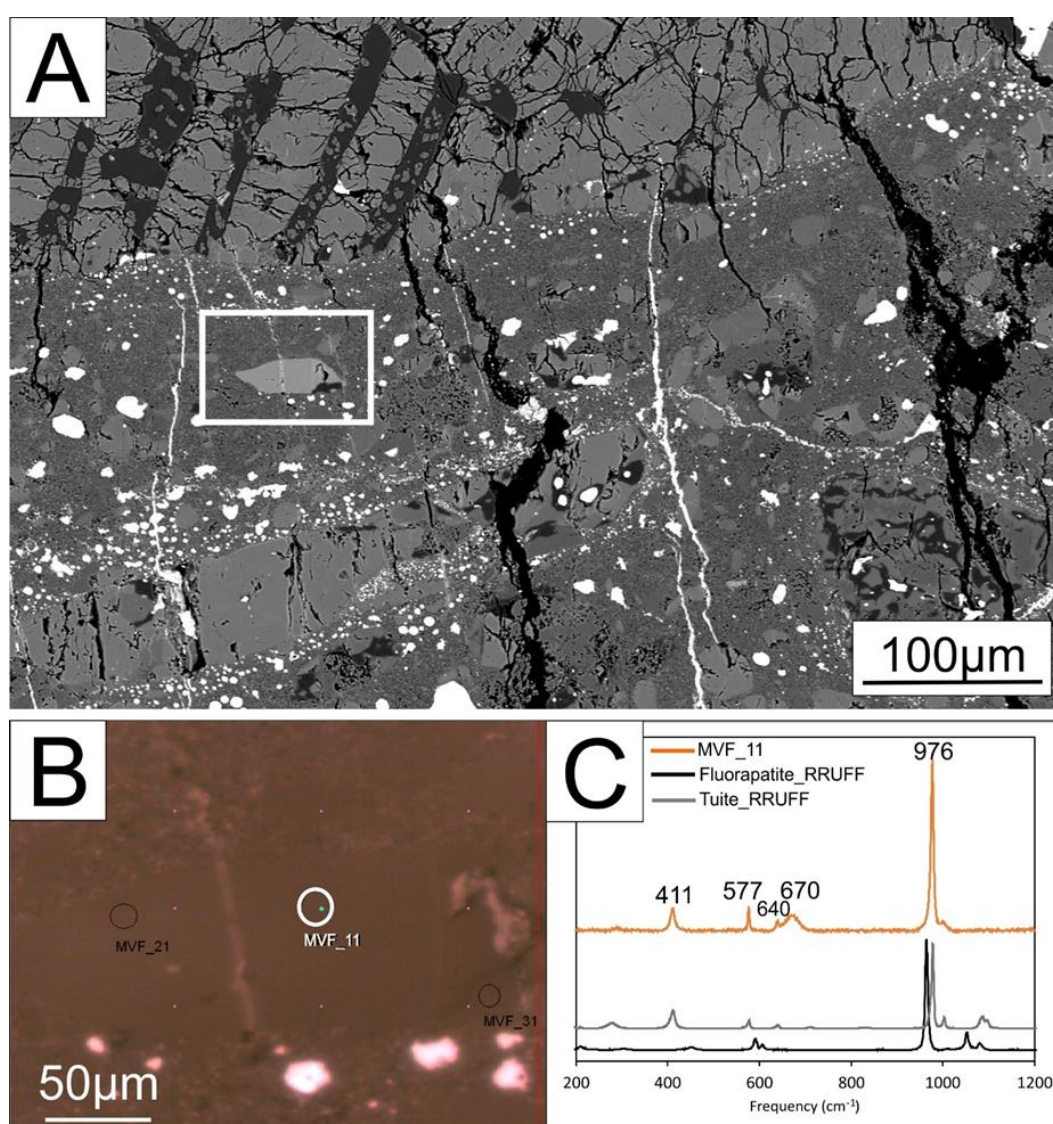


Figure 60: (A) BSE image with selected MVF_11 position in the melt vein; (B) Annotated Raman position of the tuite grain; (C) Selected Raman spectrum MVF_11 compared to referenced spectra from RRUFF database for tuite (grey line; RRUFF R120115, 532 nm) and for fluorapatite (black line; RRUFF R040098.3).

➤ Raman spectrum mv_D_d_11

The Raman spectrum mv_D_d_11 was obtained from a grain inside the melt vein of the region (see #03 position in figure 61A). The annotated position is from the core of the grain (Figs. 61B, 48B) with peaks at 821 and 851 cm^{-1} is typical of olivine (Fig. 61C). The spectrum of the forsterite from the RRUFF database (R040018.3) with peaks at ~ 825 , and 857 cm^{-1} , and the spectrum of the wadsleyite from the RRUFF database (R090004, 532 nm) with peaks at 723 and 919 cm^{-1} , are used for comparison (Fig. 61C) to identify the phase of the mineral with the most suitable peaks of the spectrum.

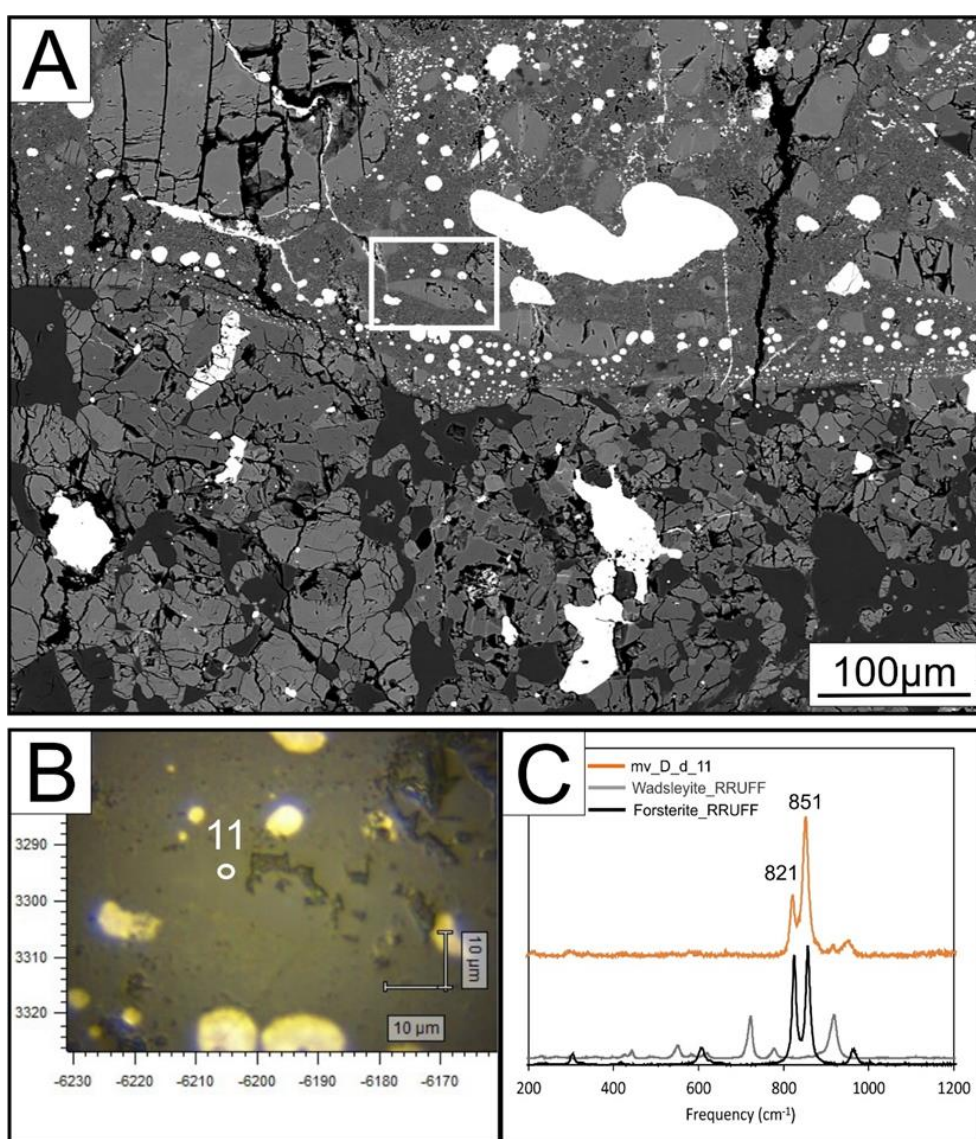


Figure 61: (A) BSE image with selected mv_D_d_11 position in the melt vein; (B) Annotated Raman position of olivine grain; (C) Selected Raman spectrum mv_D_d_11 compared to referenced spectra from RRUFF database for wadsleyite (grey line; RRUFF R090004, 532 nm) and for olivine (black line; RRUFF R040018.3).

➤ Raman spectrum mv_A3_11

The Raman spectrum mv_A3_11 was obtained from a grain inside the melt vein of the region (see #04 position in figure 62A). The annotated position is from the core of the grain (Figs. 62B, 48B) with peaks at 383, 669, 701 and 1012 cm^{-1} is typical of jadeite (Fig. 62C). The spectrum of the jadeite from the RRUFF database (R050220.3) with peaks at ~ 379 , 700, 990 and 1040 cm^{-1} , and the spectrum of the enstatite from the RRUFF database (R070418.3) with peaks at 339, 662, 681 and 1007 cm^{-1} , and the spectrum of the diopside from RRUFF database (R090004.3) with peaks at 666, and 1011 cm^{-1} are used for comparison (Fig. 62C) to identify the phase of the mineral in the spectrum.

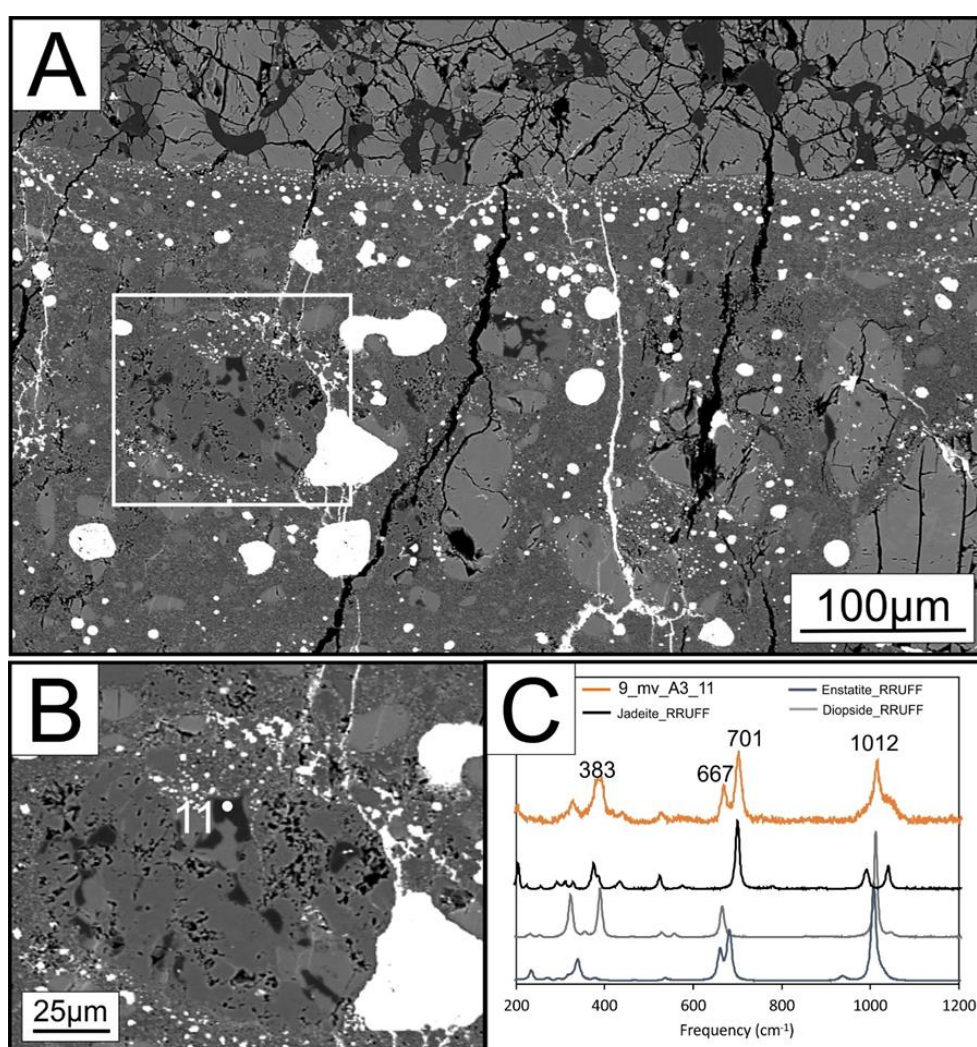


Figure 62: (A) BSE image with selected mv_A3_11 position in the melt vein; (B) Annotated Raman position of jadeite grain; (C) Selected Raman spectrum mv_A3_11 compared to referenced spectra from RRUFF database for jadeite (black line; RRUFF R050220.3), for enstatite (blue line; R070418.3), and for the diopside (grey line; RRUFF R040009.3).

➤ Raman spectra MVA1_11 & MVA1_21

The Raman spectra MVA1_11 and MVA1_21 were obtained from a grain inside the melt vein of the region (see the #05 position in figure 63A). The annotated positions are from the core of the grain (Figs. 63B, 48B) with peaks at 410, 662 and 979 cm^{-1} is typical of tuite (Fig. 63C). The spectrum of the tuite from the RRUFF database (R120115, 532 nm) with a peak at 977 cm^{-1} , and the spectrum of the wustite from Hazan *et al.*, (2013) with peaks at 305, 529, and 662 cm^{-1} , are used for comparison (Fig. 63C). Both spectra fit in the peaks that show that it is a tuite grain.

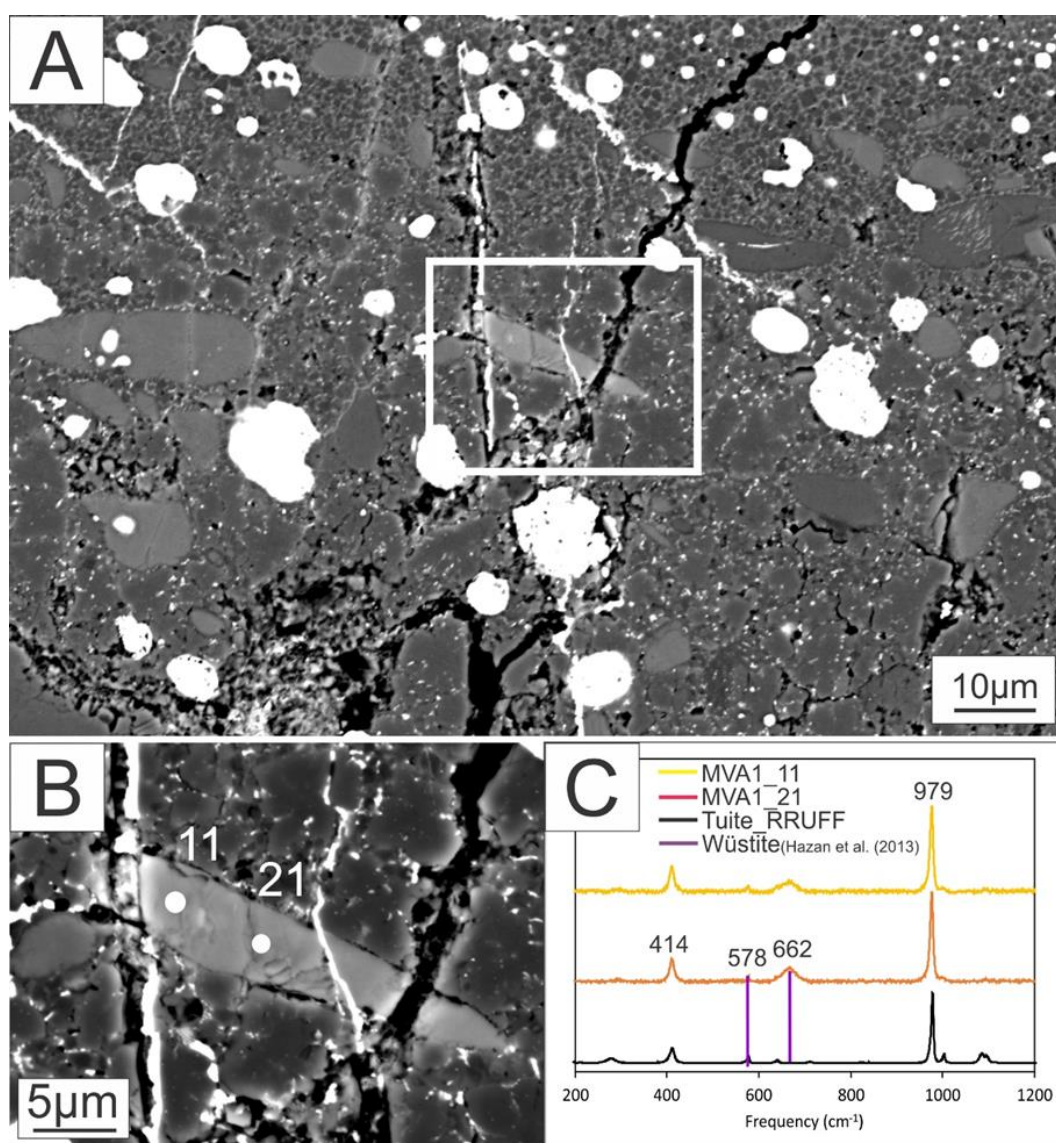


Figure 63: (A) BSE image with selected positions in the melt vein; (B) Annotated Raman position of the tuite grain; (C) Selected Raman spectrum MVA1_11 and MVA1_21 compared to referenced spectra from RRUFF database for tuite (black line; RRUFF R120115,532nm) and for wustite (purple lines; Hazan *et al.*, 2013).

➤ Raman spectrum mv_G_c_311

The Raman spectrum mv_G_c_311 was obtained from a grain inside the melt vein in the region (see #01 position in figure 64A). The annotated position is from the core of the grain (Figs. 64B, 48C) with peaks at 670, and 929 cm^{-1} is typical of majorite (Fig. 64C). The spectrum of the majorite from the RRUFF database (R210005) with peaks at 670, and 930 cm^{-1} , is used for comparison (Fig. 64C) to identify the mineral with the corresponding peaks.

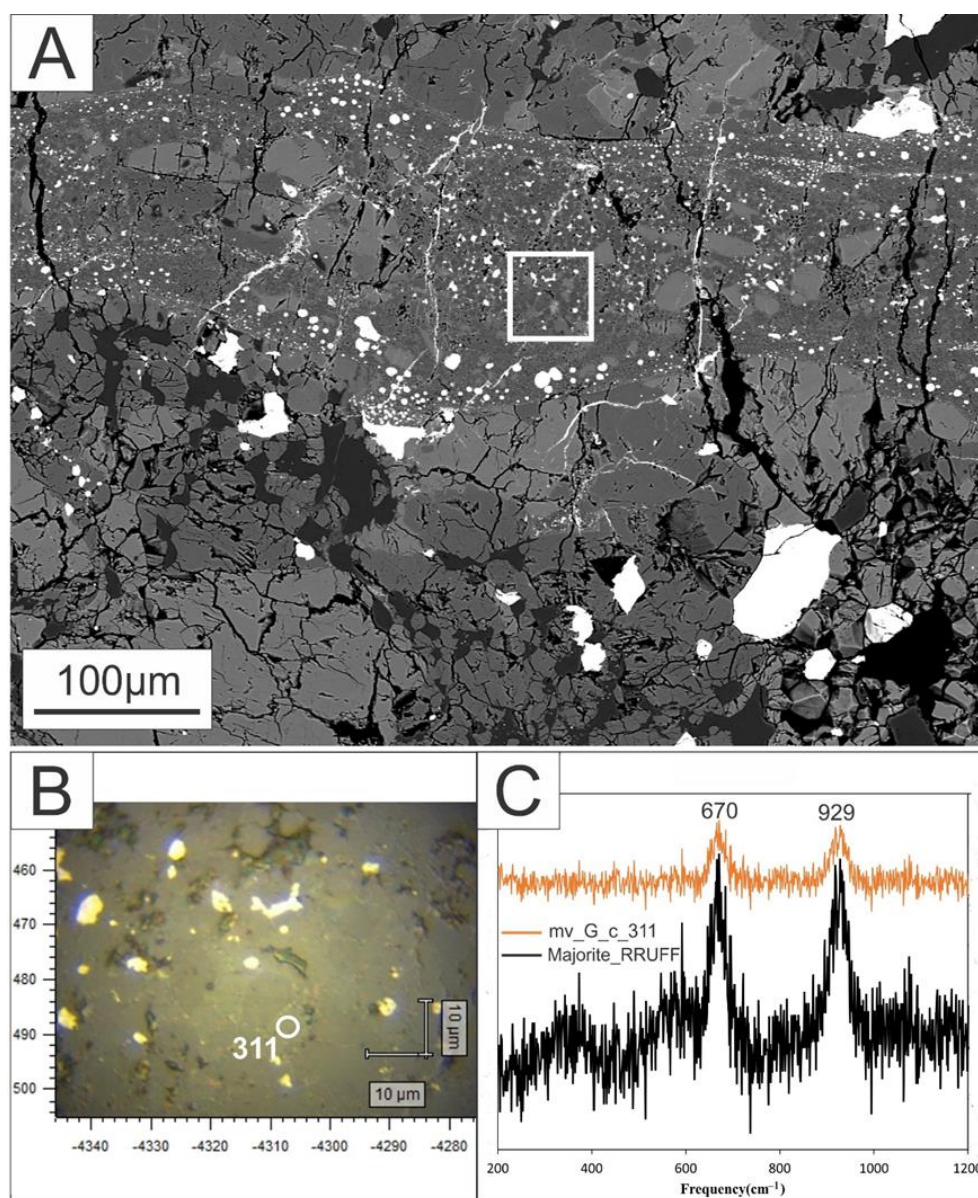


Figure 64: (A) BSE image with selected position of grain mv_G_c_311 in the melt vein, (B) Annotated Raman position at the rim of the grain, (C) Selected Raman spectrum mv_G_c_311, compared to reference spectrum for majorite (black line; RRUFF R210005).

➤ Raman spectrum mv_E1_21

The Raman spectrum mv_E1_21 was obtained from a grain inside the melt vein of the region (see #02 position in figure 65A). The annotated position is from the rim of the grain (Figs. 65B, 48C) with peaks at 667, 820, and 851 cm^{-1} are typical of olivine (Fig. 65C). The spectrum of the olivine from the RRUFF database (R040018.3) with peaks at $\sim 825 \text{ cm}^{-1}$ and 857 cm^{-1} and the spectrum of the wadsleyite from the RRUFF database (R090004, 532 nm) with peaks at 723 and 919 cm^{-1} are used for comparison (Fig. 65C), to identify the phase of the mineral, showing that the grain is forsterite.

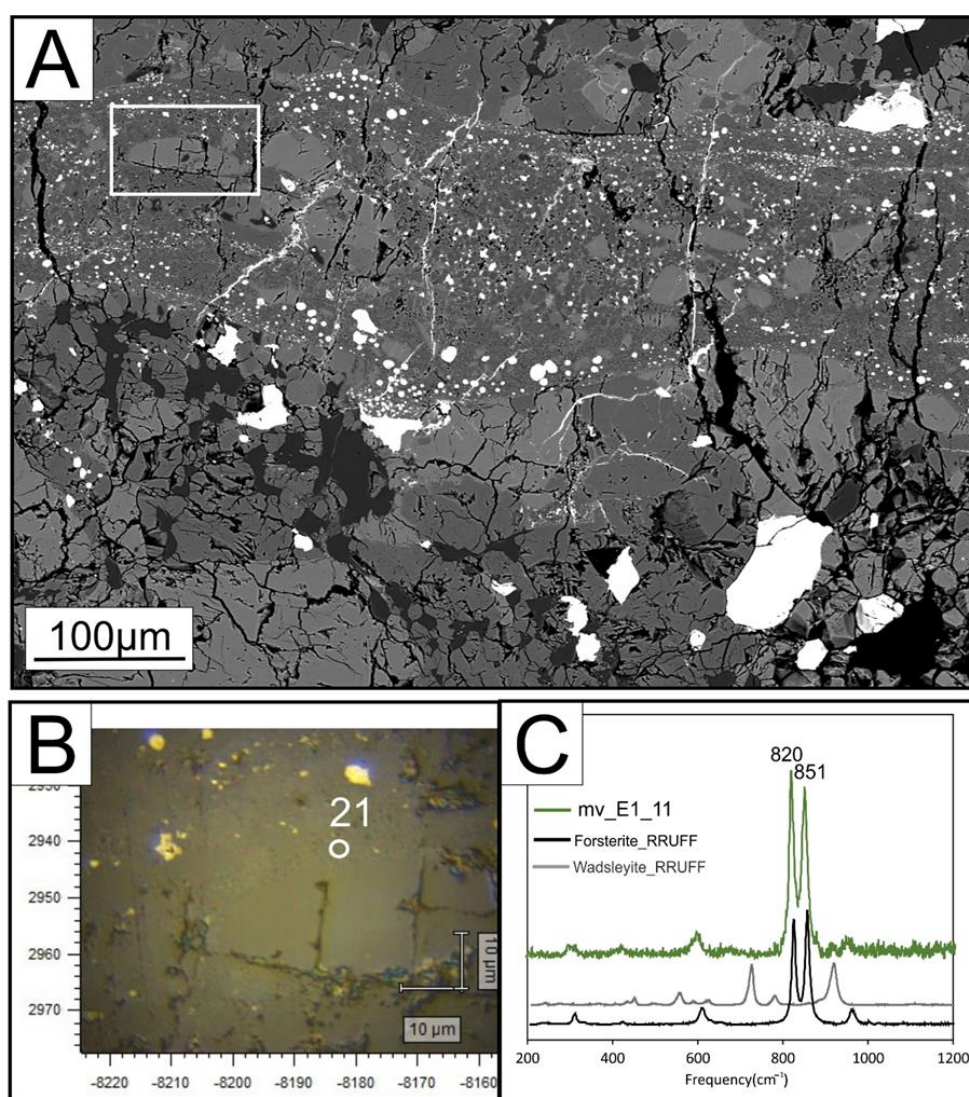


Figure 65: (A) BSE image with selected position of grain in the melt vein, (B) Annotated Raman position at the rim of the grain, (C) Selected Raman spectrum mv_E1_21, compared to reference spectra for olivine (black line; RRUFF R040018.3) and for wadsleyite (grey line; RRUFF R090004, 532 nm).

➤ Raman spectrum mv_C_A_11

The Raman spectrum mv_C_A_11 was obtained from a grain inside the melt vein of the region (see #03 position in figure 66A). The annotated position is from the core of the grain (Figs. 66B, 48C) with peaks at 381, 667, 700.5, 991, and 1040 cm^{-1} is typical of Jadeite (Fig. 66C). The spectrum of the jadeite from the RRUFF database (R050220.3) with peaks at ~ 379 , 700, 990 and 1040 cm^{-1} , and the spectrum of the omphacite from the RRUFF database (R061129, 532 nm) with peaks at 678, 1008 and 1021 cm^{-1} , are used for comparison (Fig. 66C) to define the phase of the mineral, showing that the grain is jadeite.

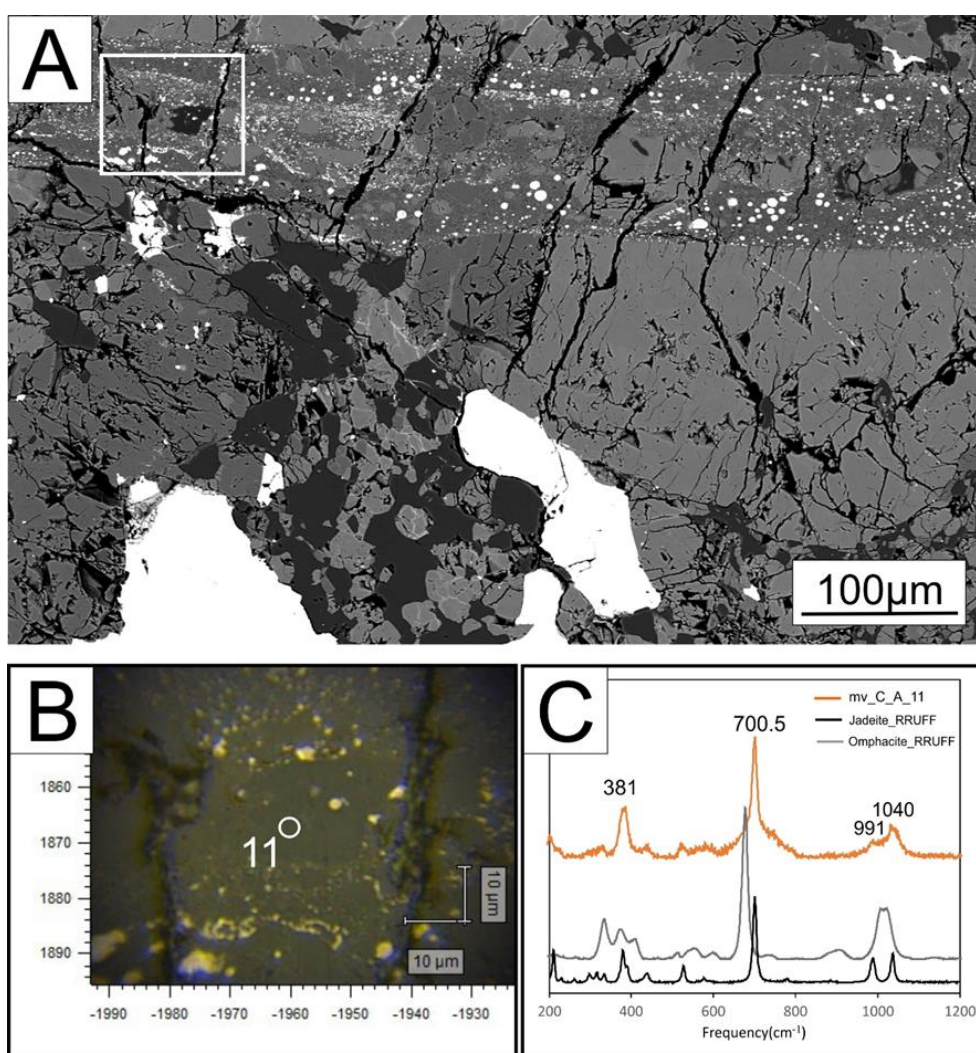


Figure 66: (A) BSE image with selected mv_C_A_11 position in the melt vein; (B) Annotated Raman position of jadeite grain; (C) Selected Raman spectrum mv_C_A_11 compared to referenced spectra from RRUFF database for Jadeite (black line; RRUFF R050220.3) and for the omphacite (grey line; RRUFF R061129, 532 nm).

4 Discussion

4.1 Classification of the Slobodka meteorite

The mineral-chemistry of silicates, metals, and sulfides, the degree of chemical homogeneity of olivines and low-Ca pyroxenes, and textural features (e.g., abundance and mean size of chondrules) are all relevant to the assignment of meteorite class, petrologic type, and shock stage. It is essential to classify the studied Slobodka meteorite sample based: (i) on the petrologic characteristics of the major chondrite group documented by Weisberg *et al.*, (2006) as illustrated in **Table 8**, and (ii) according to the petrologic type based on the criteria for classifying chondrites (**Table 9**) proposed by Van Schmus & Wood (1967).

4.1.1 Petrologic Characterization for Major Chondrite Groups

The CAI-AOA abundance in the sample is lower than 1 (vol %), eliminating the carbonaceous groups (CM, CV, CO, CK). The groundmass of the thin section reveals phenocrystal grains, hence the matrix abundance is low, with this criterion, we eliminate the (CI, CM, CO, CH, CV, CK, CB, R, K) groups. The allocation of the chondrules that are distributed in the studied thin section is in total 11.79 vol % based on the calculations using the FIJI software, and with this criterion we eliminate the (CB, EH, and EL) groups because of the high concentration. However, the results do not match the categorization of the resulting 60-80 vol % of chondrule abundance in (H, L, LL, EH, EL) groups. The metal abundance in the groundmass was calculated using the FIJI software, is about 1.17 vol %, this result is more consistent with the LL-group, so it is likely that one polished section is not sufficient to accurately determine these parameters (Weisberg *et al.*, 2006; Dodd *et al.*, 1967). The average chondrule diameter was calculated using the FIJI software to be ~0.83 mm, indicating the result of the L-group. The latter indication also stands for the olivine composition, as it has been calculated in the range of 23-26 mole% Fa (**Appendix Tables A1, A7**). Hence, the mineral-chemical data criteria and the L-group assignment are favorable (**Table 8**), also confirmed by the chemical analysis of **figure 45** chart.

Table 8: Average petrologic characteristics of the major chondrite groups (Weisberg et al., 2006).

	CI	CM	CO	CV	CK	CR	CH	CB	H	L	LL	EH	EL	R	K
Chondrule abundance (vol%)*	≪1	20 [†]	48	45	45	50–60	70	20–40	60–80	60–80	60–80	60–80	60–80	>40	27
Matrix abundance (vol%)	>99	70 [†]	34	40	40	30–50	5	≪1	10–15	10–15	10–15	2–15 [‡]	2–15 [‡]	36	73
CAI – AOA abundance (vol%)	≪1	5	13	10	10	0.5	0.1	≪1	≪1	≪1	≪1	≪1	≪1	0	≪1
Metal abundance (vol%)	0	0.1	1–5	0–5	0–5	5–8	20	60–80	8	4	2	10	10	0.1	7
Average chondrule diameter (mm)	NA	0.3	0.15	1.0	1.0	0.7	0.02	(0.2–1 cm)	0.3	0.7	0.9	0.2	0.6	0.4	0.6
Olivine composition (mol% Fa)					(<1–47) [§]		(<1–36) [§]	(2–3) [§]	(16–20) [§]	(23–26) [§]	(27–32) [§]				
	††	††	††	††	29–33	1–3¶	2¶	3¶	19.3**	25.2**	31.3**	0.4	0.4	38.0**	2.2

* Chondrule abundance includes lithic and mineral fragments.

[†] Highly variable.[‡] The amount of matrix, if any, is not well established in E chondrites.[§] Range of compositions.[¶] Mode.

** Data for equilibrated varieties.

†† Highly variable, unequilibrated.

NA = not applicable.

4.1.2 Petrologic Type

Ordinary meteorites with petrological type 3 (**Fig. 67**) are mainly inhomogeneous with the Fe/Mg ratio containing less ferrous than the associated olivine (Dodd *et al.*, 1967). Heterogeneous olivine and pyroxene crystals indicate a high degree of disequilibrium (Dodd *et al.*, 1967). It is also mentioned that pyroxene approaches the homogeneity more slowly than olivine does in the chondrite types 3 to 4 (**Fig. 67**) (Dodd *et al.*, 1967). Moreover, olivine in types 4 to 7 chondrites is homogeneous and the Fe/Mg ratio is characteristic of the average H-L-LL groups and has shown that decreasing heterogeneity parallels other criteria of increasing equilibration (Dodd *et al.*, 1967). The degree of homogeneity can be given by measuring the FeO content in many randomly selected olivine grains in a chondrite, thereby obtaining a “percent mean deviation” of the olivine or pyroxene composition (**Table 9**) (Dodd *et al.*, 1967).

Chd./type	1	2	3	4	5	6	7
CI	Shaded						
CM	Shaded						
CR	Shaded						
CH			Shaded				
CB			Shaded				
CV		Shaded					
CO			Shaded				
CK			Shaded	Shaded	Shaded	Shaded	
H			Shaded	Shaded	Shaded	Shaded	
L			Shaded	Shaded	Shaded	Shaded	Shaded
LL			Shaded	Shaded	Shaded	Shaded	
EH			Shaded	Shaded	Shaded	Shaded	Shaded
EL			Shaded	Shaded	Shaded	Shaded	
R			Shaded	Shaded	Shaded	Shaded	
K*			Shaded				

*Grouplet.

Chd. = chondrite group.

Figure 67: Diagram showing the petrologic types for each chondrite group (Weissberg *et al.* 2006).

Based on the first criterion, entitled as “the homogeneity of olivine compositions”, the minimum value of Fa is 22.81 mole%, the maximum value of Fa is 24.23 mole% and the mean

value is 23.52 mole% (Appendix **Table A7**). The mean absolute deviation is a way to measure the dispersion for a set of data values, so the calculated deviation is around ~1.4 moles % (Appendix **Table A7**), which is consistent with type 4 according to Dodd *et al.* (1967), although Dodd's statistical analysis is weak and inconsistent, and may not correctly distinguish among the more equilibrated chondrite types (L4 vs. L5 vs. L6). The majority of the low-Ca pyroxenes in the sample correspond to the orthopyroxene series (**Figs. 35-36**). The grain size of plagioclase was calculated with the FIJI software and has a mean value of ~40 μm , so the results are between 2 and 50 μm , which is most consistent with petrologic type 5. The estimated maximum Ni contents in metals (29.7 wt.%) and the mean value in sulfides (~0.2 wt.%) both suggest at least type 4 and type 3, respectively (**Appendix Tables A5-A6**). To find the clarity of chondrule/matrix boundaries both the texture of the chondrules was observed and the sample was compared with other known meteorites that have been characterized based on Van Schmus & Wood (1967). Assuming that the sample can be described as L4, the chondrules can be easily recognized with sharper edges, while if it can be classified within the L6 classification, the edges are poorly delineated. Thus, based on the chondrule boundaries, it can be reported that the Slobodka meteorite is more consistent with type 4. In conclusion, the criteria indicate that the sample is closer to the L5 classification but mostly in L4. Nonetheless, L4 is most consistent with the full list of noted indicators and also confirmed by the chemical analysis of **Figure 46** chart.

Table 9: Results of criteria for classifying the Slobodka meteorite according to petrologic type, based on Van Schmus & Wood (1967). The painted squares indicate the regions that the results revealed to this BSc Thesis.

Criterion	1	2	3	4	5	6	7
Homogeneity of olivine compositions	—	>5% mean deviations		≤5%	Homogeneous		
Structural state of low-Ca pyroxene	—	Predominantly monoclinic		>20% monoclinic	≤20% monoclinic	Orthorhombic	
Feldspar	—	Minor primary grains		Secondary <2-μm grains	Secondary 2–50-μm grains	Secondary >50-μm grains	
Chondrule glass	Altered or absent	Mostly altered, some preserved	Clear, isotropic	Devitrified	Absent		
Metal: Maximum Ni (wt%)	—	<20 taenite minor or absent	>20 kamacite and taenite in exsolution relationship				
Sulfides: Mean Ni (wt%)	—	>0.5	<0.5				
Matrix	Fine grained opaque	Mostly fine-grained opaque	Opaque to transparent	Transparent, recrystallized			
Chondrule-matrix integration	No chondrules	Sharp chondrule boundaries		Some chondrules can be discerned, fewer sharp edges		Chondrules poorly delineated	Primary textures destroyed
Carbon (wt%)	3–5	0.8–2.6	0.2–1	<0.2			
Water (wt%)	18–22	2–16	0.3–3	<1.5			

After Van Schmus and Wood (1967) with modifications by Sears and Dodd (1988), Brearley and Jones (1998), and this work.

4.2 Shock Stage Distribution

When a meteorite collides, significant shock features can be created on its surface, directly related to the shock effects in rock-forming minerals, resulting in its final shock stage distribution (Stöffler and Grieve, 2007). In order to categorize a meteorite- that has experienced a collision- into specific stage(s), it is essential to study the shock features (e.g., texture, degree of shock metamorphism and lithological components, etc.). To this trajectory, the shock features of the studied sample were characterized using the optical microscope.

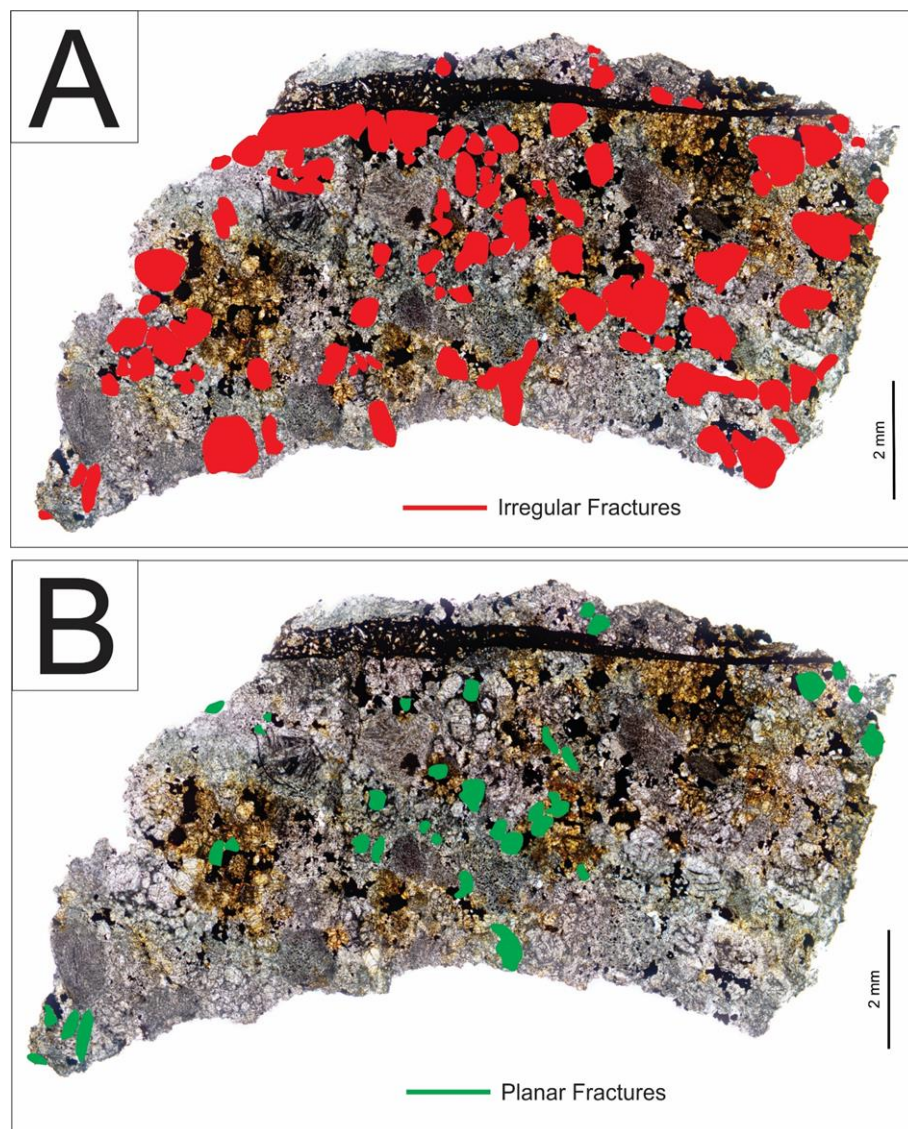


Figure 68: Illustration of the shock features: (A) Layer irregular fractures only; (B) Layer Planar Fractures only.

After studying every grain throughout the groundmass for rock-forming minerals, mostly olivine, and pyroxene, layered images of the shock features were created based on the classification scheme of Stöffler and Grieve, 2007; one only for the irregular fractures (**Fig. 68A**) and the other for the planar fractures (PFs) scattered in the whole groundmass of the studied thin section (**Fig. 68B**).

Accordingly, a shock stage classification map was additionally created illustrating the stages from S2 to S4 (**Fig. 69B**), while an image of the thin section of the meteorite is depicted for comparison (**Fig. 69A**). The distribution of the observed shock features suggests a heterogeneous shock degree, varying from as low as S2 and up to S4, based on the classification scheme of Stöffler and Grieve, 2007.

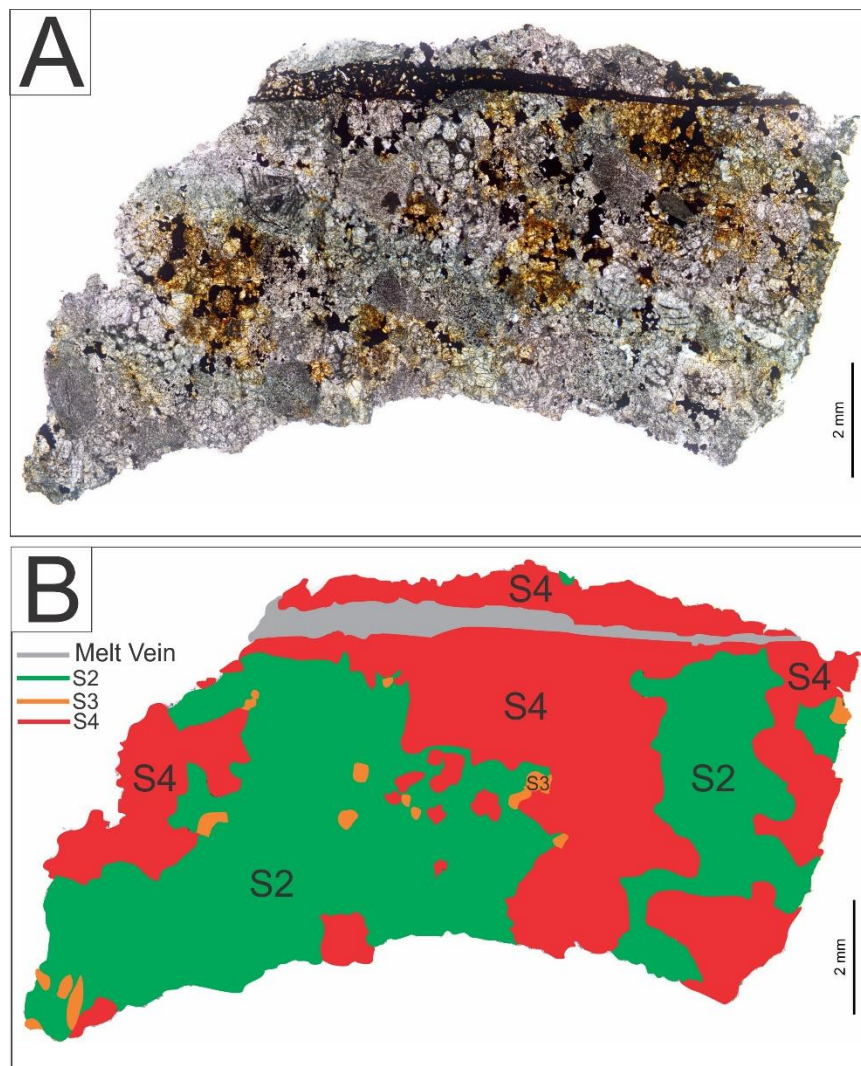


Figure 69: Image (A) image of the thin section of meteorite Slobodka; (B) illustrates the shock stage classification map of stages between S2 and S4.

4.2.1 Shock Features – Shock Classification

As mentioned above, the shock features were characterized using the optical microscope, with the magnifying lenses $\times 10$, $\times 20$, $\times 50$, $\times 100$. The results are displayed in **Table 10**. More than 100 olivine-plagioclase grains have been studied to conclude the classification and distribution of the main minerals of the meteorite in the groundmass. Focusing mainly on the olivine-pyroxene and plagioclase grains in the groundmass, it is spotted that only one olivine crystal exhibits weak mosaicism, while many more olivine grains were observed to have low-grade planar fractures and undulatory extinction. Only a few plagioclase grains that were observed exhibit undulatory extinction and there is no maskelynite. The presence of opaque shock veins suggests a heterogeneous shock degree (Stöffler and Grieve, 2007), varying from weak (S3) to moderately shocked (S4).

Table 10: The results for the shock classifications in the Slobodka meteorite based on the scheme by Stöffler & Grieve (2007). The colored rectangles correspond to the observations of the present work. *from Stöffler *et al.* (1991); **from Schmitt (2000).

Shock stage	Effects resulting from equilibration peak shock pressure		Effects resulting from local P-T-excursions	Pressure GPa* (293 K)	Pressure GPa** (293 K)	Pressure GPa** (920 K)
	Olivine	Plagioclase				
Unshocked S1	Sharp optical extinction Irregular fractures	Angular variation of extinction position: Low grade: $< 1^\circ$ High grade: $1^\circ - 2^\circ$	Sharp optical extinction Irregular fractures	none		
Very weakly shocked S2	Undulatory extinction Fractures	Angular variation of extinction position: $< 2^\circ$	Undulatory extinction Irregular fractures	none		
Weakly shocked S3	Planar fractures (PF) Undulatory extinction Irregular fractures	Low grade: maximum of 2 sets of PF High grade: 3 or more sets of PF	Undulatory extinction	Opaque shock veins, incipient formation of melt pockets (sometimes interconnected)		
Moderately shocked S4	Mosaicism (weak)	Low grade: incipient mosaicism, PF and PDF High grade: mosaicism, PF, and PDF	Low grade: undulatory extinction High grade: partially isotropic, PDF	Melt pockets, interconnected melt veins, opaque shock veins		
Strongly shocked S5	Mosaicism (strong) Planar fractures Planar deformation features (PDF)		Maskelynite (diaplectic glass)	Pervasive formation of melt pockets, veins and dykes, opaque shock veins		
Restricted to local regions in or near melt zones						
Very strongly shocked S6	Recrystallisation; yellow-brown staining; ringwoodite and wadsleyite; high pressure phases of pyroxene (e.g. majorite, akimotoite)		Shock melted (normal glass)	as in stage S5		
Shock melted	Whole rock melting and formation of melt rocks					

<div style="display: flex; justify-content: space-between; align-items: center;"> <div style="border: 1px solid black; width: 20px; height: 20px; background-color: yellow; margin-right: 5px;"></div> <div>selection for the majority of grains</div> </div> <div style="display: flex; justify-content: space-between; align-items: center; margin-top: 5px;"> <div style="border: 1px solid black; width: 20px; height: 20px; background-color: orange; margin-right: 5px;"></div> <div>selection for fewer amount of grains</div> </div> <div style="display: flex; justify-content: space-between; align-items: center; margin-top: 5px;"> <div style="border: 1px solid black; width: 20px; height: 20px; background-color: red; margin-right: 5px;"></div> <div>selection for minimum amount of grains</div> </div>	<div style="display: flex; justify-content: space-between; align-items: center;"> <div style="border: 1px solid black; width: 20px; height: 20px; background-color: blue; margin-right: 5px;"></div> <div>selection for only one grain</div> </div> <div style="display: flex; justify-content: space-between; align-items: center; margin-top: 5px;"> <div style="border: 1px solid black; width: 20px; height: 20px; background-color: lightblue; margin-right: 5px;"></div> <div>selection for the main melt vein</div> </div>
--	---

Based on remarks by Stöffler *et al.* (1991), when the shock is distributed with the shock stage classification (S4), this suggests that the groundmass experienced pressures between

30-35 GPa (293 °K). On the other hand, based on different data from various literature, the shock stage S4 might be between 25 and 30 GPa (293 °K; Schmitt, 2000), 15 and 20 GPa (293 °K; Stöffler *et al.*, 2018) or, even, 25 and 35 GPa (200-300 °C; Fritz *et al.*, 2017). This reflects the variation of the high pressures and temperatures depending on the specific shock classification scheme (**Table 11**).

Table 11: Observation of Slobodka meteorite from the thin section (NHMW-L4372) and assignment of the shock stage based on Stöffler *et al.*, 1991, Stöffler *et al.*, 2018, and Fritz *et al.*, 2017.

	SOX	UE	UE & PFs	WM & PFs	SM & PDFs	Phases in melt zones	Shock stage *	Shock stage **	Shock stage ***
Olivine	-	+	+	+	-	-	S4	S4	S4
Pyroxene	-	+	+	-	-	-	S4	S4	S4
Plagioclase	-	+	-	-	-	-	S3	S3	S3
Melt vein	-	-	-	-	-	Mj, Ab-Jd, Tu, Wds, LP	S4	S4	S4
SOX: sharp extinction; UE: undulatory extinction; PFs: planar fractures; WM; weak mosaicism; SM; strong mosaicism; PDFs: planar deformation features; Maj: majorite; Ab-Jd: albitic jadeite; Tu: tuite; Wds: wadsleyite; LP: low pressure phases; Gl: glass									
-: the feature is absent; +: the feature is present; X: feature or features are common									
*(Stöffler <i>et al.</i> , 1991), ** (Stöffler <i>et al.</i> , 2018), *** (Fritz <i>et al.</i> , 2017)									

4.3 Shock Conditions and Barometry

Through the combination of analytical methods such as Raman Spectroscopy and EPMA along with detailed observation using optical microscopy, we were able to identify the high-pressure polymorphs of various minerals in the melt vein of the Slobodka meteorite, including albitic jadeite, tuite, wadsleyite and majorite. Many scientists have studied the stability conditions of majorite and according to laboratory experiments (Ohtani *et al.*, 1991; Kato & Kumazawa, 1985; Tomioka *et al.*, 2016; Bazhan *et al.*, 2017; Heinemann *et al.*, 1997), tetragonal majorite likely crystallized with a pressure range of 17-20 GPa and high temperature at 1800 °C (**Fig. 70**), whilst above 20 GPa, the temperature ranges from 1900 °C to 2100 °C (Tomioka *et al.*, 2016) (**Fig. 70**).

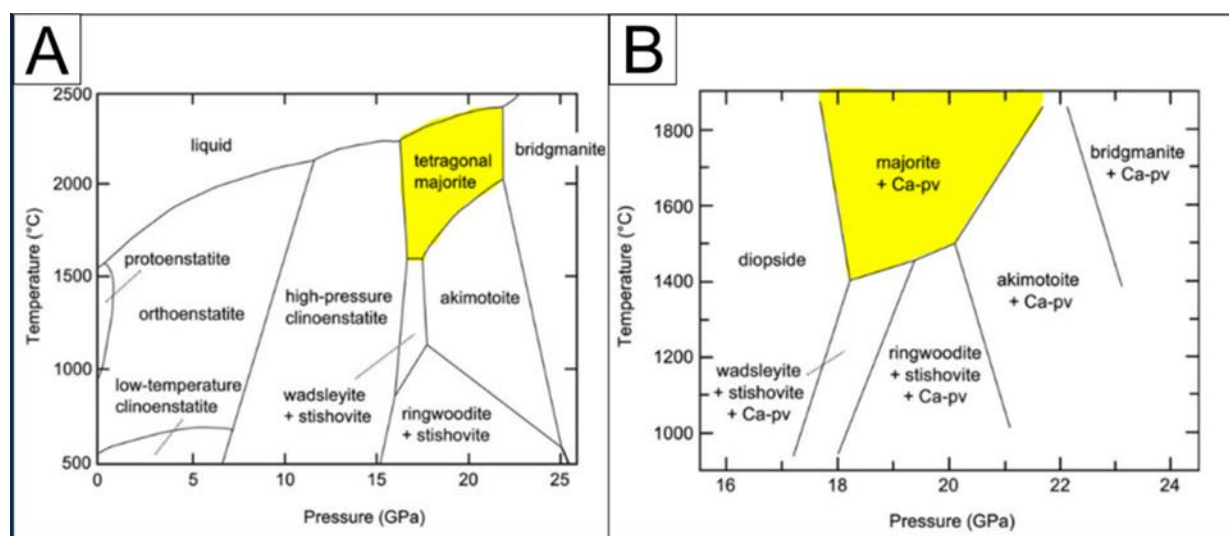


Figure 70: (A) Phase diagram of MgSiO_3 (Tomioka *et al.*, 2017); (B) Phase diagram of $\text{CaMgSi}_2\text{O}_6$ (Tomioka *et al.*, 2017); Abbreviations: Ca-Pv: CaSiO_3 -perovskite

More specifically, the majorite present in the melt veins of Slobodka has been estimated in the range of 20.2-23.1 GPa based on the Collerson barometer (Collerson *et al.*, 2010), and therefore, majorite has a temperature from 1900 °C to 2100 °C. In contrast, the pressure range for the stability of wadsleyite is lower, with 14-18 GPa, indicating temperatures lower than 1500 °C (Tomioka *et al.*, 2017) (**Fig.71**). Tuite has been studied extensively by scientists, with synthesis experiments conducted at different pressures and temperatures. Additionally, Xie *et al.* (2016) suggest that above 12 GPa and 1100 °C conditions are likely required for the transformation from merrillite and chlorapatite to tuite in the chondritic area. Also, it still can be present, based on other high-pressure phases in the melt veins of the Suizhou meteorite, with high pressures at 20-23GPa, and high temperatures estimated at the 1900-2000 °C range (Murayama *et al.* (1986); Xie *et al.*, 2003; Xie *et al.* (2013); Zhai *et al.*, 2014). Lastly, it is worthy to note herein that albitic jadeite has not been synthesized yet, and there is a suggestion that it is probably formed at 18-22 GPa as implied by the coexistence with near-end-member majorite (Ma *et al.*, 2022). Having these HP phases co-existing in the same melt vein, suggests high pressures between 12 to ~23 GPa, with high temperatures estimated to range from 1100-2100°C. The high-temperature range that has been estimated for majorite (≥ 1800 °C) present mostly in the center of the melt vein and wadsleyite (≤ 1500 °C) found at the edge of the melt vein, suggests a temperature gradient during high-pressure mineral growth of minerals under pressure, indicating that the stability field of wadsleyite can

be preserved especially when it occurs with 1-3 μm grain size, based on experimental observation, and can be formed within microseconds before quenching (Baziotis *et al.*, 2018).

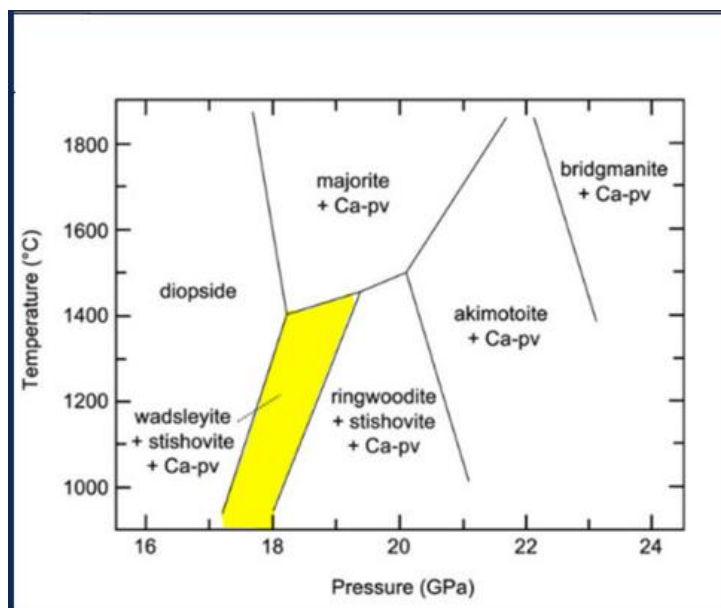


Figure 71: Phase diagram of $\text{CaMgSi}_2\text{O}_6$ (Tomioka *et al.*, 2017); Abbreviations: Ca-Pv: CaSiO_3 -perovskite

4.4 Implications of Potential Asteroid Mining

For several decades the importance of space missions has caused a significant debate about the benefits and drawbacks of carrying them out. Asteroid mining has been considered to be very beneficial for the future of space exploration to extract mineral resources, but it may take many years for such missions to become profitable. The study of meteorites has been very crucial for identifying the minerals and categorizing them into a specific meteorite group. Based on research, it has been proven that some meteorite groups are connected to specific asteroids. Therefore, by knowing the group category of a meteorite sample, we can locate its origin parent body (Norton & Clitwood, 2008).

There are three major composition classes of asteroids, the carbonaceous C-type (chondrite), the metallic M-type, and the silicate S-type (e.g., Binzel *et al.*, 1991). The asteroid belt in our solar system contains approximately a smaller amount of metal-rich (M-type) asteroids and an abundant amount of volatile-rich carbonaceous (C-type) asteroids (DeMeo *et al.*, 2015). Most importantly, it has been reported that LL chondrites have high

concentrations of rare metals, with the rarest and most useful elements found in the platinum group of metals (defined as Au, Pt, Ir, Os, Pd, Rh, and Ru; Renner *et al.*, 2000), in addition to more base metals, such as iron and nickel (Blair, 2000).

There have already been significant missions to asteroids, comets, and the Moon to conduct research on them. The Japanese Aerospace Exploration Agency (JAXA) with the Hayabusa mission provided and conducted a successful mission to retrieve a sample from a near-Earth asteroid, Itokawa, an S-type asteroid in 2005 (Yoshikawa *et al.*, 2015; Yoshikawa *et al.*, 2021). This mission was able to autonomously approach, land on, and collect data on the surface and collect a sample of the Itokawa asteroid and return to Earth. The mission was completed in 2010, and it was the first successful mission that gave the first proof that some chondrites originate in specific asteroids (Yurimoto *et al.*, 2011). Furthermore, another Japanese asteroid mission, the Hayabusa2 mission was launched in 2014 and successfully returned samples from the asteroid 162173 Ryugu in 2020 (Tsuda *et al.*, 2013). Another important mission that was sent to land on a comet, and extract samples to return them to Earth, was the Rosetta spacecraft which was operated by ESA (European Space Agency) and was launched in 2004 (Accomazzo *et al.*, 2015). Unfortunately, the mission failed to be completed and return the samples from the comet, because the spacecraft hard-landed on the comet and could not operate and continue the mission back to Earth, but scientists extracted significant information as the mission was active, before ending the operation (Accomazzo *et al.*, 2017). In addition, the last successful asteroid mission that was completed on September 2023 by NASA, was the mission OSIRIS-Rex, and the samples were collected from 101955 Bennu, a carbonaceous near-Earth asteroid (Lauretta *et al.*, 2017). Important references must be made regarding the most recent missions on the Moon as well. The recent Chang'e 5 mission and the current Chang'e 6 mission by the China National Space Administration are about robotic lunar exploration. Despite, the moon not being an asteroid, it is indeed the closest celestial object orbiting the Earth. The Chang'e 5 mission was the first China's successful lunar sample return mission from the moon (Xiao *et al.*, 2021). The scientific research that was conducted had the main goal of extracting information about the chemistry and petrography while studying the lunar regoliths and soil. The researchers discovered evidence of hydroxyl molecules that were considered to have been embedded in the lunar soil through the solar wind (Lin *et al.*, 2022), and they revealed scientific importance data, by

studying the chemical analysis and lead isotopes of the lunar basalts, proving from the samples research that they already preexisted by ~1.9 Ga earlier, expanding the chronology of the moon known until this mission's research data analysis(Che *et al.*, 2021; Li *et al.*, 2022).

Currently, the known global reserves of minerals in Earth's ores are declining, and scientists urgently need to develop new methods for obtaining critical mineral resources (Ríos Muñoz *et al.*, 2024) However, the cost of completing a single mission to retrieve samples from an asteroid is up to billions of dollars (Brophy *et al.*, 2012). Concerning these crucial factors, it is important to make asteroid mining economical due to the difficult mining nature and consider the environmental and ethical impact of such a mission. Regarding the environmental impacts of potential asteroid mining missions, some aspects of these concerns highlight that a space mission may offer a more sustainable alternative to traditional ground-based mining methods, which often lead to the release of toxic chemicals and contribute to the degradation of the environment (Dudka & Adriano, 1997; Dallas *et al.*, 2020). However, with the extraction of resources from asteroids such as water and minerals, a debatable issue is how sustainable it will be for the environment when the minerals come into contact with the earth's ecosystem, but also how human activity in outer space may affect the corresponding ecosystem (Badescu,2013). Another important aspect to consider is the impact of asteroid mining on the global economy. There is already concern about how companies will affect the outcome of future missions, with the main motive being wealth rather than other potential concerns such as resource conflicts (Peña-Ramos & Luis, 2020).

All these missions and research studies mentioned above had the ulterior purpose of studying samples from orbit bodies in outer space. It is indeed crucial to conduct research on meteorites, analyze their chemistry, and understand their origin for future exploration and potential mining of asteroids. The controversial issues, that have been explicated, will significantly impact, and transform the global economy and environment in the future, but above all, the ethical aspect is crucial to the decisions that will arise from human activity and will significantly affect its evolution.

5 CONCLUSIONS

In summary, we suggest that Slobodka is best described as an L4 ordinary chondrite. We determined the meteorite's chondrite group based on chemical analysis and the Weisberg classification scheme (Weisberg *et al.*, 2006). Also, the petrologic type of categorization was based on chemical analysis and the Van Schmus & Wood (1967) scheme. Regarding the shock stage distribution, the sample was characterized as variably shocked from S2 to S4 shock stage based on the Stöffler *et al.* (2007) scheme. The melt vein consists of four high-pressure polymorphs of albitic jadeite, tuite, majorite, and wadsleyite. Albitic jadeite, majorite, and tuite were found scattered in the melt vein, while wadsleyite was found at the rim of the melt vein close to the groundmass. Wadsleyite was identified using only Raman spectroscopy as a Raman-active mineral, as its micro-grain size made it undetectable through microprobe analysis. It's worth noticing that albitic jadeite was beam-sensitive at the microprobe analysis and after each measurement, the grain was damaged. In addition, there were micro-sized grains of majorite present, which resulted in high background noise and low intensity in its Raman spectrum. As for the shock conditions, the co-existence of these HP polymorphs suggests P between 12 to ~ 23 GPa and T range from 1100-2100 °C. Additionally, majorite grains were present in the center of the MV (≥ 1800 °C), while wadsleyite grains were found at the edge of the MV (≤ 1500 °C), indicating a temperature gradient during high-pressure mineral formation. Lastly, we discussed the importance of studying meteorites for future mineral exploitation in asteroid mining missions.

6 REFERENCES

- Accomazzo, A., Ferri, P., Lodiot, S., *et al.* (2015). Rosetta operations at the comet. *Acta Astronautica*, **115**, 434-441.
- Accomazzo, A., Ferri, P., Lodiot, S., *et al.* (2017). The final year of the Rosetta mission. *Acta Astronautica*, **136**, 354-359.
- Adcock, C.T., Tschauner, O., Hausrath, E.M., *et al.* (2017). Shock-transformation of whitlockite to merrillite and the implications for meteoritic phosphate. *Nature Communications*, **8**, 14667.
- Affatato, V., Conenna, M., Roversi, D. (2023). The Ethics of Resource Extraction in Space: a Normative Essay.
- Anthony, J.W., Bideaux, R.A., Bladh, K.W., Nichols, M.C. (2001). Handbook of mineralogy (Vol. 1). Mineral Data Publ.
- Asay J.R., Shahinpoor M. (1993). High-pressured shock compression of solids. Springer, New York, Berlin, Heidelberg, 393 pp.
- Bazhan, I. S., Litasov, K.D., Ohtani, E., Ozawa, S. (2017). Majorite-olivine–high-Ca pyroxene assemblage in the shock-melt veins of Pervomaisky L6 chondrite. *American Mineralogist*, **102(6)**, 1279-1286.
- Badescu, V. (Ed.). (2013). Asteroids: Prospective energy and material resources. Springer Science & Business Media.
- Baziotis, I., Asimow, P.D., Hu, J., *et al.* (2018). High-pressure minerals in the Château-Renard (L6) ordinary chondrite: implications for collisions on its parent body. *Scientific reports*, **8**, 9851.
- Baziotis, I.P., Ma, C., Guan, Y., *et al.* (2022a). Unique evidence of fluid alteration in the Kakowa (L6) ordinary chondrite. *Scientific Reports*, **12**, 5520.
- Baziotis, I., Xydous, S., Papoutsas, A., *et al.* (2022b). Jadeite and related species in shocked meteorites: Limitations on inference of shock conditions. *American Mineralogist*, **107**, 1868-1877.
- Baziotis, I.P., Xydous, S., Papoutsas, A., *et al.* (2023). Investigation of the shocked Viñales ordinary chondrite (L6) meteorite fall-implications for shock classification, fragmentation, and collision dynamics. *Icarus*, **390**, 115326.
- Bindi, L., Chen, M., Xie, X. (2017). Discovery of the Fe-analogue of akimotoite in the shocked Suizhou L6 chondrite. *Scientific Reports*, **7(1)**, 42674.
- Bindi, L., Brenker, F.E., Nestola, F., *et al.* (2019). Discovery of asimowite, the Fe-analog of wadsleyite, in shock-melted silicate droplets of the Suizhou L6 and the Quebrada Chimborazo 001 CB3. 0 chondrites. *American Mineralogist*, **104(5)**, 775-778.
- Binns, R.A., Davis, R.J., Reed, S.J.B. (1969). Ringwoodite, natural (Mg,Fe)₂ SiO₄ spinel in the Tenham meteorite. *Nature*, **221**, 943-944
- Binzel, R.P., Barucci, M.A., Fulchignoni, M. (1991). The origins of the asteroids. *Scientific American*, **265**, 88-95.
- Blair, B.R. (2000). The role of near-earth asteroids in long-term platinum supply. Space Resources Roundtable II: held November 8-10, 2000, in Golden, Colorado. LPI Contribution No. 1070, Lunar and Planetary Institute, Houston, p.5
- Bosi, F., Biagioni, C., Pasero, M. (2019). Nomenclature and classification of the spinel supergroup. *European Journal of Mineralogy*, **31(1)**, 183-192.

- Brearley, A.J., Jones, R.H. (1998). Chondritic meteorites. *Reviews in mineralogy and geochemistry*, **36**, 3-01.
- Brophy, J.R., Friedman, L., Culick, F. (2012). Asteroid retrieval feasibility. In 2012 IEEE Aerospace Conference (pp. 1-16). IEEE.
- Brown, G.M. (1972) Pigeonitic pyroxenes: A review, in: Shagam, R., Hargraves, R.B., Morgan, W.J. *et al.* (Eds), *Studies in Earth and Space Sciences*, vol. 132, GSA Memoir, pp. 523-534. DOI: 10.1130/MEM132-p523
- Che, X., Nemchin, A., Liu, D., *et al.* (2021). Age and composition of young basalts on the Moon, measured from samples returned by Chang'e-5. *Science*, **374**, 887-890.
- Collerson, K.D., Williams, Q., Kamber, B.S., *et al.* (2010). *Geochimica et Cosmochimica Acta*, **74**, 5939-5957.
- Connolly Jr, H.C., Desch, S.J. (2004). On the origin of the “kleine Kügelchen” called chondrules. *Chemie der Erde*, **64**, 95-125.
- Connolly Jr, H.C., Hewins, R.H. (1990). The production of chondrule textures by introducing refractory dust to superheated melts. *Meteoritics*, **25**, 354.
- Connelly, J. N., Bizzarro, M., Krot, A.N. *et al.* (2012). The absolute chronology and thermal processing of solids in the solar protoplanetary disk. *Science*, **338**, 651-655.
- Dallas, J.A., Raval, S., Gaitan, J.A., *et al.* (2020). Mining beyond earth for sustainable development: Will humanity benefit from resource extraction in outer space? *Acta Astronautica*, **167**, 181-188.
- Davidson, P.M., Mukhopadhyay, D.K. (1984). Ca-Fe-Mg olivines: phase relations and a solution model. *Contributions to Mineralogy and Petrology*, **86**, 256-263.
- DeMeo, F.E., Alexander, C.M.O., Walsh, K.J., *et al.* (2015). The compositional structure of the asteroid belt. *Asteroids IV in the Space Science Series*, DOI: 10.48550/arXiv.1506.04805.
- De Val-Borro, M., Rezac, L., Hartogh, P., *et al.* (2012). An upper limit for the water outgassing rate of the main-belt comet 176P/LINEAR observed with Herschel/HIFI. *Astronomy & Astrophysics*, **546**, L4.
- Deer, W., Howie, R.A., Zussman, J. (2013). An introduction to the rock-forming minerals, 3rd Edition, Pearson, London, UK, 712 pp. ISBN electronic: 9780903056434, ISBN print: 9780903056274, DOI: 10.1180/DHZ.
- Dodd Jr, R.T., Van Schmus, W.R., Koffman, D.M. (1967). A survey of the unequilibrated ordinary chondrites. *Geochimica et Cosmochimica Acta*, **31**, 921-951.
- Duvall G.E., Fowles G.R. (1963). Shock waves, in: Bradley, R.S. (Ed.), *High Pressure Physics and Chemistry Vol. 2*, Academic Press Inc., New York, 209-291.
- Dudka, S., Adriano, D. C. (1997). Environmental impacts of metal ore mining and processing: a review. *Journal of environmental quality*, **26(3)**, 590-602.
- Fritz, J., Greshake, A., Fernandes, V.A. (2017). Revising the shock classification of meteorites. *Meteoritics & Planetary Science*, **52**, 1216-1232.
- Flynn, G., Moore, L.B., Klöck, W. (1999). Density and Porosity of Stone Meteorites: Implications for the Density, Porosity, Cratering, and Collisional Disruption of Asteroids. *Icarus*, **142**, 97-105.
- Gamaletsos, P.N. (2023). Course notes “Introduction to Mineralogy”, School of Mineral Resources Engineering, Technical University of Crete.
- Gamaletsos, P.N. (2024a). Course notes “Systematic Mineralogy”, School of Mineral Resources Engineering, Technical University of Crete.

- Gamaletsos, P.N. (2024b). Course notes “Instrumental Methods in Mineralogy and Petrology”, School of Mineral Resources Engineering, Technical University of Crete.
- Ganuza, M.L., Ferracutti, G., Gargiulo, M.F., *et al.* (2014). The spinel explorer-interactive visual analysis of spinel group minerals. *IEEE transactions on visualization and computer graphics*, **20**, 1913-1922.
- Gastineau-Lyons, H.K., McSween Jr, H.Y., Gaffey, M.J. (2002). A critical evaluation of oxidation versus reduction during metamorphism of L and LL group chondrites, and implications for asteroid spectroscopy. *Meteoritics & Planetary Science*, **37**, 75-89.
- Ghiorso, M.S. (1984). Activity/composition relations in the ternary feldspars. *Contributions to Mineralogy and Petrology*, **87**, 282-296.
- Gillet, P., Chen, M., Dubrovinsky, L., Goresy, A.E. (2000). Natural NaAlSi₃O₈-hollandite in the shocked Sixiangkou meteorite. *Science*, **287**, 1633-1636.
- Goldstein, J.I., Ogilvie, R.E. (1965). The growth of the Widmanstätten pattern in metallic meteorites. *Geochimica et Cosmochimica Acta*, **29**, 893-920 (IN3-IN4, 897-920).
- Goldstein, J.I., Scott, E.R.D., Chabot, N.L. (2009). Iron meteorites: Crystallization, thermal history, parent bodies, and origin. *Geochemistry*, **69**, 293-325.
- Goldstein, J.I., Short, J.M. (1967). The iron meteorites, their thermal history and parent bodies. *Geochimica et Cosmochimica Acta*, **31**, 1733-1770.
- Graham, R.A. (1993). Solids under high-pressure shock compression: Mechanics, Physics, and Chemistry. Springer-Verlag New York, Inc., 221 pp. DOI: 10.1007/978-1-4613-9278-1
- Güldemeister, N., Wünnemann, K., Durr, N., Hiermaier, S. (2013). Propagation of impact-induced shock waves in porous sandstone using mesoscale modeling. *Meteoritics & Planetary Science*, **48**, 115-133.
- Hao, M., Pierotti, C.E., Tkachev, S., *et al.* (2019). The single-crystal elastic properties of the jadeite-diopside solid solution and their implications for the composition-dependent seismic properties of eclogite. *American Mineralogist*, **104**, 1016-1021.
- Hazan, E., Sadia, Y., Gelbstein, Y. (2013). Characterization of AISI 4340 corrosion products using Raman spectroscopy. *Corrosion Science*, **74**, 414-418.
- Heinemann, S., Sharp, T.G., Seifert, F., Rubie, D.C. (1997). The cubic-tetragonal phase transition in the system majorite (Mg₄Si₄O₁₂)-pyrope (Mg₃Al₂Si₃O₁₂), and garnet symmetry in the Earth's transition zone. *Physics and Chemistry of Minerals*, **24**, 206-221.
- Hodge, P.W. (1994). Meteorite craters and impact structures of the Earth. Cambridge University Press.
- Howie, R.A., R Gaines, R.V., Skinner, H.C.W., *et al.* (1997). Dana's New Mineralogy. Eighth Edition. New York and Chichester (John Wiley and Sons, Ltd.), xlvii+1819 pp. ISBN: 0-471-19310-0, *Mineralogical Magazine*, (1998), **62(3)**, 431-432. DOI: 10.1180/002646198547693.
- Hu, J., Sharp, T.G. (2022). Formation, preservation and extinction of high-pressure minerals in meteorites: temperature effects in shock metamorphism and shock classification. *Progress in Earth and Planetary Science*, **9**, 1-22.
- Huang, S., Lu, J., Prinz, M., Weisberg, M.K., *et al.* (1996). Chondrules: Their diversity and the role of open-system processes during their formation. *Icarus*, **122**, 316-346.
- Hughes, J. M., Jolliff, B.L., Rakovan, J. (2008). The crystal chemistry of whitlockite and merrillite and the dehydrogenation of whitlockite to merrillite. *American Mineralogist*, **93**, 1300-1305.
- Johnson, B.C., Bowling, T.J., Melosh, H.J. (2014). Jetting during vertical impacts of spherical projectiles. *Icarus*, **238**, 13-22.

- Kato, T., & Kumazawa, M. (1985). Garnet phase of MgSiO_3 filling the pyroxene–ilmenite gap at very high temperature. *Nature*, **316**(6031), 803-805.
- Keil, K., & Fredriksson, K. (1964). The iron, magnesium, and calcium distribution in coexisting olivines and rhombic pyroxenes of chondrites. *Journal of Geophysical Research*, **69**(16), 3487-3515.
- Lauretta, D.S., Balram-Knutson, S.S., Beshore, E., *et al.* (2017). OSIRIS-REx: sample return from asteroid (101955) Bennu. *Space Science Reviews*, **212**, 925-984.
- Li, S.J., Wang, S.J., Miao, B.K., *et al.* (2019). The density, porosity, and pore morphology of fall and find ordinary chondrites. *Journal of Geophysical Research: Planets*, **124**, 2945-2969.
- Li, C., Hu, H., Yang, M.F., *et al.* (2022). Characteristics of the lunar samples returned by the Chang'E-5 mission. *National science review*, **9**(2), nwab188.
- Lin, H., Li, S., Xu, R., *et al.* (2022). In situ detection of water on the Moon by the Chang'E-5 lander. *Science advances*, **8**, eabl9174.
- Llovet, X., Moy, A., Pinard, P.T., Fournelle, J.H. (2021). Reprint of: Electron probe microanalysis: A review of recent developments and applications in materials science and engineering. *Progress in Materials Science*, **120**, 100818, 90 pp.
- Lucas, M.P., Emery, J.P., Hiroi, T., McSween, H. Y. (2019). Spectral properties and mineral compositions of acapulcoite-lodranite clan meteorites: Establishing S-type asteroid–meteorite connections. *Meteoritics & Planetary Science*, **54**, 157-180.
- Ma, C., Tschauner, O., Beckett, J.R., *et al.* (2016). Ahrensite, $\gamma\text{-Fe}_2\text{SiO}_4$, a new shock-metamorphic mineral from the Tissint meteorite: Implications for the Tissint shock event on Mars. *Geochimica et Cosmochimica Acta*, **184**, 240-256.
- Ma, C., Tschauner, O., Kong, M., *et al.* (2022). A high-pressure, clinopyroxene-structured polymorph of albite in highly shocked terrestrial and meteoritic rocks. *American Mineralogist*, **107**, 625-630.
- McCoy T., Hutchison, R. (2004). Meteorites. A Petrologic, Chemical and Isotopic Synthesis. Cambridge Planetary Science Series, Cambridge, New York, Melbourne: Cambridge University Press. xiii+506 pp., ISBN: 0-521-47010-2, Geological Magazine (2005), **142**, 826-826. DOI: 10.1017/S0016756805281700.
- McCubbin, F.M., Jones, R.H. (2015). Extraterrestrial apatite: Planetary geochemistry to astrobiology. *Elements*, **11**, 183-188.
- McMillan, P.F., Hofmeister, A.M. (1988). Infrared and Raman Spectroscopy, in: Hawthorne F.C. (Ed.), Spectroscopic Methods in Mineralogy and Geology, Berlin, De Gruyter, 1988, pp. **99-160**. DOI: 10.1515/9781501508974-006.
- Miyahara, M., El Goresy, A., Ohtani, E., *et al.* (2008). Evidence for fractional crystallization of wadsleyite and ringwoodite from olivine melts in chondrules entrained in shock-melt veins. Proceedings of the National Academy of Sciences, **105**(25), 8542-8547.
- Miyahara, M., El Goresy, A., Ohtani, E., *et al.* (2009). Fractional crystallization of olivine melt inclusion in shock-induced chondritic melt vein. *Physics of the Earth and Planetary Interiors*, **177**, 116-121.
- Morimoto, N. (1988). Die Nomenklatur von Pyroxenen. *Mineralogy and Petrology*, **39**, 55-76.
- Müller, W. F., Hornemann, U. (1969). Shock-induced planar deformation structures in experimentally shock-loaded olivines and in olivines from chondritic meteorites. *Earth and Planetary Science Letters*, **7**, 251-264.
- Murayama, J. K., Nakai, S., Kato, M., Kumazawa, M. (1986). A dense polymorph of $\text{Ca}_3(\text{PO}_4)_2$: a high-pressure phase of apatite decomposition and its geochemical significance. *Physics of the Earth and Planetary Interiors*, **44**, 293-303.

- Nasdala, L., Smith, D.C., Kaindl, R., Ziemann, M.A. (2004). Raman spectroscopy: analytical perspectives in mineralogical research, in: A. Beran, E. Libowitzky (Eds.), *Spectroscopic methods in mineralogy*, vol. 6, European Mineralogical Union Notes in Mineralogy, Budapest, 2004, pp. **281-343**, DOI: 10.1180/EMU-notes.6.7.
- Norton, O.R., Chitwood, L.A. (2008). *Field guide to meteors and meteorites*. Springer London. ISBN: 978-1-84800-156-5, XV+287pp., eBook ISBN: 978-1-84800-157-2, DOI: 10.1007/978-1-84800-157-2
- Ohtani, E., Kagawa, N., Fujino, K. (1991). Stability of majorite (Mg,Fe)SiO₃ at high pressures and 1800°C. *Earth and Planetary Science Letters*, **102**, 158-166.
- Ono, S., Kikegawa, T., Higo, Y. (2013). In situ observation of a phase transition in Fe₂SiO₄ at high pressure and high temperature. *Physics and Chemistry of Minerals*, **40**, 811-816.
- Oulton, J., Humayun, M., Fedkin, A., Grossman, L. (2016). Chemical evidence for differentiation, evaporation, and recondensation from silicate clasts in Gujba. *Geochimica et Cosmochimica Acta*, **177**, 254-274.
- Ozawa, S., Miyahara, M., Ohtani, E., *et al.* (2014). Jadeite in Chelyabinsk meteorite and the nature of an impact event on its parent body. *Scientific Reports*, **4**, 5033.
- Pabst, A., Thrush, P.W. (1968). A dictionary of mining, mineral, and related terms. Washington (Bureau of Mines, Dept. of the Interior), 1269 pp., *Mineralogical Magazine*, (1970), **37**(289): 635-636. DOI: 10.1180/minmag.1970.037.289.21
- Papike, J.J., Prewitt, C.T., Sueno, S., Cameron, C. (1973). Pyroxenes: comparisons of real and ideal structural topologies. *Zeitschrift für Kristallographie*, **138**, 254-273.
- Peña-Ramos, J.A., Luis, F.R.R.D. (2020). Resources in space and asteroid mining: where we are and which challenges should be expected. *International Journal of Technology Management*, **82**, 197-205.
- Petrova, E.V., Grokhovsky, V.I. (2019). High pressure impacts on meteorites. *Pure and Applied Chemistry*, **91**, 1857-1867.
- Presnall, D.C. (1995). Phase diagrams of Earth-forming minerals. *Mineral physics and crystallography: A handbook of physical constants*, **2**, 248-268.
- Price, G.D. (1983). The nature and significance of stacking faults in wadsleyite, natural β -(Mg,Fe)₂SiO₄ from the Peace River meteorite. *Physics of the Earth and Planetary Interiors*, **33**, 137-147.
- Ramsden, A.R., Cameron, E.N. (1966). Kamacite and taenite superstructures and a metastable tetragonal phase in iron meteorites. *American Mineralogist*, **51**, 37-55.
- Radomsky, P.M., Hewins, R.H. (1990). Formation conditions of pyroxene-olivine and magnesian olivine chondrules. *Geochimica et Cosmochimica Acta*, **54**, 3475-3490.
- Reed, S.J.B. (2005). *Electron microprobe analysis and scanning electron microscopy in geology*. 2nd edition, Cambridge University Press, Online ISBN: 9780511610561.
- Renner, H., Schlamp, G., Kleinwächter, I., *et al.* (2000). Platinum Group Metals and Compounds. *Ullmann's Encyclopedia of Industrial Chemistry*, Wiley-VCH Verlag GmbH & Co, Published Online: 05 December 2018, DOI: https://doi.org/10.1002/9783527306732.a21_075.pub2.
- Rochette, P., Sagnotti, L., Bourot-Denise, M., *et al.* (2003) Magnetic classification of stony meteorites: 1. Ordinary chondrites. *Meteoritics & Planetary Science*, **38**, 251-268.
- Ríos Muñoz, F., Peña Ramírez, C., Meza, J., Crouch, T. (2024). Platinum Group Metals Extraction from Asteroids vs Earth: An Overview of the Industrial Ecosystems, Technologies and Risks: Mineral economics-raw materials report. *Mineral Economics*, 1-20.

- Rubin, A., Ma, C. (2021). Meteorite mineralogy. Cambridge Planetary Science, Cambridge University Press. ISBN-10: 1108484522, ISBN-13: 978-1108484527, Online ISBN: 9781108613767, DOI: <https://doi.org/10.1017/9781108613767>.
- Russell, S.S., Connolly Jr, H.C., Krot, A.N., *et al.* (2018). Chondrules: Records of protoplanetary disk processes. Russell, S.S., Connolly Jr, H.C., Krot, A.N. (Eds.), Cambridge Planetary Science, Cambridge University Press. ISBN: 9781108418010, DOI: <https://doi.org/10.1017/9781108613767>
- Schindelin, J., Arganda-Carreras, I., Frise, E., *et al.* (2012). Fiji: an open-source platform for biological-image analysis. *Nature Methods*, **9**, 676-682.
- Schmitt, R.T. (2000). Shock experiments with the H6 chondrite Kernouvé: Pressure calibration of microscopic shock effects. *Meteoritics & Planetary Science*, **35**, 545-560.
- Sharp, T.G., Hu, J. (2019). Shock Veins in Meteorites: What They Tell Us About Shock Conditions. In: 82nd Annual Meeting of The Meteoritical Society, **82**, 2157, pp. 6463.
- Shelley, D., Nesse, W.D. (1986). Introduction to Optical Mineralogy. New York, Oxford (Oxford University Press), x+325 pp., ISBN: 9780199846283, Mineralogical Magazine (1987), **51**, 329-330. DOI: 10.1180/minmag.1987.051.360.21.
- Stevens, R.E. (1944). Composition of some chromites of the western hemisphere. *American Mineralogist*, **29**, 1-34.
- Stöffler, D., Hamann, C., Metzler, K. (2018). Shock metamorphism of planetary silicate rocks and sediments: Proposal for an updated classification system. *Meteoritics & Planetary Science*, **53**, 5-49.
- Stöffler, D., Keil, K., Scott, E.R.D. (1991). Shock metamorphism of ordinary chondrites. *Geochimica et Cosmochimica Acta*, **55**, 3845-3867.
- Stöffler, D., Grieve, R.A.F. (2007). Impactites, in: Fettes, D., Desmons, J. (Eds.), Metamorphic Rocks: A Classification and Glossary of Terms, Recommendations of the International Union of Geological Sciences, Cambridge University Press, Cambridge, UK, 82-92, 111-125, and 126-242, ISBN-10: 0521868106, ISBN-13: 978-0521868105.
- Tschauner, O., Ma, C., Spray, J.G., *et al.* (2021) Stöfflerite, (Ca, Na)(Si, Al)₄O₈ in the hollandite structure: A new high-pressure polymorph of anorthite from martian meteorite NWA 856. *American Mineralogist*, **106**, 650-655.
- Tsuda, Y., Yoshikawa, M., Abe, M., Minamino, H., Nakazawa, S. (2013). System design of the Hayabusa 2 - Asteroid sample return mission to 1999 JU3. *Acta Astronautica*, **91**, 356-362.
- Tomioka, N., Fujino, K. (1999). Akimotoite, (Mg, Fe) SiO₃, a new silicate mineral of the ilmenite group in the Tenham chondrite. *American Mineralogist*, **84**, 267-271.
- Tomioka, N., Miyahara, M., Ito, M. (2016). Discovery of natural MgSiO₃ tetragonal garnet in a shocked chondritic meteorite. *Science Advances*, **2**, e1501725.
- Tomioka, N., Miyahara, M. (2017). High-pressure minerals in shocked meteorites. *Meteoritics & Planetary Science*, **52**, 2017-2039.
- Van Schmus, W.R., Wood, J.A. (1967). A chemical-petrologic classification for the chondritic meteorites. *Geochimica et Cosmochimica Acta*, **31**, 747-765, (IN7-IN10, 755-765).
- Villeneuve, J., Libourel, G., Soulié, C. (2015). Relationships between type I and type II chondrules: Implications on chondrule formation processes. *Geochimica et Cosmochimica Acta*, **160**, 277-305.

- Wang, A., Jolliff, B.L., Haskin, L.A., *et al.* (2001). Characterization and comparison of structural and compositional features of planetary quadrilateral pyroxenes by Raman spectroscopy. *American Mineralogist*, **86**, 790-806.
- Weissman, P.R. (1995). The Kuiper belt. *Annual Review of Astronomy and Astrophysics*, **33**, 327-357.
- Weisberg, M.K., McCoy, T.J., Krot, A.N. (2006). Systematics and Evaluation of Meteorite Classification, in: Lauretta, D.S., McSween Jr., H.Y. (Eds.), *Meteorites and the Early Solar System II*, The University of Arizona Press, 19-52.
- Whitney, D.L., Evans, B.W. (2010). Abbreviations for names of rock-forming minerals. *American Mineralogist*, **95**, 185-187.
- Xiao, L., Qian, Y., Wang, Q., Wang, Q. (2021). The Chang'e-5 mission. In *Sample return missions* (pp. 195-206). Elsevier.
- Xie, X., Minitti, M.E., Chen, M., *et al.* (2002). Natural high-pressure polymorph of merrillite in the shock veins of the Suizhou meteorite. *Geochimica et Cosmochimica Acta*, **66**, 2439-2444.
- Xie, X., Minitti, M.E., Chen, M., *et al.* (2003). Tuite, γ -Ca₃(PO₄)₂: a new mineral from the Suizhou L6 chondrite. *European Journal of Mineralogy*, **15**, 1001-1005.
- Xie, X., Zhai, S., Chen, M., Yang, H. (2013). Tuite, γ -Ca₃(PO₄)₂, formed by chloroapatite decomposition in a shock vein of the Suizhou L6 chondrite. *Meteoritics & Planetary Science*, **48**, 1515-1523.
- Xie, X., Gu, X., Chen, M. (2016). An occurrence of tuite, γ -Ca₃(PO₄)₂, partly transformed from Ca-phosphates in the Suizhou meteorite. *Meteoritics & Planetary Science*, **51**, 195-202.
- Yoshikawa, M., Kawaguchi, J., Fujiwara, A., Tsuchiyama, A. (2021). Chapter 6 – The Hayabusa mission, in: *Sample Return Missions: The Last Frontier of Solar System Exploration*, Elsevier, pp. 123-146, DOI: 10.1016/B978-0-12-818330-4.00006-9
- Yoshikawa, M., Kawaguchi, J., Fujiwara, A., & Tsuchiyama, A. (2015). Hayabusa Sample Return Mission, in: Michel, P., F. E. DeMeo, W. F. Bottke, R. Dotson (Eds.), *Asteroids IV* (pp. 397–418). University of Arizona Press. <http://www.jstor.org/stable/j.ctt18gzdvc.27>
- Yurimoto H., Abe K, Abe, M., *et al.* (2011). Oxygen isotopic composition of asteroidal materials returned from Itokawa by the Hayabusa mission. *Science*, **333**, 1116-1119.
- Zhai, S., Akaogi, M., Kojitani, H., *et al.* (2014). Thermodynamic investigation on β - and γ -Ca₃(PO₄)₂ and the phase equilibria. *Physics of the Earth and Planetary Interiors*, **228**, 144-149.

7 APPENDIX

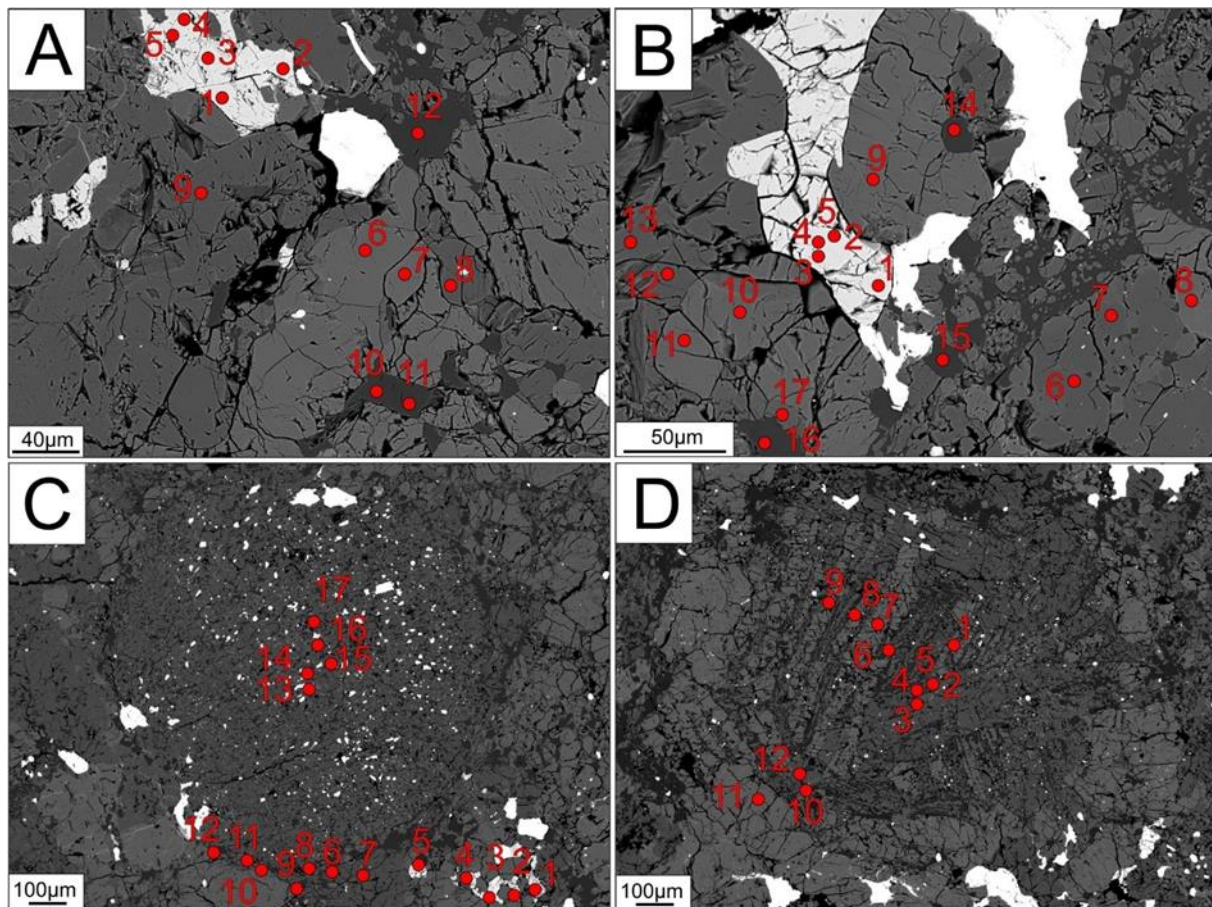


Figure A 1: BSE annotated images were taken for the Regions of interest B, C, D, and E respectively in the groundmass. Chemical composition of the annotated regions: (A) 1-5: olivine, 6 & 10-12: plagioclase, 7-9: pyroxene; (B) 1-5: chromite, 6-7, 12-13 & 17: pyroxene, 8-11: olivine, 14-16: plagioclase; (C) 1-5, 13-14 & 16: chromite, 6-9 & 11: plagioclase, 10-12: olivine, 15, 17: pyroxene; (D) 1-5: chromite, 6 & 7: olivine, 8 & 9: pyroxene, 10-12: plagioclase.

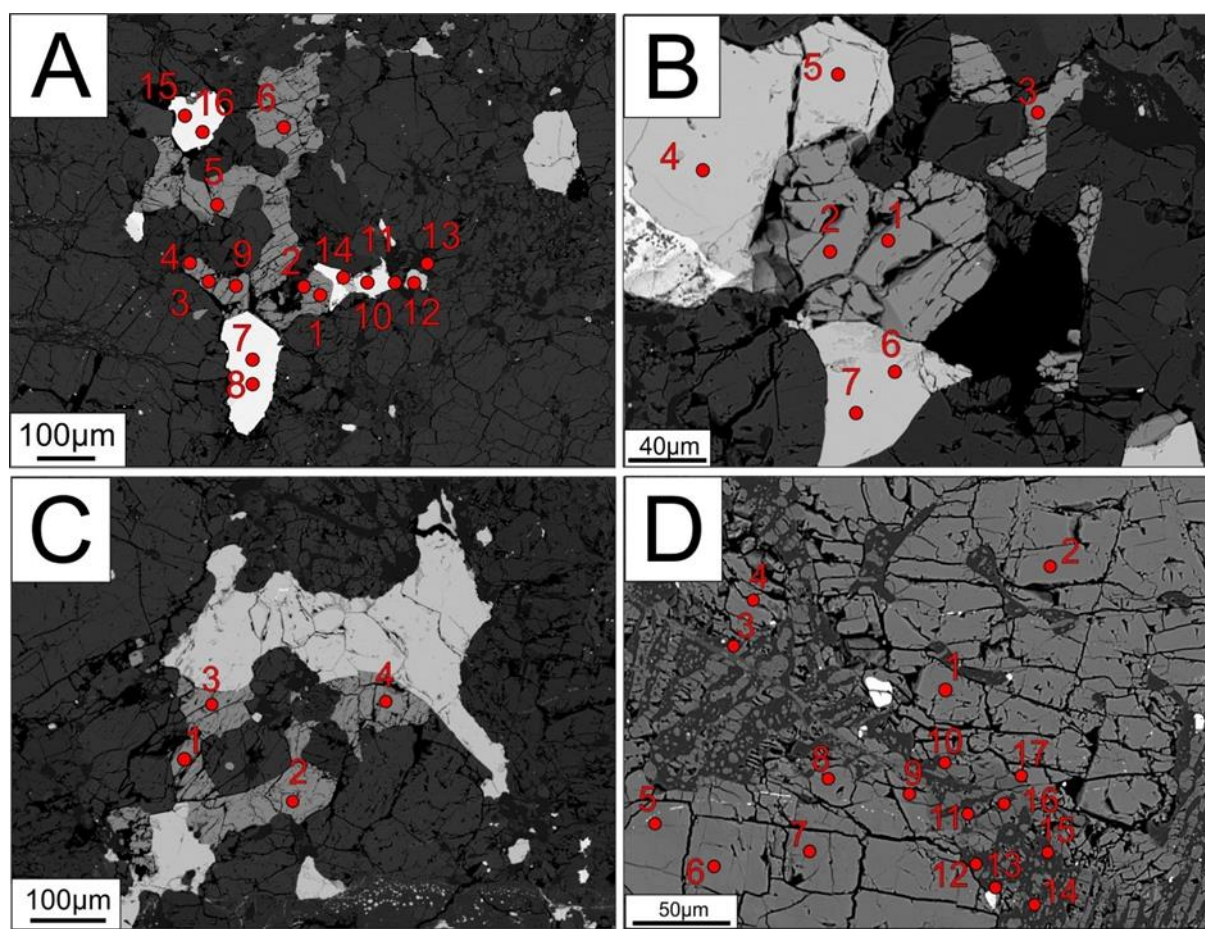


Figure A 2: BSE annotated images taken for the Regions of interest G, H, I, and J respectively in the groundmass. Chemical composition of the annotated regions: (A) 1-6 & 9: chromite, 7-8, 10-12 & 14-16: metal, 13: plagioclase; (B) 1-3: chromite, 4-7: FeS; (C) 1-4: chromite; (D) 1-2 & 5-9: olivine, 3 & 12-15: plagioclase.

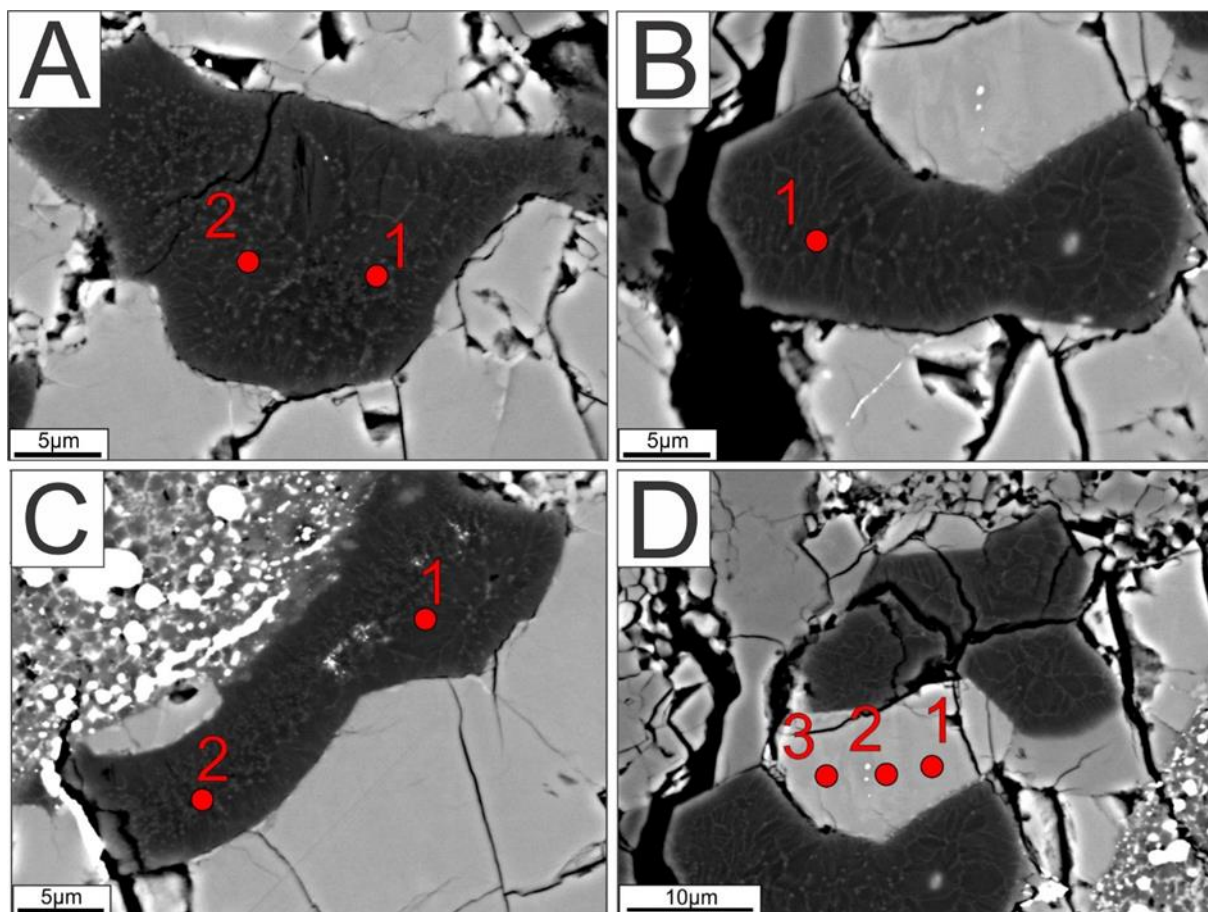


Figure A 3: BSE annotated images taken for the 2a, 2b, 2c and 2d positions respectively in the melt vein. Chemical composition of the annotated regions: (A) 1 & 2: plagioclase; (B) 1: plagioclase; (C) 1 & 2: plagioclase; (D) 1-3: olivine.

Table A 1: EPMA analysis of Olivine Group.

Olivine Group								
wt% oxides	B-Ol_1	B-Ol_2	C-Ol_1	C-Ol_2	C-Ol_3	C-Ol_4	D-Ol_1	D-Ol_2
SiO ₂	37.9	37.7	38	38.2	38.2	38.3	38.1	38.2
TiO ₂	0	0	0	0	0	0	0	0
Al ₂ O ₃	0	0	0	0	0	0	0	0
Cr ₂ O ₃	0	0	0	0.5	0.1	0	0	0
Fe ₂ O ₃	-	-	-	-	-	-	-	-
FeO	21.9	21.8	21.4	21.1	21	21.4	21.6	21.8
MnO	0.5	0.5	0.4	0.5	0.5	0.5	0.5	0.4
MgO	38.1	38.5	38.7	39.6	39.6	39.4	39	39
CaO	0	0	0	0	0	0	0	0
K ₂ O	0	0	0	0	0	0	0	0
Na ₂ O	0	0	0	0	0	0	0	0
NiO	0	0	0	0	0	0	0	0
P ₂ O ₅	0	0	0	0	0	0	0	0
Total	98.4	98.6	98.8	99.9	99.5	99.8	99.3	99.6
Numbers of ions based on 4 Oxygens								
Cations								
Si	1.001	0.995	1	0.992	0.994	0.996	0.996	0.997
Ti	0.001	0.001	0.001	0.001	0.001	0.001	0.001	0.001
Al	0	0	0	0	0	0	0	0
Cr	0.001	0	0	0.01	0.003	0.001	0.001	0
Fe(iii)	0	0	0	0	0	0	0	0
Fe(ii)	0.484	0.482	0.471	0.458	0.458	0.465	0.472	0.477
Mn	0.01	0.011	0.01	0.01	0.011	0.01	0.011	0.01
Mg	1.5	1.513	1.515	1.532	1.537	1.527	1.52	1.517
Ca	0.001	0	0.002	0	0.001	0.001	0.001	0.001
K	0	0	0	0	0	0	0	0
Na	0	0	0.001	0	0	0	0	0.001
Ni	0	0.001	0.001	0	0	0.001	0	0
P	0	0	0	0	0	0	0	0
Total cations	2.997	3.003	2.998	3.002	3.004	3.001	3.002	3.002
Total oxygens	3.999	3.999	3.999	4	4	3.998	4	3.999
Atomic percentages								
End member	mole %	mole %	mole %	mole %	mole %	mole %	mole %	mole %
Te*	0.5	0.6	0.5	0.5	0.5	0.5	0.6	0.5
Fo*	75.2	75.4	75.9	76.6	76.6	76.2	75.8	75.7
Fa*	24.3	24	23.6	22.9	22.8	23.2	23.5	23.8
Ca-Ol*	0.04	0.01	0.08	0.02	0.03	0.03	0.05	0.03
sum	100	100	100	100	100	100	100	100
Te* = $100 \cdot \text{Mn} / (\text{Mg} + \text{Mn} + \text{Ca} + \text{Fe(II)} + \text{Fe(III)})$ Fo* = $100 \cdot \text{Mg} / (\text{Mg} + \text{Mn} + \text{Ca} + \text{Fe(II)} + \text{Fe(III)})$ Fa* = $100 \cdot (\text{Fe(ii)} + \text{Fe(iii)}) / (\text{Mg} + \text{Mn} + \text{Ca} + \text{Fe(II)} + \text{Fe(III)})$ Ca-Ol* = $100 \cdot \text{Ca} / (\text{Mg} + \text{Mn} + \text{Ca} + \text{Fe(II)} + \text{Fe(III)})$								

Olivine Group							
wt% oxides	D-Ol_3	D-Ol_4	D-Ol_5	E-Ol_2	E-Ol_3	E-Ol_1	E-Ol_2
SiO ₂	38.3	38.1	38.1	38.2	38.2	38.3	38.6
TiO ₂	0	0	0	0	0	0	0
Al ₂ O ₃	0	0	0	0	0	0	0
Cr ₂ O ₃	0.1	0	0	0	0.1	0.1	0
Fe ₂ O ₃	-	-	-	-	-	-	-
FeO	22	21.4	21.6	21.1	21	21.6	21.4
MnO	0.5	0.4	0.4	0.4	0.4	0.4	0.4
MgO	39.1	38.9	39.5	39.1	39.1	38.9	38.5
CaO	0	0	0	0	0	0	0
K ₂ O	0	0	0	0	0	0	0
Na ₂ O	0	0	0	0	0	0	0
NiO	0	0	0	0	0	0.1	0
P ₂ O ₅	0	0.1	0	0.1	0.1	0	0
Total	100	99.1	99.7	99.1	99	99.5	99.1
Numbers of ions based on 4 Oxygens							
Cations							
Si	0.996	0.997	0.991	1	1	0.999	1.009
Ti	0.001	0.001	0.001	0.001	0.001	0	0.001
Al	0	0	0	0	0	0	0
Cr	0.002	0.001	0	0	0.002	0.002	0
Fe(iii)	0	0	0	0	0	0	0
Fe(ii)	0.478	0.469	0.47	0.461	0.458	0.471	0.468
Mn	0.01	0.01	0.009	0.009	0.01	0.01	0.01
Mg	1.514	1.52	1.534	1.524	1.525	1.514	1.499
Ca	0.001	0.001	0.001	0.001	0.001	0.001	0.001
K	0	0	0	0	0	0	0
Na	0	0	0.001	0.002	0	0	0.001
Ni	0	0	0.001	0	0	0.001	0
P	0	0.001	0	0.001	0.001	0	0
Total cations	3.002	2.998	3.006	2.996	2.996	2.998	2.989
Total oxygens	4	3.996	3.999	3.997	3.997	3.999	4
Atomic percentages							
End member	mole%	mole%	mole%	mole%	mole%	mole%	mole%
Te*	0.5	0.5	0.5	0.5	0.5	0.5	0.5
Fo*	75.6	76	76.1	76.4	76.5	75.9	75.8
Fa*	23.9	23.5	23.4	23.1	23	23.6	23.7
Ca-Ol*	0.03	0.07	0.04	0.04	0.04	0.05	0.05
sum	100	100	100	100	100	100	100

Olivine Group							
wt% oxides	E-Ol_3	E-Ol_4	F-Ol_rim_3	J1-Ol_1	J1-Ol_2	J1-Ol_3	J1-Ol_4
SiO ₂	38.3	37.9	37.3	38.5	38.5	38.2	38.1
TiO ₂	0	0	0	0	0	0	0
Al ₂ O ₃	0	0	0	0	0	0	0
Cr ₂ O ₃	0	0	0.1	0	0	0	0.1
Fe ₂ O ₃	-	-	-	-	-	-	-
FeO	21.9	21.6	21.4	21.8	21.5	21.8	21.9
MnO	0.5	0.5	0.5	0.4	0.4	0.5	0.4
MgO	38.9	38	38.9	39	38.9	39	38.8
CaO	0	0	0	0.1	0	0	0
K ₂ O	0	0	0	0	0	0	0
Na ₂ O	0	0	0	0	0	0	0
NiO	0	0.1	0	0	0	0	0
P ₂ O ₅	0	0	0	0	0	0	0
Total	99.6	98.1	98.1	99.7	99.5	99.6	99.5
Numbers of ions based on 4 Oxygens							
Cations							
Si	0.998	1.004	0.988	1.001	1.004	0.997	0.997
Ti	0.001	0.001	0.001	0	0.001	0	0
Al	0	0.001	0	0	0	0	0.001
Cr	0	0	0.001	0	0	0	0.002
Fe(iii)	0	0	0	0	0	0	0
Fe(ii)	0.477	0.478	0.474	0.475	0.469	0.476	0.478
Mn	0.011	0.011	0.01	0.009	0.01	0.011	0.01
Mg	1.513	1.5	1.536	1.511	1.511	1.517	1.511
Ca	0	0.001	0	0.002	0.001	0.001	0.001
K	0	0	0	0	0	0	0
Na	0.001	0	0	0.001	0.001	0	0.001
Ni	0	0.001	0.001	0	0	0	0.001
P	0	0	0	0	0	0	0
Total cations	3	2.994	3.01	2.998	2.994	3.002	2.999
Total oxygens	3.999	3.999	3.999	3.999	3.999	3.999	3.998
Atomic percentages							
End member	mole%	mole%	mole%	mole%	mole%	mole%	mole%
Te*	0.5	0.5	0.5	0.5	0.5	0.5	0.5
Fo*	75.6	75.4	76	75.7	75.9	75.7	75.6
Fa*	23.9	24	23.4	23.8	23.6	23.8	23.9
Ca-Ol*	0	0.03	0.01	0.08	0.04	0.03	0.06
sum	100	100	100	100	100	100	100

Olivine Group							
wt% oxides	J1-Ol_5	J1-Ol_6	J1-Ol_7	J1-Ol_8	MV2d-Ol_1	MV2d-Ol_2	MV2d-Ol_3
SiO ₂	38.5	38.6	38.1	38.1	38.2	38.1	38.2
TiO ₂	0	0	0	0	0	0	0
Al ₂ O ₃	0	0	0	0	0	0	0
Cr ₂ O ₃	0	0	0	0	0	0	0
Fe ₂ O ₃	-	-	-	-	-	-	-
FeO	21.6	21.7	21.5	21.2	21.4	21.3	21.5
MnO	0.4	0.5	0.5	0.5	0.4	0.5	0.4
MgO	38.7	39.1	38.9	38.6	38.6	38.6	38.3
CaO	0	0	0	0.2	0.1	0.1	0.1
K ₂ O	0	0	0	0	0	0	0
Na ₂ O	0	0	0	0	0	0	0
NiO	0	0	0	0	0	0	0
P ₂ O ₅	0	0	0	0	0	0	0.1
Total	99.3	99.9	99.1	98.6	99	98.8	98.7
Numbers of ions based on 4 Oxygens							
Cations							
Si	1.005	1.002	0.999	1.002	1.002	1.001	1.004
Ti	0.001	0.001	0.001	0.001	0.001	0.001	0.001
Al	0	0	0	0	0.001	0.001	0
Cr	0	0	0	0	0.001	0.001	0.001
Fe(iii)	0	0	0	0	0	0	0
Fe(ii)	0.471	0.471	0.471	0.465	0.47	0.467	0.473
Mn	0.01	0.011	0.01	0.01	0.009	0.01	0.01
Mg	1.506	1.512	1.518	1.513	1.507	1.51	1.5
Ca	0.001	0	0.001	0.004	0.003	0.004	0.003
K	0	0	0	0	0	0	0
Na	0	0.001	0	0.001	0	0	0.001
Ni	0	0	0	0	0.001	0.001	0
P	0	0	0	0	0	0	0.001
Total cations	2.993	2.997	3	2.996	2.994	2.996	2.991
Total oxygens	4	3.999	4	3.998	3.998	3.998	3.997
Atomic percentages							
End member	mole%	mole %	mole%	mole%	mole%	mole%	mole%
Te*	0.5	0.5	0.5	0.5	0.5	0.5	0.5
Fo*	75.8	75.9	75.9	75.9	75.7	75.8	75.5
Fa*	23.7	23.6	23.5	23.4	23.6	23.4	23.8
Ca-Ol*	0.03	0	0.05	0.22	0.16	0.2	0.14
sum	100	100	100	100	100	100	100

Table A 2: EPMA analysis of Pyroxene Group.

Pyroxene Group							
wt% oxides	B-Px_1	B-Px_2	C-Px_1	C-Px_2	C-Px_3	C-Px_4	C-Px_5
SiO ₂	54.9	54.5	55.5	55.5	55.5	55.2	53.5
Al ₂ O ₃	0.2	0.2	0.1	0.2	0.1	0.2	0.4
NiO	0	0	0	0	0	0	0
Cr ₂ O ₃	0.1	0.2	0.1	0.1	0.1	0.1	0.6
CaO	0.6	0.9	0.7	2.3	0.9	0.9	23
TiO ₂	0.2	0.2	0.2	0.2	0.2	0.2	0.5
FeO	13.5	13.2	13.2	12.2	13.2	13.2	4.5
MnO	0.4	0.5	0.5	0.4	0.5	0.4	0.2
MgO	28.6	28.4	28.9	27.9	29.1	29.2	16.7
K ₂ O	0	0	0	0	0	0	0
P ₂ O ₅	0	0	0	0	0	0	0.1
Na ₂ O	0	0	0	0.1	0	0	0.5
Total	98.6	98.2	99.1	99.1	99.7	99.4	100.2
Numbers of ions based on 6 Oxygens							
Cations							
Si	1.991	1.985	1.996	2.003	1.986	1.979	1.954
Al	0.007	0.007	0.006	0.008	0.006	0.006	0.019
Ni	0	0.001	0	0	0	0.001	0
Cr	0.003	0.006	0.002	0.004	0.002	0.004	0.018
Ca	0.024	0.036	0.025	0.09	0.034	0.035	0.9
Ti	0.007	0.005	0.005	0.006	0.006	0.006	0.013
Fe(ii)	0.41	0.403	0.397	0.369	0.395	0.395	0.136
Mn	0.014	0.015	0.015	0.013	0.014	0.013	0.008
Mg	1.544	1.542	1.551	1.501	1.554	1.559	0.912
K	0	0	0	0	0	0	0
P	0	0	0	0	0	0	0.002
Na	0.001	0.001	0.001	0.006	0.001	0.001	0.038
Total cations	4	4	4	4	4	4	4
Total oxygens	6.002	5.997	6.005	6.012	5.996	5.99	5.969
Atomic percentages							
End member	mole%	mole%	mole%	mole%	mole%	mole%	mole%
Wo*	1.2	1.8	1.3	4.6	1.7	1.8	46.2
En*	78	77.9	78.6	76.6	78.4	78.4	46.8
Fs*	20.7	20.3	20.1	18.8	19.9	19.8	7
total	100	100	100	100	100	100	100
Wo*=Ca/(Ca+Mg+Fe(II)) Si, Al assigned to tetrahedral (T) site En*= Mg/(Ca+Mg+Fe(II)) Ca,Na,Mn,Fe ²⁺ ,Mg assigned to M2 octahedral site Fe ³⁺ ,Ti,Al,Fe ²⁺ , Mg assigned to M1 octahedral site Fs*= Fe(II)/(Ca+Mg+Fe(II)) (Fe ²⁺ /Mg) assumed the same in M1 and M2							

Pyroxene Group								
wt% oxides	C-Px_6	D-Px_1	D-Px_2	D-Px_4	D-Px_5	D-Px_6	D-Px_7	D-Px_8
SiO ₂	55.2	55.1	55.2	54.2	55.4	55.1	55.2	54.5
Al ₂ O ₃	0.1	0.2	0.1	0.5	0.2	0.1	0.1	0.3
NiO	0	0	0	0	0	0	0	0
Cr ₂ O ₃	0.1	0.1	0.2	0.9	0.1	0.1	0.1	0.7
CaO	0.8	0.8	0.8	22	0.6	0.7	0.7	22.3
TiO ₂	0.2	0.2	0.2	0.5	0.2	0.2	0.2	0.3
FeO	13.3	13.3	12.9	4.9	13.4	13.6	13.5	5
MnO	0.5	0.5	0.5	0.3	0.5	0.5	0.5	0.2
MgO	29.3	28.4	28.7	16.5	29.1	29.6	29.6	17
K ₂ O	0	0	0	0	0	0	0	0
P ₂ O ₅	0	0	0	0.1	0	0	0	0.1
Na ₂ O	0	0	0	0.5	0	0	0	0.6
Total	99.7	98.5	98.7	100.5	99.4	100	100	100.9
Numbers of ions based on 6 Oxygens								
Cations								
Si	1.974	1.998	1.996	1.98	1.987	1.964	1.968	1.975
Al	0.006	0.007	0.006	0.021	0.007	0.005	0.005	0.014
Ni	0	0	0.001	0	0	0	0.001	0
Cr	0.003	0.003	0.006	0.026	0.002	0.003	0.003	0.02
Ca	0.031	0.03	0.031	0.863	0.025	0.027	0.028	0.867
Ti	0.006	0.006	0.006	0.013	0.005	0.005	0.005	0.007
Fe(ii)	0.398	0.403	0.391	0.149	0.401	0.405	0.401	0.151
Mn	0.014	0.015	0.014	0.008	0.016	0.015	0.015	0.007
Mg	1.564	1.534	1.548	0.9	1.554	1.573	1.573	0.917
K	0	0	0	0	0	0	0	0.001
P	0	0	0	0.002	0	0	0	0.001
Na	0.002	0.003	0.001	0.037	0.001	0.002	0	0.039
Total cations	4	4	4	4	4	4	4	4
Total oxygens	5.984	6.008	6.007	6.002	5.996	5.973	5.976	5.981
Atomic percentage								
End member	mole%	mole%	mole%	mole%	mole%	mole%	mole%	mole%
Wo*	1.6	1.5	1.6	45.1	1.3	1.3	1.4	44.8
En*	78.5	78	78.6	47.1	78.5	78.4	78.6	47.4
Fs*	20	20.5	19.9	7.8	20.3	20.2	20	7.8
SUM	100	100	100	100	100	100	100	100

Pyroxene Group						
wt% oxide	E-Px_1	E-Px_4	E-Px_5	E-Px_6	E-Px_7	F-Px_nearOl_8
SiO ₂	55.9	54.7	54.8	55.1	55.1	55.3
Al ₂ O ₃	0.2	0.2	0.2	0.1	0.1	0.1
NiO	0	0	0	0.1	0	0
Cr ₂ O ₃	0.1	0.2	0.1	0.1	0.1	0.2
CaO	0.6	0.8	0.7	0.6	0.7	0.6
TiO ₂	0.2	0.2	0.2	0.2	0.2	0.2
FeO	13.5	13.3	13.2	13.2	13.2	13.4
MnO	0.5	0.5	0.5	0.5	0.5	0.5
MgO	29.1	29	28.4	28.5	28.9	29.2
K ₂ O	0	0	0	0	0	0
P ₂ O ₅	0	0.2	0	0	0	0
Na ₂ O	0	0.1	0	0	0	0
Total	100.1	99.1	98.1	98.4	98.8	99.6
Numbers of ions based on 6 Oxygens						
Cations						
Si	1.994	1.972	1.994	2.001	1.992	1.983
Al	0.007	0.007	0.006	0.006	0.005	0.005
Ni	0	0	0	0.002	0	0
Cr	0.003	0.004	0.004	0.004	0.002	0.005
Ca	0.025	0.031	0.028	0.023	0.026	0.024
Ti	0.006	0.006	0.006	0.005	0.005	0.006
Fe(ii)	0.402	0.401	0.402	0.401	0.398	0.403
Mn	0.014	0.014	0.015	0.014	0.016	0.014
Mg	1.55	1.559	1.544	1.544	1.554	1.559
K	0	0	0	0	0	0
P	0	0.003	0	0	0	0
Na	0	0.003	0.001	0	0.001	0
Total cations	4	4	4	4	4	4
Total oxygens	6.004	5.985	6.005	6.011	6.001	5.994
Atomic percentages						
End member	mole%	mole%	mole%	mole%	mole%	mole%
Wo*	1.2	1.6	1.4	1.2	1.3	1.2
En*	78.4	78.3	78.2	78.5	78.6	78.5
Fs*	20.3	20.1	20.4	20.4	20.1	20.3
sum	100	100	100	100	100	100

Pyroxene Group					
wt% oxides	J1-Cpx_2	J1-Cpx_3	J1-Cpx_4	J1-Cpx_5	J1-Cpx_6
SiO ₂	54	55.2	55.6	54.6	55.3
Al ₂ O ₃	0.6	0.4	0.1	0.5	0.2
NiO	0	0	0	0	0
Cr ₂ O ₃	0.7	0.5	0.1	0.7	0.1
CaO	22.4	15.7	0.8	22.8	0.7
TiO ₂	0.5	0.4	0.2	0.5	0.2
FeO	4.1	8.2	13.4	4.1	13.2
MnO	0.2	0.3	0.5	0.3	0.5
MgO	16.5	19.3	29.2	16.7	29.4
K ₂ O	0	0	0	0	0
P ₂ O ₅	0.2	0	0	0.1	0
Na ₂ O	0.6	0.3	0	0.5	0
Total	99.8	100.3	100	100.7	99.5
Numbers of ions based on 6 Oxygens					
Cations					
Si	1.982	2.012	1.985	1.984	1.979
Al	0.024	0.016	0.006	0.021	0.006
Ni	0	0	0	0.001	0
Cr	0.021	0.015	0.003	0.019	0.002
Ca	0.88	0.615	0.031	0.889	0.027
Ti	0.015	0.011	0.006	0.013	0.006
Fe(ii)	0.126	0.249	0.4	0.124	0.394
Mn	0.007	0.009	0.015	0.008	0.015
Mg	0.901	1.05	1.553	0.904	1.57
K	0	0	0.001	0.001	0
P	0.002	0.001	0	0.001	0
Na	0.041	0.022	0	0.035	0.001
Total cations	4	4	4	4	4
Total oxygens	6.002	6.028	5.995	6.001	5.988
Atomic percentages					
End member	mole%	mole%	mole%	mole%	mole%
Wo*	46.2	32.1	1.6	46.4	1.3
En*	47.2	54.9	78.3	47.2	78.9
Fs*	6.6	13	20.2	6.5	19.8
sum	100	100	100	100	100

Table A 3: EPMA analysis of Plagioclase Group.

Plagioclase Group							
wt% oxides	B-Pl_1	B-Pl_2	B-Pl_3	C-Pl_1	C-Pl_2	C-Pl_3	D-Pl_1
SiO₂	65	64.8	65.8	65.7	66.1	66.8	65.5
TiO₂	0.1	0.1	0.1	0.1	0.1	0.1	0.1
Al₂O₃	22.7	22.6	22.9	22.4	22.4	22.1	22.2
Cr₂O₃	0	0	0	0	0	0	0
FeO	0.4	0.5	0.5	0.9	0.6	0.5	0.5
MnO	0	0	0	0	0	0	0
MgO	0	0	0	0	0	0	0
CaO	2.3	2.2	2.3	2.2	2.3	2.2	2.3
Na₂O	9.3	9	8.6	8.2	7.3	7.8	9.7
K₂O	1	1.3	1.1	1.1	1.1	1	0.8
NiO	0	0	0	0	0	0	0
P₂O₅	0	0	0	0	0	0	0
Total	100.8	100.6	101.3	100.7	99.8	100.5	101.1
Number of ions based on 8 Oxygens							
Cations							
Si	2.852	2.856	2.89	2.914	2.977	2.98	2.861
Ti	0.002	0.002	0.003	0.003	0.002	0.002	0.003
Al	1.172	1.176	1.187	1.171	1.187	1.163	1.141
Cr	0	0	0	0	0	0	0
Fe(ii)	0.016	0.019	0.019	0.035	0.022	0.02	0.018
Mn	0	0	0	0	0	0	0
Mg	0.003	0.003	0.002	0.003	0.002	0.002	0.002
Ca	0.106	0.105	0.106	0.106	0.112	0.106	0.107
Na	0.793	0.767	0.733	0.703	0.637	0.671	0.821
K	0.055	0.072	0.06	0.065	0.06	0.057	0.046
Ni	0	0.001	0.001	0.001	0	0	0.001
P	0	0	0	0	0	0	0
Total cations	5	5	5	5	5	5	5
Total oxygens	8.017	8.027	8.089	8.119	8.224	8.2	8
Atomic percentage							
End member	mole %	mole%	mole%	mole%	mole%	mole%	mole%
An*	11.1	11.1	11.8	12.1	13.8	12.7	11
Ab*	83.1	81.3	81.5	80.5	78.7	80.5	84.3
Or*	5.7	7.6	6.6	7.4	7.5	6.8	4.7
Total	100	100	100	100	100	100	100
An* = Ca/(Ca+Na+K) Ab* = Na/(Na+Ca+K) Or* = K/(K+Na+Ca)							

Plagioclase Group								
wt% oxides	D-Pl_2	D-Pl_3	D-Pl_4	E-Pl_1	E-Pl_2	F-Pl_1	F-Pl_2	J1-Pl_1
SiO ₂	66.3	66.2	65.5	66	65.8	66.4	66.8	66.7
TiO ₂	0	0.1	0.1	0.1	0.1	0.1	0.1	0.1
Al ₂ O ₃	22.8	22.7	22.1	22.7	22.7	22.4	22.3	21.9
Cr ₂ O ₃	0	0	0.1	0	0	0	0	0
FeO	0.4	0.5	0.3	0.5	0.3	0.2	0.2	0.5
MnO	0	0	0	0	0	0	0	0
MgO	0	0	0	0	0.1	0	0	0.5
CaO	2.3	2.3	2.3	2.4	2.4	2.2	2.4	3
Na ₂ O	7.8	7.9	8.1	8.9	7.8	7.5	8.4	4.3
K ₂ O	1.2	1.4	1.4	0.8	1.3	1.2	0.9	1
NiO	0	0	0	0	0	0	0	0
P ₂ O ₅	0	0	0	0	0	0	0	0.1
Total	101	101.1	99.9	101.4	100.5	100.2	101.1	97.9
Number of ions based on 8 Oxygens								
Cations								
Si	2.94	2.931	2.928	2.89	2.928	2.973	2.944	3.13
Ti	0.002	0.003	0.002	0.003	0.002	0.003	0.003	0.003
Al	1.193	1.183	1.164	1.174	1.188	1.18	1.158	1.211
Cr	0.001	0	0.002	0	0	0.001	0	0.001
Fe(ii)	0.014	0.019	0.011	0.018	0.012	0.009	0.007	0.018
Mn	0.001	0	0.001	0	0	0	0	0
Mg	0.002	0.001	0.001	0.002	0.005	0.001	0.002	0.036
Ca	0.111	0.108	0.108	0.114	0.115	0.108	0.114	0.151
Na	0.671	0.675	0.7	0.753	0.676	0.655	0.721	0.391
K	0.066	0.081	0.082	0.046	0.074	0.069	0.051	0.057
Ni	0	0	0	0.001	0	0	0.001	0
P	0	0	0	0	0.001	0	0	0.002
Total cations	5	5	5	5	5	5	5	5
Total oxygens	8.17	8.147	8.122	8.08	8.15	8.205	8.139	8.517
Atomic percentage								
End member	mole%	mole%	mole%	mole%	mole%	mole%	mole%	mole%
An*	13	12.5	12.2	12.5	13.3	13	12.9	25.2
Ab*	79.2	78.2	78.6	82.5	78.2	78.7	81.4	65.3
Or*	7.8	9.4	9.2	5	8.6	8.3	5.8	9.5
Total	100	100	100	100	100	100	100	100

Plagioclase Group								
wt% oxides	J1-Pl_2	J1-Pl_3	J1-Pl_4	MV2a-Pl_1	MV2a-Pl_2	MV2c-Pl_1	MV2c-Pl_2	MV2b-Pl_1
SiO ₂	64.7	66.2	67.4	64.8	65	64.9	65.7	65.4
TiO ₂	0.1	0.1	0.1	0.1	0	0	0.1	0.1
Al ₂ O ₃	18.8	20.3	22.2	21.8	22	22	22.2	21.9
Cr ₂ O ₃	0.1	0.1	0	0	0	0	0	0
FeO	2.2	0.8	0.6	0.6	0.6	0.6	0.7	0.5
MnO	0	0	0	0	0	0	0	0
MgO	1.7	1.5	0.2	0.1	0.1	0.1	0.2	0.1
CaO	5.1	4.1	2.6	2	2.1	2.2	2.2	2.1
Na ₂ O	2.7	3.3	4.4	10.5	9.8	10.5	10.2	10
K ₂ O	1	0.9	1	0.9	1	0.8	0.8	0.8
NiO	0	0	0	0	0	0	0	0
P ₂ O ₅	0.4	0	0.1	0	0	0	0	0
Total	96.8	97.2	98.5	100.7	100.6	101.1	102.1	101
Number of ions based on 8 Oxygens								
Cations								
Si	3.125	3.151	3.152	2.821	2.846	2.815	2.832	2.85
Ti	0.005	0.002	0.002	0.002	0.001	0.001	0.002	0.002
Al	1.073	1.137	1.221	1.119	1.135	1.125	1.13	1.127
Cr	0.004	0.004	0.001	0	0	0.001	0	0
Fe(ii)	0.091	0.03	0.024	0.021	0.023	0.022	0.026	0.018
Mn	0.001	0.002	0.001	0	0	0	0.001	0.001
Mg	0.122	0.105	0.011	0.005	0.005	0.005	0.014	0.005
Ca	0.262	0.208	0.129	0.096	0.097	0.103	0.1	0.1
Na	0.249	0.304	0.397	0.887	0.834	0.881	0.852	0.848
K	0.059	0.055	0.058	0.049	0.058	0.047	0.043	0.046
Ni	0	0	0.001	0.001	0	0.001	0	0.001
P	0.008	0.001	0.002	0	0	0	0	0
Total cations	5	5	5	5	5	5	5	5
Total oxygens	8.527	8.546	8.541	7.914	7.968	7.916	7.952	7.969
Atomic percentage								
End member	mole%	mole%	mole%	mole%	mole%	mole%	mole%	mole%
An*	45.9	36.6	22	9.3	9.8	10	10	10.1
Ab*	43.7	53.7	68	86	84.3	85.5	85.6	85.3
Or*	10.4	9.7	10	4.7	5.9	4.5	4.3	4.6
Total	100	100	100	100	100	100	100	100

Table A 4: EPMA analysis of Spinel Group.

Spinel Group							
wt% oxides	E_Chtr_2	E_Chtr_3	D_Chtr_1	D_Chtr_2	D_Chtr_3	D_Chtr_4	D_Chtr_5
SiO₂	0	0	0	0	0	0	0
Al₂O₃	5.9	5.7	6.1	5.9	6	5.8	6.1
NiO	0	0	0.1	0.1	0	0	0
Cr₂O₃	56.6	55.8	57.3	57.6	57.6	57.6	57.7
TiO₂	2.8	2.9	2.4	2.3	2.3	2.7	2.1
FeO	30.3	30.4	30.2	30.6	30.7	30.6	29.9
MnO	0.5	0.5	0.6	0.5	0.6	0.6	0.5
MgO	2.6	2.5	2.4	2.4	2.5	2.5	2.4
Na₂O	0	0	0.1	0	0	0	0
V₂O₃	0.7	0.7	0.8	0.8	0.8	0.8	0.8
ZnO	0.2	0.3	0.3	0.4	0.3	0.4	0.3
Total	99.7	98.9	100.3	100.4	100.7	101	99.9
Number of ions based on 4 Oxygens							
Cations							
Si	0.003	0.001	0.001	0	0	0.001	0
Al	0.365	0.379	0.367	0.371	0.362	0.385	0.373
Ni	0	0.003	0.001	0	0	0	0.001
Cr	2.377	2.404	2.418	2.408	2.405	2.432	2.416
Ti	0.158	0.13	0.121	0.123	0.143	0.112	0.125
Fe(ii)	0.913	0.895	0.906	0.904	0.902	0.889	0.896
Mn	0.016	0.018	0.016	0.017	0.016	0.017	0.019
Mg	0.135	0.129	0.125	0.134	0.133	0.127	0.128
Na	0	0.002	0	0.001	0	0.001	0
V	0.029	0.034	0.035	0.033	0.033	0.035	0.034
Zn	0.008	0.009	0.009	0.007	0.011	0.008	0.011
Total cations	3	3	3	3	3	3	3
Total oxygens	4.004	4.003	4	3.998	4.005	4.006	4.003

Spinel Group							
wt% oxides	C_Chrr_1	C_Chrr_2	C_Chrr_3	C_Chrr_4	B_Chrr_1	B_Chrr_2	B_Chrr_3
SiO₂	0	0	0	0	0	0	0
Al₂O₃	5.9	5.8	5.7	5.7	6	6.2	5.9
NiO	0	0	0.1	0	0.1	0	0
Cr₂O₃	57.4	58.1	56.7	57.9	56.8	58	57.3
TiO₂	2.3	2.9	2.9	3	2.6	1.9	2.6
FeO	30.2	30.4	30.5	30.6	30.4	30.4	30.5
MnO	0.6	0.6	0.6	0.6	0.5	0.6	0.6
MgO	2.4	2.6	2.6	2.5	2.5	2.5	2.6
Na₂O	0	0	0	0	0	0	0
V₂O₃	0.8	0.8	0.8	0.8	0.9	0.9	0.8
ZnO	0.4	0.2	0.3	0.3	0.4	0.4	0.2
Total	100.3	101.5	100.2	101.3	100.2	100.9	100.6
Number of ions based on 4 Oxygens							
Cations							
Si	0	0	0	0	0.002	0	0.001
Al	0.357	0.359	0.352	0.375	0.383	0.369	0.355
Ni	0.001	0.001	0	0.003	0.001	0	0.002
Cr	2.416	2.387	2.412	2.39	2.42	2.4	2.375
Ti	0.151	0.157	0.156	0.139	0.101	0.138	0.136
Fe(ii)	0.892	0.905	0.898	0.902	0.893	0.899	0.931
Mn	0.017	0.018	0.016	0.015	0.017	0.018	0.016
Mg	0.137	0.135	0.133	0.131	0.131	0.139	0.134
Na	0	0	0.001	0	0.001	0	0
V	0.034	0.035	0.035	0.036	0.036	0.035	0.033
Zn	0.006	0.008	0.007	0.011	0.01	0.006	0.006
Total cations	3	3	3	3	3	3	3
Total oxygens	4.011	4.006	4.011	4.003	3.997	4.004	3.989

Spinel Group							
wt% oxides	B_Ch_4	B_Ch_5	G_Ch_1	G_Ch_2	G_Ch_3	G_Ch_4	G_Ch_5
SiO₂	0	0	0	0	0	0	0
Al₂O₃	5.6	5.9	5.8	6.1	5.7	5.7	5.5
NiO	0.1	0	0	0	0.1	0.1	0
Cr₂O₃	56.3	57.4	58.3	57	57	56.6	57
TiO₂	2.5	2.6	2.5	2.6	2.9	2.7	3.1
FeO	31.3	30.1	30	29.6	30.5	29.9	30.3
MnO	0.5	0.5	0.6	0.6	0.6	0.5	0.5
MgO	2.5	2.6	2.5	2.1	2.6	2.6	2.5
Na₂O	0	0	0	0	0	0	0
V₂O₃	0.8	0.8	0.8	0.7	0.8	0.8	0.7
ZnO	0.2	0.4	0.3	0.2	0.2	0.3	0.3
Total	99.9	100.3	100.8	99	100.3	99.3	100
Number of ions based on 4 Oxygens							
Cations							
Si	0	0	0	0	0.002	0	0.001
Al	0.368	0.359	0.39	0.357	0.361	0.346	0.341
Ni	0.001	0.001	0	0.002	0.003	0	0.003
Cr	2.412	2.44	2.43	2.394	2.402	2.408	2.398
Ti	0.139	0.132	0.143	0.155	0.144	0.165	0.164
Fe(ii)	0.892	0.885	0.891	0.905	0.895	0.902	0.902
Mn	0.016	0.017	0.017	0.018	0.016	0.015	0.015
Mg	0.136	0.131	0.111	0.135	0.137	0.134	0.141
Na	0	0.001	0.001	0	0.001	0	0.001
V	0.034	0.036	0.031	0.033	0.034	0.032	0.033
Zn	0.01	0.008	0.007	0.006	0.009	0.009	0.007
Total cations	3	3	3	3	3	3	3
Total oxygens	4.007	4.01	4.021	4.006	4.005	4.011	4.006

Spinel Group								
wt% oxides	G_Chrr_6	H_Chrr_1	H_Chrr_2	H_Chrr_3	I_Chrr_1	I_Chrr_2	I_Chrr_3	I_Chrr_4
SiO ₂	0	0	0	0	0	0	0	0
Al ₂ O ₃	5.5	5.8	5.9	5.7	5.8	5.7	5.9	5.9
NiO	0.1	0	0	0	0	0.1	0	0
Cr ₂ O ₃	57.3	57	57.5	55.9	56.1	57.5	57.5	57.5
TiO ₂	3.1	2.8	2.8	2.7	2.8	3	2.6	2.7
FeO	30.6	30.2	30.1	30.2	30.6	30.2	30.2	30.2
MnO	0.5	0.5	0.6	0.6	0.6	0.6	0.6	0.6
MgO	2.7	2.7	2.6	2.6	2.6	2.6	2.5	2.5
Na ₂ O	0	0	0	0	0	0	0	0
V ₂ O ₃	0.8	0.8	0.9	0.7	0.8	0.7	0.8	0.8
ZnO	0.3	0.3	0.3	0.3	0.3	0.4	0.4	0.3
Total	100.8	100.1	100.7	98.7	99.6	100.8	100.5	100.6
Number of ions based on 4 Oxygens								
Cations								
Si	0.001	0	0	0	0	0	0	0
Al	0.341	0.362	0.37	0.365	0.364	0.355	0.368	0.369
Ni	0.003	0.001	0	0	0	0.002	0	0
Cr	2.398	2.4	2.406	2.382	2.373	2.406	2.411	2.413
Ti	0.164	0.149	0.147	0.144	0.152	0.16	0.14	0.145
Fe(ii)	0.902	0.896	0.889	0.908	0.911	0.891	0.894	0.892
Mn	0.015	0.016	0.017	0.017	0.018	0.017	0.017	0.017
Mg	0.141	0.141	0.136	0.142	0.138	0.137	0.131	0.132
Na	0.001	0	0	0	0	0.001	0	0
V	0.033	0.033	0.037	0.032	0.033	0.032	0.035	0.035
Zn	0.007	0.009	0.008	0.008	0.009	0.01	0.009	0.009
Total cations	3	3	3	3	3	3	3	3
Total oxygens	4.006	4.006	4.011	3.998	3.999	4.009	4.008	4.011

Table A 5: EPMA analysis of Metal Group

Metal Group					
wt%	G_Metal_4	G_Metal_5	G_Metal_1	G_Metal_2	G_Metal_4
P	0	0	0	0	0
Si	0	0	0	0	0
Ni	6	6	26.9	26.6	28.5
Fe	94.2	93.7	73.1	73.7	72.3
Mn	0	0	0	0	0
S	0	0	0	0	0
Ti	0	0	0	0	0
Co	0.7	0.8	0.3	0.3	0.2
Cr	0	0	0	0	0
Total	101	100.5	100.3	100.7	101.1
Cations					
Co	0.007	0.007	0.002	0.003	0.002
Ni	0.057	0.057	0.259	0.255	0.272
Fe	0.936	0.935	0.739	0.742	0.726
Total	1	1	1	1	1

Metal Group				
wt%	G_Metal_5	H_Metal_1	H_Metal_2	H_Metal_3
P	0	0	0	0
Si	0	0	0	0
Ni	29.7	28.4	27.9	29.2
Fe	70.7	71.9	73.0	71.0
Mn	0	0	0	0
S	0	0	0	0
Ti	0	0.1	0.1	0
Co	0.3	0.2	0.3	0.3
Cr	0.1	0	0	0
Total	100.8	100.6	101.3	100.4
Cations				
Co	0.002	0.002	0.002	0.002
Ni	0.285	0.273	0.266	0.28
Fe	0.712	0.725	0.731	0.717
Total	1	1	1	1

Table A 6: EPMA analysis of Sulfide Group.

Sulfide Group						
wt%	G_FeS_1	G_FeS_3	H_FeS_1	H_FeS_2	H_FeS_3	H_FeS_4
P	0	0	0	0	0	0
Si	0	0	0	0	0	0
Ni	0	0.2	0	0	0	0
Fe	63.6	62.8	63.4	64	63.7	63.8
Mn	0	0	0	0	0	0
S	35.1	35.2	35	35.3	35.2	35.3
Ti	0	0	0	0	0	0
Co	0	0	0.1	0	0.1	0
Cr	0	0.1	0.1	0.1	0.1	0
Total	98.9	98.3	98.4	99.3	99	99.2
Cations						
Fe	1.019	1.011	1.019	1.02	1.019	1.018
S	0.979	0.985	0.979	0.98	0.98	0.981
Total	2	2	2	2	2	2

Table A 7: Homogeneity of olivine composition.

Calculation for the Fa homogeneity					
Point	Comment	Fa(mole%)	Point	Comment	Fa(mole%)
126	B-Ol_1	24.2	168	E-Ol_3	23.9
127	B-Ol_2	24	172	E-Ol_4	24.1
135	C-Ol_1	23.9	176	F-Ol_rim_5	23.4
136	C-Ol_2	22.9	180	J1-Ol_1	23.8
137	C-Ol_3	22.8	181	J1-Ol_2	23.6
138	C-Ol_4	23.2	182	J1-Ol_3	23.8
151	D-Ol_1	23.5	183	J1-Ol_4	23.9
152	D-Ol_2	23.8	184	J1-Ol_5	23.7
153	D-Ol_3	23.8	185	J1-Ol_6	23.6
161	D-Ol_4	23.5	186	J1-Ol_7	23.5
162	D-Ol_5	23.4	187	J1-Ol_8	23.4
164	E-Ol_2	23.1	202	MV2d-Ol_1	23.6
165	E-Ol_3	23	203	MV2d-Ol_2	23.5
166	E-Ol_1	23.6	204	MV2d-Ol_3	23.8
167	E-Ol_2	23.7			
Minimum Fa	22.8(mole%)				
Maximum Fa	24.2(mole%)				